Overlapping Grid Spectral Collocation Methods for Solving Unsteady MHD Nanofluid Flow Over Stretching Surfaces

A THESIS SUBMITTED TO THE UNIVERSITY OF KWAZULU-NATAL

FOR THE DEGREE OF DOCTOR OF PHILOSOPHY

IN THE COLLEGE OF AGRICULTURE, ENGINEERING AND SCIENCE

By

Folarin Oluwaseun Jamiu

School of Mathematics, Statistics & Computer Science

February 2024

Contents

Abstract

This study comprehensively explores diverse magneto-hydrodynamic (MHD) nanofluid flow phenomena over various stretching surfaces with distinctive physical and mathematical attributes. Firstly, we investigated the entropy generation of an unsteady MHD nanofluid flow over a porous inclined stretching surface, incorporating velocity slip and viscous dissipation. Then, the solution methodology utilizing spectral quasilinearization method (SQLM) on overlapping grids for analyzing electromagnetic MHD tangent hyperbolic nanofluid flow over an inclined stretchable Riga surface was considered. This study considers the Dufour effect, activation energy, and heat generation, enriching the understanding of complex fluid dynamics.

Next, we explored the unsteady squeezing flow and heat transport involving silicon SiO_2/kerosene oil nanofluid around radially stretchable parallel rotating disks. Particularly, the upper disk oscillates, adding an extra layer of dynamism to the system that develops a negative pressure situation, which has vast applications in modern-day engineering and medical sciences. Moving on, we employed the bivariate simple iteration method on overlapping grids to analyze unsteady ternary hybrid nanofluid flow with a magnetic dipole over an oscillatory stretching surface. This investigation offers insights into the intricate interplay of magnetic effects and oscillatory stretching, contributing to the broader field of magnetohydrodynamics.

Lastly, the thesis explores the numerical analysis of unsteady Casson ternary hybrid nanofluid flow over a bidirectionally stretching sheet. This study incorporates motile gyrotactic microorganisms and nanoparticle shape factors. This collective body of work contributes to the fundamental understanding of nanofluid dynamics and showcases the versatility of numerical methods in solving complex fluid flow problems across diverse geometries. The findings presented in this thesis pave the way for future advancements in nanofluid research and hold significant implications for various engineering applications.

Overall, the inclusion of overlapping grids in the regular SQLM, BSIM and BSQLM greatly improve their performances in terms of accuracy, computational efficiency, robustness, and ability to effectively tackle complex fluid flow problems.

Declaration 1 - Plagiarism

I, **Folarin Oluwaseun Jamiu**, declare that;

1. The research reported in this thesis, except where otherwise indicated, is my original work.
2. This thesis has not been submitted for any degree or examination at this or any other university.
3. This thesis does not contain other persons' data, pictures, graphs or other information, unless specifically acknowledged as being sourced from other persons.
4. This thesis does not contain other persons' writing, unless specifically acknowledged as being sourced from other researchers. Where other written sources have been quoted, then:
   (a) Their words have been re-written but the general information attributed to them has been referenced,
   (b) Where their exact words have been used, then their writing has been placed in italics and inside quotation marks, and referenced.
5. This thesis does not contain text, graphics or tables copied and pasted from the Internet, unless specifically acknowledged, and the source being detailed in the thesis and in the references sections.

Signed [redacted] Date 02 June 2024

Declaration 2 - Publications

Details of contribution to publications that form part and/or include research presented in this thesis done by the student under the supervision of Prof. S.P. Goqo and Dr. H. Mondal:

1. Entropy Generation of Unsteady MHD Nanofluid Flow Over A Porous Inclined Stretching Surface With Velocity Slip and Viscous Dissipation. Journal of Nanofluids 12, 6(2023),1666-1679. https://doi.org/10.1166/jon.2023.2025

2. EMHD Tangent Hyperbolic Nanofluid Flow Over An Inclined Stretchable Riga Surface With Duffour Effect, Activation Energy And Heat Generation, [**Under review**].

3. Unsteady Squeezing Flow And Heat Transport Of SiO_2/Kerosene Oil Nanofluid Around Radially Stretchable Parallel Rotating Disks With Upper Disk Oscillating. Propulsion and Power Research [**Accepted, December, 2023**].

4. Analysis Of Unsteady Ternary Hybrid Nanofluid Flow With Magnetic Dipole Over An Oscillatory Stretching Surface, [**Under review**]

5. Exploring Numerical Analysis Of Unsteady Casson Ternary Nanofluid Flow Over A Bidirectionally Stretching Surface with Motile Gyrotactic Microorganisms And Nanoparticle Shape Factor, [**Under review**].

Signed [redacted] 02 June 2024

Folarin Oluwaseun Jamiu Date

[redacted]

Signed .... 02 June 2024

Prof. S.P. Goqo Date

Signed [redacted] .... 02 June 2024

Dr. H. Mondal Date

Acknowledgements

Above all, I thank God for providing me with the strength, knowledge, abilities, and opportunities to embark on and successfully conclude this research study.
I extend my deepest gratitude to my supervisors, Prof. S.P. Goqo and Dr. H. Mondal, for their guidance, insightful feedback, and continuous support, which have been the cornerstone of this journey. Your mentorship has been invaluable, shaping not only the trajectory of this thesis but also my growth as a researcher. Sincere appreciation to my friends, Mr. Kazeem Adegbola, Dr. Oyewole Olawale, Dr. H.A. Abass, Dr. Grace Ogwo, Dr. Akindele, and Mr. Sibonelo, for their support and encouragement all through this journey.
I extend special appreciation to the administrators within the School of Mathematics, Statistics, and Computer Science at the University of KwaZulu-Natal.
To my family: Mrs. Folarin, Mr. and Mrs. Ayeni, Sanni Iyabo, Sanni Aminat, Folarin Raphael, Folarin Segun, Oluwatise Ayeni, Temiloluwa Ayeni, Awe Tomiwa, thank you all for your unwavering support, encouragement, and understanding. Your collective belief in my abilities has been a driving force, and I am profoundly grateful for the sacrifices made to see me through this academic journey.

Chapter 1

Introduction

1.1 Background and motivation

Recently, studying nanofluid dynamics has become very important because nanoparticles in fluids improve heat transfer and fluid flow properties [1–3]. Nanoparticles often enhance fluid flow in practical situations, particularly when prioritizing energy efficiency, as they improve thermal conductivity compared to regular fluids [4]. Nanofluids are such fluids in which nanosized particles like metal, metallic oxide, or polymer are combined with base fluids like water, oil, and ethylene so that the particles do not settle. This fluid has a great and considerable industrial and biomedical application in heat and mass transfer. According to studies, nanofluids perform better than regular fluids in terms of heat transfer. It is used for its significant properties in various regions, such as high thermal conductivity, solidity, cooling, and heat transfer. Furthermore, the economic state of operating nanofluids is also affordable as its costs are low. Hybrid nanofluid is a generalized form of nanofluid. Hybrid nanofluids involve two or more types of nanoparticles in a regular fluid; it works as a very good conductor [5, 6]. It can be made of Alumina and Titanium with water, Silver and Zinc oxide with water, single wall carbon nanotube and Alumina with Ethylene glycol, to mention a few. The application of nanofluid and hybrid nanofluid in industrial production is remarkable. They are used to better control heat in devices like freezers, air conditioners, and generators. They also improve the performance of motor pumps and are used in solar energy systems, thermal energy, heat exchangers, making polymers, gas turbines, geothermal energy, aerospace, and wind flow technology. The application of nanofluid-hybrid nanofluid in drug delivery in human bodies is highly considerable. As the applications of nanofluids extend into diiferent man-made fields, there is an increasing demand for a comprehensive understanding of their behaviour under complex conditions. This study addresses this need by focusing on the multi-scale modelling and analysis of advanced nanofluid flows, particularly those influenced by unsteady magnetohydrodynamics (MHD), electromagnetic hydrodynamics (EMHD), and various complex geometries.

Magnetohydrodynamic (MHD) flow comprises an analysis of the behaviour of fluids with electrical conductivity, encompassing substances like plasmas, liquid metals, and ionized gases when subjected to the influence of magnetic fields. MHD flow is a comparatively new and significant area in fluid dynamics. When an electrically conductive fluid passes through a magnetic field, it initiates an electrical field, generating a current that modifies the force acting on the body [7]. According to Faraday's law, if a conductor carries electricity and passes through a magnetic field, an external force tries to move the conductor perpendicularly to the electric field along with the direction of motion and vice versa [8]. The term used to describe this particular force is the Lorentz force. The basic equations of MHD flow are based on the Navier-Stokes equations and Maxwell's equations of electromagnetism. It is associated with the electric-mechanical energy conversion. Plasma, salt-water solution, and molten metal are examples of MHD fluid. MHD fluid has various industrial and technical applications, such as coolant and heating of metal extraction, separation of cells, controlling blood motion during surgery, dynamo, etc. In MHD flow, the motion of the conductive fluid is coupled with electromagnetic effects, creating a dynamic interaction between fluid motion and magnetic fields. Integrating magnetic fields introduces a new layer of complexity to nanofluid dynamics [9]. The unsteady MHD component of this research seeks to unravel the interplay between the magnetic field and nanofluid flow over-stretching and inclined surfaces. Understanding these interactions is crucial for applications where magnetic fields are employed to manipulate nanofluids for enhanced heat transfer or other innovative engineering processes.

Electromagnetic Magnetohydrodynamic flow is a specialized aspect of magnetohydrodynamics that incorporates electrical conductivity and electromagnetic effects into studying fluid dynamics. In EMHD, the conductive fluid under consideration is not only subject to the influence of magnetic fields but also exhibits electrical conductivity, allowing for additional electromagnetic phenomena. The governing equations of EMHD flow are extensions of the magnetohydrodynamic equations, incorporating the effects of electric fields, currents, and electrical conductivity. These equations combine the principles of fluid dynamics, electromagnetism, and electrical conductivity to describe the behaviour of the electrically conductive fluid in the presence of both fluidic and electromagnetic forces. The tangent hyperbolic constitutive equation provides a robust mathematical framework to account for the fluid's non-Newtonian nature. This model effectively captures the fluid's shear-thinning characteristics. Integrating electromagnetic hydrodynamics and tangent hyperbolic nanofluid model further extends the exploration in this study; in particular, the flow is considered along a surface inclined to stretch. The incorporation of heat generation, viscous dissipation, and nanoparticle shapes in this study aims to deepen our understanding of the intricate relationships between these factors, shedding light on the dynamics of nanofluids in environments where electromagnetic forces play a significant role.

Stretching surfaces are important elements in studying fluid mechanics, particularly in the context of boundary layer flows. A flow produced by stretching an elastic material is called flow through a stretching sheet. It can move on its plane with a velocity that varies with the distance from the locus of a fixed point. The shear stress produces the flow. Stretching sheets are usually made of metal or polymer. During the manufacturing of the sheet, the substances are in the molten stage while driven through an extrusion die. After that, it cooled and solidified a distance from the die before reaching the cooling phase. The adjacent fluid particles move due to the tangential velocity the sheet produces and change its convection. The same situation occurs during the production of plastic or rubber sheets. Going through a gaseous media through the unsolidified material where the stretching force is unsteady is essential. Moreover, the cooling process of a huge metal sheet in a bath is another example of the same class, which can be an electrolyte. Under these circumstances, the shrinking sheet triggers the fluid flow. Blowing of glass, casting, fibre spinning, and production of rubber sheets also belong to the flow induced by stretching the sheet. Because of the higher viscosity near the surface, the surface is assumed to influence the liquid (sheet) but not conversely. Flows on stretching surfaces are considered under appropriate boundary conditions, such as uniform and non-uniform stretching velocities and rotating disks with uniform velocity, sometimes referred to as an axisymmetric stretching sheet. Stretching and inclined surfaces are common in various engineering applications, such as coating processes and material deposition [10]. Investigating nanofluid flows over these surfaces, especially in unsteady MHD and EMHD, is motivated by the practical challenges associated with controlling and optimizing fluid behaviour in such complex geometries. This study includes heat generation and viscous dissipation, reflecting real-world scenarios where energy transfer and dissipation are critical considerations. The understanding gained from these aspects contributes to developing more efficient and sustainable thermal management systems.

Nanoparticle shape is an often-overlooked parameter in nanofluid studies [11,12]. Nanoparticle shape analysis opens avenues for tailoring nanofluid properties to meet specific engineering requirements, offering the potential for improved heat transfer, enhanced behaviour characteristics, and optimized performance in a wide range of applications. By incorporating this aspect into the analysis, this study seeks to unravel how different shapes influence nanofluid behaviour, offering valuable insights for designing nanofluids tailored to specific applications. The exploration of nanofluid flows with a magnetic dipole represents a step toward understanding how magnetic fields affect the dynamics of nanofluids in a broader sense. This research is motivated by the potential applications of controlled magnetic fields in manipulating nanofluid behaviour for various engineering purposes.

To investigate a flow problem, a mathematical model is established by considering several laws of conservation and boundary conditions. In this study, we considered numerical modelling and solution of PDEs that describe flow, thermal, and mass transfers in problems of different configurations filled with nanofluids and hybrid nanofluids. Most of the practical models in fluid dynamics are in the form of differential equations. Differential equations are pivotal in describing the fundamental principles governing fluid dynamics. The study of fluid motion, whether in the context of liquids or gases, relies on formulating and solving differential equations that capture the conservation laws of mass, momentum, and energy. The governing equations for fluid dynamics are typically derived from the principles of continuum mechanics, providing a mathematical framework for understanding and predicting fluid characteristics [13–16]. To capture these models' real-world processes, they are frequently expressed as extremely convoluted partial differential equation systems. Sometimes, these equations must be modified into ODEs to be easily solved via traditional analytical or numerical methods. However, some important physical characteristics may need to be recovered to transform the differential equations from partial to ordinary. Therefore, developing methods to handle ODEs and PDEs without loss is important. The

ODEs may still preserve all the aspects of the physical nature of the problem. Researchers have devised various computational techniques, including finite differences, finite elements, and finite volume methods, which apply to solving complex nonlinear PDEs. However, the computational efficiency of such numerical methods may be compromised by the need for a substantial number of grid points to attain precise outcomes. This research mainly focuses on analyzing and solving different fluid dynamics problems using robust numerical solution techniques such as SQLM, overlapping SQLM, BSQLM, and BSSIM. Researchers have shown these methods to be accurate and computationally efficient with fewer grid points. [17–19].

This thesis addresses a critical gap in the understanding of advanced nanofluid flows by employing a multi-scale approach. The motivation is rooted in the necessity to unlock the full potential of nanofluids in various engineering applications, from heat exchangers to biomedical devices, by comprehensively modelling and analyzing the intricate interplay of magnetic fields, complex geometries, heat generation, viscous dissipation, motile microorganism, and nanoparticle shapes. The findings of this research are anticipated to pave the way for innovations in nanofluid technology and contribute to the development of more efficient and sustainable engineering solutions. Furthermore in this chapter, we will highlight brief discussions on each of the focal points of the research and relevant numerical techniques in the literature. The concluding part of this chapter presents the research objectives and thesis structure statement.

1.2 Newtonian and non-Newtonian fluids

Fluids are a fundamental aspect of physics and engineering, and their behaviour is often categorized based on their viscosity response to shear stress. Studying Newtonian and non-Newtonian fluids is very important, especially for thermal and mass transfer in commercial and industrial systems. Newtonian fluids flow easily, and the force needed to move them is directly proportional to their flow. Non-Newtonian fluids, however, have more complicated flow behaviour. This distinction has wide-ranging implications in various industrial processes, from food manufacturing to pharmaceuticals. Newtonian fluids are characterized by a constant viscosity, meaning the fluid's resistance to flow remains consistent regardless of the applied stress or shear rate. Fluids such as air, water and most common liquids and gases exhibit this type of behaviour [20]. The simplicity of Newtonian fluid behaviour makes it a convenient assumption in various fluid mechanics analyses. On the other hand, non-Newtonian fluids exhibit a variable viscosity, where the viscosity is influenced by factors such as shear rate, temperature, and time [21]. The relationship between shear stress and shear rate in non-Newtonian fluids is nonlinear and often described by constitutive equations specific to the fluid type [22,23]. Non-Newtonian fluids exhibit different rheological behaviours, and various mathematical models have been developed to characterize and describe their flow properties. These models include power law, Carreau, Oldroyd - B, Jeffreys, Maxwell, and Casson. Non-Newtonian fluids exhibit non-isothermal, viscoelastic behaviour where viscosities are either independent of applied shear rates (Boger fluids) or whose viscosities are shear-rate dependent (Oldryd-B fluids). The complexity of these fluids makes understanding the behaviour of non-Newtonian fluids a very challenging task in recent times. Non-Newtonian fluids are crucial in various industrial processes, such as food manufacturing, pharmaceuticals, and cosmetics, where their unique flow properties are intentionally utilized. The vast applicability of non-Newtonian fluids has earned recognition, and as such, different models under some interesting physical conditions have been presented in literature [24–26]. Behaabadi et al. [27] conducted a study examining the rheological characteristics and heat transfer efficiency of multi-walled carbon nanotube (MWCNT)-water nanofluid flow within vertical tubing. Eshgarf and Afrand [28] explored the impact of temperature on non-Newtonian fluids, highlighting a significant decrease in viscosity and elastic modulus with rising temperature. Entropy production in non-Newtonian flows was studied by Khan et al. [29] and Riaz et al. [30], revealing the suppression of flow velocity and increased entropy production rate with heightened Darcy and electric field parameters. Wang et al. [31] investigated a radiative flow scenario with non-Newtonian characteristics, encompassing considerations of entropy generation and a dual chemical process. Waqas [32] investigated thermal transfer phenomena within the flow of ferromagnetic non-Newtonian fluids, and Yoshino et al. [33] applied the Boltzmann technique to investigate the flow of non-Newtonian fluids within a cylinder having a porous surface. In this study, we have focused on non-Newtonian nanofluid models with different configurations and conditions.

1.2.1 Casson fluid model

The Casson fluid model, first proposed by Casson [34], has emerged as a powerful tool for analyzing various flow scenarios. This model captures the unique behaviour of plastic fluids, characterized by shear thinning, yield stress, and higher shear viscosity. Notably, when the wall shear stress significantly exceeds the yield stress, the Casson fluid behaves as a Newtonian fluid [35]. The model can estimate the flow characteristics of different fluids, like bodily fluids, foams, cosmetics, and syrups. This has cemented its status as a leading model for non-Newtonian fluids with a yield value. Casson fluid research is important in many areas, including heat transfer mechanisms, food manufacturing, bioengineering methods, and a wide range of mechanical, chemical, and industrial applications. Researchers have investigated the properties of Casson fluids in many geometrical configurations as a result of these numerous uses. Oyelakin et al. [36] utilized SQLM to examine MHD Casson nanofluid flow across a time-varying stretchable surface. Their findings unveiled that when the Casson fluid parameter increased, the fluid exhibited Newtonian behaviour. Similarly, Nandkeolyar [37] utilized SQLM for analysis of MHD Casson transport characteristics along an elongating sheet. Their findings demonstrated that elevating the yield stress decreased the thickness of the momentum boundary layer along the x-axis and mitigated variations in shear stress along the same axis. These investigations highlight the rich research landscape surrounding Casson fluid and its applications. As researchers continue to explore the model, it is poised to be prominent in advancing the understanding of complex fluid flow phenomena across various scientific and engineering disciplines.

1.3 Nanofluid, hybrid and ternary hybrid nanofluid

Nanofluids consist of colloidal suspensions comprising solid particles at the nanometer scale, typically metallic or oxide nanoparticles, dispersed within a regular fluid, like water, engine oil, kerosene, or ethylene glycol, as originally proposed by Choi and Eastman. [38]. These fluids demonstrate improved thermal characteristics relative to their base fluids, making them promising candidates for applications in industrial processes, technology, biomedical, and various engineering processes. The presence of nanoparticles in nanofluids enhances convective heat transfer, making them promising for applications in heat exchangers, cooling systems, automobiles and thermal management [39]. Researchers have extensively explored nanofluid models for different physical configurations [40–43]. Employing single and multi-phase models, Saha and Paul [44] explored heat and mass transfers along with entropy generation in the movement of a fluid consisting of titanium oxide and water through a pipeline. Their findings revealed a higher thermal transference coefficient in the multi-phase model and emphasized the significance of different boundary conditions in achieving optimal outcomes. Domairry and Hatami [45] employed the differential transformation approach to solve equations involving copper-water fluid flow between parallel plates. The findings showed that increasing nanoparticle percentage, Eckert number, and squeezing parameter improved heat transfer in the nanofluid. Hatami and Ganji [46] addressed challenges posed by the viscoelasticity of the fluid, using Runge–Kutta technique in examining the movement of nanofluid via a porous space in-between two cylindrical surfaces. Shah et al. [47] examined the influences of thermal radiation and the Hall current parameter on the transport of micropolar nanofluid across a rotating surface. The results demonstrated diminished velocity characteristics as Hall current was elevated, and a significant thermal spike associated with rising thermophoresis was observed. Li et al. [48] aimed to enhance the efficiency of a compact heat exchanger by utilizing an Al_2O_3 nanofluid within a micro-channel featuring protrusions and dimples. Kameswaran et al. [49] investigated combined influences of binary processes, the Soret effect, as well as internal friction on magnetohydrodynamic nanofluid flow near a contracting sheet. Results unveiled that utilizing a copper-water nanofluid led to a reduced thermal transfer rate compared to a mercury-water nanofluid, a revelation contradicting theoretical predictions attributed to copper's superior thermal conductivity in contrast to mercury. Oyelakin et al. [50] explored the influence of transient nanofluid flow along a stretching sheet with convective boundary conditions about the Casson parameter, thermal dissipation, and magnetic field effects. Dhlamini et al. [51] examined impacts of internal energy and chemical reactions on convective nanofluid transport over boundless sheet, observing how a higher thermophoretic number facilitated flux away from the plate surface, consequently diminishing the mass flux profile.

Hybrid nanofluids are advanced fluid systems that combine different types or sizes of nanoparticles in a regular fluid. This combination is designed to harness synergistic effects of multiple nanoparticles and enhance specific fluid properties beyond what can be achieved with individual nanofluids. Compared to single-nanoparticle nanofluids, hybrid nanofluids offer better stability in terms of dispersion and, hence, reduce the issue of nanoparticle agglomeration. Saima and Nawaz [52] used the finite volume method to analyze improvement in fluid thermal performance using micro-structured configurations with hybrid nanoparticles. They observed a notable increase in the thermal efficiency of the working fluid due to the presence of hybrid micro-structure components. Eid and Nafe [53] presented an analysis of fluid dynamics and heat transfer phenomena caused by an exponentially shrinking surface coated with hybrid nanoparticles comprising magnetite (Fe_3O_4) and copper dispersed in ethylene glycol. A significant discovery highlights that increasing the concentration of Fe_3O_4 nanoparticles boosts the heat transfer rate of the hybrid nanofluid under shrinking conditions, whereas the reverse trend is observed in an expanding scenario. Recently, researchers have taken the concept of hybrid nanofluids further by introducing a third component, such as additives or additional nanoparticles, to the fluid system. This new fluid type is called ternary hybrid nanofluid; this approach aims to achieve more sophisticated control over the fluid's properties for specific applications [54]. Ramzan et al. [55] explored the two-dimensional flow of a Carreau-ternary hybrid nanofluid under the influence of a magnetic field over a stretching surface. The study demonstrated that higher values of the radiation parameter correlated with increased heat transfer rates.

1.4 Thermophoresis and Brownian motion

Nanofluids, consisting of nanoparticles suspended in a base fluid, are crucial in enhancing heat and mass transfer in fluid flow systems [56]. The nanoparticles within these fluids experience various phenomena that influence their behaviour and impact the overall flow dynamics. One such phenomenon is thermophoresis, which occurs due to temperature gradients in the fluid. When subjected to a temperature gradient, nanoparticles experience a force that causes them to move randomly, distinct from the buoyancy-driven motion observed in natural convection. This thermophoretic force alters the distribution of nanoparticles within the fluid, influencing the system's overall characteristics related to the transfer of heat and mass. The thermophoretic force acting on a particle can be described by the Soret coefficient, which quantifies the mobility of particles in response to a temperature gradient. When a temperature gradient is applied to a fluid containing suspended particles, the particles experience a force directed from regions of higher temperature to lower temperature or vice versa, depending on their thermal properties and the characteristics of the fluid medium. Thermophoresis has significant implications in various fields, including heat transfer enhancement, aerosol science, and particle deposition processes. In nanofluid-based heat transfer systems applications, thermophoresis plays a crucial role in controlling the distribution and transport of nanoparticles within the fluid, thereby influencing heat transfer rates and overall system performance.

Brownian motion refers to the random motion of particles suspended in a fluid caused by collisions with surrounding molecules [57]. In the case of nanofluids, the change in kinetic energy resulting from temperature differences leads to a non-uniform velocity profile within the system. As the nanoparticles undergo Brownian motion, their kinetic energy is converted into thermal energy, thereby enhancing the fluid's overall thermal profile. The random motion of particles in Brownian motion arises from thermal fluctuations in the fluid, leading to erratic trajectories for each particle. The trajectory of a particle undergoing Brownian motion is characterized by its stochastic nature, which exhibits unpredictable movements with continuous changes in direction and velocity. In nanofluids, Brownian motion plays a critical role in dispersing nanoparticles within the fluid and influencing their transport properties. The random movements of nanoparticles lead to their dispersion throughout the fluid, affecting properties such as viscosity, thermal conductivity, and heat transfer coefficients. Brownian motion also contributes to nanofluid's stability and rheological behaviour, influencing their flow characteristics and overall performance in various engineering applications.

1.5 Flows through porous media

Fluid flow through porous media is critical in various natural and engineering processes. Porous media are materials characterized by interconnected void spaces, known as pores, within a solid matrix. These include soils, rocks, biological tissues, and engineering materials like filters and membranes. A porous medium is a very important factor when experimenting with fluid flow. When fluid passes through a porous medium, fluid particles may get stuck in those pores, which causes a reduction in the velocity of the fluid. Darcy's law and mass conservation can investigate the behaviour of fluid flow in this kind of medium. Understanding the behaviour of fluids in porous media is essential for optimizing processes such as groundwater remediation, oil recovery, filtration, and drug delivery. Researchers and engineers can analyze and predict fluid flow behaviour in porous media by employing principles such as Darcy's law and mass conservation, improving process efficiency and resource utilization [58].
Porosity, a fundamental property of porous media, quantifies the volume of void space within the medium relative to its total volume. Expressed as a decimal, fraction, or percentage, porosity (denoted as p) is mathematically defined as:

$$p = \frac{\upsilon}{V}$$

Where, υ represents the volume of the void spaces or pores within a material. It is the total volume of the empty spaces that can be filled with fluids (such as water, air, or oil) within the porous medium, and V represents the total volume of the material, including both the solid matrix and the void spaces. The equation illustrates that porosity p ranges between 0 and 1, exclusive, representing the fraction of space within the medium. When $v = V$, indicating that the entire volume is filled with solid material and devoid of void space, the porosity is 0, implying the medium is non-porous or comprises a free fluid phase [59]. Porosity is a fundamental parameter in characterizing porous materials and is crucial in various fields such as hydrogeology, petroleum engineering, soil science, and materials science. The measurement of the ability of a porous medium to permit the fluid to flow through it is called the permeability of the medium. It depends on the characteristics of both the solid and fluid. The unit of the permeability is Darcy, and so it can be obtained from Darcy's law.

Darcy's law describes the flow passing through a porous medium. It was formulated experimentally by Henry Darcy in 1856. This experiment is similar to the fluid flow through the capillary tubes (Hagen-Poiseuille flow). Darcy's law is comparable with Fourier's law of heat conduction or Fick's law of diffusion. Darcy's law states that the velocity is linearly proportional to the pressure gradient. Mathematically, it is defined by:

$$\tilde{v} = -\frac{k}{\mu}\nabla p$$

where $\tilde{v}$ is the fluid velocity, k is the medium's permeability, μ is the viscosity and ∇P is the pressure gradient. Darcy's law is valid for Newtonian fluid having low Reynolds number, high viscous fluid (creeping flow), laminar incompressible fluid, constant porosity and permeability, homogenous and isotropic medium. It is not applicable for medium with large pores because, in this medium, fluid drains out immediately due to gravity, making it difficult to maintain laminar flow. For incompressible fluid in a porous medium, the pressure is Laplacian, $\nabla^2 p = 0$ and the stream function is bi-harmonic ($\nabla^4 \psi = 0$). Darcy's law can be applied when the order of the Reynold number, Re, is less than one. If it is between 1 and 10, we have a transition state. When the order of the Reynold number is greater than one, we apply the modified Darcy's law, Darcy-Forchheimer law or simply non-Darcy law, which considers inertial effects. The mathematical expression in this case is given as follows:

$$-\nabla p = \frac{k}{\mu}\tilde{v} + b\rho|\tilde{v}|\tilde{v}$$

where, $b = \frac{1.75(1-p)}{p^3 d}$ is an experimental constant which depends on the porosity and diameter of the pores, d. The Darcy's and modified Darcy's laws cannot be applied to Power fluids. Power law fluids are a subclass of non-Newtonian fluids whose viscosity depends on shear stress. The mathematical form of Darcy's law for power-law fluid is given by:

$$\tilde{v}^n = -\frac{k}{\mu}\nabla p$$

where n is the power law index. If n=1, we have the Darcy's Law for Newtonian fluids. The most useful application of Darcy's law is oil extraction from the underground petroleum reservoir. Researchers are investigating the oil enhancement process by polymer flooding, steam flooding, chemical reaction flooding, etc, to reduce the viscous fingering and enhance the oil recovery, in a process known as EOR (enhanced oil recovery). A theoretical investigation of the behaviour of power fluid in a porous medium has been done in Chapter 3, which will be significant for EOR.

1.6 Classifications of flow

Flow classification is crucial in fluid dynamics for understanding and analyzing the behaviour of fluids in various situations. Fluid flows can be classified based on several criteria, including velocity distribution, turbulence, and external forces acting on the fluid. Here, we'll explore different classifications of flows:

1.6.1 Steady and unsteady flows

Steady and unsteady flows play an important role in understanding fluid dynamics, with their distinction based on the temporal dependence of fluid properties at different points within the fluid domain [60, 61]. In a steady flow, the fluid properties, such as velocity, density, temperature, and pressure, remain constant concerning time at each point throughout the fluid motion. Mathematically, this is expressed as the partial derivative of the fluid property concerning time being zero ($\frac{\partial P}{\partial t} = 0$), where P represents any fluid property varying with spatial coordinates (x, y, z). For instance, the fluid properties do not change with time in steady flow through a pipe [62]. Conversely, the fluid properties exhibit temporal variations at different points within the fluid domain in an unsteady flow. Here, the partial derivative of the fluid property concerning time is non-zero ($\frac{\partial P}{\partial t} \neq 0$), indicating time-dependent behaviour. For instance, consider the velocity of a flow at two different instants of time, $t = t_1$ and $t = t_2$. If the velocity changes from $1ms^{-1}$ to $2ms^{-1}$ between these instants, the flow is deemed unsteady despite uniformity in velocity distribution at any given instant. This illustrates that while the flow may exhibit uniform characteristics spatially, its temporal variability renders it unsteady [63]. Moreover, classifying a flow as steady or unsteady is relative and contingent upon the observer's frame of reference. For instance, imagine someone standing on a bridge observing a speedboat traversing the water beneath. From their vantage point, they perceive fluctuations in water velocity as the boat moves past, thus deeming the flow unsteady. However, if the same observer were aboard the boat, they would experience a consistent water velocity relative to the boat's motion, leading to the perception of a steady flow. Hence, classifying a flow as steady or unsteady is inherently subjective and contingent upon the observer's reference frame. This example underscores the notion that the distinction between steady and unsteady flows is not absolute but context-dependent. The same flow can exhibit different characteristics based on the observer's reference frame, highlighting the nuanced nature of fluid dynamics analysis.

1.6.2 Uniform and non-uniform flows

Uniform and non-uniform flows represent two fundamental classifications in fluid dynamics, describing the spatial variation in flow characteristics such as velocity, pressure, and density across the fluid domain [64]. In a uniform flow, the flow properties remain constant at every point within the fluid domain. This means that the velocity, pressure, and other flow parameters do not change as one moves from one point to another within the fluid. Mathematically, the velocity vector and other flow properties are constant concerning position for a uniform flow. This can be expressed as:

$$\frac{\partial \mathbf{V}}{\partial \mathbf{r}} = 0$$

Where $\mathbf{V}$ and $\mathbf{r}$ are velocity and position vectors. Uniform flow includes flow through a long straight pipe with a constant cross-sectional area and flow in a long open channel with a constant depth and slope [65].

In contrast, non-uniform flow is characterized by variations in flow properties across different points within the fluid domain. This means that the velocity, pressure, or other flow parameters change from one location to another. Non-uniform flow can arise due to changes in the geometry of the flow domain, such as variations in channel width, changes in the cross-sectional area of a pipe, or the presence of obstacles or boundaries affecting flow. Mathematically, non-uniform flow is described by non-zero velocity gradients, indicating spatial variations in flow properties. This can be expressed as:

$$\frac{\partial \mathbf{V}}{\partial \mathbf{r}} \neq 0$$

Understanding the distinction between uniform and non-uniform flows is crucial in various engineering applications, including hydraulic engineering, aerodynamics, and heat transfer. Proper characterization of flow patterns and gradients is essential for designing efficient systems, predicting flow behaviour, and ensuring the optimal performance of engineering structures and devices [66].

1.6.3 Rotational and irrotational flows

Rotational and irrotational flows are two important classifications in fluid dynamics, describing the behaviour of fluid motion about the presence or absence of fluid rotation [67].

In a rotational flow, fluid particles exhibit rotational motion as they move through the flow field. This means the fluid elements possess angular momentum and experience rotation about their axes as they translate through space. In other words, the velocity vectors at different points in the flow field induce a net rotation of the fluid particles. Mathematically, rotational flow is characterized by non-zero vorticity, representing fluid elements' local spinning motion. The presence of vorticity in rotational flow implies that the curl of the velocity field is non-zero:

$$\nabla \times \mathbf{V} \neq 0$$

Rotational flows include flow around a propeller, vortex shedding behind a cylinder, and swirling motion in tornadoes and hurricanes. The fluid motion exhibits a distinct swirling pattern in these cases, and the vorticity varies spatially throughout the flow field [68, 69].

In contrast, irrotational flow is characterized by the absence of fluid rotation. In an irrotational flow, fluid particles move without inducing rotational motion about their axes as they translate through space. This means that the velocity vectors at different points in the flow field are aligned and do not produce any net rotation of the fluid particles. Mathematically, irrotational flow is represented by zero vorticity:

$$\nabla \times \mathbf{V} = 0$$

Irrotational flow is often observed in practical scenarios, including idealized fluid systems such as potential flows and flows over streamlined bodies. In these cases, the fluid motion is smooth and lacks the swirling patterns associated with rotational flows. Examples of irrotational flows include flow over an airfoil at low attack angles and through a long, straight pipe with smooth walls. The presence or absence of vorticity influences phenomena such as drag, lift, and turbulence and plays a significant role in the design and optimization of engineering systems ranging from aircraft wings to hydraulic turbines [70, 71].

1.6.4 Laminar, transitional and turbulent flows

Laminar flow is a smooth, orderly flow regime characterized by the fluid moving in parallel layers, with little to no mixing between adjacent layers. In laminar flow, fluid particles move along well-defined paths, and the velocity profile across the flow remains relatively constant. This results in a predictable and stable flow pattern with minimal turbulence and mixing [72, 73]. Laminar flow is typically observed at low Reynolds numbers, where viscous forces dominate over inertial forces. Examples of laminar flow include the flow of viscous fluids through small pipes, blood flow in capillaries, and the gentle flow of water in a quiet stream [74]. Turbulent flow is a chaotic, disorderly flow regime characterized by irregular fluctuations in velocity and pressure throughout the flow field [75, 76]. In turbulent flow, fluid particles move erratically, with swirling eddies and vortices forming spontaneously. These turbulent eddies enhance mixing and momentum exchange, increasing fluid dispersion and energy dissipation. Turbulent flow is typically observed at high Reynolds numbers, where inertial forces dominate over viscous forces. Examples of turbulent flow include the flow in rivers and streams, airflow over buildings and aircraft wings, and the mixing of fluids in industrial processes. Transitional flow occurs at intermediate Reynolds numbers between laminar and turbulent flow regimes. In transitional flow, the flow behaviour exhibits characteristics of both laminar and turbulent flows, with intermittent fluctuations in velocity and flow patterns. As the Reynolds number increases, the laminar flow may become unstable, leading to small-scale turbulent eddies and increased mixing within the flow [77,78]. Transitional flow is often observed during the transition phase from laminar to turbulent flow in various fluid systems, such as through pipes, boundary layers over surfaces, and airflow around vehicles. The choice of flow regime significantly influences the design, performance, and efficiency of engineering systems, ranging from pipelines and heat exchangers to aircraft and vehicles. By characterizing the flow regime accurately, engineers can optimize the design and operation of fluid systems to achieve desired performance and functionality.

1.7 Heat, mass and motile microorganisms transfers

Heat transfer analysis in nanofluid flow is a dynamic area of research with widespread implications for improving thermal management systems [79]. One of the primary features of nanofluids is their significantly enhanced thermal conductivity compared to regular fluids. The superior heat transfer performance of nanofluids makes them attractive for applications in heat exchangers, cooling systems, and thermal management, with enhanced conductivity that allows for improved heat dissipation and more efficient thermal transport. The effective thermal conductivity of a nanofluid is influenced by factors such as particle size, shape, concentration, and the choice of base fluid; however, mechanisms such as Brownian motion, thermophoresis, and convection contribute to the overall heat transfer behaviour in nanofluids [80,81]. Mass transfer in nanofluid flow involves the movement of chemical species within a fluid containing nanoscale solid particles dispersed in a base fluid with diffusion and convection. While much of the focus in nanofluid research has been on thermal properties, mass transfer is also a critical aspect, especially in application areas (such as transport of therapeutic agents and drug delivery in biomedical, water treatment and remediation in environmental processes) where the transport of species, such as ions or reactants, is essential [82]. Considerable research has been conducted on heat and mass transfer in nanofluids. This includes studies such as that of Makinde et al. [83], which investigated combined effects of buoyancy forces and thermal transference on the mass flux and heat exchange within a nanofluid flowing past a shrinkable, heated sheet. Tlili et al. [84] investigated the coupled heat and mass transfer phenomena in nanofluid flow along a wedge geometry, incorporating the Navier slip condition and convective boundary considerations. Khan et al. [85] examined numerical heat and mass transfer analysis in a heated vertical plate geometry using a third-grade nanofluid model, considering potential nanoparticle interactions. Ali et al. [86] investigated heat transfer in a rotating magnetohydrodynamic flow system with convective cooling, focusing on the direct link between heat/mass transfer rates and velocity slip conditions.

Motile microorganism transfer analysis in nanofluid flow involves understanding how the presence of nanoscale solid particles in a fluid affects the behaviour and transport of motile microorganisms. This study area is particularly relevant in biotechnology, environmental science, and biomedical engineering, where the interaction between microorganisms and nanoparticles in a fluid medium can have significant implications [87]. Different researchers have examined the idea of motile microorganisms in nanofluids. In particular, Waqas et al. [88] extensively analyzed gyrotactic motile microorganisms' impacts on pseudoplastic nanofluid flow over a bidirectionally stretching Riga surface with exponential heat flux. The outcome of their research showcased the reverse relationship between motile microorganisms and Peclet number. The basic mechanisms of microorganisms' movements are convection transport (transport via the nanofluid), self-propelled motion and Brownian movement (usually due to diffusion processes).

1.8 Boundary layers

In fluid dynamics, boundary layers play an important role in characterizing the behaviour of flow near solid surfaces. Boundary layers are regions where significant gradients in velocity, temperature, concentration, or other properties occur due to the influence of the adjacent surface. Understanding the dynamics of different boundary layers is crucial for various applications, from heat transfer and mass transport to biological processes involving microbial activity. Throughout this study, we explored velocity, thermal, concentration, and microbes' boundary layers. The velocity boundary layer is crucial in fluid dynamics, particularly in understanding fluid flow behaviour near solid surfaces. According to White [89], it is a fine region near a solid boundary where the velocity of the fluid undergoes a significant transition from zero at the wall (due to the no-slip condition) to the free-stream velocity away from the surface. This phenomenon occurs due to the dominance of viscous effects near the boundary, leading to a gradual increase in velocity across the boundary layer. The thickness of the velocity boundary layer grows with distance from the surface, and its characteristics depend on the flow regime, whether laminar or turbulent. Researchers often employ mathematical models and experimental techniques to study velocity boundary layers. For instance, the classical approach to analyzing laminar boundary layers was pioneered by Prandtl, who introduced the concept of boundary layer equations to describe the velocity profile near a solid surface. These equations, coupled with appropriate boundary conditions, allow researchers to predict the velocity distribution within the boundary layer and determine key parameters such as the boundary layer thickness and shear stress [90].

Like the velocity boundary layer, the temperature boundary layer is another important phenomenon in heat transfer applications. According to Incropera and DeWitt [91], it is a region near a solid surface where significant gradients in temperature occur due to convective heat transfer between the surface and the fluid. Thermal energy is transferred from the solid surface to the surrounding fluid within the temperature boundary layer through conduction and convection. As a result, the temperature gradually changes from the wall temperature to the bulk fluid temperature across the boundary layer. Understanding temperature boundary layers is crucial for optimizing heat exchangers, thermal management systems, and various industrial heat transfer processes.

The concentration boundary layer, such as chemical reactions or pollutant dispersion, is critical in mass transport processes. According to Bird et al. [92], it is the region near a solid surface where significant gradients in concentration occur due to diffusion and convection processes. Mass transfer phenomena govern the transport of substances between the fluid and the surface within the concentration boundary layer. As a result, the concentration of dissolved or suspended substances varies from the surface to the bulk fluid. By solving appropriate transport equations and boundary conditions, researchers can predict concentration profiles within the boundary layer and assess the efficiency of mass transfer processes in various environmental and industrial systems.

In recent years, increasing interest has been in studying boundary layers associated with microbial activity in fluid environments. Microbial boundary layers refer to regions near solid surfaces where microorganisms, such as bacteria and algae, form biofilms or colonies. These boundary layers are characterized by gradients in microbial concentration, metabolic activity, and nutrient availability, which play a crucial role in microbial behaviour and ecosystem dynamics [93]. Understanding microbial boundary layers is essential for various applications, including wastewater treatment, bioremediation, and medical microbiology.

1.9 Thermal radiation and nanoparticle shapes

Thermal radiation is the process by which energy is emitted, transmitted, and absorbed as electromagnetic waves due to the temperature difference between surfaces. It is a significant mode of heat transfer in high-temperature applications, such as solar energy systems, spacecraft re-entry, and nuclear reactors. In nanofluids, the presence of nanoparticles influences the fluid's radiative properties, which explains the applications in solar collectors, radiators, heat exchangers, and thermophotovoltaic devices, to mention a few. Pal [94] stressed the importance of incorporating thermal radiation to model the flow and heat transfer in a viscous fluid flowing past a dynamically moving stretching sheet. The governing equations for nanofluid flow with thermal radiation can be derived from the mass, momentum, and energy conservation laws. The energy equation includes a term for radiative heat transfer, typically modelled using the Rosseland approximation. The Rosseland approximation is a simplified method for calculating radiative heat transfer in a participating medium, such as a nanofluid. It assumes that the radiation intensity is proportional to the temperature gradient [95, 96]. Rosseland's approximation can be modelled linearly or non-linearly. Linear thermal radiation is a simplified model of thermal radiation that assumes that the intensity of the radiation is proportional to the temperature difference between the emitting and absorbing surfaces. This model is often used in nanofluid flow applications because it is relatively simple to compute and can provide reasonable results for low-temperature applications. Several studies have investigated the effects of linear thermal radiation on nanofluid flow. These studies have shown that linear thermal radiation can significantly impact the heat transfer and flow characteristics of nanofluids [97, 98]. Nonlinear thermal radiation is a more complex model of thermal radiation that accounts for the variation of the radiation intensity with temperature. This model is more accurate than linear thermal radiation for high-temperature applications. Studies have shown that nonlinear thermal radiation can increase the heat transfer rate from a hot surface to a nanofluid by up to 40% [99, 100]. In the current study, we have considered both linear and nonlinear Rosseland approximations in the different models used.

The shape of nanoparticles can significantly impact the properties and performance of nanofluids. For example, nanoparticles with non-spherical shapes, such as cylinders, platelets, or needles, can have a higher surface area-to-volume ratio than spherical nanoparticles. This can enhance heat transfer, rheological properties, and other important characteristics of nanofluids [101–103]. In chapters 5 and 6, we have examined the influence of differently shaped nanoparticles in ternary hybrid nanofluid flow concerning distinct physical geometries.

1.10 Boundary conditions

Boundary conditions are the interactions between the fluid and its surroundings at the domain's boundaries, providing essential constraints for solving fluid flow problems. Boundary conditions are crucial for solving fluid dynamics problems because they define the physical constraints and interactions at the domain's boundaries. These conditions ensure the mathematical model accurately represents the physical system under consideration [104]. By imposing appropriate boundary conditions, engineers and scientists can simulate real-world fluid flow scenarios and predict the behaviour of fluids in different environments. Different boundary conditions include Dirichlet boundary Condition, Neumann boundary condition, mixed boundary condition, periodic boundary condition, and inlet and outlet boundary conditions. Dirichlet boundary condition specifies the value of the dependent variable (e.g. velocity, temperature, pressure) directly at the boundary [105]. For example, in flow along a surface, the Dirichlet boundary condition may prescribe the velocity of the fluid at the surface. Neumann boundary conditions specify the gradient of the dependent variable normal to the boundary. For instance, in heat transfer problems, a Neumann boundary condition may define the heat flux rate across the boundary. Mixed boundary conditions combine elements of both Dirichlet and Neumann conditions. They specify both the value of the dependent variable and its normal gradient at the boundary. In this study, we have applied these conditions concerning different nanofluid configurations.

In an impermeable flat plate, the velocity boundary condition is $u = 0$ for no slip and $v = 0$ for impermeability at the surface ($y = 0$). For porous sheet $v = v_0$ at the surface. For a linear stretching sheet, it can be taken as $u = u_w(x) = ax$. While for the bidirectional linear stretching sheet, stretch velocity along $y-$ direction $v = v_w(x) = bx$ is incorporated. In the case of nonlinear stretching surface (exponentially stretching sheet), $u = u_w(x) = ax^m$, for bidirectional stretching sheet in this case, $v = v_w(x) = bx^n$. A slip boundary condition occurs when the relative velocity of the fluid and the stretching sheet is nonlinear. Slip velocity condition at the surface can be assumed as $u = u_w + k\frac{\partial u}{\partial y}$. Beyond the boundary layer ($y \to \infty$), the velocity achieves the ambient velocity U_∞ in boundary layer approximation. For thermal boundary conditions, when the heat transfer rate is very high, the wall temperature condition is the Dirichlet boundary condition, i.e. $T = T_w$ at $y = 0$. When there is an extremely low rate of heat exchange, the boundary condition can be taken as $\frac{\partial T}{\partial y}|_{y=0} = 0$, which is the Neumann boundary condition and the wall is adiabatic or works as an insulator. But when the nature of heat transfer is in-between this two-above situation, the mixed convective thermal boundary condition is considered, $-k\frac{\partial T}{\partial y}|_{y=0} = h_f(T_w - T_f)$, h_f is the heat transfer coefficient of the fluid and T_f is the fluid temperature. The ambient thermal condition is T_∞. We have considered similar boundary conditions for concentration. Another type of wall concentration in scenario of nanofluid movement across an elongating sheet, we used in chapter 2 which is given by $D_B \frac{\partial C}{\partial y} + \frac{D_T}{T_\infty}\frac{\partial T}{\partial y} = 0$, it means there is no the wall mass flux.

1.11 Numerical solution techniques

The complexity of the partial differential equations in fluid dynamics requires using robust numerical methods to solve them. Analytical methods often fall short when dealing with nonlinear partial differential equations (PDEs) that characterize real-world fluid systems. Consequently, engineers and scientists rely heavily on numerical approaches to analyze, design, and optimize these systems. Analytical solution techniques such as transform methods, perturbation, Adomian decomposition, homotopy are limited in usage for nonlinear PDEs because they become very cumbersome, and convergence of the solution is not guaranteed on time. Liao [106] examined a direct comparison between homotopy analysis and homotopy perturbation methods. The major advantages of the homotopy method over homotopy perturbation which include ability to handle strong non-linear problems, better stability, better convergence, more systematic approach to controlling solution errors and less reliance on good inital guesses were highlighted. On the other hand, numerical techniques allow us to approximate the solutions of governing equations that describe fluid flow, heat transfer, and other phenomena related to fluids. Despite the diverse array of existing numerical techniques for solving nonlinear differential equations, such as the famous Runge-Kutta [107], finite difference [108], finite element [109], element free Galerkin [110], and Keller-Box method [111], these approaches often face limitations in terms of computational efficiency, convergence rates, and the need for dense grids to achieve accuracy. The ongoing pursuit of more effective numerical techniques for addressing nonlinear problems continue to be an area of ongoing interest and research. Among the various approaches, spectral methods have emerged as promising options due to their advantageous computational characteristics. These methods offer reduced computational expenses, faster convergence rates, and the capability to achieve precise solutions with minimal grid points, particularly for smooth solutions. The spectral collocation method stands out as particularly suitable for practical applications. Recent advancements in spectral collocation-based techniques encompass the spectral perturbation method, spectral homotopy analysis method, spectral quasilinearization method, bivariate spectral local linearization method, and bivariate spectral quasilinearization method. The techniques listed exhibit swift convergence and yield accurate outcomes within short-time domains. However, their accuracy may deteriorate when applied to larger computational domains. SQLM and BSQLM have been augmented by incorporating overlapping grid domains to overcome this limitation.

1.11.1 The Finite Difference Method (FDM)

The finite difference method is a numerical technique widely used for solving PDEs by discretizing the differential operators with finite difference approximations. It has a rich history dating back to Euler's development around 1768 and subsequent improvements by Runge circa 1908. Since the 1950s, with the advent of computers, FDM applications have become widespread, given their simplicity and effectiveness in solving differential equations. The finite difference technique discretizes the solution domain in space and time. The primary idea is to approximate derivatives using differential quotients. When discretizing, errors are introduced, including discretization errors. Replacing continuous operators with finite differences introduces discretization errors, an inherent consequence of numerical methods. [112]. Different versions of the FDM exist, each characterized by the form of discretization employed. The finite difference method offers a variety of approaches, from basic "explicit" and "implicit" methods to the sophisticated "Crank-Nicolson" scheme. But the innovation doesn't stop there; "nonstandard" methods explore uncharted territories. [113]. Despite their differences, these methods share the fundamental principle of approximating derivatives through finite differences.

Many theoretical investigations have been undertaken to evaluate the finite difference method's precision, robustness, and convergence attributes. Researchers have explored different aspects of FDM applications, including the study by Wang and Lin [114], who examined an inverse problem utilizing the finite-difference approach. It was observed that while implicit method needs greater computational resources than the explicit method, it provides enhanced accuracy and consistent outcomes. The FDM has found applications in various fields, showcasing its versatility. For instance, Tayakout et al. [115] explored various control volumes within a catalytic membrane reactor through the application of finite differences, demonstrating the effectiveness of this method for addressing optimization challenges. Singer and Turkel [116] investigated the Helmholtz equation in both one and two dimensions by employing the finite difference technique to advance higher-order finite difference methodologies. Kalis [117] devised a proficient method of differentiation for solving problems about thermal transference. Yuste and Acedo [118] inquire into fractional diffusion equations by utilizing explicit finite differences, showcasing the method's potential extension to higher dimensions, with findings consistent with exact solutions. Researchers have extended the application of FDM With countless forms and functionalities of differential equations. Meerschaert and Tadjeran [119] examined some category of fractional PDEs with initial-boundary conditions within a limited domain, employing the finite difference method and presenting precise outcomes. Martino et al. [120] applied this numerical technique to conquer the Fisher equation, and Chen et al. [121] leveraged the implicit version for the fractional reaction-subdiffusion equation, attaining accurate results consistent with exact solutions. Researchers have extended the application of FDM to address a broad spectrum of differential equations. With its long history and continual advancements, the finite difference method remains an effective instrument for tackling various PDEs. Its simplicity, versatility, and applicability to diverse problem domains make it a staple in numerical analysis and computational mathematics. However, FDM has limitations regarding accuracy, boundary treatment, convergence, and handling certain problem characteristics. Ongoing research continues to refine and extend the capabilities of the FDM, ensuring its relevance in dealing with complex problems across various scientific and engineering disciplines.

1.11.2 The Finite Element Method (FEM)

The Finite Element Method (FEM) is a powerful numerical technique widely utilized for solving partial differential equations (PDEs) and modelling complex physical phenomena in various scientific and engineering applications. This method has found extensive use in addressing problems related to thermal transference, fluid transport, structural analysis, and other multidisciplinary domains. Domain of the model is discretized into smaller geometric elements in the Finite Element Method, and the governing equations are approximated over these elements. This initial step involves strategically chopping the problem domain into manageable pieces represented by nodal values. For linear problems, this translates into a set of well-behaved algebraic equations. The Finite Element Method (FEM) demonstrates two primary features that enhance its efficacy. Firstly, it approximates the finite physical domain elements in a piecewise technique. Secondly, it locally approximates discretized problems, resulting in a sparse system, which proves advantageous for solving large systems. The FEM has found successful application across a diverse array of complex problems, including those featuring intricate geometry, complex constraints, and varied loading conditions [122, 123]. Goldstein [124] employed the finite element method to solve a Helmholtz-type boundary value problem in an unbounded region with infinite borders. Hiltunen [125] leveraged the computational power of the finite element method to solve equations governing the behaviour of particles flowing within a system at constant temperature and steady flow conditions, confirming the method's precision and reliability. Chowdhury and Narasimhan [126] utilized the integrated finite element approach to address equations concerning fracture and delamination phenomena in solid materials, showcasing its suitability for tackling structural problems. Tezduyar [26] extensively examined the finite element method's utilization for dealing with moving limits and bonds, highlighting its effectiveness in managing dynamic and evolving scenarios. Nagrath et al. [127] studied the dynamics of incompressible bubbles in three dimensions employing the finite element approach, offering valuable insights into intricate fluid phenomena. Roy et al. [128] examined complexities involved in the exchange of heat throughout the phases of liquefaction, compaction, and solidification during the selective laser additive manufacturing process. Their study employed FEM to provide insights into the thermal dynamics involved in this advanced manufacturing process. The Finite Element Method is a cornerstone in numerical analysis and computational modelling through its adaptability and versatility. FEM typically provides higher accuracy compared to finite difference methods, especially when using higher-order elements and finer meshes. It also provides a flexible framework for handling various boundary conditions, including complex and mixed ones. FEM uses piecewise polynomial interpolation functions within each element, allowing for smooth and continuous approximations of the solution across the domain. Its widespread use in addressing complex and diverse problems across various scientific and engineering disciplines is a testament to its effectiveness. However, FEM comes with some major disadvantages, such as complexity in its implementation, the introduction of errors as a result of repeated numerical integration over each element, high computational cost, numerical instability and poor convergence behaviour due to the formation of ill-conditioned matrices.

1.11.3 Spectral quasilinearization method (SQLM)

The SQLM represents a flexible computational technique that integrates the Newton-Raphson quasilinearization method and Chebyshev spectral collocation for solving nonlinear differential equations. It builds upon the foundations laid by Bellman and Kalaba [129] by introducing the Newton-Raphson quasilinearization method (QLM) to provide a generalized perspective for numerically addressing nonlinear differential equations. This method approximates nonlinear DEs using the Taylor series expansion, assuming negligible differences between active and preceding iterations. This simplifies the equations for efficient solutions. Following this, the Chebyshev spectral method is utilized to resolve the resultant set of linearized equations [130]. This method has demonstrated effectiveness in various fluid mechanics and heat transfer applications [131–134]. In their study, Motsa et al. [135] successfully employed the SQLM to tackle nonlinear PDEs governing unsteady boundary-layer flow phenomena. SQLM showcased impressive computational effectiveness, excelling in both precision and speed. Utilizing the SQLM, [136] explored an investigation into the intricacies of mixed convection involving a micropolar fluid near a porous vertical plate subjected to specific heat exchange conditions. The study identified the existence of multiple flow solutions for certain parameter combinations, highlighting the non-uniqueness of the flow behavior under such conditions. [137–141]. Employing the SQLM, [142] investigated heat transfer characteristics of a nanofluid flow subjected to a stretchable plate and an inclined magnetic field. The Cattaneo-Christov heat flux model was employed to account for the non-equilibrium heat transfer behaviour. The approach exhibited swift convergence and furnished precise solutions, enabling the examination of how physical parameters impact fluid dynamics and entropy generation. Alharbey et al. [143] employed the SQLM method to explore the characteristics of a boundary-layer flow involving a micropolar fluid transport across horizontal plate immersed in a non-Darcy porous medium. Their investigation delved into variations in rotational speed, heat level distribution, and entropy generation, offering valuable insights into the fluid's behaviour under diverse conditions. The Spectral Quasilinearization Method has emerged as a valuable computational tool for addressing nonlinear dynamics problems. It offers numerous accuracy, efficiency, convergence, and versatility advantages across various types of nonlinear ordinary differential equations. However, it does have certain limitations related to sensitivity to initial conditions, stability, computational expense, and complexity of implementation. In this research, the SQLM was utilized in Chapter 2 to solve the system of nonlinear ODEs derived after introducing self-similarity transformations to the PDEs governing the flow problem. The SQLM's capability to effectively handle complex equations while yielding precise solutions, in contrast to finite difference and finite element techniques, influenced its selection as the numerical technique for this investigation.

1.11.4 Bivariate spectral quasilinearization method (BSQLM) and Bivariate simple iteration method (BSIM)

Conventional time discretization methods based on implicit finite differences often need help with accuracy, demanding substantial computational resources (time and grid points) to deliver acceptable solutions. In response to this challenge, Motsa et al. [144] introduced a pioneering method known as the BSQLM. This innovative approach independently applies spectral collocation techniques across both spatial and space domains. The BSQLM combines existing methodologies such as the QLM technique, the Chebyshev spectral collocation method, and bivariate Lagrange interpolation polynomials, implemented on carefully selected Chebyshev-Gauss-Lobatto grid points. This distinctive combination has notably improved solution accuracy, especially within shorter computational timeframes. Mburu et al. [145] examined the numerical study of an unsteady nanofluid flow using BSQLM. Their findings indicated a substantial augmentation in the flow rate, thermal level, and compositional content profiles with heightened reaction speeds, implemented magnetic fields, and heat radiation effects. Additionally, they highlighted the computational efficiency of BSQLM when utilized for boundary layer problems spanning large computational domains. Oyelakin et al. [146] investigated the interplay between Theoretical investigation of unsteady mixed-convection phenomena within a nanofluid-saturated permeable material, employing the BSQLM. Goqo et al. [147] utilized the BSQLM to explore the fascinating realm of entropy generation in MHD flow. Their investigation reveals that the Reynolds number and heat emission are the key players influencing the entropy generation rate. The diverse applications of BSQLM to different models showcased its remarkable versatility and effectiveness. Its ability to handle complex problems across various fields makes it a valuable tool for researchers seeking to examine fluid flows and heat transfers [148–150].

The bivariate simple iteration method (BSIM) is a computational approach for solving nonlinear PDEs. It is a generalization of the simple iteration method (SIM) that is applicable for resolving sets of nonlinear equations. The BSIM is a strong and dynamic technique that can be applied to various problems. This technique involves treating all linear functions as unknown while simultaneously considering nonlinear functions as known and unknown. The nonlinear functions are initially assumed to be known based on an established initial solution conforming to the boundary conditions to accomplish this goal. Subsequently, the highest-order derivative function is treated as unknown, while the remaining functions are assumed to be known. However, the scope of this rule is limited to the function components of the specific equation being solved [151]. An advantage of linearizing using simple iteration method is that it does not require evaluating derivatives as in quasi-linearization method.

1.11.5 Overlapping SQLM, BSQLM and BSIM

The overlapping spectral quasilinearization method is a powerful numerical technique for solving nonlinear PDEs introduced by Mkhwatshwa [152]. It combines the SQLM with an overlapping grid strategy to overcome the limitations of the SQLM, which can become inaccurate with size increase in computation domain. The overlapping grid technique entails partitioning the computational domain into smaller subdomains, with the SQLM solved independently on each subdomain. These subdomains are overlapped, allowing the solution from one subdomain to serve as the initial estimate for the solution on the subsequent subdomain. This approach enhances the accuracy of the SQLM, particularly for expansive computational domains. Leveraging this innovative method facilitated the effective utilization of the modified SQLM in addressing the governing equations for 3-D magnetohydrodynamic Casson nanofluid tranport across a stretchable sheet [153, 154].

The overlapping bivariate spectral quasilinearization method (OBSQLM) has emerged

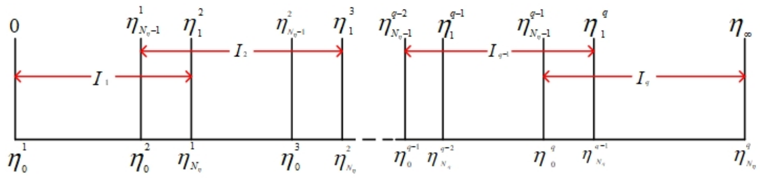

Figure 1.1: Overlapping grid ($\eta - domain$)

as a powerful numerical technique for solving nonlinear PDEs. Combining the strengths of BSQLM and the overlapping grid strategy, the OBSQLM offers impressive accuracy, efficiency, and versatility [155]. This is also the case for overlapping BSIM. We have employed overlapping BSIM and BSQLM in chapters 5 and 6. Also, we implemented the overlapping SQLM in chapters 3 and 4 of this thesis. In general, the overlapping grid methods offer reduced domain decomposition errors, enhanced convergence rates and improved handling of complex geometries. These major advantages have informed our choice of overlapping methods in this study.

1.12 Thesis aims and objectives

This study aims to comprehensively investigate and analyze diverse magnetohydrodynamic nanofluid flow phenomena over various stretching surfaces with distinctive physical and mathematical characteristics, apply advanced computational methodologies for solving unsteady magnetohydrodynamic (MHD) nanofluid flow over stretching surfaces through the utilization of overlapping grid spectral collocation methods, and contribute to the fundamental understanding of complex fluid dynamics and its applications.
The specific objectives of this thesis are as follows:

- Advance the fundamental understanding of nanofluid dynamics across diverse flow scenarios, including unsteady MHD nanofluid flow over a porous inclined stretching surface, electromagnetic MHD tangent hyperbolic nanofluid flow over inclined stretchable Riga surface, unsteady squeezing flow and heat transport involving silicon SiO_2/kerosene oil nanofluid around radially stretchable parallel rotating disks, unsteady ternary hybrid nanofluid flow with a magnetic dipole over an oscillatory stretching surface and unsteady Casson ternary nanofluid over bidirectionally stretching surface.

- Demonstrate the effectiveness of powerful numerical methods such as SQLM, overlapping SQLM, BSIM and BSQLM for solving complex fluid flow problems. By applying these methods to analyze the diverse magneto-hydrodynamic nanofluid flow phenomena described, the study aims to showcase their capability to accurately capture the underlying physics and provide insights into the complex fluid dynamics of nanofluids.

- Examine and interpret the complex interactions between various physical parameters influencing nanofluid behaviour. This objective involves identifying, examining, and interpreting the intricate interactions between various physical parameters, such as velocity slip, viscous dissipation, Dufour effect, activation energy, heat generation, magnetic effects, oscillatory stretching, motile gyrotactic microorganisms, and nanoparticle shape factors, that influence the behaviour of nanofluids. By systematically studying these interactions within different flow scenarios, the study aims to work out the underlying mechanisms governing nanofluid dynamics and provide valuable insights into optimizing nanofluid-based engineering applications.

- Contribute significant knowledge to nanofluid research, paving the way for future advancements and unlocking new engineering applications. By comprehensively exploring diverse magneto-hydrodynamic nanofluid flow phenomena and showcasing the ability of numerical methods to handle intricate fluid flow scenarios in various geometries, highlighting their broad applicability, the research seeks to broaden the understanding of nanofluid dynamics and inspire further research and innovation in this rapidly evolving field.

1.13 Thesis layout

This thesis is structured into seven distinct sections. The first chapter serves as an introductory overview of the research. Moving forward, Chapter 2 delves into an intricate entropy generation analysis concerning an unsteady MHD nanofluid model, specifically examining its behaviour over a porous inclined stretching surface while incorporating elements such as velocity slip and viscous dissipation. This chapter employs the SQLM to solve the formulated model. Chapter 3 explores a different facet, focusing on an overlapping grid SQLM solution detailing the EMHD tangent hyperbolic nanofluid flow over an inclined stretchable Riga surface. Notably, this analysis incorporates the Dufour effect, activation energy, and heat generation into its framework. Chapter 4 details unsteady squeezing flow and heat transport of SiO_2/kerosene oil nanofluid around radially stretchable parallel disks with upper disk oscillating. The numerical solution for this model was done via overlapping SQLM.

Chapter 5 explores the unsteady analysis of ternary hybrid nanofluid flow with magnetic dipole over an oscillatory stretching surface. The analysis was carried out using an overlapping bivariate simple iteration method. In Chapter 6, an exploration is undertaken into the numerical examination of the dynamics of unsteady ternary hybrid nanofluid flow over a sheet that stretches bidirectionally. This investigation integrates the presence of motile gyrotactic microorganisms and the influence of nanoparticle shape factors, employing the overlapping bivariate spectral quasilinearization method. As the culmination of our research endeavour, Chapter 7 serves as a conclusive summary, wherein we delineate the principal discoveries of our study and contemplate potential avenues for future expansions.

Chapter 2

Entropy generation of unsteady MHD nanofluid flow over a porous inclined stretching surface with velocity slip and viscous dissipation

This chapter presents a comprehensive numerical investigation of the effects of inclined variable magnetic field, velocity slip, thermal radiation, and viscous dissipation on the entropy generation of an unsteady magnetohydrodynamic (MHD) nanofluid flow over an inclined stretching sheet in a porous medium. The governing partial differential equations are non-dimensionalized and transformed using suitable similarity transformations, resulting in a set of non-linear ordinary differential equations. These equations are solved utilizing the Spectral Quasi-Linearization Method (SQLM), a powerful numerical technique. The study systematically analyzes the impact of various factors on the flow characteristics by numerically solving the equations and discussing the results in detail. Tables and graphs are utilized to illustrate the numerical findings. Key physical quantities such as skin friction, Nusselt number, and local Sherwood number are calculated and presented in tables for further analysis. The aligned angle of the variable magnetic field ranging from 0^o to 90^o significantly influences the fluid flow rate, temperature, mass flux, and entropy generation, as indicated by variations in the Bejan number, and the inclination of the stretching sheet as well as the porosity of the medium are found to exert notable influences on the fluid flow rate, temperature, and mass flux.

Journal of Nanofluids
Vol. 12, pp. 1666–1679, 2023
(www.aspbs.com/jon)

ARTICLE

Entropy Generation of Unsteady Magnetohydrodynamics Nanofluid Flow Over a Porous Inclined Stretching Surface with Velocity Slip and Viscous Dissipation

Folarin Oluwaseun[1], **Sicelo Goqo**[1], **and Hiranmoy Mondal**[2,*]

[1] *School of Mathematics, Statistics and Computer Science, University of KwaZula-Natal, Private Bag X01, Scottsvile, Pietermaritzburg-3209, South Africa*
[2] *Department of Applied Mathematics, Maulana Abul Kalam Azad University of Technology, West Bengal, Kolkata 700064, India*

The numerical investigation of the effects of inclined variable magnetic field, velocity slip, thermal radiation and viscous dissipation on the entropy generation of an unsteady MHD nanofluid flow over an inclined stretching sheet in a porous medium has been carried out here. The non-dimensional non-linear governing ordinary differential equations obtained after suitable similarity transformations are solved by SQLM. Effects of important factors of the model on the flow characteristics were numerically analysed and discussed in details with tables and graphs. Important physical quantities of skin friction, Nusselt number and the local Sherwood number were calculated and illustrated on tables. The aligned angle of the variable magnetic field between 0° and 90° was found to significantly influence the fluid flow rate, temperature, mass flux and entropy generation through the Bejan number. The velocity slip slip was found to have no signicant effects on the mass flux, however it influenced significantly the fluid flow rate and temperature. The inclination of the stretching sheet and the porosity of the medium were also found to influence the fluid flow rate, temperature and mass flux.

KEYWORDS: Nanofluids, MHD, Entropy Generation, Inclined Stretching Sheet, Inclined Variable Magnetic Field, Thermal Radiation, Viscuous Dissipation.

1. INTRODUCTION

Boundary layer flow and heat transfer over stretching surface has in recent years gained researchers' attentions as a result of its many theoretical and practical applications in engineering and industrial processes, some of which include aerodynamics, extrusion of plastic sheets, continuous cooling, hot rolling, electronic chips, glass blowing, spinning of fibers and polymer extractions, to mention a few. Sakiadis[47] in 1961 was first to consider the boundary layer flow on a moving continuous solid surface. Some years later, Crane[15] extended the concept introduced by Sakiadis to a stretching sheet with linearly varying surface speed and presented an exact analytical solution for the steady two dimensional stretching surface in a quiescent fluid. Over the years, researchers have explore the different aspects of boundary layer flow and heat transfer following the pace-setting works of Crane.

*Author to whom correspondence should be addressed.
Email: hiranmoymondal@yahoo.co.in
Received: 7 April 2022
Accepted: 10 April 2022

Extensive and thorough reviews of the convection through porous media have been reported by different authors[11,30,32,34–37,42,51] in particular. Krishna et al.[38] insightfully investigated MHD flow of viscous fluid past an infinite vertical porous plate with focus on the soret and joule effects taking into consideration the hall effects. Hayat et al.[27,28] worked on fluid flow on porous media. Cortell[13] examined the flow and heat transfer of a fluid through porous medium over a stretching surface with internal heat generation.

Suction/Injection has many engineering applications. Ahmad and Khan[6] studied boundary layer flow past a stretching plate with suction, heat and mass transfer and with variable conductivity. Most of the industrial processes mentioned earlier take place at high temperature and as such the effect of thermal radiation play significant role in controlling the heat in these processes. Effects of thermal radiation and magneto-hydrodynamics on Ree-Eyring fluid flows through porous medium with slip boundary conditions was examined by Ramesh and Eytoo.[43] The study of radiation-absorption and Dufour effects on magnetohydrodynamic rotating flow of a nanofluid over a semi-infinite vertical moving plate with a constant heat source was carried out by Ameer Ahamad et al.[8] Abd-El Aziz[1] considered thermal radiation effects on magnetohydrodynamic mixed convection flow of a micropolar fluid past a continuously moving semi-infinite plate for high temperature. Effects of viscous dissipation and radiation on the thermal boundary layer over a non-linearly stretching sheet was investigated by Cortell.[14]

Unsteady boundary layer flow over a porous stretching surface embedded in a porous medium in the presence of heat source or sink was investigated by Elbashbeshy et al.[19] The effects of thermal radiation and heat transfer over an unsteady stretching surface embedded in a porous medium in the presence of heat source or sink was studied by Elbashbeshy and Emam.[18] Goqo et al.[23] investigated the combined effects of a magnetic field and a convective boundary condition on unsteady Jeffrey nanofluid flow over a shrinking sheet with thermal radiation and heat generation. Ismael et al.[31] examined mixed convection in a nanofluid filled-cavity with partial slip subjected to constant heat flux and inclined magnetic field. Heat and mass transfer on free convective flow of amicropolar fluid through a porous surface with inclined magnetic field and hall effects was discussed by Krishna et al.[33] Ganga et al.[22] studied the effects of inclined magnetic field on entropy generation in nanofluid over a stretching sheet in the presence of partial slip and nonlinear thermal radiation. Hayat et al.[26] considered the influence of inclined magnetic field on peristaltic flow of an incompressible Williamson fluid in an inclined channel with heat and mass transfer, putting into consideration Convective conditions of heat and mass transfer with Viscous dissipation and Joule heating. Unsteady hydro magnetic Couette flow of a viscous incompressible electrically conducting fluid in a rotating system in the presence of an inclined magnetic field taking Hall current into account was studied by Seth et al.[20,48] carried out an analysis of unsteady MHD natural convective flow, transfer of mass, and radiation past linearly accelerated slanted plate inserted in an immersed permeable medium with uniform permeability, variable temperature, and concentration within the sight of a slanted magnetic field.

The effects of thermally developed Brownian motion and thermophoresis diffusion in non-Newtonian nanofluid through an inclined stretching surface with effect of chemical reaction and thermal radiation was investigated by Gupta et al.[5,25] investigated the unsteady flow of Powell-Eyring fluid past an inclined stretching sheet, when the unsteadiness in the flow is due to the time-dependence of the stretching velocity and wall-temperature. The unsteady magnetohydrodynamics (MHD) flow of nanofluid with variable fluid properties over an inclined stretching sheet in the presence of thermal radiation and chemical reaction was studied by Mjankwi et al.[40] taking into account the effect of variable fluid properties in thermal conductivity and diffusion coefficient. Rashad et al.[45] studied MHD mixed convection of localized heat source/sink in a nanofluid-filled lid-driven square cavity with partial slip. Chamkha et al.[12] considered the impact of partial slip on magneto-ferrofluids mixed convection flow in enclosure.

Entropy generation analysis is pivotal the researchers and engineers in the this modern day as it plays major role in figuring out how to reduce the overall health loss in a system which in turns helps to increase the efficiency of the system. Comprehensive works and reviews have been done on the concepts of entropy generation of different fluid models and geometries[3,9,24,29,39,50,52] all reported on entropy generation analysis. In particular, Rashad et al.[46] presented MHD mixed convection and entropy genaration of nanofluid in a lid-driven u-shaped cavity with internal heat and partial slip. Chamkha et al.[10] invegtigated the effects of partial slip on entropy generation and MHD combined convection in a lid-driven porous enclosure saturated with a Cu–water nanofluid.

In accordance to the above literature reviews, we have seen a significant research gap in terms of entropy generation analysis of unsteady MHD nanofluid flow over a porous inclined stretching surface with velocity slip, thermal radiation and viscous dissipation in the presence of inclined variable magnetic field. The present study therefore has been carried to fill this gap numerically with the following main objectives:

- Present a model that demonstrates a viscuous, incompressible, radiating, electrically conducting nanofluid flow over an inclined stretching sheet in the presence of a variable magnetic field and in a porous medium.
- Implement appropriate similarity transformations to the governing equations to obtain system of non-linear ODE that are solved numerically using SQLM
- Analyze numerically the entropy generation analysis of the presented model
- Examine and physically interprete the dominant parameters of the presented model as they influence the fluid and boundary characteristics.

2. MATHEMATICAL FORMULATION OF THE PROBLEM

We have considered a two dimensional MHD nanofluid flow under the following prescribing assumptions:

- The nanofluid is incompressible, viscous, radiating and electrically conducting
- The flow is over an inclined unsteady sheet at $y = 0$, stretching with velocity of $U_w(x, t)$ in a porous medium
- The flow is unsteady due to the unsteadiness of the stretching sheet
- The surface temperature, $T_w(x, t)$ and the concentration at the surface, $C_w(x, t)$, are considered to be time-dependent and varying along the stretching sheet

ARTICLE

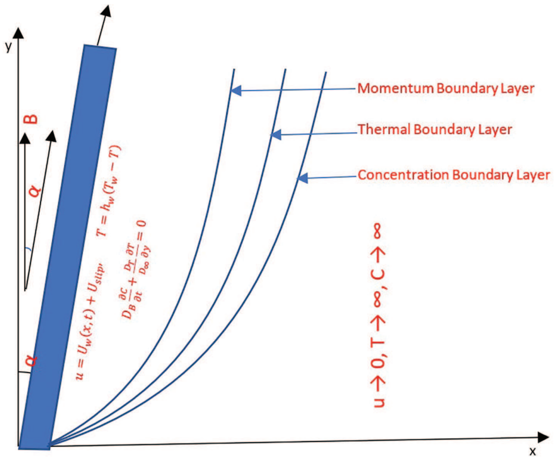

Fig. 1. Physical description of the modeled flow.

- An inclined variable magnetic field along the inclination of the stretching sheet is applied.

As used by Ref. [16], the variable magnetic field is defined as $B = B_0 x^{(m-1)/2}(1-\beta t)^{-1/2}$. Where B_0 is the magnetic field strength, m is a positive integer and β is a constant. Using $m = 1$, reduces the variable magnetic field to be strictly a function of time, as, $B(t) = B_0(1-\beta t)^{-1/2}$. The physical situation described under these conditions is depicted in the schematic diagram (see Fig. 1) and hence, the continuity, momentum and energy equations following[4,16,22] are given as:

$$\frac{\partial u}{\partial x} + \frac{\partial v}{\partial y} = 0 \tag{1}$$

$$\begin{aligned}\frac{\partial u}{\partial t} + u\frac{\partial u}{\partial x} + v\frac{\partial v}{\partial y} &= \nu\frac{\partial^2 u}{\partial y^2} - \frac{\sigma B^2(t)}{\rho}(\sin^2\gamma)u - \frac{\nu}{\kappa}u - \frac{C_b}{\sqrt{\kappa}}u^2 \\ &\quad + g\beta_T(T-T_\infty)\cos\alpha + g\beta_C(C-C_\infty)\cos\alpha\end{aligned} \tag{2}$$

$$\begin{aligned}\frac{\partial T}{\partial t} + u\frac{\partial T}{\partial x} + v\frac{\partial T}{\partial y} &= \alpha\frac{\partial^2 T}{\partial y^2} - \frac{1}{\rho C_p}\frac{\partial q_r}{\partial y} + \frac{\mu}{\rho C_p}\left(\frac{\partial u}{\partial y}\right)^2 + \frac{\sigma B^2(t)}{\rho C \rho} \\ &\quad \times (\sin^2\gamma)u^2 + \tau\left(D_B\frac{\partial T}{\partial y}\frac{\partial C}{\partial y} + \frac{D_T}{T_\infty}\left(\frac{\partial T}{\partial y}\right)^2\right)\end{aligned} \tag{3}$$

$$\frac{\partial C}{\partial t} + u\frac{\partial C}{\partial x} + v\frac{\partial C}{\partial y} = D_B\frac{\partial^2 C}{\partial y^2} - K_r(C-C_\infty) \tag{4}$$

The appropriate boundary boundary conditions for Eqs. (1)–(4) following[16,17] are:

$$u = u_w(x,t) + u_{\text{slip}}; \quad v = v_w;$$

$$T = -K_w\frac{\partial T}{\partial y} = h_w(T_w - T); \quad D_B\frac{\partial C}{\partial T} + \frac{D_T}{T_\infty}\frac{\partial T}{\partial y} = 0;$$

$$\text{at } y = 0, \ t > 0 \tag{5}$$

$$u \to 0; \quad T \to \infty; \quad C \to \infty \quad \text{as } y \to \infty$$

Where (u, v) are the components of the velocity along x-direction and y-direction respectively, ν is the kinematics coefficient of viscosity, σ is the electrical conductivity, D_B and D_T are mass and thermophoretic coefficients of diffusivity, $\tau = (\rho C)_p/(\rho C)_f$ is the effective heat capacity of the nanoparticles and the base fluid, K_r is the chemical reaction parameter, $C_b/\sqrt{\kappa}$ is the inertia coefficient of the porous medium, C_b is the drag coefficient, B is the magnetic field strength of the applied variable magnetic field, ρ is the density of the fluid, q_r is the radiative heat flux, $\alpha = K/\rho C_p$ is the thermal diffusivity, K is the thermal conductivity of the fluid, C_p is the specific heat capacity at constant pressure, T is the temperature of the fluid and C is the concentration of the fluid.

As you used by,[16] the velocity of the stretching sheet is given as:

$$U_w(x,t) = \frac{bx}{(1-\beta t)} \tag{6}$$

Valid for $t\beta < 1$, unless $\beta = 0$

The surface temperature and concentration are chosen as follows:

$$T = T_\infty + T_0\left[\frac{bx^2}{2\nu}\right](1-\beta t)^{-3/2} \tag{7}$$

$$C = C_\infty + C_0\left[\frac{bx^2}{2\nu}\right](1-\beta t)^{-3/2} \tag{8}$$

The thermal radiation heat flux, q_r is used according to Rosseland approximation as:

$$q_r = -\frac{4\sigma *}{3K}\frac{\partial T^4}{\partial y} \tag{9}$$

where, $\sigma*$ and K are the Stefan-Boltzmann constant and the mean absorption coefficient, respectively. In accordance to what was done by Raptis,[44] the fluid-phase temperature differences within the flow are assumed to be sufficiently small so that T^4 may be expressed as a linear function of temperature, T. By Taylor's series expansion about the free stream temperature, T_∞ we have:

$$T^4 = T_\infty^3 + 4T_\infty^3(T-T_\infty) + 6T_\infty^2(T-T_\infty)^2$$

Neglecting higher order terms from the above equation, we can obtain an approximate expression for T^4 as:

$$T^4 \simeq 4T_\infty^3 T - 3T_\infty^4$$

$$\Rightarrow \frac{\partial q_r}{\partial y} = -\frac{16\sigma^* T_\infty^3}{3K}\frac{\partial^2 T}{\partial y^2}$$

So the energy Eq. (3) becomes

$$\frac{\partial T}{\partial t} + u\frac{\partial T}{\partial x} + v\frac{\partial T}{\partial y}$$

$$= \alpha\frac{\partial^2 T}{\partial y^2} + \frac{1}{\rho C_\rho}\frac{16\sigma^* T_\infty^3}{3K}\frac{\partial^2 T}{\partial y^2} + \frac{\mu}{\rho C_\rho}\left(\frac{\partial u}{\partial y}\right)^2 + \frac{\sigma B^2(t)}{\rho C\rho} \times (\sin^2\gamma)u^2 + \tau\left(D_B\frac{\partial T}{\partial y}\frac{\partial C}{\partial y} + \frac{D_T}{T_\infty}\left(\frac{\partial T}{\partial y}\right)^2\right) \quad (10)$$

3. METHODS OF SOLUTION

The governing partial differential equations can be transformed to system of non-linear ordinary differential equations by introducing similarity transformation variables. Following,[16] we introduce the following appropriate similarity transformations:

$$\eta = \left[\frac{b}{\nu}\right]^{1/2}(1-\beta t)^{-(1/2)}y \quad (11)$$

$$\psi = (\nu b)^{1/2}(1-\beta t)^{-1/2}xf(\eta) \quad (12)$$

$$T = T_\infty + T_0\left[\frac{bx^2}{2\nu}\right](1-\beta t)^{-3/2}\theta(\eta) \quad (13)$$

$$C = C_\infty + C_0\left[\frac{bx^2}{2\nu}\right](1-\beta t)^{-3/2}\phi(\eta) \quad (14)$$

Where ψ is the stream function which satisfies the continuity Eq. (1). The components of the velocity are then given by:

$$u = \frac{\partial\psi}{\partial y} = U_w f'(\eta) = \frac{bx}{(1-\beta t)}f'(\eta) \quad (15)$$

$$v = -\frac{\partial\psi}{\partial x} = -\left(\frac{\nu b}{1-\beta t}\right)^{1/2} f(\eta) \quad (16)$$

Implementing the similarity transformation (11)–(16) in Eqs. (1)–(4) along with the boundary conditions (5), the following set of non linear ordinary differential equations are obtained:

$$f''' + ff'' - (1+Fr)f'^2 - (A + M^2\sin^2\gamma + K_1)f' - \frac{\eta}{2}f'' + (\lambda_1\cos\alpha)\theta + (\lambda_2\cos\alpha)\phi = 0 \quad (17)$$

$$(3R+4)\theta'' + 3RP_r\Big[f\theta' - 2f'\theta + E_c(f'')^2 + M^2E_c\sin^2\gamma(f')^2 + Nb\phi'\theta' + N_t(\theta')^2 - \frac{A}{2}(3\theta + \eta\theta')\Big] = 0 \quad (18)$$

$$\phi'' + Sc\left[f\phi' - 2f'\phi - \frac{A}{2}(3\phi + \eta\phi') - Cr\phi\right] = 0 \quad (19)$$

subject to the boundary conditions:

$$f(\eta) = S, \quad f'(\eta) = 1 + S_f f''(\eta), \quad \theta(\eta) = 1, \quad \phi(\eta) = 1, \quad \text{at } \eta = 0, \quad (20)$$
$$f'(\eta) \to 0, \quad \theta(\eta) \to 0, \quad \phi(\eta) \to 0 \quad \text{as } \eta \to \infty$$

Where $Fr = C_b x/\sqrt{\kappa}$ is the local inertia coefficient, $A = \beta/b$ is the unsteadiness parameter, $M = \sqrt{\sigma/(b\rho)}B_0$ is the magnetic parameter, $K_1 = (\nu/(b\kappa))(1-\beta t)$ is the porosity parameter, $\lambda_1 = Gr_T/Re_x^2$, $Gr_T = (g\beta_T(T_w - T_\infty)x^3)/\nu^2$ is the thermal Grashof number, $\lambda_2 = Gr_C/Re_x^2$, $Gr_C = (g\beta_C(C_w - C_\infty)x^3)/\nu^2$ is the concentration Grashof number, $C_r = (K_r/b)(1-\beta t)$ is the chemical reaction parameter, $S_c = \nu/D_B$ is the Schmidt number, $E_c = (b^2x^2)/(C_p(1-\beta t)^2(T_w - T_\infty))$ is the Eckert number, $R = K\kappa/(4\sigma * T_\infty^3)$ is the radiation parameter and $S = -V_w\sqrt{(1-\beta t)/(b\nu)}$ is the suction parameter, $P_r = \nu/\alpha$ is the Prandtl number, $N_t((\tau D_T(T_w - T_\infty))/\nu T_\infty)$ is the Thermophoresis parameter, $N_b = (\tau D_B(C_w - C_\infty))/\nu$ is the Brownian motion parameter, $\theta(\eta) = (T - T_\infty)/(T_w - T_\infty)$ and $\phi(\eta) = (C - C_\infty)/(C_w - C_\infty)$ are the non-dimensional temperature and concentration respectively.

The physical quantities of interest are the skin friction coefficient, C_{fx}, Nusselt number, N_{ux} and the local Sherwood number, Sh_x, which according to[16] are given by:

$$C_{f_x} = \frac{2\mu(\partial u/\partial y)_{y=0}}{\rho U_w^2} = f''(0)2Re_x^{-(1/2)} \quad (21)$$

$$N_{u_x} = \frac{x\,((-K\partial T/\partial y) + q_r)_{y=0}}{K(T_w - T_\infty)} = -\theta'(0)\left(1 + \frac{4}{3R}\right)Re_x^{1/2} \quad (22)$$

$$Sh_x = \frac{x\,(\partial C/\partial y)_{y=0}}{C_w - C_\infty} = -\phi'(0)Re_x^{1/2} \quad (23)$$

Where $Re_x = (U_w x)/\nu$ is the local Reynold's number which is dependent on the velocity of the stretching sheet.

4. NUMERICAL SOLUTION

The system of non-linear ordinary differential equations (17)–(19) were solved subject to the boundary conditions (3) using spectral quasi-linearization method ($SQLM$), a technique chosen for its efficiency and speed in solving systems of differential equations. $SQLM$ is a Chebyshev pseudo spectral based method that have been successfully used to solve non-linear boundary layer flow problems described by systems of ordinary differential equations,.[41] The quasi-linearization technique is essentially a generalized Newton–Raphson Method that was originally used by Fornberg.[21]

This technique starts linearization of the system of non-linear ODE using the Taylor series expansion. To achieve this we express (17)–(19) in terms of the operators F, T and H as;

$$F[f, f', f'', f''', \theta, \phi] = 0$$
$$T[\theta, \theta', \theta'', f, f', f'', \phi'] = 0$$
$$H[\phi, \phi', \phi'', f] = 0$$

ARTICLE

Taking F_r, T_r and H_r as the initial guesses, the Taylor's series expansion applied to (17)–(19), we obtain the following;

$$F_r+\frac{\partial F}{\partial f'''}(f'''_{r+1}-f'''_r)+\frac{\partial F}{\partial f''}(f''_{r+1}-f''_r)+\frac{\partial F}{\partial f'}(f'_{r+1}-f'_r)$$
$$+\frac{\partial F}{\partial f}(f_{r+1}-f_r)+\frac{\partial F}{\partial \theta}(\theta_{r+1}-\theta_r)+\frac{\partial F}{\partial \phi}(\phi_{r+1}-\phi_r)=0$$

$$T_r+\frac{\partial T}{\partial \theta''}(\theta''_{r+1}-\theta''_r)+\frac{\partial T}{\partial \theta'}(\theta'_{r+1}-\theta'_r)+\frac{\partial T}{\partial \theta}(\theta_{r+1}-\theta_r)$$
$$+\frac{\partial T}{\partial f''}(f''_{r+1}-f''_r)+\frac{\partial T}{\partial f'}(f'_{r+1}-f'_r)+\frac{\partial T}{\partial f}(f_{r+1}-f_r)$$
$$+\frac{\partial T}{\partial \phi'}(\phi'_{r+1}-\phi'_r)=0$$

$$H_r+\frac{\partial H}{\partial \phi''}(\phi''_{r+1}-\phi''_r)+\frac{\partial H}{\partial \phi'}(\phi'_{r+1}-\phi'_r)$$
$$+\frac{\partial H}{\partial \phi}(\phi_{r+1}-\phi_r)+\frac{\partial H}{\partial f'}(f'_{r+1}-f'_r)+\frac{\partial H}{\partial f}(f_{r+1}-f_r)=0$$

Where, r-terms and the $(r+1)$-terms represent the previous and current solutions. Separating the $(r+1)$-terms to the left and the r-terms along with F_r, T_r and H_r to the right in each case, we obtain

$$(a_{0,r}D^3+a_{1,r}D^2+a_{2,r}D^1+a_{3,r}I)f_{r+1}+(a_{4,r}I)\theta_{r+1}$$
$$+(a_{5,r}I)\phi_{r+1}=R_f$$

$$(b_{3,r}D^2+b_{4,r}D^1+b_{5,r}I)f_{r+1}+(b_{0,r}D^2+b_{1,r}D^1+b_{2,r}I)$$
$$\times\theta_{r+1}+(b_{6,r}I)\phi_{r+1}=R_t$$

$$(c_{3,r}D^1+c_{4,r}I)f_{r+1}+(c_{0,r}D^2+c_{1,r}D^1+c_{2,r}I)\phi_{r+1}=R_h$$

Where D^3, D^2, D^1 are the scaled differential matrices, I is identity matrix and the coefficients defined as follows;

$$\frac{\partial F}{\partial f'''}=a_{0,r}=1 \quad \frac{\partial F}{\partial f''}=a_{1,r}=f-\frac{A\eta}{2}$$
$$\frac{\partial F}{\partial f'}=a_{2,r}=-2(1+Fr)f'-A-M^2\sin^2\gamma-K_1$$
$$\frac{\partial F}{\partial f}-=a_{3,r}=f'' \quad \frac{\partial F}{\partial \theta}=a_{4,r}=\lambda_1\cos\alpha$$
$$\frac{\partial F}{\partial \phi}=a_{5,r}=\lambda_2\cos\alpha$$
$$\frac{\partial T}{\partial \theta''}=b_{0,r}=3R+4$$
$$\frac{\partial T}{\partial \theta'}=b_{1,r}=3RP_r\left(f+N_b\phi'+2N_t\theta'-\frac{A\eta}{2}\right)$$
$$\frac{\partial T}{\partial \theta}=b_{2,r}=3RP_r\left(-2f'-\frac{3A}{2}\right) \quad \frac{\partial T}{\partial f''}=b_{3,r}=6RP_rE_cf''$$
$$\frac{\partial T}{\partial f'}=b_{4,r}=3RP_r(-2\theta+2M^2E_c\sin^2\gamma f')$$
$$\frac{\partial T}{\partial f}=b_{5,r}=3RP_r\theta'$$
$$\frac{\partial T}{\partial \phi'}=b_{6,r}=3RP_rN_b\theta'$$
$$\frac{\partial H}{\partial \phi''}=c_{0,r}=1$$
$$\frac{\partial H}{\partial \phi'}=c_{1,r}=S_c\left(f-\frac{A\eta}{2}\right)$$
$$\frac{\partial H}{\partial \phi}=c_{2,r}=S_c\left(-2f'-\frac{3A}{2}-C_r\right)$$
$$\frac{\partial H}{\partial f'}=c_{3,r}=-2S_c\phi \quad \frac{\partial H}{\partial f}=c_{4,r}=S_c\phi'$$

So the new system of equations becomes:

$$\begin{aligned}A_{11}f_{r+1}+A_{12}\theta_{r+1}+A_{13}\phi_{r+1}&=R_f\\ A_{21}f_{r+1}+A_{22}\theta_{r+1}+A_{23}\phi_{r+1}&=R_t\\ A_{21}f_{r+1}+A_{22}\theta_{r+1}+A_{23}\phi_{r+1}&=R_h\end{aligned}\tag{24}$$

In matrix form, we have;

$$\begin{bmatrix}A_{11}&A_{12}&A_{13}\\A_{21}&A_{22}&A_{23}\\A_{31}&A_{32}&A_{33}\end{bmatrix}\begin{bmatrix}f_{r+1}\\\theta_{r+1}\\\phi_{r+1}\end{bmatrix}=\begin{bmatrix}R_f\\R_t\\R_h\end{bmatrix}\tag{25}$$

Where

$$A_{11}=a_{0,r}D^3+a_{1,r}D^2+a_{2,r}D^1+a_{3,r}I$$
$$A_{12}=a_{4,r}I$$
$$A_{13}=a_{5,r}I$$
$$A_{21}=b_{3,r}D^2+b_{4,r}D^1+b_{5,r}I$$
$$A_{22}=b_{0,r}D^2+b_{1,r}D^1+b_{2,r}I$$
$$A_{23}=b_{6,r}I$$
$$A_{31}=c_{3,r}D^1+c_{4,r}I$$
$$A_{32}=0$$
$$A_{33}=c_{0,r}D^2+c_{1,r}D^1+c_{2,r}I$$
$$R_f=a_{0,r}f'''_r+a_{1,r}f''_r+a_{2,r}f'_r+a_{3,r}f_r+a_{4,r}\theta_r$$
$$+a_{5,r}\phi_r-F_r$$
$$R_t=b_{0,r}\theta''_r+b_{1,r}\theta'_r+b_{2,r}\theta_r+b_{3,r}f''_r+b_{4,r}f'_r$$
$$+b_{5,r}f_r+b_{6,r}\phi_r-T_r$$
$$R_h=c_{0,r}\phi''_r+c_{1,r}\phi'_r+c_{2,r}\phi_r+c_{3,r}f'_r+c_{4,r}f_r-H_r$$

The appropriate initial guesses satisfying the boundary conditions for $f(\eta)$, $\theta(\eta)$ and $\phi(\eta)$ are:

$$f_0(\eta)=\frac{1}{1+S_f}(e^{-\eta}-1)+S\tag{26}$$

$$\theta_0(\eta) = e^{-\eta} \tag{27}$$

$$\phi_0(\eta) = e^{-\eta} \tag{28}$$

Imposing the boundary conditions (3), we have;

$$\left[\begin{array}{ccc|cccc|cccc}
D^1_{1,1} & \dots\ \dots & D^1_{1,N+1} & 0 & \dots & \dots & 0 & 0 & \dots & \dots & 0 \\
 & A_{11} & & & A_{12} & & & & A_{13} & & \\
D^1_{N,1} - S_f D^2_N & \dots\ \dots & D^1_{N,N+1} - S_f D^2_{N,N+1} & 0 & \dots & \dots & 0 & 0 & \dots & \dots & 0 \\
0 & \dots\ \dots & 1 & 0 & \dots & \dots & 0 & 0 & \dots & \dots & 0 \\
\hline
 & 0\ \dots\ \dots\ 0 & & 1 & 0 & \dots & 0 & 0 & \dots & \dots & 0 \\
 & A_{21} & & & A_{22} & & & & A_{23} & & \\
 & 0\ \dots\ \dots\ 0 & & 0 & 0 & \dots & 1 & 0 & \dots & \dots & 0 \\
\hline
 & 0\ \dots\ \dots\ 0 & & 0 & \dots & \dots & 0 & 1 & 0 & \dots & 0 \\
 & A_{31} & & & A_{32} & & & & A_{33} & & \\
 & 0\ \dots\ \dots\ 0 & & 0 & \dots & \dots & 0 & 0 & 0 & \dots & 1
\end{array}\right]$$

$$\begin{bmatrix} f_{r+1}(\eta_0) \\ \vdots \\ f_{r+1}(\eta_N) \\ f_{r+1}(\eta_{N+1}) \\ \theta_{r+1}(\eta_0) \\ \vdots \\ \theta_{r+1}(\eta_{N+1}) \\ \phi_{r+1}(\eta_0) \\ \vdots \\ \phi_{r+1}(\eta_{N+1}) \end{bmatrix} = \begin{bmatrix} 0 \\ \vdots \\ 1 \\ S \\ 0 \\ \vdots \\ 1 \\ 0 \\ \vdots \\ 1 \end{bmatrix}$$

5. ENTROPY GENERATION ANALYSIS

Entropy generation analysis is an important concept as it shows areas of a physical model for a thermal system where there is more heat dissipation. It is central to making improvements on the efficiency of a thermal system. Minimizing the entropy generation of a system ensures an increase in the efficiency of the system. The local volumetric rate of entropy generation in the presence of inclined magnetic field is given by:

$$S'''_{Gen} = \frac{\kappa}{T^2_\infty}\left(1 + \frac{16\sigma^* T^3_\infty}{3K}\right)\left(\frac{\partial T}{\partial y}\right)^2 + \frac{\mu}{T_\infty}\left(\frac{\partial u}{\partial y}\right)^2 + \frac{\sigma B_0^2}{T_\infty}(\sin^2\gamma)u^2 + \frac{RD_B}{C_\infty}\left(\frac{\partial C}{\partial y}\right)^2 + \frac{RD_B}{T_\infty}\left(\frac{\partial C}{\partial y}\frac{\partial T}{\partial y}\right) \tag{29}$$

Each term of (29) is contributed by different aspects of the fluid model. The first term is irreversibility as a result of the heat transfer, the second term is the entropy generation as a result of the effect of the magnetic field, the third and fourth terms are irreversibilities due to the diffusion effects. Effective entropy generation analysis is carried out by first calculating the entropy generation number is which defined as the ratio of the local volumetric rate of entropy generation and the entropy generation characteristics rate, S'''_0. The characteristics rate of entropy generation is given by:

$$S'''_0 = \frac{\kappa(\Delta T)^2}{x^2 T^2_\infty} = \frac{\kappa(T_w - T_\infty)^2}{x^2 T^2_\infty} \tag{30}$$

The entropy generation number, N_E, which is defined as the ratio of the local volumetric rate of entropy generation, S'''_{Gen} and the entropy generation characteristics rate, S'''_0, gives the effective entropy generation analysis of the system. Using the similarity transformations (11)–(16) the non-dimensional form of this ratio is as given below:

$$N_E = Re(1+N_r)\theta'^2 + \frac{ReBr}{\Pi} f''^2 + \frac{M^2 E_c Pr}{\Pi}\sin^2\gamma f'^2 + \zeta Re\left(\frac{\Omega}{\Pi}\right)^2 \phi'^2 + \zeta Re\left(\frac{\Omega}{\Pi}\right)\phi'\theta' \tag{31}$$

Where

$$Re = \frac{u_w(x)x}{\nu}, \quad Br = \frac{\mu u_w^2(x)}{k\Delta T}, \quad Pr = \frac{\nu\rho c_\rho}{\kappa},$$
$$\zeta = \frac{C_\infty RD_B}{k}, \quad \Pi = \frac{T_w - T_\infty}{T_\infty}, \quad E_c = \frac{u_w^2(x)bx^2}{\nu c_\rho(T_w - T_\infty)},$$
$$M^2 = \frac{\sigma B_0^2}{\rho b}, \quad \Omega = \frac{C_w - C_\infty}{C_\infty} \tag{32}$$

E_c in this case is the local Eckert number.

Separating Eq. (31) into the irreversibility due to the heat transfer, N_1 and the entropy generation number caused by diffusive irreversibility together with entropy generation as a result of the magnetic field, (N_2). Both N_1 and N_2 are expressed with respect to the terms of Eq. (31):

$$N_1 = Re(1+N_r)\theta'^2, \quad N_2 = \frac{ReBr}{\Pi} f''^2 + \frac{M^2 E_c Pr}{\Pi}\sin^2\gamma f'^2 + \zeta Re\left(\frac{\Omega}{\Pi}\right)^2 \phi'^2 + \zeta Re\left(\frac{\Omega}{\Pi}\right)\phi'\theta' \tag{33}$$

The idea of separating the contributions of the different terms of the entropy generation number allows us to determine which of the contributions dominate in the entropy generation analysis. We seek to establish if the heat transfer dominates the diffusive irreversibility and magnetic field entropy generation. To achieve this, we obtain the Bejan number, Be, which is mostly considered as the parameter at which the entropy generation is at its least.

$$Be = \frac{N_1}{N_E} \tag{34}$$

6. DISCUSSION OF RESULTS

The non-dimensional governing equations are solved numerically by spectral quasi-linearization method and the computed results are presented in tables and figures. Table I: Results here show that in the absence of magnetic interaction parameter (M), local inertia coefficient (F_r), porosity parameter (K_1), thermal Grashof number (λ_1), concentration Grashof number (λ_2), chemical reaction parameter (C_r), Eckert number (E_c), thermophoresis parameter (N_t) and brownian motion parameter (N_b), the

ARTICLE

Table I. Comparison of numerical results for $-\theta'(0)$ of the present study with the results of El-Aziz,[2] Shateyi and Motsa[49] and Anjali.[16] $R = 10^5$, $S_c = 0.22$, $S_f = 0$, $E_c = 0$, $K1 = 0$, $F_r = 0$, $N_t = 0$, $N_b = 0$, $C_r = 0$, $\lambda_1 = 0$, $\lambda_2 = 0$.

A	Pr	El-Aziz[2]	Shateyi and Motsa[49]	Anjali[16]	Present Study
0.8	0.1	0.4517	0.45149	0.45150	0.45216073
0.8	1.0	1.6728	1.67285	1.67284	1.67284531
0.8	10	5.70503	5.70598	5.70588	5.70597890
1.2	0.1	0.5087	0.50850	0.50845	0.50866087
1.2	1.0	1.818	1.81801	1.81801	1.81800501
1.2	10	6.12067	6.12102	6.12103	6.12102446
2.0	0.1	0.606013	0.60352	0.60371	0.60352878
2.0	1.0	2.07841	2.07841	2.07841	2.07841323
2.0	10	6.88506	6.88615	6.88622	6.88615123

numerical solution obtained for the non-dimensional rate of heat transfer agree greatly with that of Abd El-Aziz,[2] Shateyi and Motsa[49] and Anjali Devi.[16]

The overall effects of flow and fluid parameters, which include; unsteadiness parameter, A, velocity slip, S_f, suction parameter, S, alignment angle, γ of the variable magnetic field, angle of inclination, α of the unsteady stretching sheet, the local Eckert number, E_c, the Brownian motion parameter, N_b, the thermophoresis parameter, N_t, the Reynolds number, Re, Brinkman number, Br, on the fluid velocity, temperature, concentration and entropy generation profiles are investigated here.

Table II: illustrates the effects of some of the parameters earlier listed on the skin friction, Nusselt and the local Sherwood numbers. The skin friction coefficient, Nusselt number and Sherwood number are characteristics of the fluid flow at the boundary layers. Skin friction coefficient presents the proportion of the local frictional force per unit area that is experienced at the boundary layer as shear stress. Nusselt number evaluates the ratio of the heat transfer by convection to heat transfer by conduction under the same conditions. Sherwood number as a boundary layer characteristics describes the mass flux process at the boundary layers. It can be observed, that the skin friction decreases for increasing values of unsteadiness parameter, A, suction parameter, S, alignment angle, γ of the magnetic field, angle of inclination, α of the unsteady sheet, which physically represents a reduction in the surface drag to the fluid flow and a reverse trend is observed for increasing values of the velocity slip parameter, S_f. The Nusselt and the local Sherwood numbers increase with increasing values of unsteadiness parameter, A and suction/injection parameter, S. Also both the Nusselt and the local Sherwood number decrease with increasing values of; S_f, γ and α which indicates decline in the heat transfer rate at the stretching sheet, though the variation is observed to be irregular in the cases of γ and α.

Table II. Impact of A, S_f, γ and α on the skin friction coefficient, C_{fx},Nusselt number, N_{ux} and the local Sherwood number, Sh_x. For $R = 5.0$, $S_c = 0.22$, $S_f = 0$, $E_c = 0$, $K_1 = 0.2$, $F_r = 1.0$, $N_t = 0.1$, $N_b = 0.1$, $C_r = 0.5$, $\lambda_1 = 0.2$, $\lambda_2 = 0.4$.

A	S_f	S	γ	α	$f''(0)$	$-\theta'(0)$	$-\phi'(0)$
0	0.5	1.0	$\pi/4$	$\pi/6$	−0.94667	0.92354782	0.58790793
0.5					−0.97992	1.15614388	0.71778018
1.0					−1.00886	1.33539248	0.82359597
1.5					−1.03464	1.48633522	0.91495571
2.0					−1.05792	1.61956696	0.99660121
1.0	0	1.0	$\pi/4$	$\pi/6$	−2.31718	1.49043746	0.89727436
	0.5				−1.00812	1.33539257	0.82359370
	1.0				−0.65625	1.28321074	0.79934859
	1.5				−0.38934	1.23903542	0.77900526
	2.0				−0.27740	1.21904238	0.76984922
1.0	0.5	−1.0	$\pi/4$	$\pi/6$	−0.75324	0.89210223	0.66290983
		0			−0.87396	1.08095675	0.73561066
		1			−1.00886	1.33539263	0.82359370
		2			−1.14375	1.66756816	0.93220004
1.0	0.5	1.0	0	$\pi/6$	−0.94765	1.36023573	0.83667527
			$\pi/6$		−1.02678	1.32840432	0.81999581
			$\pi/4$		−1.00886	1.33539257	0.82359370
			$\pi/3$		−0.95650	1.35654795	0.83470318
			$\pi/2$		−1.01435	1.33323596	0.82247971
1.0	0.5	1.0	$\pi/4$	0	−0.90350	1.38207915	0.84944679
				$\pi/6$	−1.00886	1.33539257	0.82359370
				$\pi/3$	−1.16631	1.25715862	0.78073374
				$\pi/2$	−1.09100	1.29608021	0.80198039

Figure 2 depicts the influence of velocity slip, S_f on the velocity, temperature and concentration profiles. Increasing values of S_f increases the temperature and concentration profiles, a reverse trend is observed for the velocity profile which implies that the velocity of the fluid near the sheet is not the same anymore with the velocity of the stretching sheet. This means that in the presence of increasing velocity slip, the sheet's pulling is only partially communicated to the fluid flow.

Effects of the angle of inclination, α, of the stretching sheet on the velocity, temperature and concentration profiles are demonstrated in Figure 3. It is observed from the graphs that increasing values of α have no significant effects on the concentration and temperature profiles at the surface of the sheet but later on within the boundary layers, the effects become significant enough to show increasing trends in the profile and then the effect become less significant again at the end of the boundary layers. An overall decrease is observed in the velocity profile for increasing values of α. The effects is seen in such a way that the profile decreases rapidly from a maximum value at the surface of the sheet until it attains a minimum within the boundary layer and it increases afterwards due to reduction in buoyancy. We note that the case $\alpha = 0$ describes the vertical fluid flow and the case $\alpha = \pi/2(90°)$ describes the horizontal fluid flow. Similar observations are made in Figure 4 for increasing values of the porosity of the medium. Reduction in the velocity of the fluid in the case is due to the reduction in space for the fluid by increasing porosity.

Figure 5 depict the behaviours of the velocity, temperature and concentration profiles for the different values of the aligned angle, γ, of the magnetic field. It is seen that

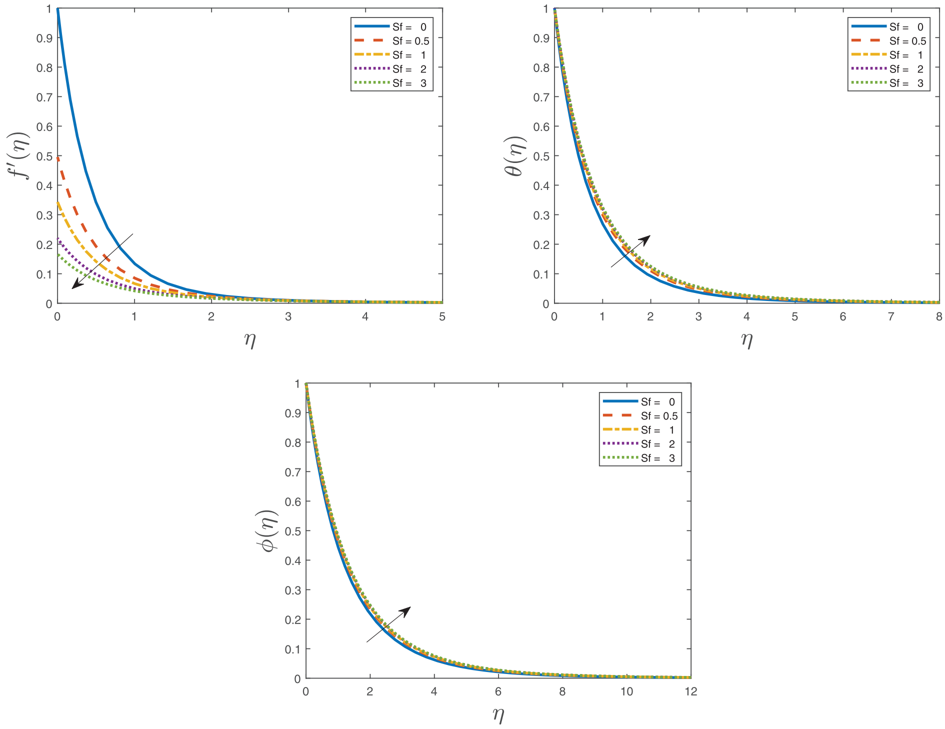

Fig. 2. Effect of slip velocity, S_f on: (a) velocity profile (b) temperature profile and (c) concentration profile. $A = 1$ $P_r = 0.71$, $R = 5$, $S_c = 0.22$, $E_c = 0.01$, $K_1 = 0.2$, $F_r = 1.0$, $N_t = 0.1$, $N_b = 0.1$, $C_r = 0.22$, $M^2 = 1.0$, $\lambda_1 = 0.2$, $\lambda_2 = 0.4$, $\alpha = \pi/6$, $\gamma = \pi/2$, $S = 1.0$.

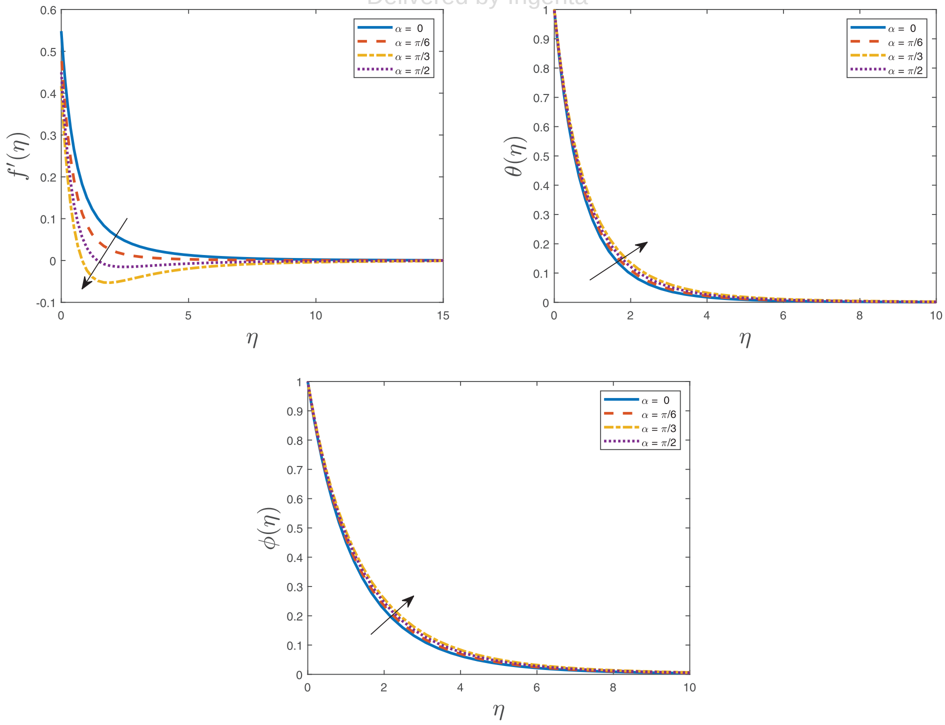

Fig. 3. Effect of angle of inclination, α of the plate on: (a) velocity profile (b) temperature profile and (c) concentration profile. $A = 1$ $P_r = 0.71$, $R = 5$, $S_c = 0.22$, $E_c = 0.01$, $K_1 = 0.2$, $F_r = 1.0$, $N_t = 0.1$, $N_b = 0.1$, $C_r = 0.5$, $M^2 = 1.0$, $\lambda_1 = 0.2$, $\lambda_2 = 0.4$, $S_f = 0.5$, $\gamma = \pi/4$, $S = 1.0$.

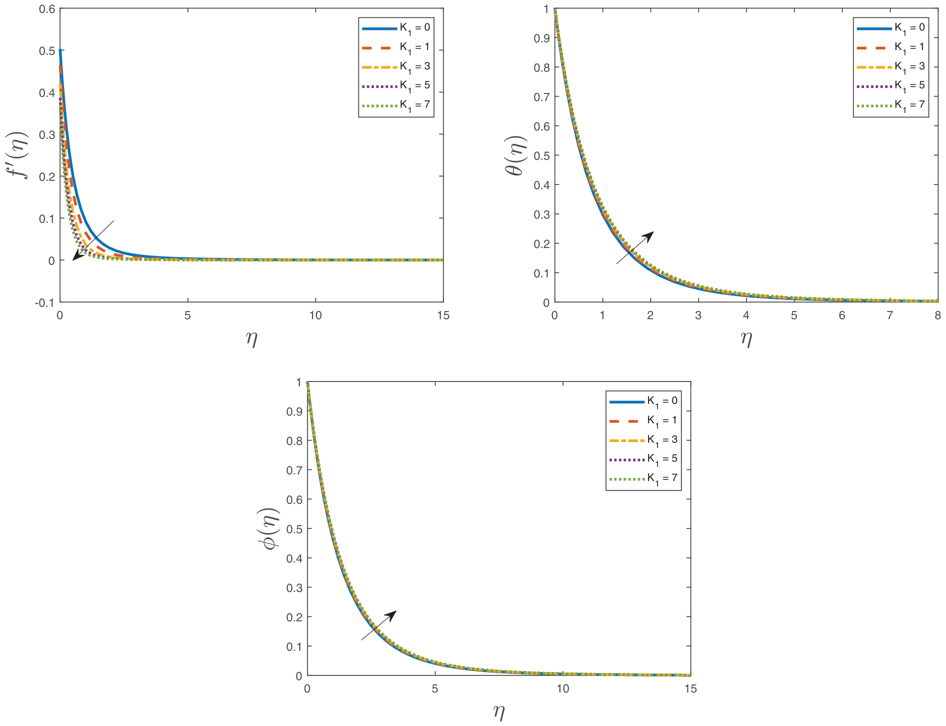

Fig. 4. Effect of porosity, K_1, on the: (a) velocity profile (b) temperature profile and (c) concentration profile. $A = 1$ $P_r = 0.71$, $R = 5$, $S_c = 0.22$, $E_c = 0.01$, $\alpha = \pi/6$, $F_r = 1.0$, $N_t = 0.1$, $N_b = 0.1$, $C_r = 0.22$, $M^2 = 1.0$, $\lambda_1 = 0.2$, $\lambda_2 = 0.4$, $S_f = 0.5$, $\alpha = \pi/6$, $S = 1.0$.

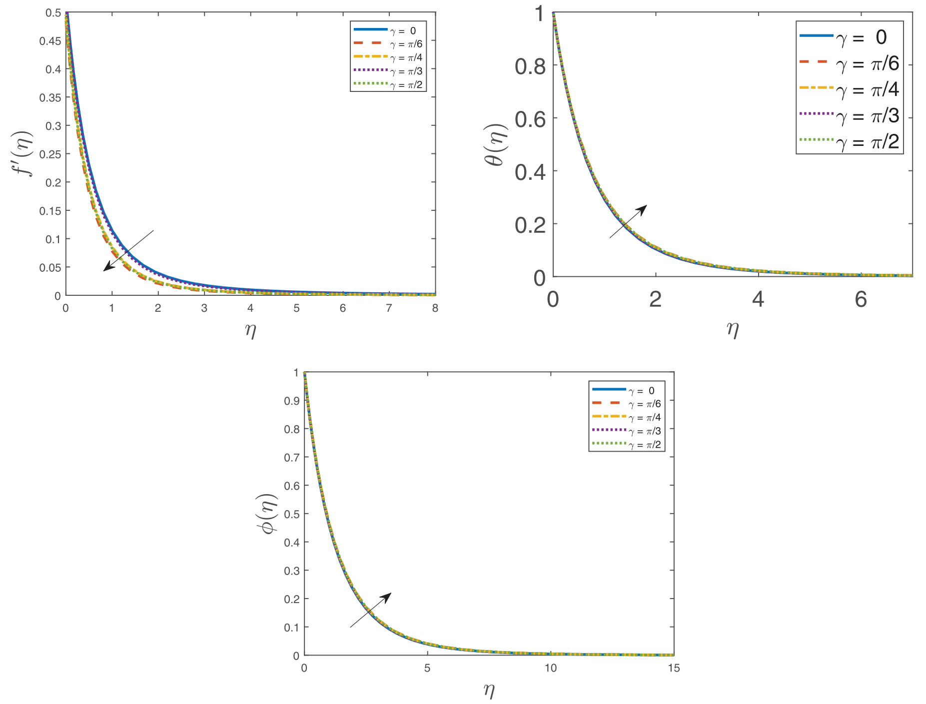

Fig. 5. Effect of aligned angle, γ of the magnetic field on: (a) velocity profile (b) temperature profile and (c) concentration profile. $A = 1$ $P_r = 0.71$, $R = 5$, $S_c = 0.22$, $E_c = 0.01$, $K_1 = 0.2$, $F_r = 1.0$, $N_t = 0.1$, $N_b = 0.1$, $C_r = 0.22$, $M^2 = 1.0$, $\lambda_1 = 0.2$, $\lambda_2 = 0.4$, $S_f = 0.5$, $\alpha = \pi/6$, $S = 1.0$.

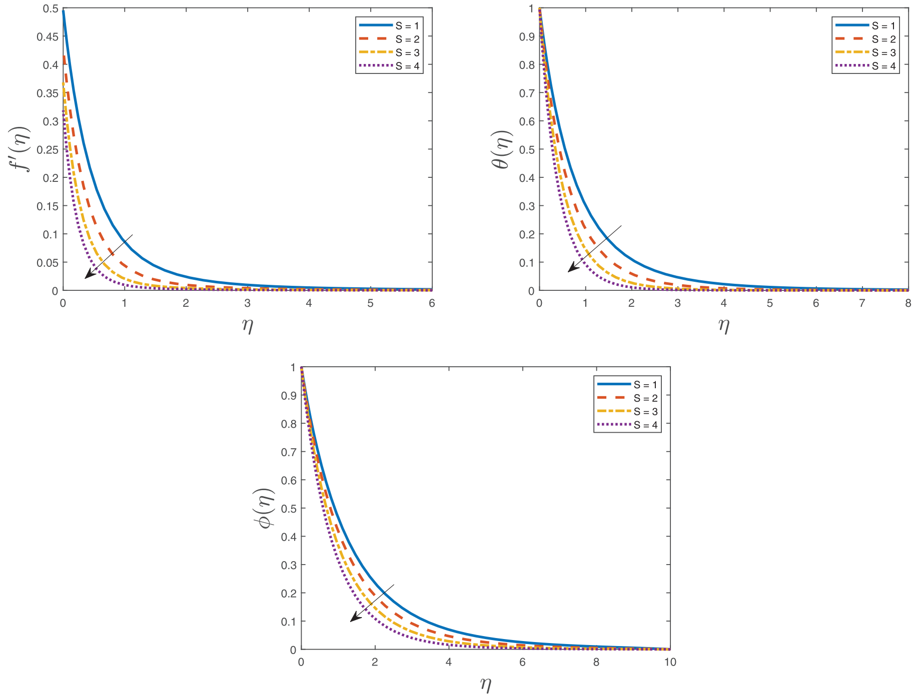

Fig. 6. Effect of suction parameter, S on: (a) velocity profile (b) temperature profile and (c) concentration profile. $A = 1$ $P_r = 0.71$, $R = 5$, $S_c = 0.22$, $E_c = 0.01$, $K1 = 0.2$, $F_r = 1.0$, $N_t = 0.1$, $N_b = 0.1$, $C_r = 0.22$, $M^2 = 1.0$, $\lambda_1 = 0.2$, $\lambda_2 = 0.4$, $S_f = 0.5$, $\alpha = \pi/6$, $\gamma = \pi/4$.

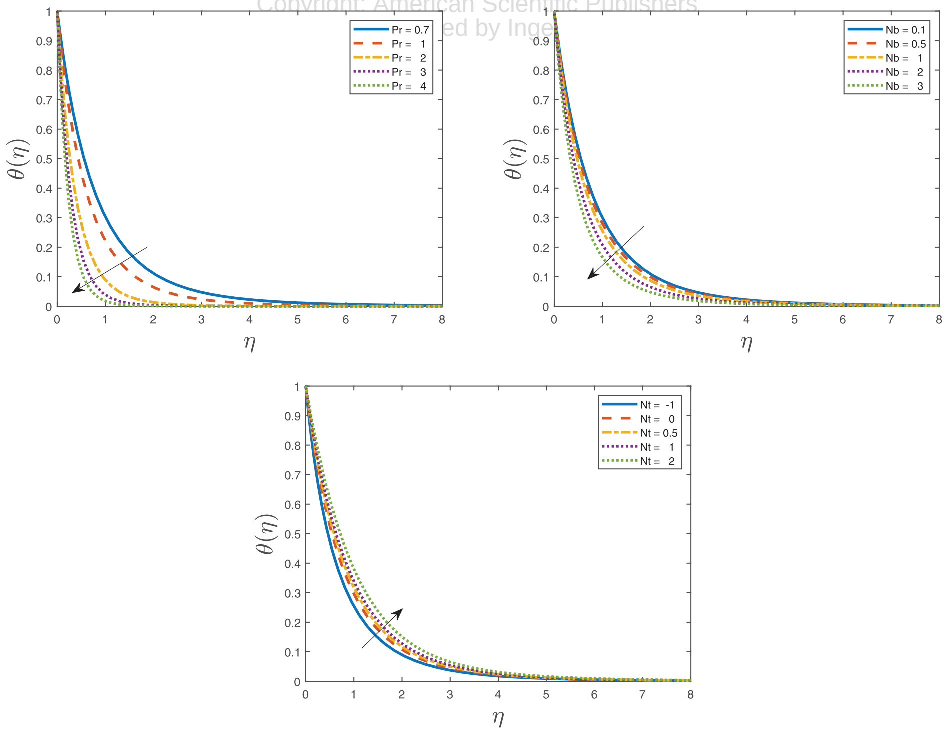

Fig. 7. (a) Effect of Prandtl number on the temperature profile (b) Effect of the Brownian motion parameter on the temperature profile and (c) Effect of the Thermophoresis parameter on the temperature profile. $A = 1$ $P_r = 0.71$, $R = 5$, $S_c = 0.22$, $E_c = 0.01$, $K_1 = 0.2$, $F_r = 1.0$, $C_r = 0.22$, $M^2 = 1.0$, $\lambda_1 = 0.2$, $\lambda_2 = 0.4$, $\alpha = \pi/6$, $\gamma = \pi/2$, $S = 1.0$.

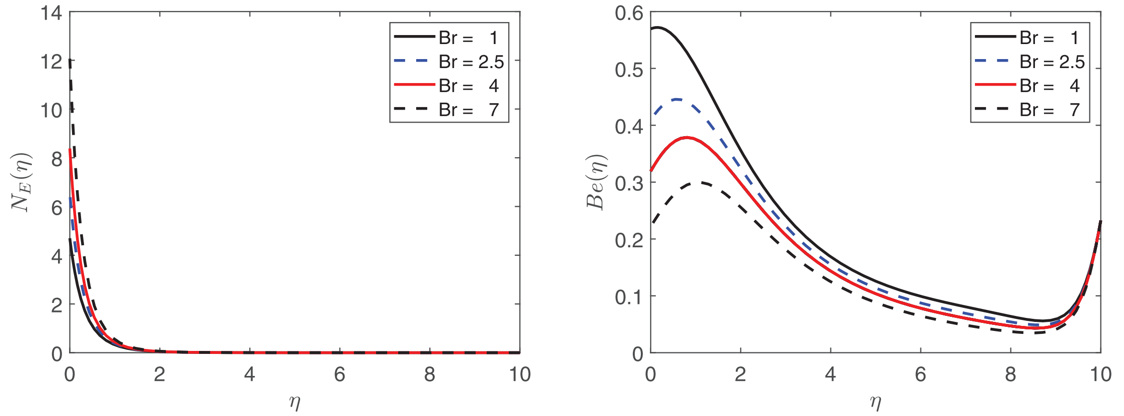

Fig. 8. (a) Effect of Brinkman number on entropy generation number, N_E (b) effect of Brinkman number on Bejan number, Be. $Re = 1.0$, $\zeta = 0.01$, $E_c = 0.01$, $N_r = 0.5$, $\Pi = 0.2$, $\Omega = 2.0$, $Pr = 0.71$, $M^2 = 1.0$.

enhanced values of γ between 0^0 and $\pi/2(90°)$ decreases the velocity profile and increase the temperature and concentration profiles. This is because the enhanced values of γ strengthens the magnetic field which in turns causes the formation of a force that opposes the motion of the fluid, hence slows down the fluid flow. This opposing force is the Lorentz force. The aligned angle case $\gamma = 0$ produces no magnetic effect on the fluid flow and the case $\gamma = \pi/2(90°)$ produces the transverse magnetic field effect on the fluid flow.

Figure 6 demonstrate the impact of suction parameter, S, on the velocity, temperature and concentration profiles. It is evident from the graphs that, increasing values of S, drop the velocity, temperature and concentration profiles. Suction brings about significant reduction in the velocity of the fluid as it makes the fluid move closer to the sheet where the viscosity is more. The thermal boundary layer thickness is reduced as fluids at the ambient conditions are brought closer to the surface in the presence of suction, similar observations are made for concentration profile.

Figure 7 depict the effects of Prandtl number, brownian motion parameter and thermophoresis parameter on the temperature profile. Increasing values of the Prandtl number, Pr, which is the ratio of the momentum diffusivity to thermal diffusivity, makes the thermal boundary layer to reduce in thickness and as such the thermal diffusivity is reduced. Reducing the thermal diffusivity means that the fluid conducts thermal energy less relative to it storing thermal energy. The brownian motion parameter, N_b, decreases the temperature profile for enhanced values, which is in complete agreement with what was reported by Ahmad et al.[7] Increasing values of the thermophoresis parameter, N_t, pulls up the temperature profile, this also agrees with what has been reported in different studies.

From Figure 8, we see the entropy generation number for a fixed value of the Brinkman number decreases slowly from the surface of the sheet as it moves farther away. Increasing values of, Br, increases the entropy generation number which implies increase in the heat transfer rate. Similar trends can be seen in the entropy generation for increasing values of Prandtl number, Pr, Reynolds number, Re and the dimensionless parameter, Ω. The variations in thermal radiation, N_r and aligned angle, γ of the magnetic field have no significant effect on the entropy generation number. However, for a fixed for each of the trends are the same as the ones observed in cases of, Br, Pr, Re and Ω. In Figure 8, for a fixed value of the Brinkman number, Br, the Bejan number, Be, increases close to the surface of the sheet to a maximum value, after which it falls rapidly until it reaches a minimum value and rises again towards the end of the boundary layer. The initial increase becomes more significant with increasing value of Br. The overall decrease of Be implies that the diffusive irreversibility and irreversibility due to magnetic field dominate the irreversibility due to heat transfer. In Figure 9, we see that increasing values of the Prandtl number, Pr, drops the Bejan number which means the irreversibility due to diffusion and magnetic field dominates the irreversibility due to heat transfer. The Bejan number, Be, attains it minimum value quickly when $Pr = 1$, being that its maximum value closer to the sheet surface is lesser compare to when $Pr > 1$. However, $Pr > 1$ values give lower minimum values for Be which inturns result in better minimum entropy generation and hence improve the overall efficiency of the sytsem.

Variation in Reynolds number show no significant effect on the Bejan number. However, for a fixed value of Re, Be rises to a maximum value in the vicinity of the sheet, after which it drops quickly until a minimum value is attained and then it rises again as seen in Figure 10. In Figure 11, an overall rise in Be for increasing values of the radiation parameter, N_r, which suggests that the combined contribution of diffusive and magnetic irreversibility to the entropy generation is less compare to the compare to the contribution of the irreversibility due to heat transfer. Similar but reverse trends are observed in Figures 12 and 13 for

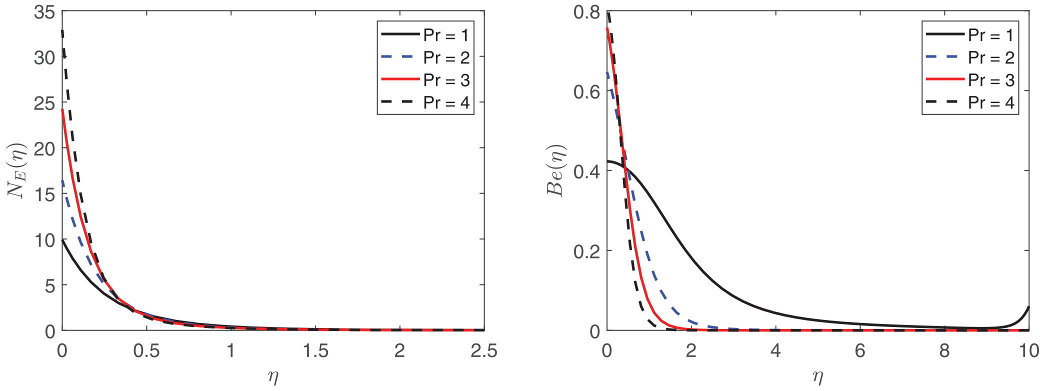

Fig. 9. (a) Effect of Prandtl number on entropy generation number, N_E (b) effect of Prandtl number on Bejan number, Be. $Re = 1.0$, $\zeta = 0.01$, $E_c = 0.01$, $N_r = 0.5$, $\Pi = 0.2$, $\Omega = 2.0$, $Br = 4.0$, $M^2 = 1.0$.

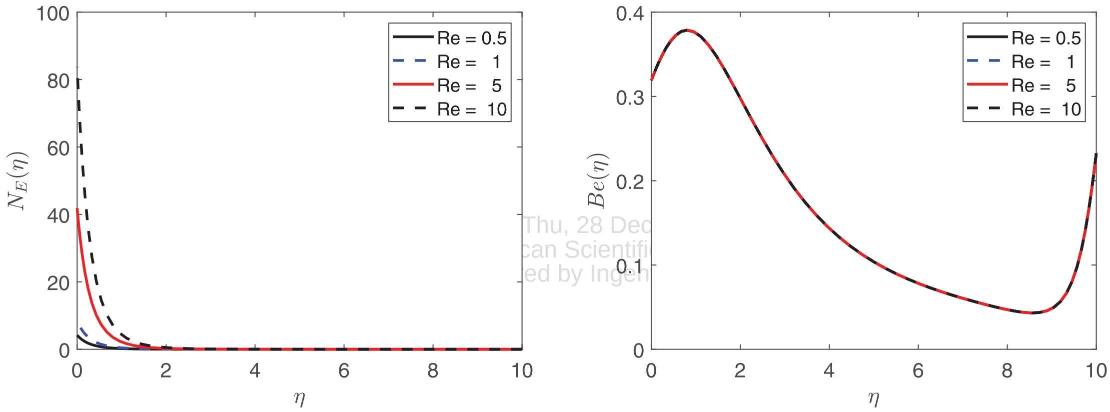

Fig. 10. (a) Effect of Reynolds number on entropy generation number, N_E (b) Effect of Reynolds number on Bejan number, Be. $Br = 4.0$, $\zeta = 0.01$, $E_c = 0.01$, $N_r = 0.5$, $\Pi = 0.2$, $\Omega = 2.0$, $Pr = 0.71$, $M^2 = 1.0$.

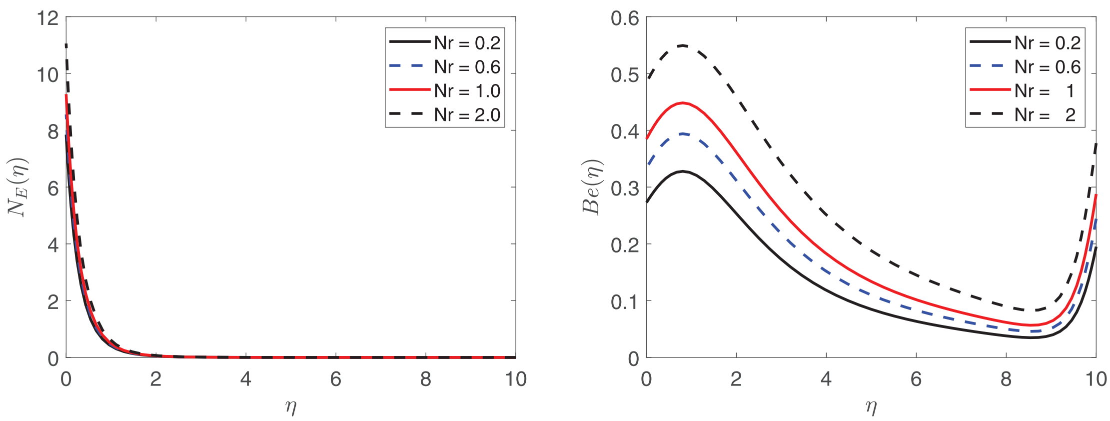

Fig. 11. (a) Effect of radiation parameter on entropy generation number, N_E (b) Effect of radiation parameter on Bejan number, Be. $Re = 1.0$, $\zeta = 0.01$, $E_c = 0.01$, $Br = 4.0$, $\Pi = 0.2$, $\Omega = 2.0$, $Pr = 0.71$, $M^2 = 1.0$.

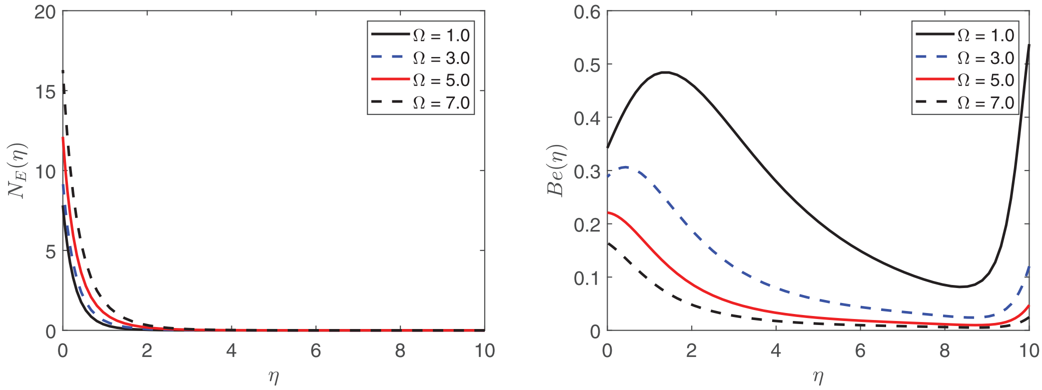

Fig. 12. (a) Effect of dimensionless parameter, Ω on entropy generation number, N_E (b) Effect of dimensionless parameter, Ω on Bejan number, Be. $Re = 1.0$, $\zeta = 0.01$, $E_c = 0.01$, $N_r = 0.5$, $\Pi = 0.2$, $\Omega = 2.0$, $Pr = 0.71$, $M^2 = 1.0$.

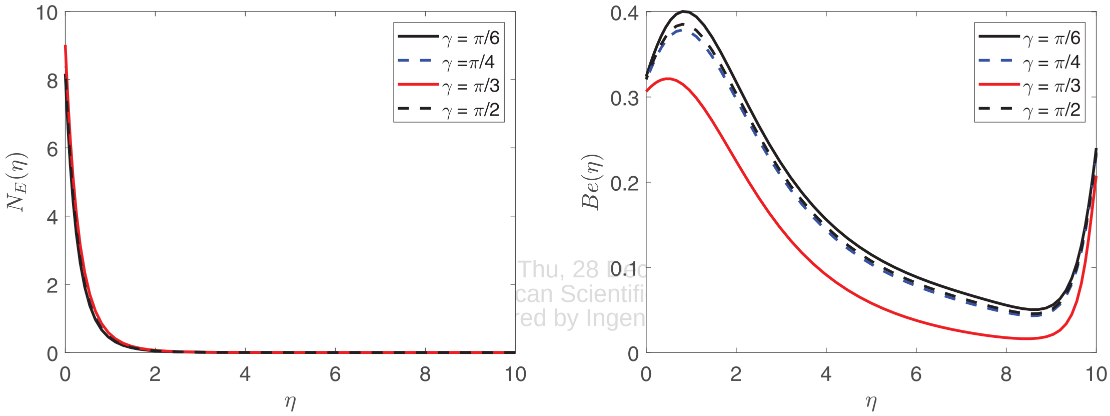

Fig. 13. (a) Effect of aligned angle of the magnetic field on entropy generation number, N_E (b) Effect of aligned angle of the magnetic field on Bejan number, Be. $Re = 1.0$, $\zeta = 0.01$, $E_c = 0.01$, $N_r = 0.5$, $\Pi = 0.2$, $\Omega = 2.0$, $Pr = 0.71$, $M^2 = 1.0$.

increasing values of the dimensionless parameter, Ω and the aligned angle, γ of the magnetic field.

7. CONCLUSION

In this study, we have employed the spectra quasilinear method to investigate the entropy generation of an unsteady MHD nanofluid over a porous inclined stretching sheet in the presence of velocity slip, thermal radiation, viscous dissipation and inclined variable magnetic field. The effects of pertinent fluid characteristics and parameters have been studied, with the results presented in tables and graphs and from these, we are able to make the following concluding remarks:

- Velocity slip has positive and significant effects on the temperature and concentration profiles whereas opposite is the case for the velocity profile.
- Increasing values of angle of inclination, α and the porosity, K_1 slow down the fluid and hence decrease the velocity profile, whereas the cases of temperature and concentration are opposite for increasing values of α
- Enhancement in the values of the aligned angle, γ, of the magnetic field between 0 and 90°, decreases the velocity profile and increases the temperature and concentration profile.
- Improvements on the values of the suction reduces significantly the velocity, temperature and concentration profiles.
- Increasing values of Pr and Nb drop the temperature profile and makes the concentration profile rises with increasing values of N_t
- Increasing values of Br, Pr, Re and Ω increase the heat transfer rate
- Increasing N_r and γ have no significant effects on the entropy generation number, N_E
- Increasing values of N_r increases the Bejan number, Be
- Enhancements in the values of Ω, Pr and γ reduces the Bejan number.

References and Notes

1. M. Abd-El Aziz, *Acta Mechanica* 187, 113 (**2006**).

2. M. Abd El-Aziz, *International Communications in Heat and Mass Transfer* 36, 521 (**2009**).

3. T. N. Abdelhameed, *Scientific Reports* 11, 1 (**2021**).

4. M. I. Afridi, M. Qasim, I. Khan, S. Shafie, and A. S. Alshomrani, *Entropy* 19, 10 (**2016**).

5. M. I. Afridi, M. Qasim, I. Khan, S. Shafie, and A. S. Alshomrani, *Entropy* 19, 10 (**2017**).

6. N. Ahmad and N. Khan, 7, 51 (**2000**).

7. S. Ahmad, A. Ahmad, K. Ali, H. Bashir, and M. F. Iqbal, *Alexandria Engineering Journal* 60, 4931 (**2021**).

8. N. Ameer Ahamad, M. Veera Krishna, and A. J. Chamkha *Journal of Nanofluids* 9, 177 (**2020**).

9. S. Baag, S. R. Mishra, G. C. Dash, and M. R. Acharya, *Ain Shams Engineering Journal* 8, 623 (**2017**).

10. A. J. Chamkha, A. M. Rashad, T. Armaghani, and M. A. Mansour, *Journal of Thermal Analysis and Calorimetry* 132, 1291 (**2018**).

11. A. J. Chamkha, A. M. Rashad, M. A. Mansour, T. Armaghani, and M. Ghalambaz, *Physics of Fluids* 29, 052001 (**2017**).

12. A. J. Chamkha, A. M. Rashad, A. I. Alsabery, Z. M. A. Abdelrahman, and H. A. Nabwey, *Journal of Thermal Science and Engineering Applications* 12, 051002 (**2020**).

13. R. Cortell, *Fluid Dynamics Research* 37, 231 (**2005**).

14. R. Cortell, *Physics Letters A* 372, 631 (**2008**).

15. L. J. Crane, *Zeitschrift für angewandte Mathematik und Physik ZAMP* 21, 645 (**1970**).

16. S. P. Devi Anjani and D. Kumari Vasantha, *Ain Shams Engineering Journal* 9, 1161 (**2018**).

17. M. Dhlamini, H. Mondal, P. Sibanda, and S. Motsa, *International Journal of Ambient Energy* 1 (**2020**).

18. E. Elbashbeshy, and T. G. Emam, *Thermal science* 15, 477 (**2011**).

19. E. M. A. Elbashbeshy, D. M. Yassmin, and A. A. Dalia, *African Journal of Mathematics and Computer Science Research* 3, 68 (**2010**).

20. M. F. Endalew, and A. Nayak, *Heat TransferâŁ"Asian Research* 48, 42 (**2019**).

21. B. Fornberg, *A practical guide to pseudospectral methods*, Number 1. Cambridge university press (**1998**).

22. B. Ganga, M. Govindaraju, and A. K. Abdul Hakeem, *Iranian Journal of Science and Technology, Transactions of Mechanical Engineering* 43, 707 (**2019**).

23. S. P. Goqo, S. Mondal, P. Sibanda, and S S Motsa, *Journal of Computational and Theoretical Nanoscience* 13, 7483 (**2016**).

24. M. Govindaraju, N. V. Ganesh, B. Ganga, and A. K. Abdul Hakeem, *Journal of the Egyptian Mathematical Society* 23, 429 (**2015**).

25. S. Gupta, Devendra Kumar, and Jagdev Singh, *International Journal of Heat and Mass Transfer* 118, 378 (**2018**).

26. T. Hayat, Shahida Bibi, M. Rafiq, A. Alsaedi, and F. M. Abbasi, *Journal of magnetism and magnetic materials* 401, 733 (**2016**).

27. T. Hayat, Rahila Naz, and S. Abbasbandy, *Transport in porous media* 87, 355 (**2011**).

28. T. Hayat, R. Sajjad, Z. Abbas, M. Sajid, and A. A. Hendi, *International Journal of Heat and Mass Transfer* 54, 854 (**2011**).

29. G. Ibáñez, A. López, J. Pantoja, and J. Moreira, *International Journal of Heat and Mass Transfer* 100, 89 (**2016**).

30. D. B. Ingham, and I. Pop, *Transport phenomena in porous media*, Elsevier (**1998**).

31. M. A. Ismael, M. A. Mansour, A. J. Chamkha, and A. M. Rashad, *Journal of Magnetism and Magnetic Materials*, 416, 25 (**2016**).

32. M. Veera Krishna, N. Ameer Ahamad, and A. J. Chamkha, *Alexandria Engineering Journal* 59, 565 (**2020**).

33. M. Veera Krishna, P. V. S. Anand, and A. J. Chamkha, *Special Topics & Reviews in Porous Media: An International Journal* 10 (**2019**).

34. M. Veera Krishna, and A. J. Chamkha, *Results in Physics* 15, 102652 (**2019**).

35. M. Veera Krishna, and A. J. Chamkha, *Numerical Methods for Partial Differential Equations* 37, 2150 (**2021**).

36. M. Veera Krishna, K. Jyothi, and A. J. Chamkha, *International Journal of Fluid Mechanics Research* 45 (**2018**).

37. M. Veera Krishna, K. Jyothi, and A. J. Chamkha, *Journal of Porous media* 23 (**2020**).

38. M. Veera Krishna, B. V. Swarnalathamma, and A. J. Chamkha, *Journal of Ocean Engineering and Science* 4, 263 (**2019**).

39. A. Lopez, G. Ibanez, J. Pantoja, J. Moreira, and O. Lastres, *International Journal of Heat and Mass Transfer* 107, 982 (**2017**).

40. M. A. Mjankwi, V. G. Masanja, E. W. Mureithi, and M. N. James, *International Journal of Mathematics and Mathematical Sciences* 2019 (**2019**).

41. S. S. Motsa, P. G. Dlamini, and M. Khumalo, *Advances in Mathematical Physics* 2014 (**2014**).

42. D. A. Nield, A. Bejan, et al., *Convection in porous media*, Springer (**2006**), Vol. 3.

43. K. Ramesh, and S. A. Eytoo, *Multidiscipline Modeling in Materials and Structures* (**2019**).

44. A. Raptis, *International Communications in Heat and Mass Transfer* 25, 289 (**1998**).

45. A. M. Rashad, M. A. Ismael, A. J. Chamkha, and M. A. Mansour, *Journal of the Taiwan Institute of Chemical Engineers* 68, 173 (**2016**).

46. A. M. Rashad, M. A. Mansour, T. Armaghani, and A. J. Chamkha, *Physics of Fluids* 31, 042006 (**2019**).

47. B. C. Sakiadis, *AIChE Journal* 7, 26 (**1961**).

48. G. S. Seth, R. Nandkeolyar, and M. S. Ansari (**2012**).

49. S. Shateyi, and S. S. Motsa, *Mathematical Problems in Engineering* 2009 (**2009**).

50. T. Tayebi, and A. J. Chamkha, *International Journal of Numerical Methods for Heat & Fluid Flow* 30, 1115 (**2019**).

51. M. Veera Krishna, N. Ameer Ahamad, and A. J. Chamkha, *Journal of Nanofluids* 10, 259 (**2021**).

52. U. M. Zahid, Y. Akbar, and F. M. Abbasi, *Chinese Journal of Physics* 67, 330 (**2020**).

ARTICLE

Chapter 3

EMHD tangent hyperbolic nanofluid flow over an inclined stretchable Riga surface with duffour effect, activation energy and heat generation

This chapter focuses on the analysis of electromagnetohydrodynamic tangent hyperbolic nanofluid flow over an inclined stretchable Riga plate, with particular interest in the applications in thermal nuclear reactors, flow meters, industrial food processors, biomedical, and chemical engineering. The research explores the effects of key parameters such as the Dufour effect, activation energy, and heat generation on the fluid flow characteristics. In chapter 2, we have seen that the traditional SQLM efficiently solves ODEs. However, this method's accuracy, flexibility, computational efficiency, and convergence can be improved, and introducing the overlapping grid helps achieve this. In this chapter, we have employed the overlapping SQLM in solving ODEs obtained after the governing system of PDEs has been transformed using suitable transformations. The numerical results are presented in tables and figures, accompanied by extensive analysis of the overall influences of essential modelled variables on plate surface characteristics, velocity, temperature, and mass flux distributions.

EMHD Tangent Hyperbolic Nanofluid Flow Over An Inclined Stretchable Riga Surface With Duffour Effect, Activation Energy And Heat Generation

Folarin Oluwaseun [a]

Sicelo Goqo [a]

Hiranmoy Mondal [b*]

Sibonelo Nzama [a]

[a] *School of Mathematics, Statistics and Computer Science,University of KwaZula-Natal, Private Bag X01, Scottsvile, Pietermaritzburg-3209, South Africa*

[b] *Department of Applied Mathematics, Maulana Abul Kalam Azad University of Technology, West Bengal, Kolkata-700064, India*

Abstract

Continuous rigorous efforts are currently being made in the comprehensive studies of tangent hyperbolic nanofluid flow in relations to Riga plates as the applications of such configuration grow more in the construction and operations of thermal nuclear reactors, flow meters, industrial food processors, biomedical and chemical engineering. This work seeks explore the analysis of electromagnetohydrodynamic (EMHD) tangent hyperbolic nanofluid fluid flow over an inclined stretchable Riga plate with Duffour effect, activation energy and heat generation has been examined in the research work. The controlling system of PDEs were duly converted with the aid suitable transformations to obtain a system of ODEs that are nonlinear. The system of ODEs were solved using the overlapping grid SQLM and the numerical results presented in tables and figures with extensive analysis of overall influences of essential modeled variables on plate surface characteristics, velocity, temperature and mass flux distributions. The results obtained numerically present that the surface characteristics of the fluid in terms of the skin friction drag declines as M,n,We,Gr_T and Gr_C are elevated.The velocity field grows with enhancements of Gr_T and Gr_C, and it falls for growing values of We,n and S.The temperature distribution displays improvements as N_r,θ_w,Bi,N_t and N_b and it goes down for improving values of Gr_T,Gr_C and E_a.Mass flux distribution declines for improving values of Sc, k_1, N_t and N_b and appreciates for growing values of E_a.

Key words: Tangent hyperbolic nanofluids, EMHD, Inclined stretchable riga surface, Duffour effect,Activation energy,Heat generation,Overlapping grids special quasi - linearization method.

1. Introduction

The vast applicability of non - Newtonian tangent hyperbolic fluid flows in food industry, fossil fuel extractions, medical sciences, polymer industry, chemical and processing engineering has made it a significant area on researchers' maps. The classical Navier - Stokes governing fluid equations become insufficient in the simulations of the pertinent properties of such fluids and hence, the need for more constitutive equations. The complexities of the connection between the shear stress and the rate of strains along with the viscoelastic properties of the non - Newtonian fluids makes the general governing equations more rigorous compare to the classical Navier - Stokes equations. Extensive researches have been done in the mathematical formulation and numerical simulations of non - Newtonian fluid flows.

*Corresponding author.
Email address : hiranmoymondal@yahoo.co.in (H. Mondal)

Rjagopal[24], in his contribution to this area, explained in details the mechanics of non - Newtonian fluids. Crochet et al [9], extensively discussed numerical methods in the solutions for finding the solutions of non - Newtonian fluid mechanics. Sarpkaya [28] analyzed the flow of non - Newtonian fluids in a magnetic field. Perrin et al, examined the experimental and modelling of non - Newtonian and Newtonian fluid flows in pore network micro models.[11, 23, 8, 7, 23] presented different ideas on non - Newtonian fluids.

Tangent hyperbolic fluid flow describes a particular example of non - Newtonian fluid flows. The interaction of such fluid with magnetic field and heat generation was reported by Rehman et al. [26]. Akbar et al. [2] presented numerical solutions of magnetohyrodynamic boundary layer flow of tangent hyperbolic fluid towards a stretching sheet. Pardeep et al. [17] examined the notion of using tangent hyperbolic nanofluid flow as the foundation for a numerical simulation of nanoparticle size and thermal radiation. Ullah [32], made his own contribution by investigating MHD tangent hyperbolic fluid flow in tandem of an expanding layer. Hayat et al. [14] considered flow of a tangent hyperbolic radiating fluid with convective conditions and chemically - based process. Series solutions were presented by Nadeem and Akbar [20] tangent hyperbolic fluid flows in evenly distributed sloped tubes.

A Riga plate is a plane surface with permanent magnets and electrical electrodes arranged in alternatively. The plate arrangement develops electromagnetic hydrodynamic behaviour in the fluid flowing over it with an exponentially decreasing Lorentz force. Riga plate was first developed by Gailitis [10]. With this development, different models involving the use of Riga plate have been presented. Based on activation energy of tangent hyperbolic nanofluid, Waqas et al. [33] conducted a numerical analysis for bio - convection flow in the vicinity of a Riga plate. Mahdy and Hoshoudy [18] explored the boundary layer electromagnetohydrodynamic flow for time - dependent tangent hyperbolic nanofluid over a convectively heated Riga plate with chemical reaction. The flow of nanofluid past a Riga plate was discussed by Ahmad et al [1]. Pantokratoras [21] presented interesting results on Blasius and Sakiadis flow along a Riga plate. Hayat, Abbas et al. [13] examined how a Riga plate with a varying thickness that is actively heated via convection is affected by flow of nanofluid in its vicinity. Pantokratoras and Magyari discussed EMHD fux from a Riga plate to a free - convection boundary layer [22].

The Duffour effect, which is sometimes called the diffusion - thermo, basically describes flux of energy owing to differences in concentration. The Soret effect, sometimes referred to as thermal - diffusion, represents mass flux as a result of temperature - gradient. Combining effect of these produces a mass concentration gradient resulting from irreversible processes. The applicability of this particularly in geosciences, petrochemical engineering and chemical engineering has led to extensive research studies. In a recent research work, Sindhu and Gireesha [29], described the soret and duffour properties on non - Newtonian fluids. Subba Rao et al., presented steady state transport phenomena on induced magnetic field modelling for nonNewtonian tangent hyperbolic fluid from an isothermal sphere with soret and duffour effects. Using Runge - Kutta - Merson and shooting method, Bhatti et al analyzed the impact of soret and duffour on magnetised nanofluid in respect of tangent hyperbolic flow with hall current which passes over a nonlinear porous stretchable layer.

With respect to the foregoing review of literatures, a research gap has been identified in terms of the analysis of tangent hyperbolic nanofluid fluid flow over an inclined stretchable Riga plate with duffour effect, activation energy and heat generation. The current study seeks to adequately fill this gap through numerical methods; particularly using overlapping grids spectral quasi-linearization method. The main objectives of this numerical investigation are therefore stated thus :

- Present a model that describes a tangent hyperbolic nanofluid flow over an inclined stretchable Riga plate.
- Employ appropriate similarity transformation to the system of nonlinear PDEs to obtain a system of nonlinear ordinary ODEs which then solved using the overlapping grids spectral quasi - linearization method.
- Examine numerically the duffour effect,activation energy and heat generation
- Examine and discuss the salient parameters as they influence the fluid characteristics.

2. Model development

In consideration here is a flow of tangent hyperbolic nanofluid over a stretching inclined Riga plat, which produces an electromagnetic field described by the Grinberb concept as $F = \frac{\pi J_0 M_0 e^{-\frac{\pi}{l} y}}{8}$. The

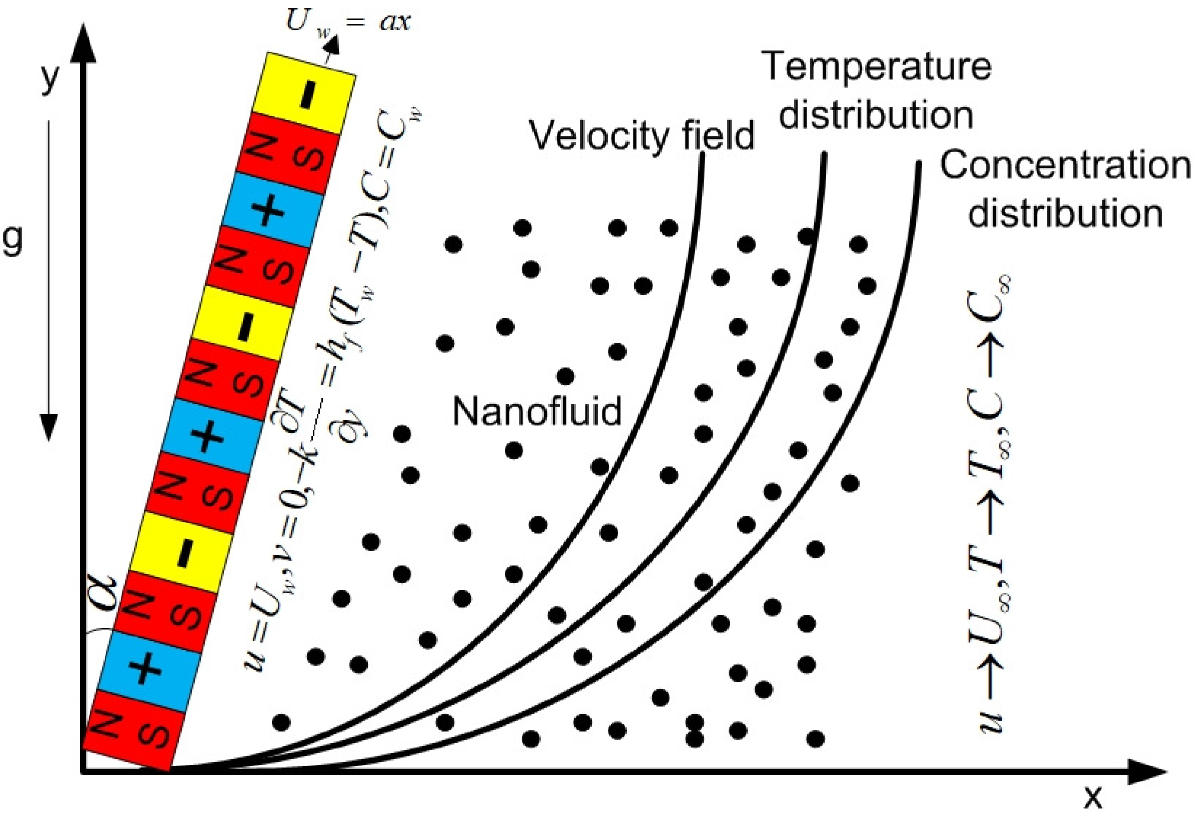

Figure 1: Physical Description

Riga plate which is inclined at angle, α with y - axis, stretches with a linear velocity of $U_w = ax$ and experiences the duffour effect, nonlinear thermally radiative, heat generation and activation energy.The fluid temperature at the plate surface is T_w ,the fluid ambient temperature is T_∞. Surface concentration is C_w , the ambient fluid concentration is C_∞. The characteristics of the nanofluids are described by the Brownian motion and the thermophoresis terms. The set up is observed in the two - dimensional cartesian coordinate.

The physical situation described under these conditions is depicted in the figure and hence, the controlling nonlinear PDEs as used by [[15], [30],[25],[33],[4],[16]] are :

$$\frac{\partial u}{\partial x} + \frac{\partial v}{\partial y} = 0, \tag{1}$$

$$u\frac{\partial u}{\partial x} + v\frac{\partial u}{\partial y} = \nu(1-n)\frac{\partial^2 u}{\partial y^2} + \sqrt{2}\nu n\Gamma\frac{\partial u}{\partial y}\frac{\partial^2 u}{\partial y^2} + \frac{\pi J_0 M_0 e^{-\frac{\pi}{l}y}}{8\rho} + \cos\alpha g\beta_T(T-T_\infty) + \cos\alpha g\beta_C(C-C_\infty) \tag{2}$$

$$u\frac{\partial T}{\partial x} + v\frac{\partial T}{\partial y} = \frac{\kappa}{\rho c_p}\frac{\partial^2 T}{\partial y^2} + \tau\left[D_B\frac{\partial C}{\partial y}\frac{\partial T}{\partial y} + \frac{D_T}{T_\infty}\left(\frac{\partial T}{\partial y}\right)\right] - \frac{1}{(\rho c_p)_f}\frac{\partial q_r}{\partial y} + \frac{Q}{(\rho c_p)_f}(T-T_\infty) + \frac{D_m K_T}{C_s C_p}\frac{\partial^2 C}{\partial y^2} \tag{3}$$

$$u\frac{\partial C}{\partial x} + v\frac{\partial C}{\partial y} = D_B\frac{\partial^2 C}{\partial y^2} - \kappa\left(\frac{T}{T_\infty}\right)^m (C-C_\infty)e^{\left(-\frac{E_1}{\kappa_T}\right)} \tag{4}$$

Applicable boundary conditions are :

$$\begin{aligned} &u = U_w = ax; v = 0; -\kappa\tfrac{\partial T}{\partial y} = h_f(T_w - T); C = C_w; \quad at \;\; y = 0 \\ &u \to U_\infty; T \to T_\infty; C \to C_\infty; \quad as \;\; y \to \infty \end{aligned} \tag{5}$$

Where,C_s is concentration susceptibility, Q is the heat generation parameter, n is power law exponent, c_p is the fluid specific heat capacity, ρ is the density, J_0 is the current density in the electrodes, M_0 is the magnetisation of the permanent magnets in the Riga plate.
Invoking the Rosseland diffusion approximation, q_r,which is the heat flux and it is given by $q_r = -\frac{4\sigma^*}{3k^*}\frac{\partial T^4}{\partial y}$,

where σ^* is the Stephan Boltzmann constant and k^* is the mean absorption coefficient and T^4 can be expressed as $T^4 = T_\infty^4[1 + (\theta_w - 1)\theta]^4$. θ_w is the wall temperature excess ratio parameter given as $\theta_w = \frac{T_w}{T_\infty}$.
The governing nonlinear partial differential equations are adequately converted into a system of nonlinear ODEs using the appropriate transformations given as :

$$\begin{aligned} &u = axf'(\eta), v = -\sqrt{a\nu_f} f(\eta), \eta = \sqrt{\tfrac{a}{\nu_f}} y \\ &\theta = \tfrac{T-T_\infty}{T_w-T_\infty}, \phi(\eta) = \tfrac{C-C_\infty}{C_w-C_\infty} \end{aligned} \tag{6}$$

The resulting system of nonlinear ODEs and the suitable boundary conditions are :

$$((1-n) + nWef^{''})f^{'''} + ff^{''} - (f^{'})^2 + Me^{(-S\eta)} + \cos(\alpha)Gr_T\theta + \cos(\alpha)Gr_C\phi = 0 \tag{7}$$

$$\begin{aligned} &[1 + N_r(1 + (\theta_w - 1)\theta)^3]\theta^{''} + 3N_r(\theta_w - 1)(1 + (\theta_w - 1)\theta)^2(\theta^{'})^2 \\ &\qquad + Pr[N_b\theta^{'}\phi^{'} + N_t(\theta^{'})^2 + f\theta^{'} + Q\theta + Du\phi^{''}] = 0 \end{aligned} \tag{8}$$

$$\phi^{''} + S_c f\phi^{'} - S_c k_1 N_b(1 + \delta\theta)^m e^{(-\frac{E_a}{1+\delta\theta})}\phi = 0 \tag{9}$$

$$\begin{aligned} &f^{'}(\eta) = 1; f(\eta) = 0; \theta^{'}(\eta) = -Bi(1 - \theta(\eta)); \phi(\eta) = 1; \quad at \quad \eta = 0 \\ &f^{'}(\eta) = 0; \theta(\eta) = 0; \phi(\eta) = 0; \quad as \quad \eta \to \infty \end{aligned} \tag{10}$$

Here, we have defined the dimensionless parameter in the equations 7 - 10 as; N_r represent the thermal radiation parameter, We is the Weissenberg number, N_t stands for the Thermophoresis parameter, N_b is the Brownian motion parameter, E_a is the activation energy, Du is the duffour efffect, δ represent the heat basis constant, Gr_T is the local temperature Grashof number, Gr_C is the local mass Grashof number, Bi is the Biot number. These parameters are given as follows :
$N_r = \frac{16\sigma^* T_\infty^3}{3\kappa^*\kappa}$, $Gr_T = \frac{g\beta_T x(T_w - T_\infty)}{U^2}$, $Gr_C = \frac{g\beta_T x(C_w - C_\infty)}{U^2}$, $\delta = \frac{(T_w - T_\infty)}{T_\infty}$
$E_a = \frac{E_1}{\kappa T_\infty}$, $Du = \frac{D_m \kappa_T (C_w - C_\infty)}{\nu_f C_s C_p (T_w - T_\infty)}$, $k_1 = \frac{\kappa}{a}$, $\tau = \frac{(\rho c_p)_p}{(\rho c_p)_f}$
$N_t = \frac{\tau D_T (T_w - T_\infty)}{T_\infty \nu_f}$, $N_b = \frac{\tau D_B (C_w - C_\infty)}{\nu_f}$, $We = \sqrt{\frac{2a^3x^2}{\nu_f}}\Gamma$
At the Riga plate surface, the vital characteristics of the nanofluid are the skin friction coefficient(C_f), the Nusselt number (Nu_x) and the Sherwood number (Sh_x). In the current study, these boundary properties are defined locally as follows :

$$C_f = \frac{\tau_w}{\rho U_w^2}, \quad Nu_x = \frac{xq_w}{\kappa(T_w - T_\infty)}, \quad Sh_x = \frac{xq_m}{D_B} \tag{11}$$

Where

$$\begin{aligned} &\tau_w = \left[(1-n)\frac{\partial u}{\partial y} + \frac{n\Gamma}{\sqrt{2}}\left(\frac{\partial u}{\partial y}\right)^2\right]_{y=0}, \quad q_m = -D_B\left(\frac{\partial C}{\partial y}\right)_{y=0} \\ &\qquad q_w = -\left[\left(\frac{16\sigma^* T^3}{3\kappa^*} + \kappa\right)\frac{\partial T}{\partial y}\right]_{y=0} \end{aligned} \tag{12}$$

Applying the similarity transformation 6, we obtain the dimensionless forms of the skin friction coefficient, Nusselt number and Sherwood number as follows :

$$\begin{aligned} &C_f\sqrt{Re_x} = \frac{n}{2}We(f^{''}(0))^2 + (1-n)f^{''}(0), \qquad \frac{Sh_x}{\sqrt{Re_x}} = -\phi(0) \\ &\qquad \frac{Nu_x}{\sqrt{Re_x}} = -(1 + N_r\theta_w^3)\theta^{'}(0) \end{aligned} \tag{13}$$

Where, Re_x is the local Reynold number defined as $Re_x = \frac{ax^2}{\nu_f}$

3. Numerical Solution Technique

The method of overlapping grid spectral quasilinearization has been employed here. Overlapping grid SQLM is an iterative solution method that involves the idea of breaking the solution domain into multi - domain of overlapping grids, quasilinearization [6], spectral collocation and Langrange interpolation with Gauss - Lobatto grid points [31].
The semi - infinite domain for the current problem is defined in terms of a truncated interval of integration $I = [0, \eta_\infty]$, which is then splitted into q - overlapping sub - domains defined as :

$$I_l = [\eta_0^l, \eta_{N_\eta}^l], \quad l = 1, 2, 3, \ldots, q$$

Discretization of the subinterval, I_l into $N_\eta + 1$ collocation points takes place with the domain having a constant length, given by :

$$L = \frac{\eta_\infty}{q + (1-q)\frac{(1-\cos\left(\frac{\pi}{N_\eta}\right))}{2}} \tag{14}$$

The end point which signifies the total length of the domain is obtained with the aid of the Gauss - Lobatto collocation points $z_i = \cos\left(\frac{\pi i}{N_\eta}\right), \quad i = 0, 1, 2, 3, \ldots, N_\eta$ as :

$$\eta_\infty = \frac{L}{2}\left(1 - \cos\left(\frac{\pi}{N_\eta}\right)\right)(1-q) + qL$$

For precision, we have used $\eta_\infty = 10$ in the current study.
The system of non - linear ODE 7 - 9 are linearized using the quasilinearization method as in regular SQLM, with the variable coefficients given as follows :

$$a_{0,r} = \frac{\partial F}{\partial f_r'''} = (1-n) + nWef_r'', \quad a_{1,r} = \frac{\partial F}{\partial f_r''} = nWef_r''' + f_r, \quad a_{2,r} = \frac{\partial F}{\partial f_r'} = -2f_r'$$

$$a_{3,r} = \frac{\partial F}{\partial f_r} = f_r'', \quad a_{4,r} = \frac{\partial F}{\partial \theta_r} = \cos(\alpha)Gr_T, \quad a_{5,r} = \frac{\partial F}{\partial \phi_r} = \cos(\alpha)Gr_C$$

$$b_{0,r} = \frac{\partial T}{\partial \theta_r''} = 1 + N_r(1+(\theta_w-1)\theta_r)^3, \quad b_{1,r} = \frac{\partial T}{\partial \theta_r'} = 6N_r(\theta_w-1)(1+(\theta_w-1)\theta_r)^2\theta_r' + Pr(N_b\phi_r' + 2N_t\theta_r' + f_r)$$

$$b_{2,r} = \frac{\partial T}{\partial \theta_r} = 3N_r(\theta_w-1)(1+(\theta_w-1)\theta_r)^2\theta'' + 6N_r(\theta_w-1)^2(1+(\theta_w-1)\theta_r)\theta_r'^2 + PrQ, \quad b_{3,r} = \frac{\partial T}{\partial f_r} = Pr\theta_r'$$

$$b_{4,r} = \frac{\partial T}{\partial \phi_r''} = PrDu, \quad b_{5,r} = \frac{\partial T}{\partial \phi_r'} = PrN_b\theta_r'$$

$$c_{0,r} = \frac{\partial H}{\partial \phi_r''} = 1, \quad c_{1,r} = \frac{\partial H}{\partial \phi_r'} = Scf_r, \quad c_{2,r} = \frac{\partial H}{\partial \phi_r} = -Sck_1N_b(1+\delta\theta_r)^m e^{-\left(\frac{E_a}{1+\delta\theta_r}\right)}, \quad c_{3,r} = \frac{\partial H}{\partial f_r} = Sc\phi_r'$$

$$c_{4,r} = \frac{\partial H}{\partial \theta_r} = -Sck_1N_b(1+\delta\theta_r)^{m-2}(m(1+\delta\theta_r) + E_a)e^{-\left(\frac{E_a}{1+\delta\theta_r}\right)}$$

We consider the transformation of each interval $I_l = [\eta_0^l, \eta_{N_\eta}^l$ into $z \in [-1, 1]$ by the use of the linear transformation $\eta_i^l = \frac{L}{2}(z_i + 1)$, $z_i = \cos\left(\frac{\pi i}{N_\eta}\right)$. Applying the spectral collocation using the differential matrix D on the interval $[-1, 1]$, we obtain the derivatives of the unknown functions in a system of equation given as :

$$\left.\begin{aligned} A_{11}f_{r+1} + A_{12}\theta_{r+1} + A_{13}\phi_{r+1} = R_f^l \\ A_{21}f_{r+1} + A_{22}\theta_{r+1} + A_{23}\phi_{r+1} = R_\theta^l \\ A_{31}f_{r+1} + A_{32}\theta_{r+1} + A_{33}\phi_{r+1} = R_\phi^l \end{aligned}\right\} \tag{15}$$

Where each matrix $A_{\varrho,\varsigma}$ $(\varrho = 1, 2, 3; \varsigma = 1, 2, 3)$ is of the order $(N+1) \times (N+1)$ and the vectors R_f^l, R_θ^l and R_ϕ^l are each of the order $(N+1) \times 1$ [19].

We obtain a less dense matrix system after imposing the boundary conditions and this is given as :

$$\left[\begin{array}{cccc|cccc|cccc}
D^{(q)}_{0'0} & D^{(q)}_{0,1} & \dots & D^{(q)}_{0,N_\eta} & 0 & 0 & \dots & 0 & 0 & 0 & \dots & 0\\
 & A_{11} & & & & A_{12} & & & & A_{13} & & \\
D^{l}_{N_\eta-1,0} & D^{l}_{N_\eta-1,1} & \dots & D^{l}_{N_\eta-1,N_\eta} & 0 & 0 & \dots & 0 & 0 & 0 & \dots & 0\\
0 & 0 & \dots & 1 & 0 & 0 & \dots & 0 & 0 & 0 & \dots & 0\\ \hline
0 & 0 & \dots & 0 & 1 & 0 & \dots & 0 & 0 & 0 & \dots & 0\\
 & A_{21} & & & & A_{22} & & & & A_{23} & & \\
0 & 0 & \dots & 0 & D^{l}_{N_\eta,0} & D^{l}_{N_\eta,1} & \dots & D^{l}_{N_\eta,N_\eta}-Bi & 0 & 0 & \dots & 0\\ \hline
0 & 0 & \dots & 0 & 0 & 0 & \dots & 0 & 1 & 0 & \dots & 0\\
 & A_{31} & & & & A_{32} & & & & A_{33} & & \\
0 & 0 & \dots & 0 & 0 & 0 & \dots & 0 & 0 & 0 & \dots & 1
\end{array}\right]
\left[\begin{array}{c}
f^{q}_{(0,r+1)}\\ \vdots \\ f^{1}_{(N_\eta,r+1)}\\ f^{1}_{(N_\eta+1,r+1)}\\ \hline
\theta^{q}_{(0,r+1)}\\ \vdots \\ \theta^{1}_{(N_\eta+1,r+1)}\\ \hline
\phi^{q}_{(0,r+1)}\\ \vdots \\ \phi^{1}_{(N_\eta+1,r+1)}
\end{array}\right]$$

$$=\left[\begin{array}{c}
0\\ \vdots \\ 1\\ S\\ \hline 0\\ \vdots \\ 1\\ \hline 0\\ \vdots \\ 1
\end{array}\right]$$

With the following suitable initial guesses, the system is solved :

$$f_0(\eta) = 1 - e^{-\eta}, \qquad \theta_0(\eta) = \left(\frac{Bi}{1+Bi}\right) e^{-\eta} \qquad \phi_0(\eta) = e^{-\eta} \tag{16}$$

4. Results and discussion

With the aid of MATLAB, we have obtained the numerical solution of the system of ODE using the overlapping grids spectral quasilinearization method and considered the graphs of the velocity, temperature and mass flux profiles with respect to the pertinent dominating parameters. For the validation of solutions, we have compared our results for $-\theta(\eta)$ to the results for $-\theta(\eta)$ presented by researchers [5, 12, 27, 3] in the past, for varying values of the Prandtl number, Pr, as shown in Table 1. The high degree of consensus in the numerical values of $-\theta(0)$ seen in Table 1 greatly substantiate the numerical results of this study.

Table 1: Comparison of numerical results for $-\theta'(0)$ of the current study with the results of Hassanien et al [12], Salleh and Nazar [27], Fadilah et al [3] and Asogwa et al. [5].$N_r = 0$,$N_b = 0$, $N_t = 0$, $Q = 0$, $Du = 0$, $\theta_w = 1$, $\alpha = 90^o$

Pr	Hassanien et al.[12]	Salleh and Nazar [27]	Fadilah et al. [3]	Asogwa et al. [5]	Current Study
0.72	0.46325	0.46317	0.4632	0.46321	0.463192
1.0	0.58198	0.58198	0.582	0.58198	0.582010
3.0	1.16525	1.16522	1.1652	1.16522	1.165242
7.0		1.89548	1.8954	1.89548	1.895400
10.0	2.30801	2.30821	2.3081	2.30820	2.308001

The essence of Table 2, Table 3 and Table 4 is to reveal the behaviour of the boundary layer characteristics of the fluid, namely ; the skin friction coefficient, Nusselt number and Sherwood number for varying values of determining parameters.

It can be seen from Table 2 that the skin friction coefficient drops for improving positive values of the modified magnetic parameter, M,power law exponent, n, the Weissenberg number, We, local temperature Grashof number, Gr_T and local mass Grashof number, Gr_C. This trend describes a decrease in the Riga surface drag on the fluid. In Table 3, elevated values of the thermal radiation number,N_r, temperature ratio parameter, θ_w, Prandtl number, Pr, and Biot number, Bi, are accompanied by corresponding increases in the value of the local Nusselt number, which indicate increases in the heat transfer rate at the Riga plate surface. On the other hand, steady declines in the heat transfer rate at the Riga plate surface are observed for increasing values of the thermophoresis parameter, N_t, Brownian motion parameter, N_b, Weissenberg number, We, heat generation parameter, Q,

Duffour effect, Du and the power law exponent, n.
Table 4 shows the values of the local Sherwood number being enhanced at the Riga plate surface for increasing values of the Schimdt number, Sc, thermal exponent term, m, heat basis constant, δ, and the chemical reaction constant, k_1, which demonstrates high mass transfer at the boundary. In contrast, the mass transfer at the boundary decreases for improving values of Weissenberg number, We, power law exponent, n and activation energy term, E_a.
In the physical interpretation of the model, the temperature Grashof number is the dimensionless thermal bouyancy parameter that that represents the ratio of buoyancy forces to viscous forces. As the Gr_T number increases, the buoyancy forces, which arise from the density difference between the hot fluid and the surrounding fluid, become more dominant. These buoyancy forces act to counteract the viscous forces that resist fluid motion, leading to an increase in the velocity distribution, this is as seen in Figure 2.

Table 2: Variation of $-C_{f_x}\sqrt{Re_x}$ for different values of N, M, We,Gr_T and Gr_C. $\alpha = 45^o$ $N_r = 0.2$,$N_b = 0.4$, $N_t = 0.5$, $Q = 0.2$, $Du = 0.3$, $\theta_w = 0.5$,$E_a = 0.2$, $k_1 = 0.1$, $Bi = 0.2$

M	n	We	Gr_T	Gr_C	$-C_{f_x}\sqrt{Re_x}$
0	0.2	0.5	0.5	0.5	0.615347
0.5					0.417272
1.0					0.219826
0.1	0				0.677217
	0.1				0.628140
	0.2				0.575819
	0.3				0.519280
	0.4				0.456806
	0.2	0			0.588958
		0.5			0.575819
		1.0			0.561927
		0.5			0.575819
			1.0		0.528054
			2.0		0.441365
			3.0		0.362610
			4.0		0.289340
			0.5	0.5	0.575819
				1.0	0.420289
				2.0	0.130772

Figure 3 shows that elevated values of the local mass Grashof number brings about increments in the velocity field in the momentum boundary layer as a result of the reduction in the Riga plate surface drag which implies less opposition to the fluid flow over the plate surface due to the combined effects of enhanced buoyancy forces, and reduced viscosity due to Dufour effect.
Figure 4 displays steady declines in the velocity profile with improving values of S owing to the increase in viscosity of the fluid in connection to the width of the permanent magnets and electrodes that makes up the Riga plate.
Figure 5 presents the influence of the power law exponent, n, on the velocity of the fluid in the momentum boundary layer. The power-law exponent (n) in the power-law model represents the non-Newtonian behavior of the nanofluid. As n increases, the nanofluid exhibits stronger shear-thinning behavior, meaning that its viscosity decreases with increasing shear rate. This reduced viscosity at higher shear rates leads to a decrease in the overall velocity distribution.
Figure 6 depicts the characteristics of the velocity field with respect to the Weissenberg number variation. Weissenberg number describes the comparison of the elastic and viscous forces of the fluid which in turns results in decrease in the fluid flow velocity.
Figure 7 displays the effect of thermal radiation parameter, N_r. It can be seen clearly that increasing values of N_r enhances the thermal boundary layers and hence strengths heat transfer between the plate and the ambient fluids. It is worth noting that for effective cooling process, the thermal radiation must be maintained at the barest minimum.
Figure 8 exhibits the characteristics of the temperature boundary layers with varying values of the temperature ratio parameter, θ_w. Increasing values of θ_w implies increase in the plate surface temperature in relation to the ambient temperature. Enhancement in the plate surface temperature increases the temperature of the fluid and spikes the temperature distribution.
Figure 9 depicts the behaviour of the temperature distribution as the temperature Grashof number, Gr_T,

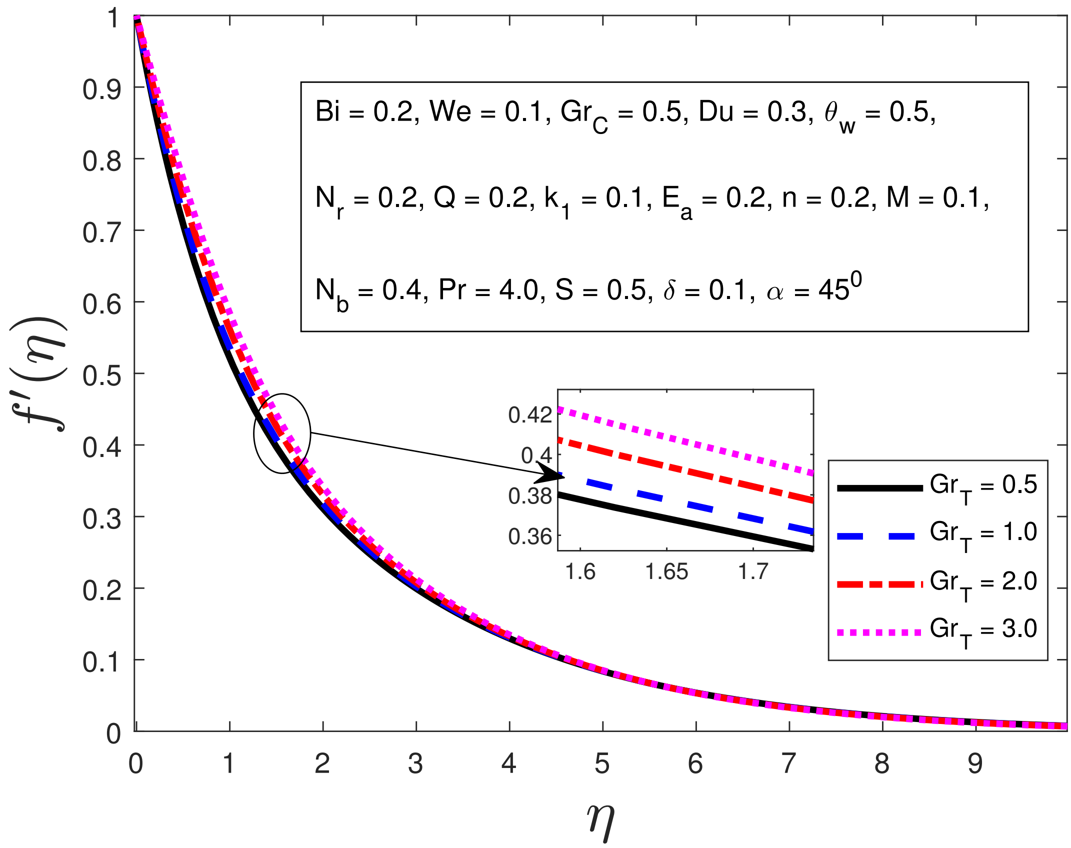

Figure 2: Consequence of Gr_T on the velocity field

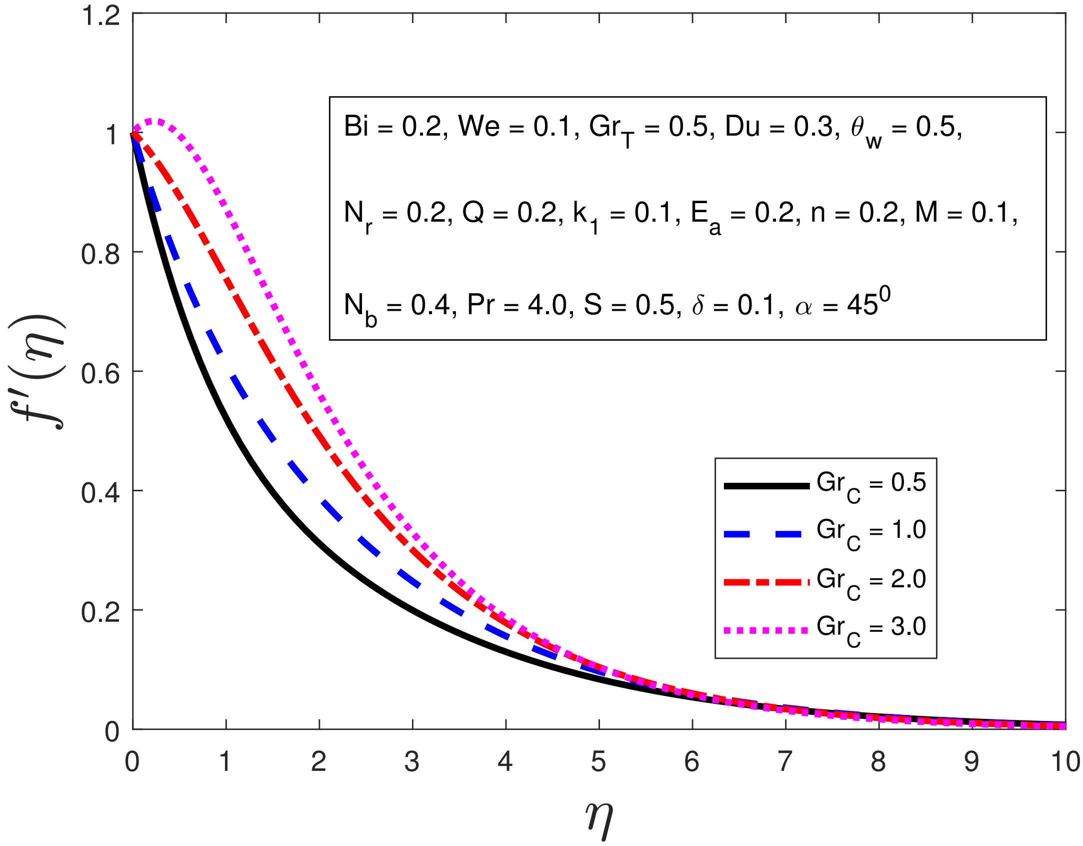

Figure 3: Consequence of Gr_C on the velocity field

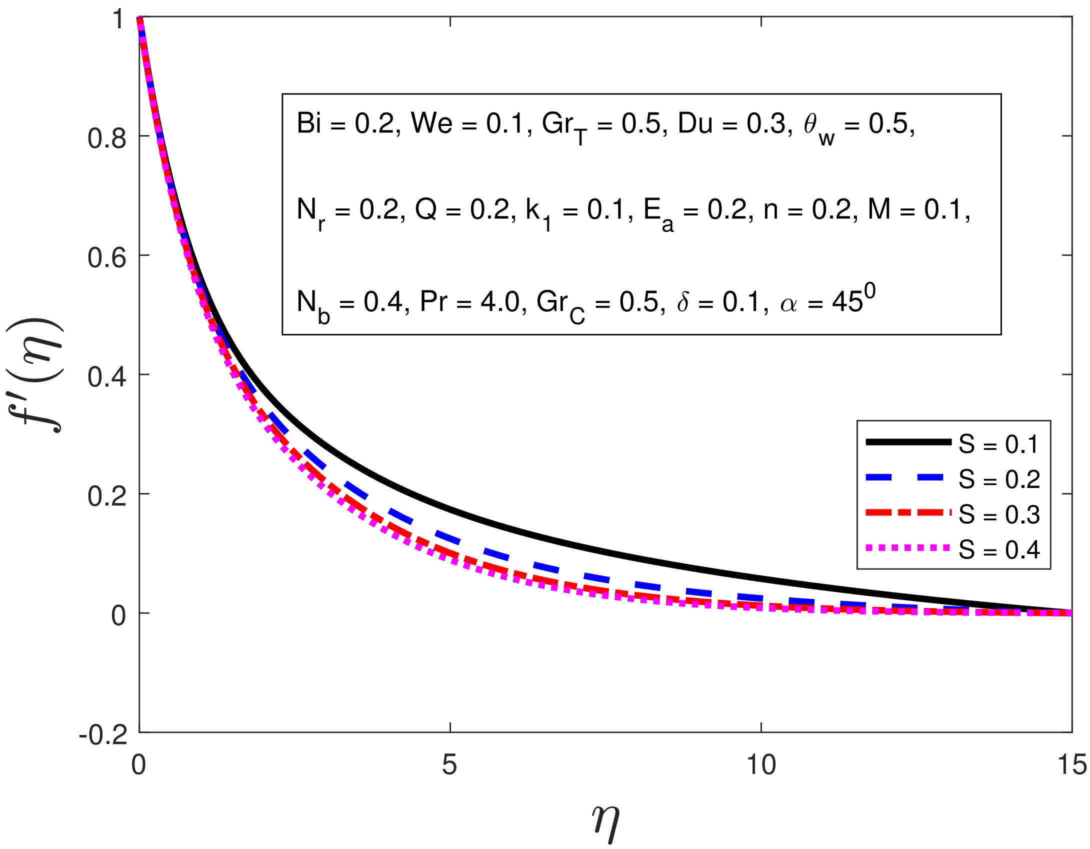

Figure 4: Consequence of S on the velocity field

Table 3: Variation of $\frac{-Nu_x}{\sqrt{Re_x}}$ for different values of N_t, N_r, N_b, θ_w, Pr, Q, Du and Bi. $E_a = 0.2$, $k_1 = 0.1$, $M = 0.1$, $\alpha = 45^o$

N_t	N_r	N_b	θ_w	Pr	Q	Du	Bi	n	We	$\frac{-Nu_x}{\sqrt{Re_x}}$
0	0.2	0.4	0.5	6.8	0.2	0.3	0.2	0.2	0.5	0.141418
0.1										0.138703
0.3										0.131083
0.5	0									0.102696
	0.5									0.126464
	2.0									0.156619
	4.0									0.185876
	0.2	0.1								0.141559
		0.2								0.135369
		0.3								0.127248
		0.4	1.2							0.154732
			1.8							0.250638
			2.0							0.300712
			0.5	0.72						0.104082
				1.0						0.111578
				2.0						0.122504
				3.0						0.125437
				6.8	0					0.161816
					0.1					0.148713
					0.2					0.115475
						0.1				0.159159
						0.2				0.145932
						0.3				0.131593
							0.1			0.071055
							0.2			0.115475
							0.3			0.125029
							0.2	0		0.119159
								0.3		0.112757
								0.5		0.102334
								0.2	0	0.116193
									0.5	0.115475
									1.5	0.113719

increases. Enhancing the thermal buoyancy parameter cools the plate surface and hence visible declines are observed in the temperature profile.
Figure 10 shows the influence of the mass Grashof number, Gr_C, on the temperature profile. It can be seen that the temperature profile falls for improving values of Gr_C.

Biot number, Bi, in its physical interpretation describes how the thermal gradient applied at the surface of a body will make the internal temperature of the body to vary appreciably or not in space. In Figure 11, increasing values of Bi prompt corresponding increases in the temperature distribution. It is worth noting from the physical interpretation that larger values of Bi corresponds to greater convective heat at the plate surface which brings about rise in the temperature gradient and hence increasing the fluid temperature with lower thermal resistance. This conclusively improves the convective heat transfer.

Presented in Figure 12, is the impact of the thermophoresis parameter, N_t, on the temperature distribution. The driving force for thermodiffusion phenomenon is the temperature gradient which ensures continuous movements of molecules of the fluid within the hot and cold regions. This continuous motion brings warmer fluids to the plate surface and hence the temperature distribution enhances.
Consequence of varying values of the Brownian motion parameter, N_b, on the temperature distribution can be seen in Figure 13. Improving values of N_b instigates continuous fluctuations of the fluid molecules which results in enhancement of the fluid temperature and hence spike in the temperature distribution.
Figure 14 reveals the results of rising values of Duffour effect, Du, on the temperature field. A steady climb can be seen in the temperature field as the Duffour effect increases owing to mass transfer driven by temperature gradient.

Figure 15 and Figure 16 exhibit the effects of improving activation energy, E_a, on the temperature and mass

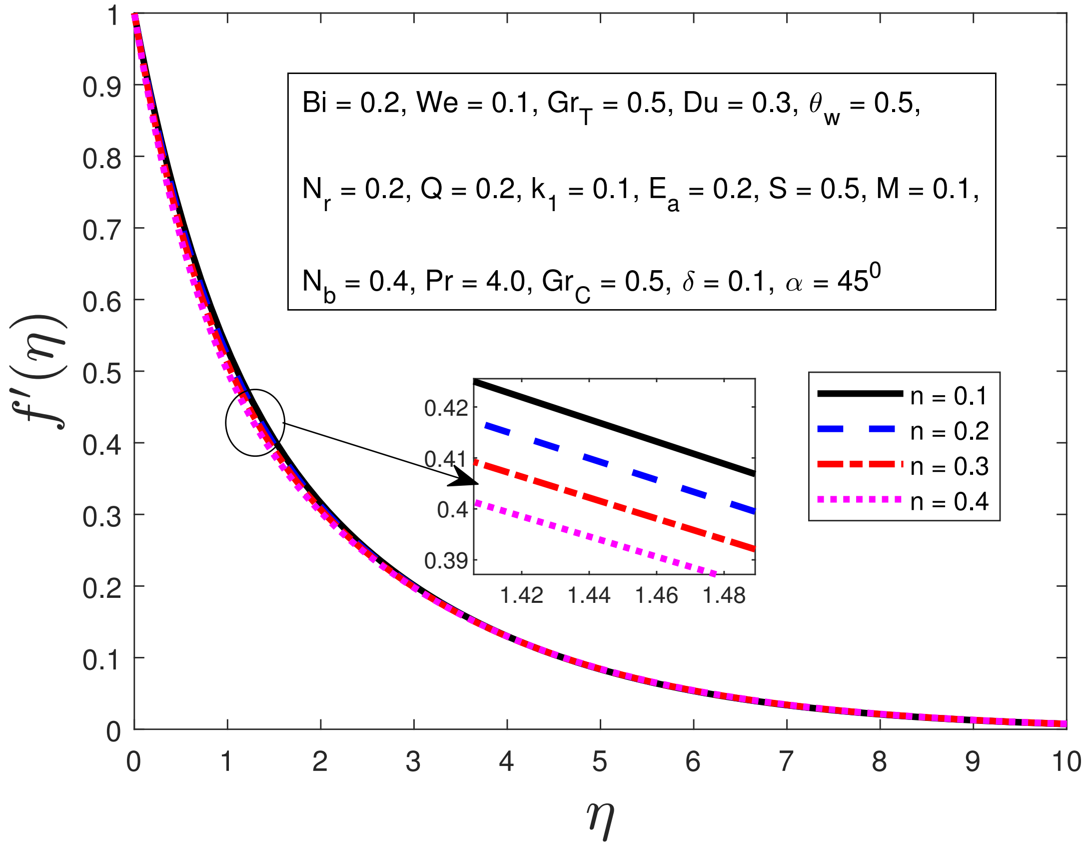

Figure 5: Consequence of n on the velocity field

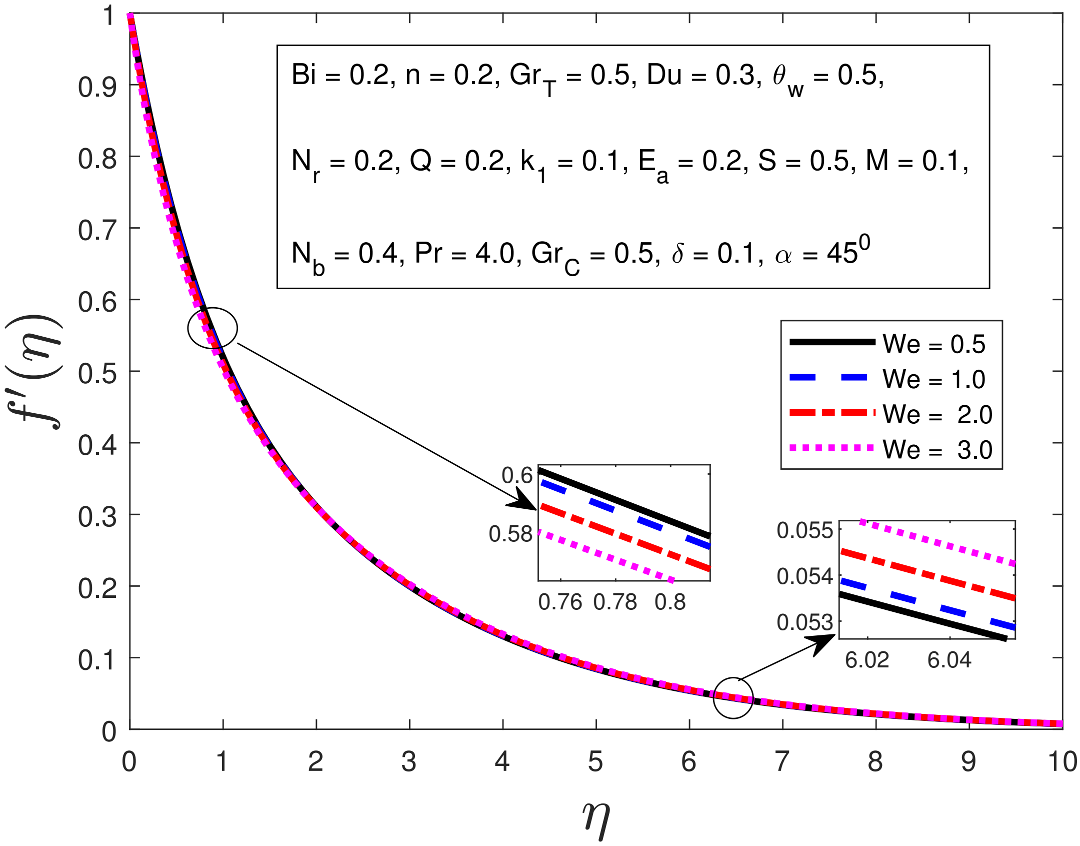

Figure 6: Consequence of We on the velocity field

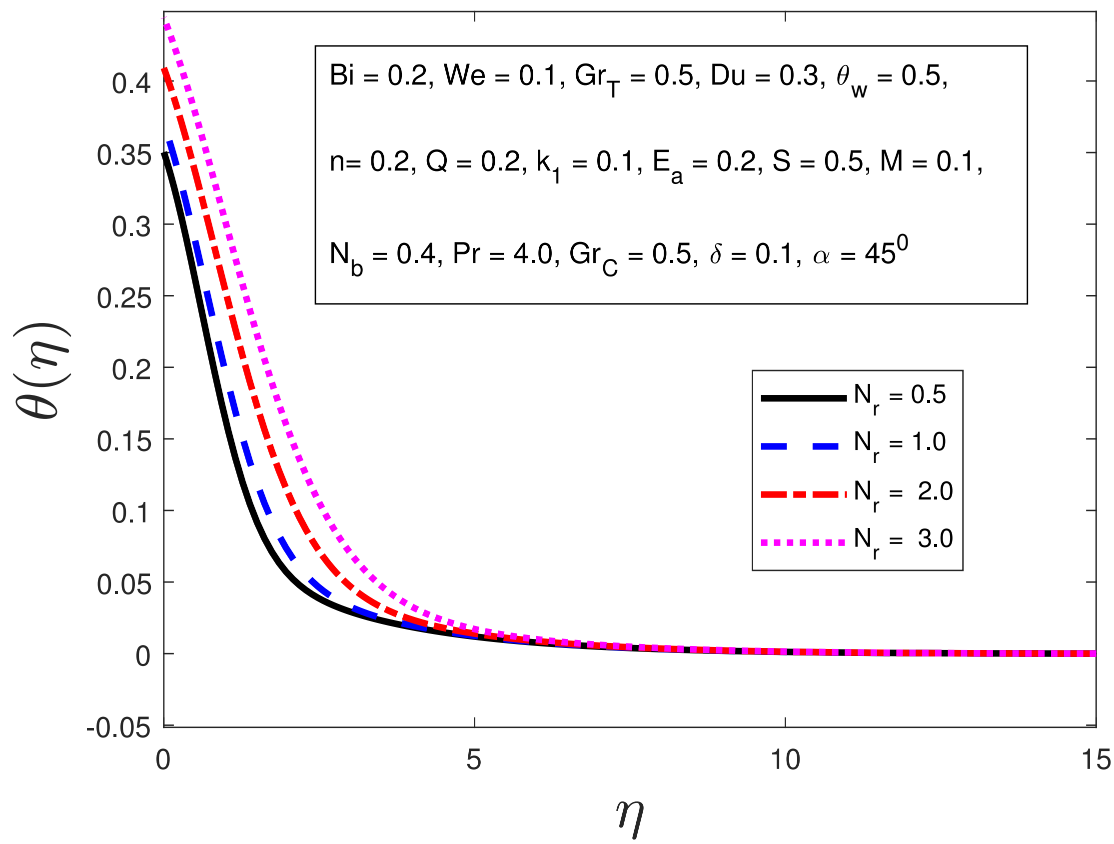

Figure 7: Consequence of N_r on the temperature distribution

Table 4: Variation of $\frac{Sh_x}{\sqrt{Re_x}}$ for different values of Sc,We,n,m, E_a,δ and k_1. $\theta_a = 0.5$, $N_r = 0.2$, $M = 0.1$, $\alpha = 45^o$, $Bi = 0.2$, $N_t = 0.5$, $Pr = 6.8$, $Q = 0.2$, $N_b = 0.4$, $S = 1.0$, $GrT = 0.5$, $GrC = 0.5$, $Du = 0.3$

Sc	We	n	m	E_a	δ	k_1	$\frac{Sh_x}{\sqrt{Re_x}}$
0.1	0.5	0.2	0.2	0.2	0.5	0.1	0.179146
0.22							0.264335
0.3							0.316166
0.22	0						0.264838
	0.5						0.264335
	1.5						0.263248
	0.5	0.1					0.268389
		0.3					0.262085
		0.5					0.256920
		0.2	0.2				0.264335
			0.3				0.264449
			0.4				0.264564
			0.2	0.1			0.265712
				0.3			0.263074
				0.4			0.261920
				0.2	0.1		0.264000
					0.2		0.264087
					0.3		0.264172
					0.5	0.2	0.278333
						0.3	0.291944
						0.4	0.305506

flux distributions respectively. Increasing values of E_a decreases the rate of chemical reaction within the fluid which in turns reduces the mass transfer and as such improves the mass flux distribution. Enhancing E_a shows reverse effect on the temperature field.
Figure 17 shows the influence of Schmidt number, Sc, on the mass flux distribution. Schmidt number describes the interaction between momentum and mass transfer. Physically, it connects the relative thickness of the momentum and concentration boundary layers. Enhanced Sc significantly reduces the mass flux distribution.
Figures 18 and 19 show dropping mass flux distribution in response to elevations in the magnitudes of the temperature Grashof and mass Grashof numbers which further elaborate the understanding reached from figures 9 and 10.
Figure 20 displays the effect of chemical reaction parameter, k_1, on the mass flux distribution. It can be seen that increasing k_1 enhances the mass transfer which brings about declines in the mass flux distribution.

5. Conclusion

The problem of two - dimensional EMHD tangent hyperbolic nanofluid flow over an inclined stretching Riga surface in the presence of Duffour effect, activation energy and heat generation was presented in this research work. Employing MATLAB program, we obtained numerical results through overlapping grids spectral quasilinearization method. The results were compared to available relating literatures for validation, from which the present results were found to be in complete consensus. From this current study the following overall deductions are reached :

1. The skin friction coefficient moves downwards for elevated values of M, n, We, Gr_T and Gr_C which demonstrate reduction in the Riga plate surface drag.
2. Improved values of the Nusselt number accompanies increasing values of N_r, θ_w, Pr and Bi. The trend is reversed for N_t, N_b, We, Q, Du and n.
3. Enhanced values of the Sherwood number which demonstrates high mass flux at the boundary occurs for increasing values of Sc, m , δ and k_1. Reverse is the case for improving values of We,n and E_a.
4. The fluid velocity grows for greater values of Gr_T and Gr_C and declines for growing values of S, n and We.
5. The temperature distributions go up for increasing values of N_r, θ_w, Bi, N_t and N_b. However it goes down for increasing values of Gr_T,Gr_C and E_a.
6. The mass flux distributions decline for higher values of Sc, k_1, N_t and N_b and appreciates for increasing values of E_a.

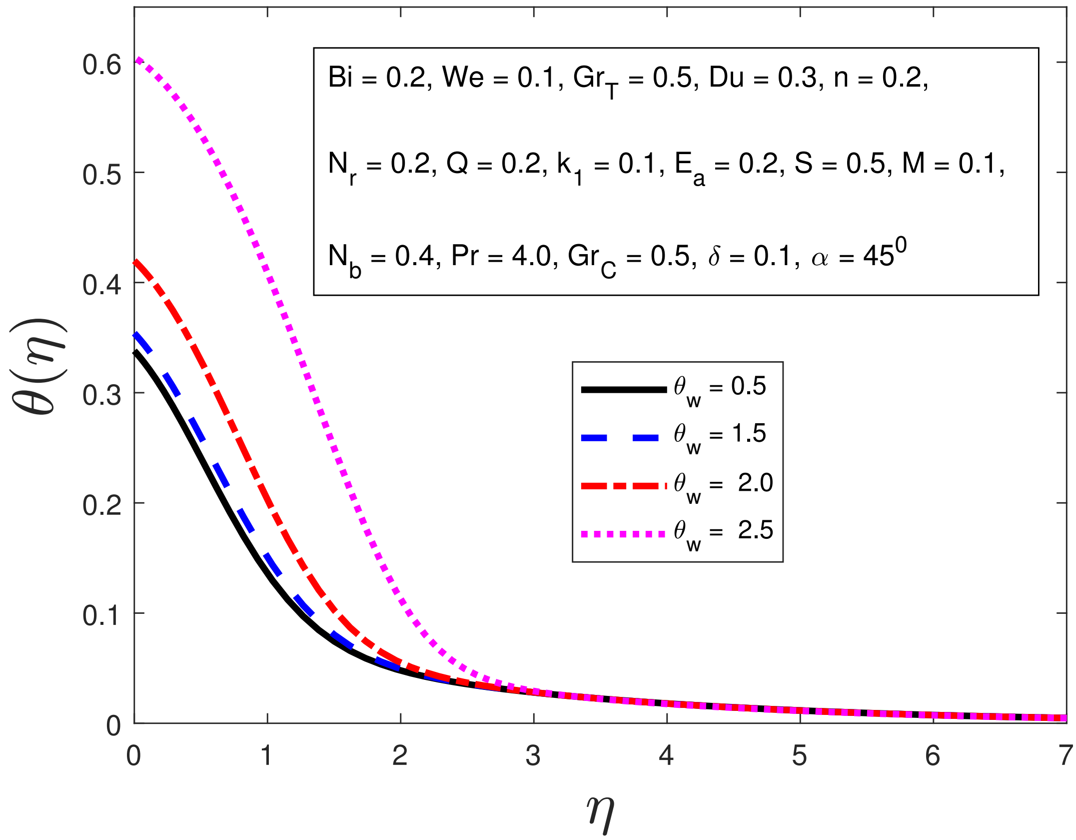

Figure 8: Consequence of θ_w on the temperature distribution

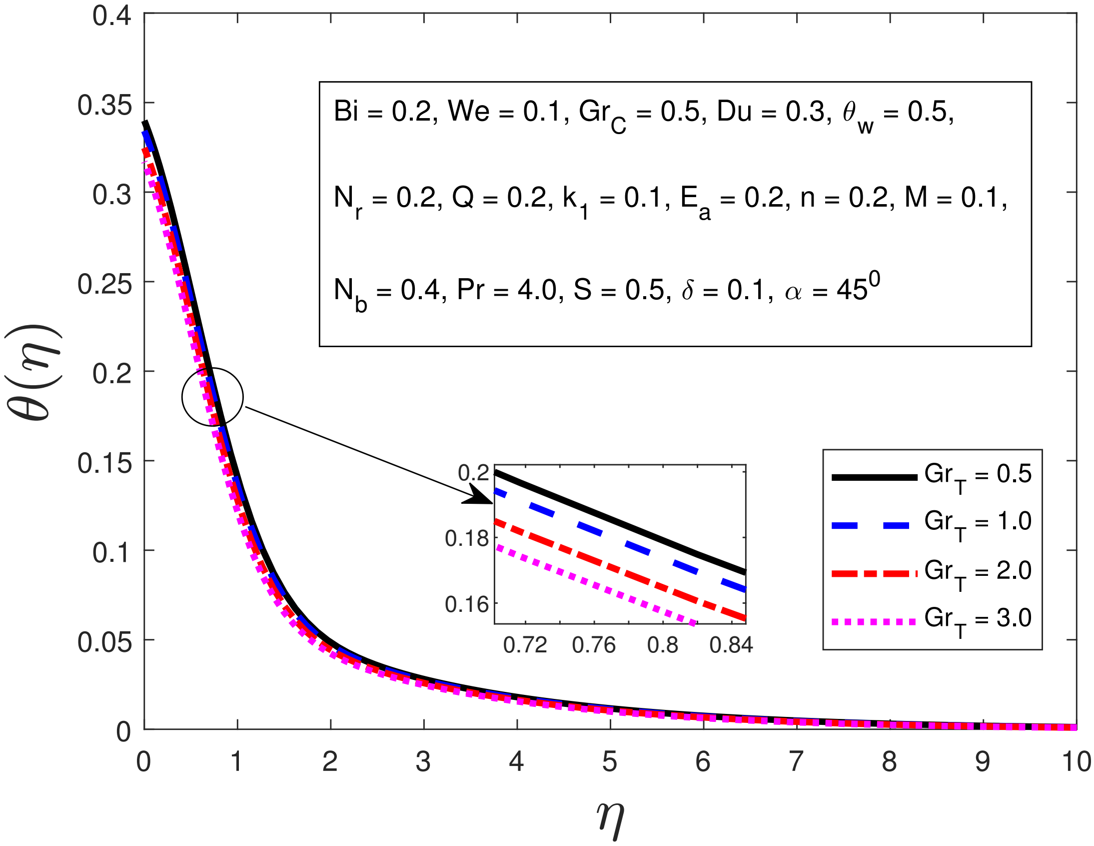

Figure 9: Consequence of Gr_T on the temperature distribution

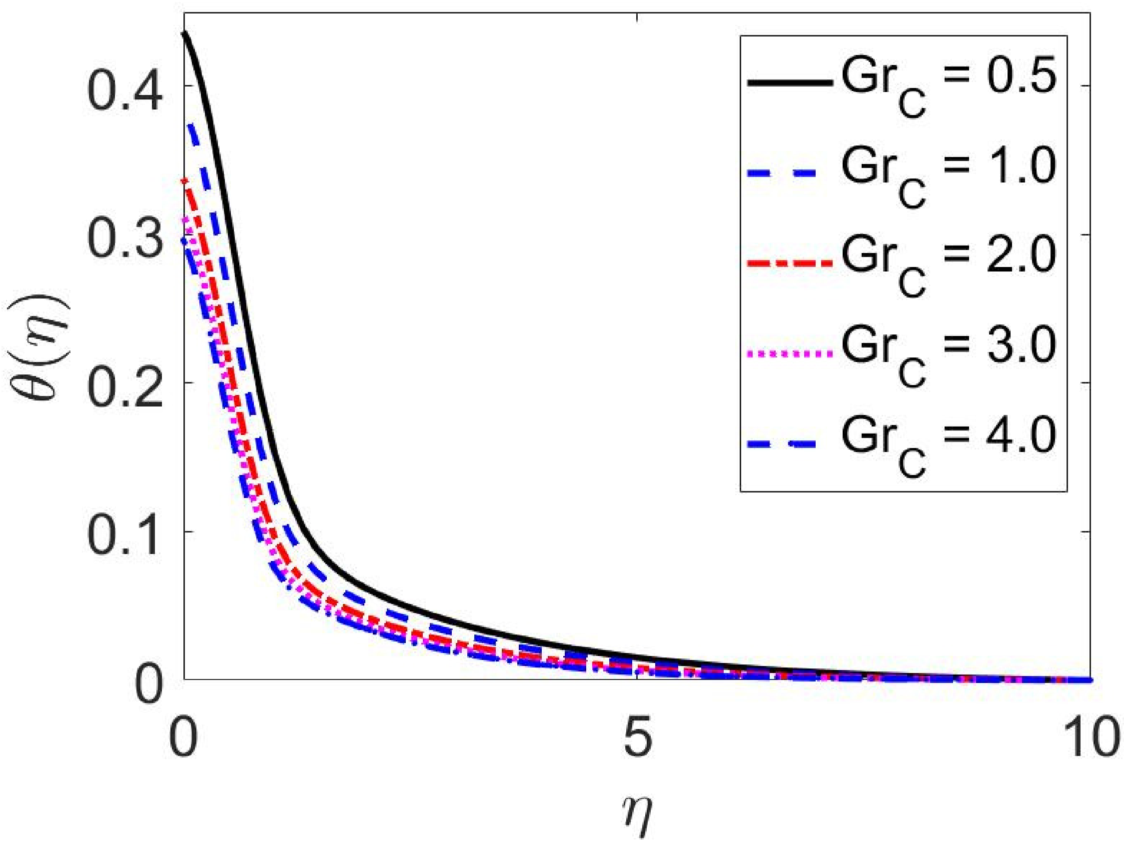

Figure 10: Consequence of Gr_C on the temperature distribution

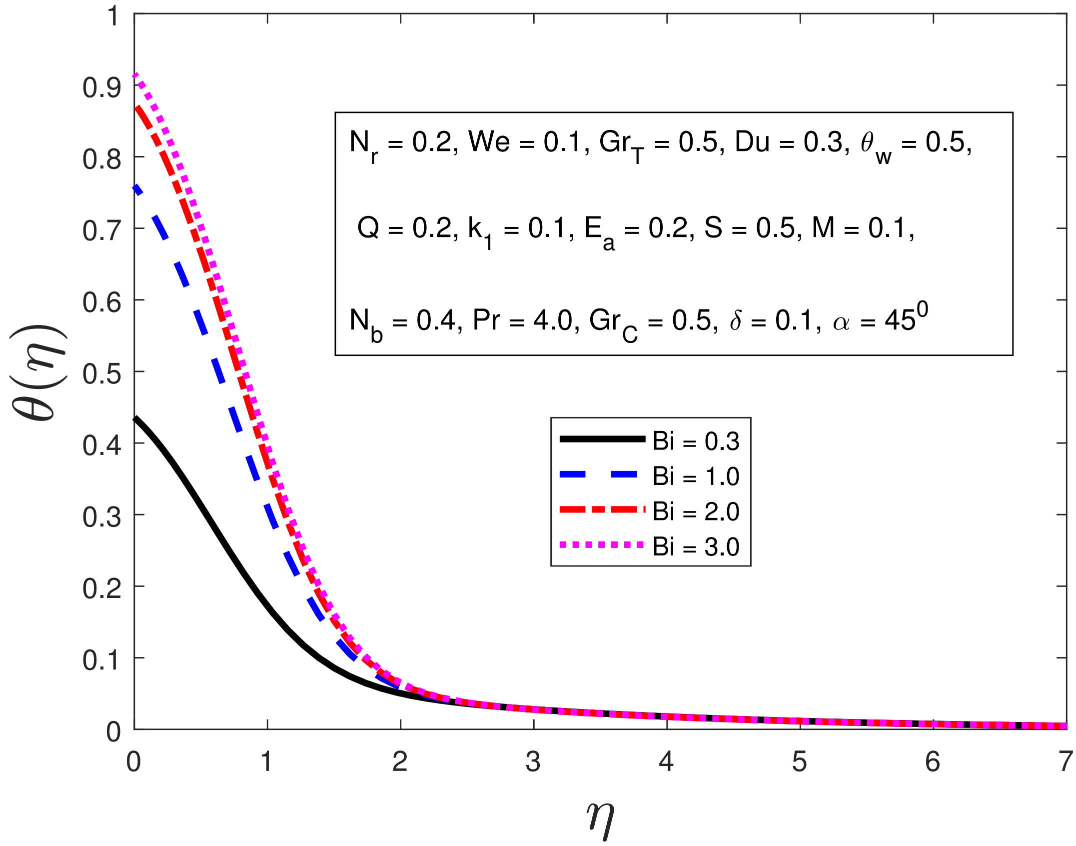

Figure 11: Consequence of Bi on the temperature distribution

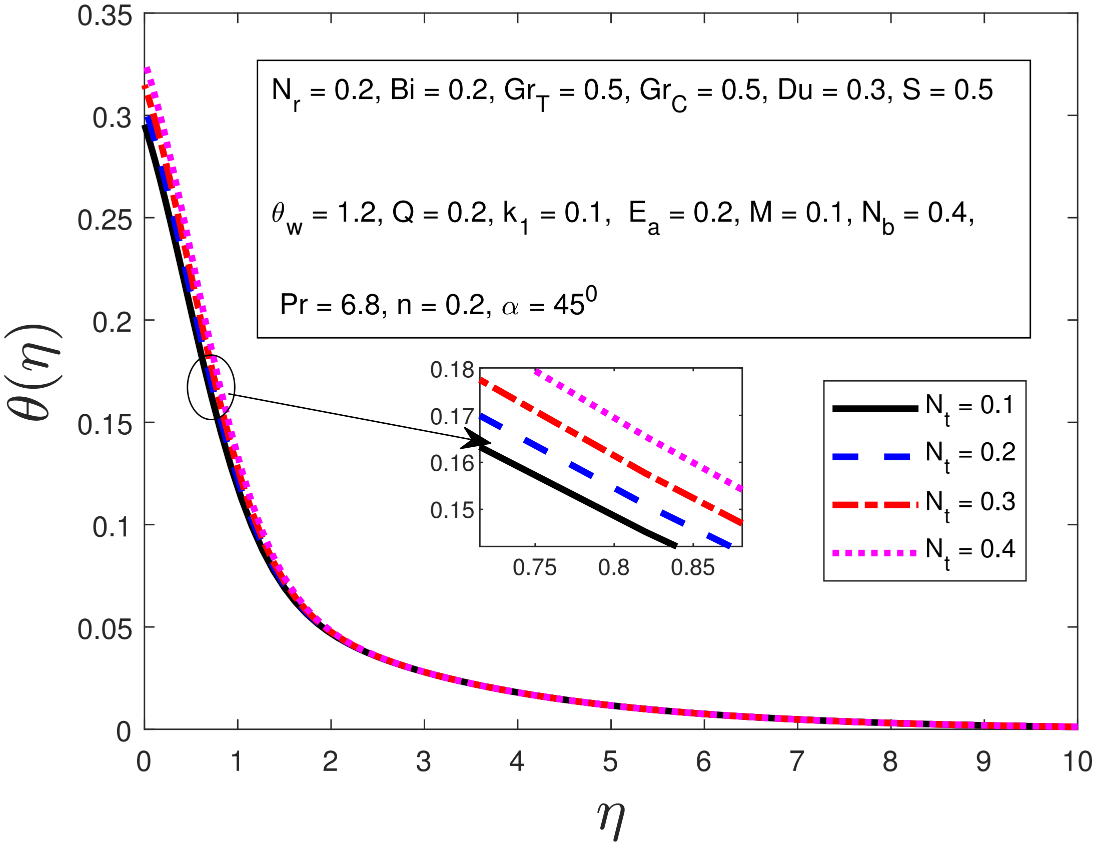

Figure 12: Consequence of N_t on the temperature distribution

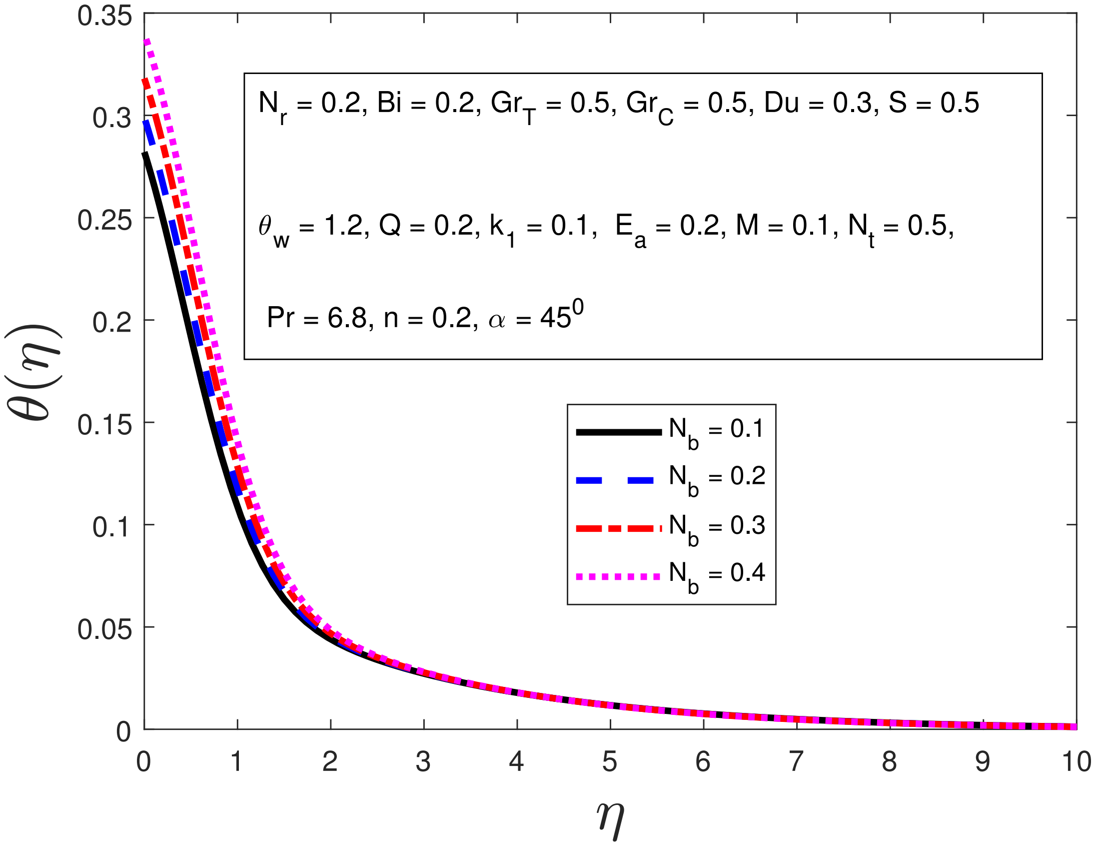

Figure 13: Consequence of N_b on the temperature distribution

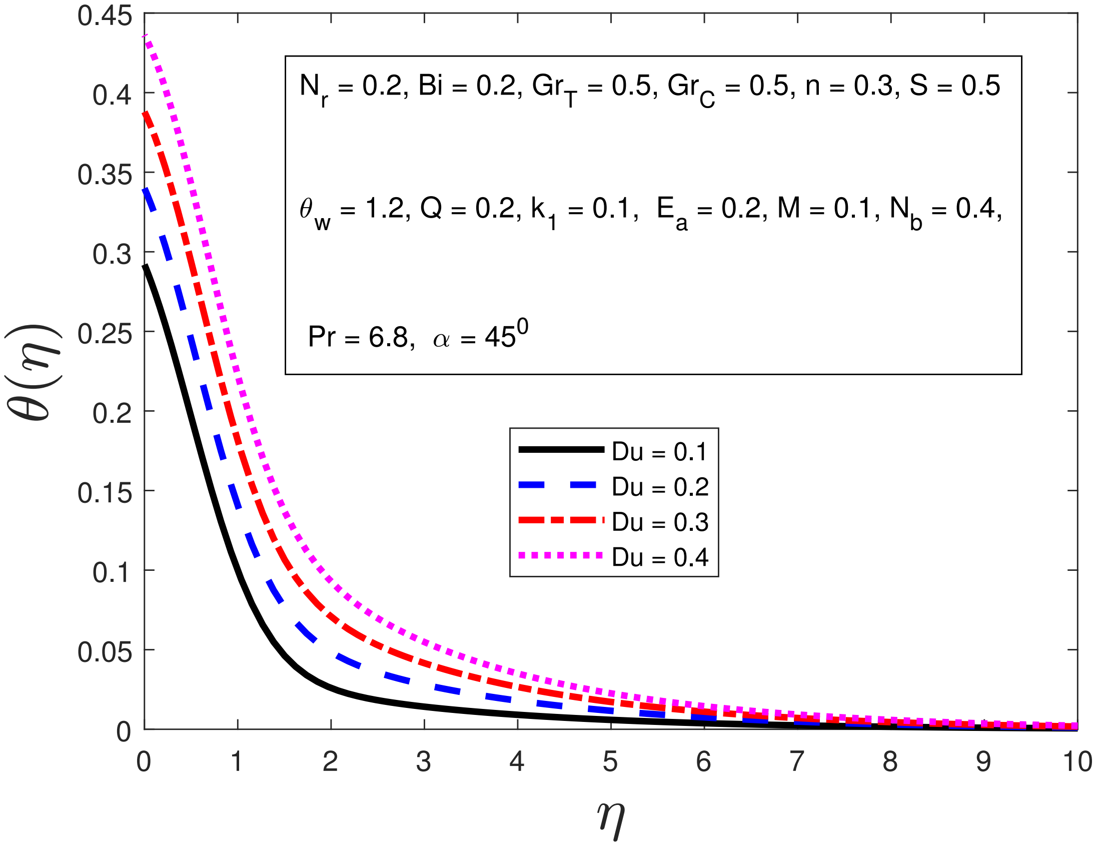

Figure 14: Consequence of Du on the temperature distribution

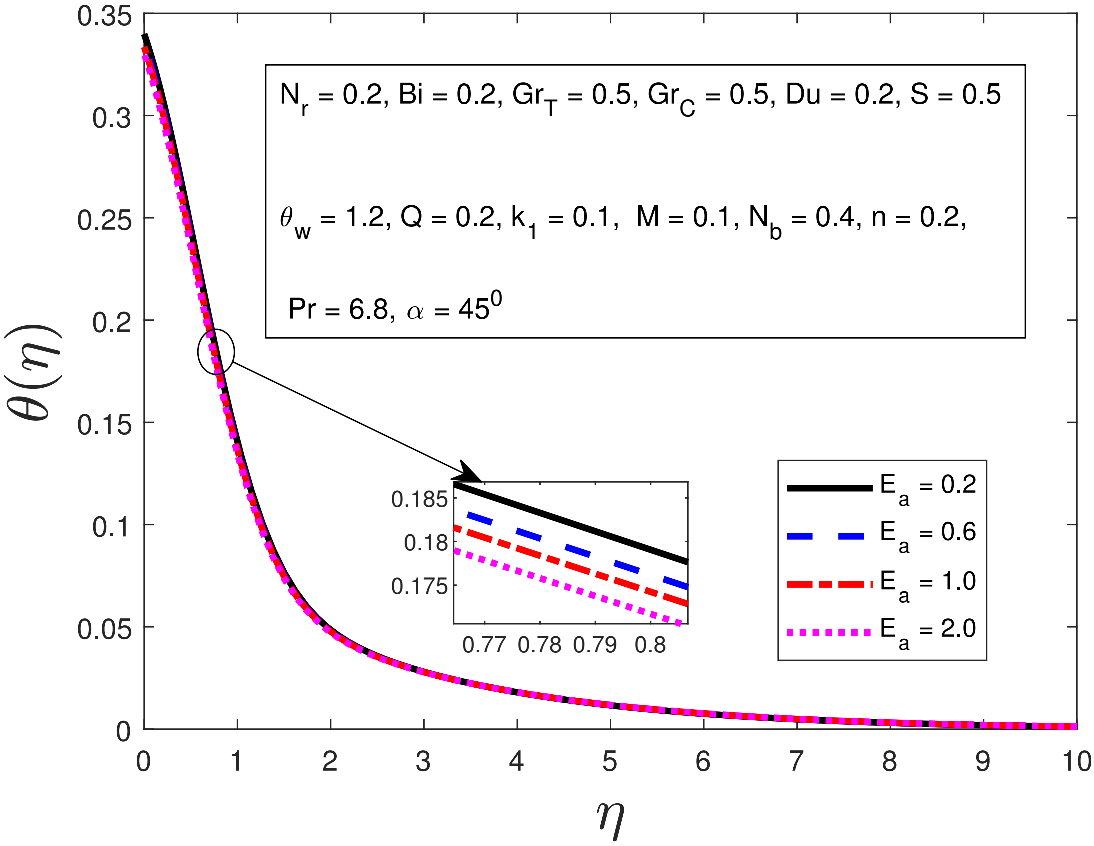

Figure 15: Consequence of E_a on the temperature distribution

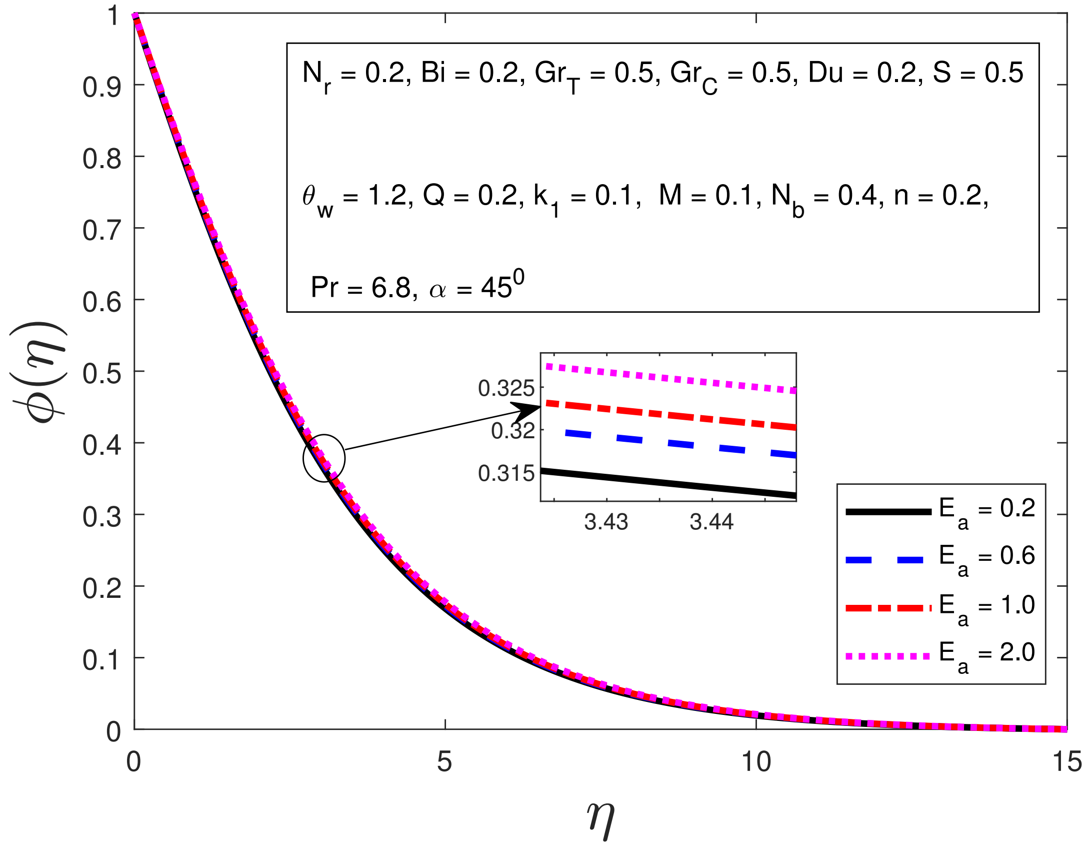

Figure 16: Consequence of E_a on the mass flux distribution

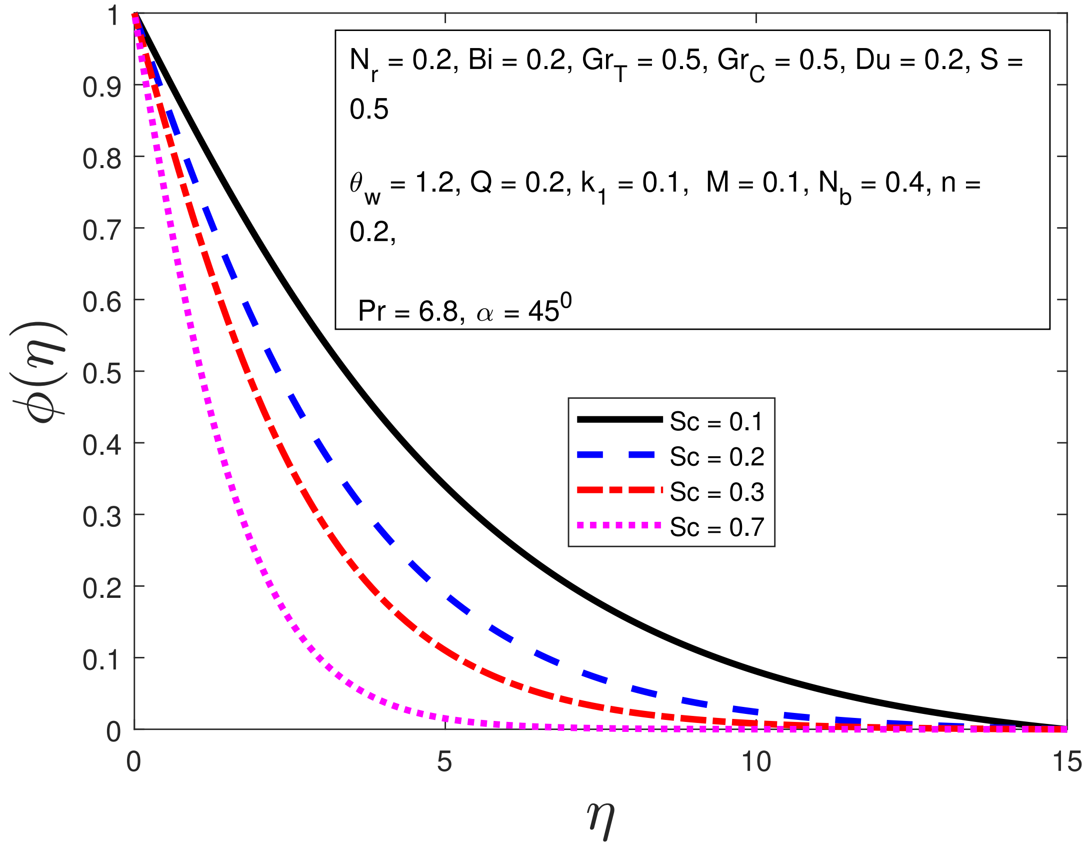

Figure 17: Consequence of Sc on the mass flux distribution

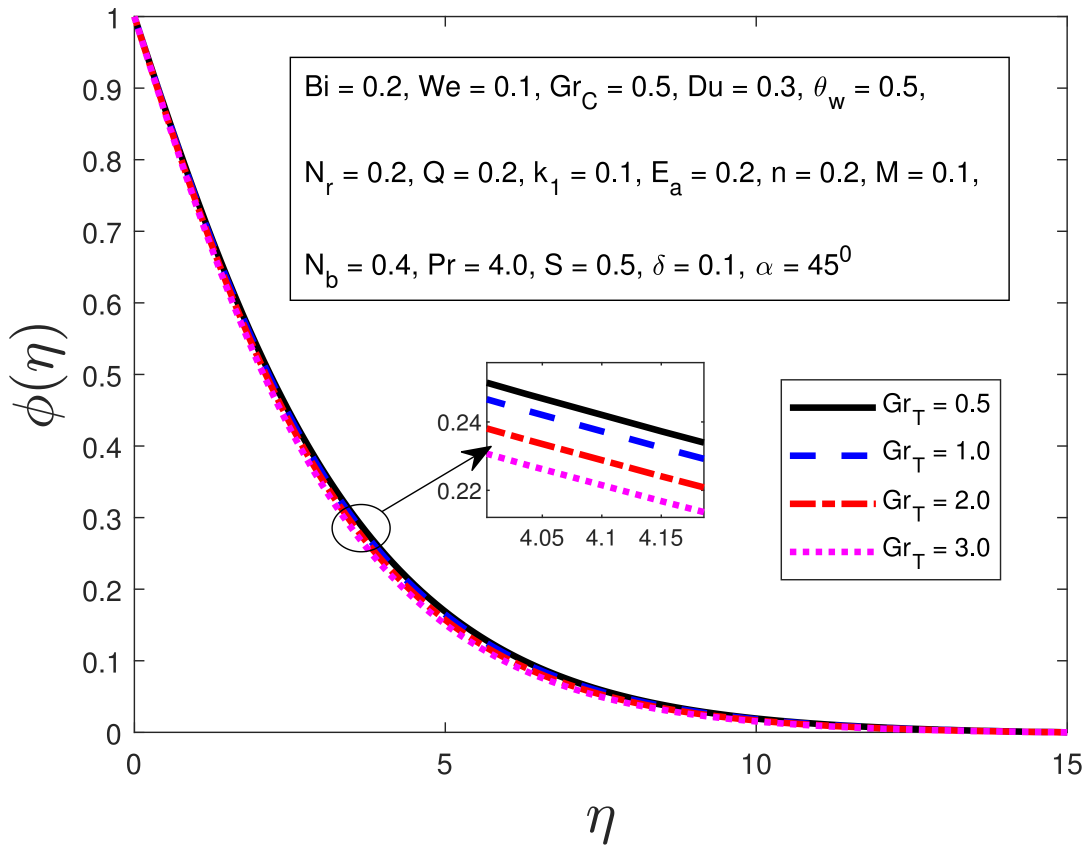

Figure 18: Consequence of Gr_T on the concentration profile

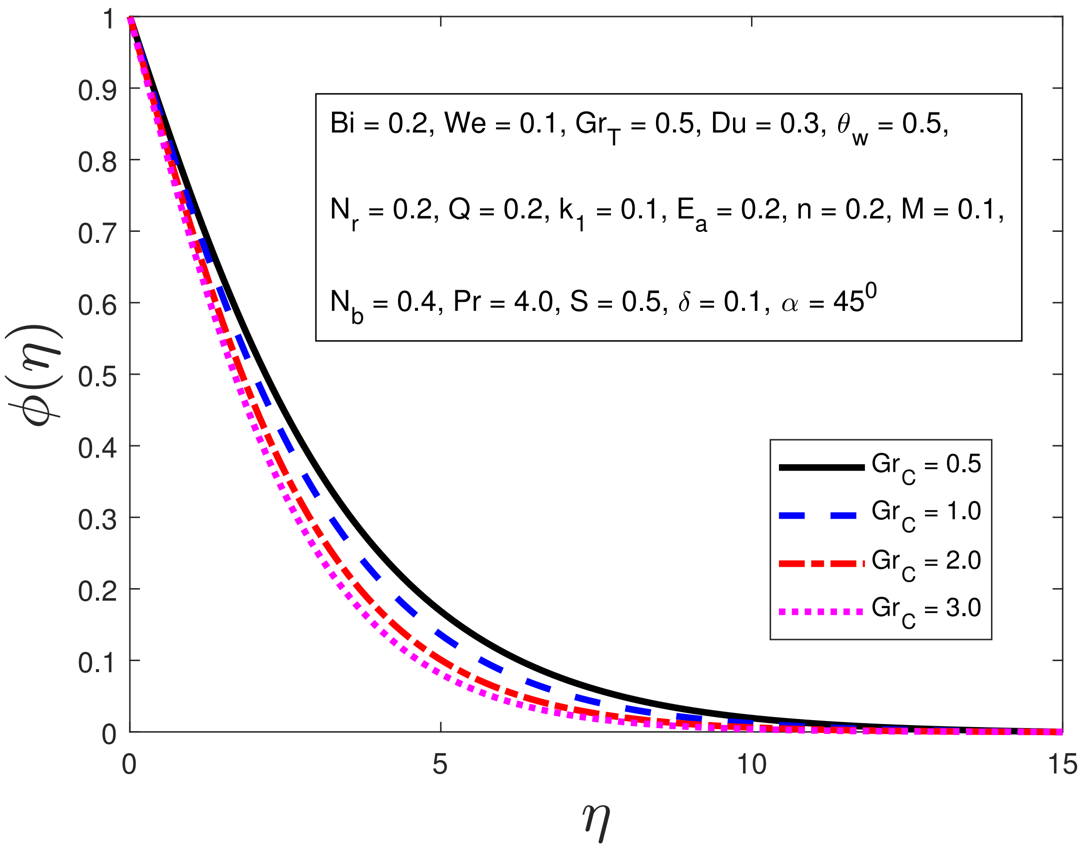

Figure 19: Consequence of Gr_C on the mass flux distribution

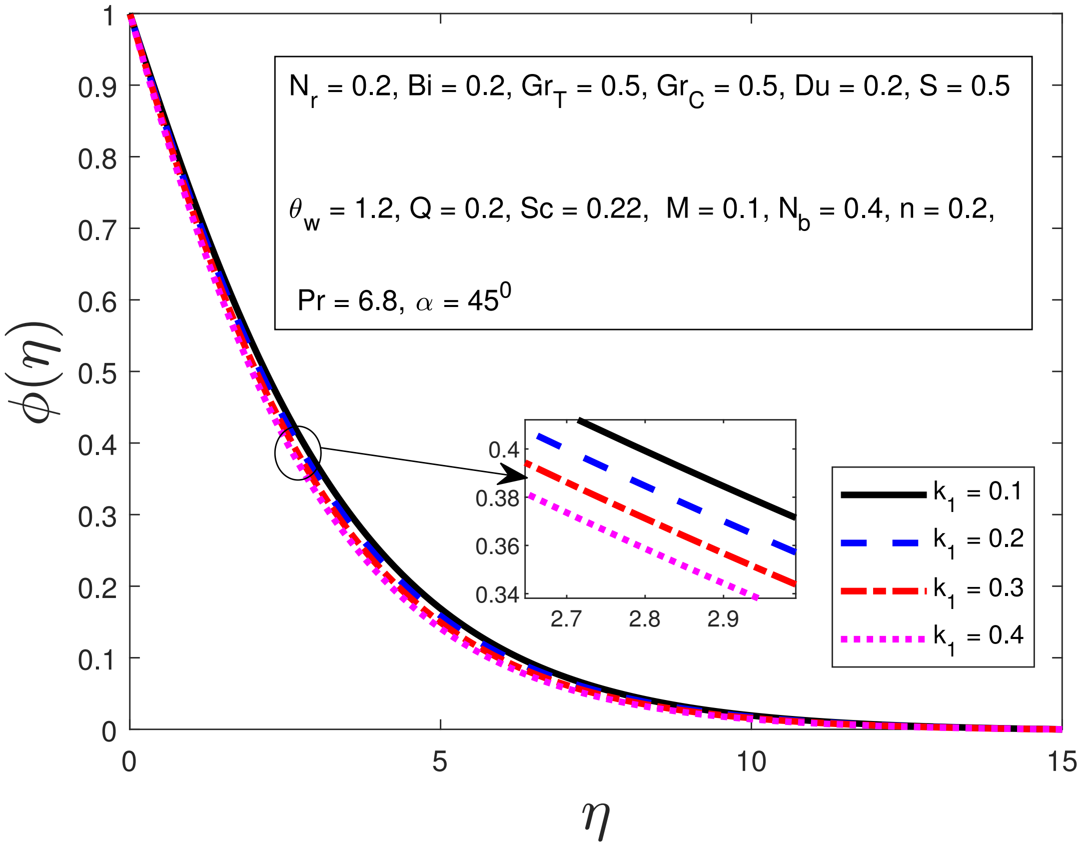

Figure 20: Consequence of k_1 on the mass flux distribution

References

[1] Ahmad, A., S. Asghar, and S. Afzal (2016). Flow of nanofluid past a riga plate. *Journal of Magnetism and Magnetic materials 402*, 44–48.

[2] Akbar, N. S., S. Nadeem, R. U. Haq, and Z. Khan (2013). Numerical solutions of magnetohydrodynamic boundary layer flow of tangent hyperbolic fluid towards a stretching sheet. *Indian journal of Physics 87*(11), 1121–1124.

[3] Ali, F. M., R. Nazar, N. M. Arifin, and I. Pop (2011). Mhd boundary layer flow and heat transfer over a stretching sheet with induced magnetic field. *Heat and Mass transfer 47*(2), 155–162.

[4] Asogwa, K. K., M. Alsulami, B. Prasannakumara, and T. Muhammad (2022). Double diffusive convection and cross diffusion effects on casson fluid over a lorentz force driven riga plate in a porous medium with heat sink: An analytical approach. *International Communications in Heat and Mass Transfer 131*, 105761.

[5] Asogwa, K. K., B. S. Goud, N. A. Shah, and S.-J. Yook (2022). Rheology of electromagnetohydrodynamic tangent hyperbolic nanofluid over a stretching riga surface featuring dufour effect and activation energy. *Scientific Reports 12*(1), 1–17.

[6] Bellman, R. E. and R. K. Quasilinearization (1965). *Nonlinear Boundary-Value Problems.* American Elsevier Publishing Co., Inc., New York.

[7] Böhme, G. (2012). *Non-Newtonian fluid mechanics.* Elsevier.

[8] Chhabra, R. P. (2010). Non-newtonian fluids: an introduction. In *Rheology of complex fluids*, pp. 3–34. Springer.

[9] Crochet, M. and K. Walters (1983). Numerical methods in non-newtonian fluid mechanics. *Annual Review of Fluid Mechanics 15*(1), 241–260.

[10] Gailitis, A. (1961). On the possibility to reduce the hydrodynamic drag of a plate in an electrolyte. *Appl. Magnetohydrodynamics, Rep. Inst. Phys. Riga 13*, 143–146.

[11] Hartnett, J. P. and M. Kostic (1989). Heat transfer to newtonian and non-newtonian fluids in rectangular ducts. In *Advances in heat transfer*, Volume 19, pp. 247–356. Elsevier.

[12] Hassanien, I., A. Abdullah, and R. Gorla (1998). Flow and heat transfer in a power-law fluid over a nonisothermal stretching sheet. *Mathematical and computer modelling 28*(9), 105–116.

[13] Hayat, T., T. Abbas, M. Ayub, M. Farooq, and A. Alsaedi (2016). Flow of nanofluid due to convectively heated riga plate with variable thickness. *Journal of Molecular Liquids 222*, 854–862.

[14] Hayat, T., S. Qayyum, B. Ahmad, and M. Waqas (2016). Radiative flow of a tangent hyperbolic fluid with convective conditions and chemical reaction. *The European Physical Journal Plus 131*(12), 1–13.

[15] Hayat, T., I. Ullah, A. Alsaedi, and B. Ahmad (2017). Modeling tangent hyperbolic nanoliquid flow with heat and mass flux conditions. *The European Physical Journal Plus 132*(3), 1–15.

[16] Khatun, S., M. M. Islam, M. Mollah, S. Poddar, M. Alam, et al. (2021). Emhd radiating fluid flow along a vertical riga plate with suction in a rotating system. *SN Applied Sciences 3*(4), 1–14.

[17] Kumar, P., H. Poonia, L. Ali, and S. Areekara (2022). The numerical simulation of nanoparticle size and thermal radiation with the magnetic field effect based on tangent hyperbolic nanofluid flow. *Case Studies in Thermal Engineering 37*, 102247.

[18] Mahdy, A. and G. Hoshoudy (2019). Emhd time-dependant tangent hyperbolic nanofluid flow by a convective heated riga plate with chemical reaction. *Proceedings of the Institution of Mechanical Engineers, Part E: Journal of Process Mechanical Engineering 233*(4), 776–786.

[19] Mkhatshwa, M. P. (2020). *Overlapping grid spectral collocation methods for nonlinear differential equations modelling fluid flow problems.* Ph. D. thesis.

[20] Nadeem, S. and N. S. Akbar (2010). Series solutions for the peristaltic flow of a tangent hyperbolic fluid in a uniform inclined tube. *Zeitschrift Für Naturforschung A 65*(11), 887–895.

[21] Pantokratoras, A. (2011). The blasius and sakiadis flow along a riga-plate. *Progress in Computational Fluid Dynamics, An International Journal 11*(5), 329–333.

[22] Pantokratoras, A. and E. Magyari (2009). Emhd free-convection boundary-layer flow from a riga-plate. *Journal of engineering mathematics 64*(3), 303–315.

[23] Pinho, F. and J. Whitelaw (1990). Flow of non-newtonian fluids in a pipe. *Journal of non-newtonian fluid mechanics 34*(2), 129–144.

[24] Rajagopal, K. R. (1993). Mechanics of non-newtonian fluids. *Pitman Research Notes in Mathematics Series*, 129–129.

[25] Rasool, G., A. Shafiq, and D. Baleanu (2020). Consequences of soret–dufour effects, thermal radiation, and binary chemical reaction on darcy forchheimer flow of nanofluids. *Symmetry 12*(9), 1421.

[26] Rehman, K. U., A. S. Alshomrani, M. Malik, I. Zehra, and M. Naseer (2018). Thermo-physical aspects in tangent hyperbolic fluid flow regime: a short communication. *Case studies in thermal engineering 12*, 203–212.

[27] Salleh, M. and R. Nazar (2008). Numerical solutions of the boundary layer flow and heat transfer over a stretching sheet with constant wall temperature and heat flux. In *Proceedings of the Third International Conference on Mathematical Sciences ICM*, pp. 1260–1267.

[28] Sarpkaya, T. (1961). Flow of non-newtonian fluids in a magnetic field. *AIChE Journal 7*(2), 324–328.

[29] Sindhu, S. and B. Gireesha (2022). Scrutinization of unsteady non-newtonian fluid flow considering buoyancy effect and thermal radiation: Tangent hyperbolic model. *International Communications in Heat and Mass Transfer 135*, 106062.

[30] Sithole, H., H. Mondal, S. Goqo, P. Sibanda, and S. Motsa (2018). Numerical simulation of couple stress nanofluid flow in magneto-porous medium with thermal radiation and a chemical reaction. *Applied Mathematics and Computation 339*, 820–836.

[31] Trefethen, L. N. (2000). *Spectral methods in MATLAB.* SIAM.

[32] Ullah, Z., G. Zaman, and A. Ishak (2020). Magnetohydrodynamic tangent hyperbolic fluid flow past a stretching sheet. *Chinese Journal of Physics 66*, 258–268.

[33] Waqas, H., A. Kafait, T. Muhammad, and U. Farooq (2022). Numerical study for bio-convection flow of tangent hyperbolic nanofluid over a riga plate with activation energy. *Alexandria Engineering Journal 61*(2), 1803–1814.

Chapter 4

Unsteady squeezing flow and heat transport of SiO_2/kerosene oil nanofluid around radially stretchable parallel rotating disks with upper disk oscillating

This chapter presents detailed fluid mobility and thermal transport analysis within two rotating stretchable disks, focusing on applying SiO_2/kerosene nanofluid. The top disk is simulated to oscillate with a periodic velocity, continuously squeezing the nanofluid within a porous medium and inducing perpendicular flow to the magnetic field. Additionally, thermal radiation effects are incorporated into the heat transfer model to enhance the accuracy of the analysis. The governing non-linear partial differential equations describing the fluid mobility structure and thermal transport are transformed into a non-linear ordinary differential equations system using suitable non-dimensional variables. These ODEs are then numerically solved using the overlapping SQLM employed in chapter 3. The chapter examines the consequences of various pertinent parameters on pressure, temperature, velocity, skin drag coefficient, and thermal transport rate. The findings are elucidated in detail with figures and tables, providing insights into the flow structure and its implications. Key observations from the numerical simulations include the development of negative pressure situations under prescribing conditions. Such phenomena have vast applications in modern medical engineering, particularly in constructing air pressure stabilizers used in medical isolation and wound therapy physiology.

Propulsion and Power Research 2024;xxx(xxx):1–16

http://ppr.buaa.edu.cn/

Propulsion and Power Research

www.sciencedirect.com

ORIGINAL ARTICLE

Unsteady squeezing flow and heat transport of SiO_2/kerosene oil nanofluid around radially stretchable parallel rotating disks with upper disk oscillating

Folarin Oluwaseun[a], Sicelo Goqo[a], Hiranmoy Mondal[b,*]

[a]*School of Mathematics, Statistics and Computer Science, University of KwaZulu-Natal, Private Bag X01, Scottsvile, Pietermaritzburg 3209, South Africa*
[b]*Department of Applied Mathematics, Maulana Abul Kalam Azad University of Technology, West Bengal, Kolkata 700064, India*

Received 26 June 2023; accepted 20 December 2023
Available online XXXX

KEYWORDS

Nanofluids;
Unsteady;
Squeezing;
Stretchable;
Overlapping spectral quasi-linearization;
SiO_2;
Kerosene;
Rotating disks

Abstract In this study, we have analyzed fluid mobility and thermal transport of the SiO_2/kerosene nanofluid within two rotating stretchable disks. The top disk is simulated to be oscillating with a periodic velocity and squeezing continuously the nanofluid within a porous medium and making the fluid to flow perpendicularly to the situated magnetic field. Thermal radiation effects are considered in the heat transfer model. The non-linear (NL) PDEs that describe the nanofluid mobility structure and thermal transport are transformed into system of NL-ODEs by introducing adequately suitable non-dimensional variables after which the NL-ODEs were numerically solved via spectral quasi-linearization method (SQLM) on overlapping grids. The consequences of several pertinent parameters of the model on pressure, temperature, velocity, skin drag coefficient and thermal transport rate are examined and elucidated in detail with the aid of figures and tables. It was found that the flow structure with prescribing conditions develops negative pressure situation which has vast applications in modern day

*Corresponding author.
E-mail address: hiranmoymondal@yahoo.co.in (Hiranmoy Mondal).
Peer review under responsibility of Propulsion and Power Research.

Production and Hosting by Elsevier on behalf of KeAi

https://doi.org/10.1016/j.jppr.2024.02.005

medical engineering, especially in the construction of air pressure stabilizers used in medical isolation and wound therapy physiology.

1. Introduction

Nanofluids have become the contemporary heat transfer fluids of choice in many engineering, industrial, domestic and pharmaceutical processes especially in the construction of refrigerators, heat ex-changers, chillers, radiators and electronic device cooling components. The advantages in heat transfer rates afforded by nanofluids over the regular fluids such as water, ethylene -glycol and oil are the driving force for its preference. A typical nanofluid consist of nanometer-sized particles of metals or non-metals or metallic oxides or non-metallic oxides as colloidal suspension in a based fluid. Common nanoparticles used are Cu, Fe, Ag, Ti, CuO, Al_2O_3, TiO_2, SiO_2, etc. The pioneering work on the development of the concept of nanofluids can be traced to Masuda et al. [1], which formed the basis on which Choi and Eastman [2] presented their ground breaking report on the enhancing fluids thermal conductivity with nanoscale zeolite. These works have paved way for rigorous experimental and numerical research works by numerous researchers.

The effective thermal conductivity of copper nanoparticle in ethylene-glycol based nanofluid was observed to be elevating abnormally in a report by Eastman et al. [3]. Twari and Das [4] described how surface characteristics are greatly influenced for nanofluids within a differentially heated powered square cavity with two sided cover. Zhang et al. [5] investigated the flow caused by MHD and heat transmission of nanofluids in porous media, chemical reaction and variable surface thermal flux. Sheikholeslami and Ellahi [6] reported an investigation on hydrothermal treatment of electrohydrodynamic nanofluid in a chamber with sinusoidal upper wall. Turkyilmazaglu [7] explored analytical approaches of single- and multi-phased models for condensation of nanofluid film flow and heat transmission. Ref. [8] used two-phased models to analyze the impacts of thermal radiation on heat transport and MHD nanofluid flow. Hayat et al. [9] gave insights into analysis of MHD three dimensional flow of nanofluid in the presence of convective conditions. Rashidi et al. [10] presented analysis of the simulation of nanofluid flow and entropy generation in a single slope solar still using the volume of fluid model. Thermally radiative three-dimensional flow of Jeffrey nanofluid with internal heat and magnetic field was analyzed numerically by Shehzad et al. [11]. The study of MHD three-dimensional flow of nanofluid with velocity slip and non-linear thermal radiation was presented by Hayat et al. [12]. More researchers [13–19] have worked with nanofluids using different models and geometric structures.

Researchers have made attempts to conduct more thorough examinations of spinning disk fluid problems modeled in the wake of the ground-breaking work of Von Karman [20] in reducing the governing full system of equations for the solution of such fluid problems. Cochran [21] presented numerical solution of Von Karman problem. The idea of heat transfer by laminar flow from a rotating plate was examined by Millsaps and Pohlhausen [22]. The numerical analysis of thermal radiative maxwell nanofluid flow due to a stretching porous rotating disk was published by Ref. [23]. Acharya et al. [24] examined how Hall current affects radiative nanofluid across spinning disks by offering a hybrid approach solution. Ref. [25] conducted a computational research on the impact of nanoparticle form on an Al_2O_3-silicon oil nanofluid flow over a spinning disk that is being stretched radially. Tassaddiq et al. [26] analyzed hybrid nanofluid over a rotating disk for thermal and mass transfers. Ref. [27] studied Buonogiorno model for MHD nanofluid flow over a rotating disk with the effects of partial slip. Yin et al. [28] presented nanofluid transition and thermal exchange over a revolving disk with uniform radial stretching rate. Bioconvection flow of Casson nanofluid by rotating disk with motile microorganisms was analyzed by Ref. [29]. Tulu and Ibrahim [30] investigated MHD slip flow of CNT-Ethylene glycol nanofluid due to a stretchable spinning disk with Cattaneo-Christov heat flux model. Bilal et al. [31] demonstrated the numerical approximation of microorganisms hybrid nanofluid flow induced by a wavy fluctuating spinning disc.

Fluid problems with geometrical structures of coaxially rotating disks have particularly become an exciting research area owing to the vast applicability in the constructions and operations of gas turbines, medical devices, rotating disk apparatus, evaporators and extractors to mention a few. A computational investigation into heat exchange and viscous fluid flow in a dual revolving flexible disk setup was done by Shamshuddin et al. [32] using a non-Fourier thermal flux model. Ahmed [33] examined the phenomenon of heat transference and spiraling flow of MHD in a Maxwell fluid powered by twin co-axially spinning disks with varying thermodynamic conductivity. With main reference to the influence of thermal radiation restrictions, Mosayebidorcheh [34] carried out heat transfer studies in carbon nanotube-water between rotating disks. Using Cattaneo-Christov heat flux with homogeneous and heterogeneous processes, Dianchen Lu et al. [35] described an unsteady squeezing nanoliquid flow that is carbon-nanotubes based. Ramzan et al. [36] studied the computational evaluation of an unsteady flow in a nanofluid made of carbon nanotubes that is centered amid two spinning disks with Hall current coatings and homogeneous-heterogeneous processes. Hayat et al. [37] analyzed partial slip effects in the flow of magnetite-Fe_3O_4 nanoparticles between rotating stretchable disks. Yaseen et al. [38] employed the Darcy-Forchheimer Cattaneo-Christov heat flux model to characterize the radiative flow of MOS_2-SiO_2/kerosene oil amid twin vertically parallel revolving disks. Alharbi et al. [39] presented insight into Hall current in the hybrid sequeezing nanofluid flow amid two rotating disks in a thermally stratified medium. Ref. [40] demonstrated the significance of induced hybridized metallic and non-metallic oxides (Cu-TiO_2) nanoparticles to uplift thermophysical attributes of water. Refs. [41–44] all recently presented interesting ideas on coaxially rotating disks using different models of nanofluids.

Extensive literature review indicates that a rich pool of research on nanofluid flows between parallel rotating disks is available. However, not much has been done on unsteady squeezing nanofluid flows amid stretching rotating disks with one of the disks, preferably the upper disk in continuous vertical oscillatory motion. The current study is focused on this scientific research gap by considering an unsteady squeezing flow of SiO_2/kerosene oil around radially stretchable spinning disks as the upper disk vertically oscillates continuously with a periodic velocity. Computational solutions of the prescribed model are presented using overlapping grid spectral quasi-linearization method via MATLAB codes. Consequences of essential parameters in the model with physical interpretations on the skin friction coefficient, heat transfer rate, fluid velocity characteristics, temperature and pressure distributions are presented and subsequently discussed. The main objectives of this numerical investigations are: therefore stated thus:

1) Present a numerical simulation of SiO_2/kerosene nanofluid within two rotating stretchable disks with the upper disk oscillating continuously.
2) Invoke and implement appropriate self similarity transformation on the system of non-linear PDEs that describes the flow to convert to system of non-linear ODEs.
3) Obtain numerical solutions of the non-linear ODEs using spectral quasi-linearization on overlapping grids.
4) Examine the boundary layer characteristics of the nanofluid in this type of set up.
5) Examine and discuss the significance of the upper oscillating disk on the fluid characteristics.
6) Examine and discuss the paramount modeled parameter as they influence the fluid characteristics.

2. Physical elucidation of the problem

This study considers compressing and releasing of an electrically conducting nanofluid in porous medium amid twin vertically parallel, stretchable spinning disks. Kerosene as the based fluid with silicon-oxide, SiO_2 contributing the nanoparticles to form the nanofluid being considered in this work. The disk at the bottom, $z=0$, rotates with a constant rotational velocity Ω_{LD} in θ-direction and stretches radially at the rate, a_1. The disk at the top which also rotates with a constant rotational velocity, Ω_{UD} in θ-direction and stretches at a rate of a_2 in radial direction is at an instantaneous distance of $z=d(t)=h-a\sin(t)$, $0<a<h$, from bottom position disk. The disk at the top possesses continual oscillatory velocity, $\tilde{v}_3=d'(t)=-a\cos(t)$, which allows it to continuously squeeze with period 2π. When $t=0$, the disk at the top is at rest vertically, $z=h$ above bottom position disk. When $0<t\leq\frac{\pi}{2}$, the disk at the top squeezes continuously downwards until it stops at the distance $z=h-a$, at $t=\frac{\pi}{2}$ from the bottom disk. After this, the top disk starts to continuously squeeze upwards until a gap of $z=h+a$ exist between the disks, during time interval $\frac{\pi}{2}<t\leq\frac{3\pi}{2}$. Joule's heating and thermal radiation form the significant parts of the energy equation considered here. The whole setup is simulated in cylindrical coordinates (r,θ,z), with the components of the velocity given by; $(\tilde{v}_1,\tilde{v}_2,\tilde{v}_3)$. The temperatures at the disks are T_{LD} and T_{UD}.The flow field in the model is exposed to a fixed magnetic field that is applied perpendicularly to fluid field flow.

Physical situation described under these conditions is depicted in Figure 1 and hence, the NE-PDEs following [45–47] are:

$$\frac{\partial\tilde{v}_1}{\partial r}+\frac{\partial\tilde{v}_3}{\partial r}=-\frac{\tilde{v}_1}{r}, \tag{1}$$

$$\rho_{nf}\left(\frac{\partial\tilde{v}_1}{\partial t}+\tilde{v}_1\frac{\partial\tilde{v}_1}{\partial r}-\frac{(\tilde{v}_2)^2}{r}\tilde{v}_3\frac{\partial\tilde{v}_1}{\partial z}\right)\frac{\partial P}{\partial r} \\ =\mu_{nf}\left(\frac{\partial^2\tilde{v}_1}{\partial r^2}+\frac{1}{r}\frac{\partial\tilde{v}_1}{\partial r}-\frac{\tilde{v}_1}{r^2}+\frac{\partial^2\tilde{v}_1}{\partial z^2}\right)-\sigma_{nf}B_0^2\tilde{v}_1-\frac{\mu_{nf}}{\kappa_0}\tilde{v}_1, \tag{2}$$

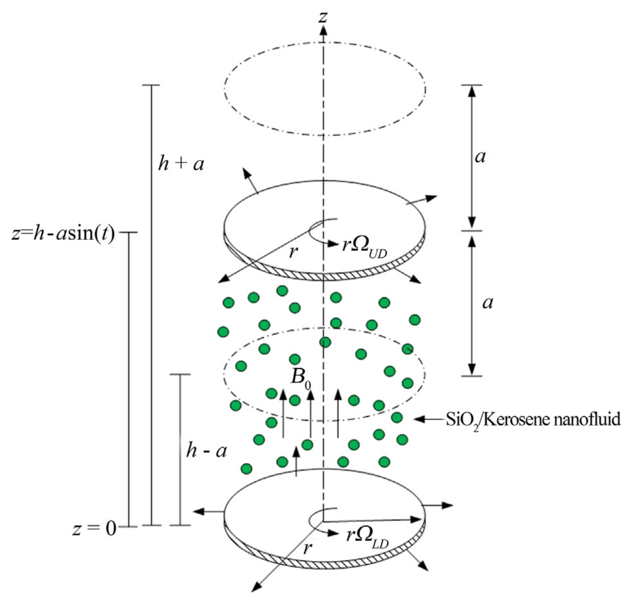

Figure 1 Flow schematic of the model.

$$\rho_{nf}\left(\frac{\partial\tilde{v}_2}{\partial t}+\tilde{v}_1\frac{\partial\tilde{v}_2}{\partial r}+\frac{\tilde{v}_1\tilde{v}_2}{r}+\tilde{v}_3\frac{\partial\tilde{v}_2}{\partial z}\right)=\mu_{nf}\left(\frac{\partial^2\tilde{v}_2}{\partial r^2}+\frac{1}{r}\frac{\partial\tilde{v}_2}{\partial r}-\frac{\tilde{v}_2}{r^2}+\frac{\partial^2\tilde{v}_2}{\partial z^2}\right)-\sigma_{nf}B_0^2\tilde{v}_2-\frac{\mu_{nf}}{\kappa_0}\tilde{v}_2, \tag{3}$$

$$\rho_{nf}\left(\frac{\partial\tilde{v}_3}{\partial t}+\tilde{v}_1\frac{\partial\tilde{v}_3}{\partial r}+\tilde{v}_3\frac{\partial\tilde{v}_3}{\partial z}\right)+\frac{\partial P}{\partial z}=\mu_{nf}\left(\frac{\partial^2\tilde{v}_3}{\partial r^2}+\frac{1}{r}\frac{\partial\tilde{v}_3}{\partial r}+\frac{\partial^2\tilde{v}_3}{\partial z^2}\right), \tag{4}$$

$$\frac{\partial T}{\partial t}+\tilde{v}_1\frac{\partial T}{\partial r}+\tilde{v}_3\frac{\partial T}{\partial z}=\left(\frac{k_{nf}}{(\rho C_p)_{nf}}+\frac{16\sigma^* T_{UD}^3}{3k^*(\rho C_p)_{nf}}\right)\left(\frac{\partial^2 T}{\partial r^2}+\frac{\partial^2 T}{\partial z^2}+\frac{1}{r}\frac{\partial T}{\partial r}\right)+\frac{\sigma_{nf}B_o^2}{(\rho C_p)_{nf}}\left((\tilde{v}_1)^2+(\tilde{v}_2)^2\right), \tag{5}$$

As used by Ref. [47], the applicable limiting situations are:

$$\tilde{v}_1=ra_1,\ \tilde{v}_2=r\Omega_{LD},\ \tilde{v}_3=0, T=T_{LD},\ \text{at}\ z=0,$$

$$\tilde{v}_1=ra_2,\ \tilde{v}_2=r\Omega_{UD},\ \tilde{v}_3=-a\cos(t),\ T=T_{UD},$$

$$\text{at}\ z=h-a\sin(t), \tag{6}$$

where: σ^* is the Boltzmann's constant, k^* is the absorption coefficient,

$$\text{Dynamic viscosity}=\mu_{nf}=\frac{\mu_f}{(1-\phi)^{2.5}},$$

$$\text{Density}=\rho_{nf}=(1-\phi)\rho_f+\rho_s\phi,$$

$$\text{Heatcapacity}=(\rho C_p)_{nf}=(1-\phi)(\rho C_p)_f+(\rho C_p)_s\phi,$$

$$\text{Thermal conductivity}=\frac{k_{nf}}{k_f}=\frac{k_s+2k_f-2\phi(k_f-k_s)}{k_s+2k_f+2\phi(k_f-k_s)},$$

$$\text{Electricalconductivity}=\sigma_{nf}=(1-\phi)\sigma_f+\sigma_s\phi$$

In order to solve the system of partial differential Eqs. (1)–(5) subject to the boundary conditions (6) numerically, we introduce the following suitble similarity transformations to help transform the system of NE-PDEs to a system of NE-ODEs which are then solved using the overlapping spectral quasilinearization method.

$$\tilde{v}_1=\frac{r\Omega_{LD}}{(h-a\sin(t))^2}f'(\eta),\ \tilde{v}_2=\frac{r\Omega_{LD}}{(h-a\sin(t))^2}g(\eta),$$
$$\tilde{v}_3=\frac{-2\Omega_{LD}}{h-a\sin(t)}f(\eta),\ \theta=\frac{T-T_{UD}}{T_{LD}-T_{UD}},\ \eta=\frac{z}{h-a\sin(t)},$$

$$p=\frac{\rho_f\Omega_{LD}\nu_f}{(h-a\sin(t))^2}\left(P(\eta)+\frac{r^2}{2(h-a\sin(t))^2}\epsilon\right), \tag{7}$$

NL-ODEs obtained are:

$$C_1C_2f'''+Re\left(2ff''+g^2-(f')^2-C_2\left(\frac{M_p\sigma_{nf}}{\sigma_f}+C_1k_p\right)f'+S_qRe(2f'+\eta f'')-C_2\epsilon=0,\right. \tag{8}$$

$$C_1C_2g''+2Re(fg'-f'g)-C_2\left(\frac{M_p\sigma_{nf}}{\sigma_f}+C_1k_p\right)g+S_qRe(2g+\eta g')=0, \tag{9}$$

$$C_2P'=-2S_qRe(f+\eta f')-4Reff'-2C_1C_2f'', \tag{10}$$

$$\frac{1}{P_r}\frac{k_{nf}}{k_f}(1+R_{nd})\theta''+C_3(2f+\eta S_q)\theta'+C_3\left[M_pE_k\frac{\sigma_{nf}}{\sigma_f}\left((f')^2+g^2\right)\right]=0, \tag{11}$$

where:

$$C_1=\frac{1}{(1-\phi)^{2.5}},$$

$$C_2=\frac{1}{\left((1-\phi)+\frac{\rho_s}{\rho_f}\phi\right)},$$

$$C_3=\left((1-\phi)+\frac{(\rho C_p)_s}{(\rho C_p)_f}\phi\right),$$

Here, we have defined the dimensionless constants and parameters as $E_k=\frac{r^2\Omega_{LD}^2(T_{LD}-T_{UD})}{(h-a\sin(t))^4}$ is the localized Eckert number, $M_p=\frac{\sigma_f B_o^2(h-a\sin(t))^2}{\mu_f}$ represents the Hartmann number, $P_r=\frac{\nu_f(\rho C_p)_f}{k_f}$ represents the Prandtl number, $S_q=-\frac{a\cos(t)(h-a\sin(t))}{\Omega_{LD}}$ is the squeezing parameter, which controls the vertical oscillatory motion of the disk at the top. For $S_q<0$, the upper disk squeezes downwards and upwards when $S_q>0$, $S_1=\frac{(h-a\sin(t))^2a_1}{\Omega_{LD}}$ and $S_2=\frac{(h-a\sin(t))^2a_2}{\Omega_{LD}}$ are the stretching parameters of the two disks, Φ_1 and Φ_2 are the rotation parameters.

The transformed limiting situations are:

$$f'(0)=S_1, f(0)=0,\ g(0)=\Phi_1,\ \theta(0)=1,\ P(0)=0$$

$$f(1)=\frac{S}{2}, f'(1)=S_2,\ g(1)=\Phi_2,\ \theta(1)=0 \tag{12}$$

For simplicity, we eliminate ϵ from (8) by differentiating with respect to η, to get

$$C_1C_2f^{iv}+2Re(ff'''+gg') - C_2\left(\frac{M_p\sigma_{nf}}{\sigma_f}+C_1k_p\right)f''+S_qRe(2f''+\eta f''')=0 \quad (13)$$

ϵ being the pressure parameter can be determined as follows:

$$\epsilon=C_1f'''+\frac{Re}{C_2}\left(2ff''+g^2-(f')^2\right)-\left(\frac{M_p\sigma_{nf}}{\sigma_f}+C_1k_p\right)f' +\frac{S_qRe}{C_2}(2f'+\eta f'') \quad (14)$$

Subject to boundary conditions (12), the pressure parameter, ϵ becomes

$$\epsilon=C_1f'''(0)+\frac{Re}{C_2}\left(\left(f'(0)^2\right)-\left(g(0)^2\right)\right) -\left(\frac{M_p\sigma_{nf}}{\sigma_f}+C_1k_p\right)f'(0)+\frac{S_qRe}{C_1}(2f'(0) +\eta f''(0)) \quad (15)$$

We can obtain the pressure function from (10) by integrating with respect to η, taking the limit of integration from $0-\eta$.

$$P=-2\left[C_1(f'(\eta)-f'(0))+\frac{Re}{C_2}f^2(\eta)+\frac{\eta S_qRe}{C_2}f(\eta)\right] \quad (16)$$

In the quest of examining the behavior of the flow, some physical characteristics are defined, which include the total shear stresses, τ_w, at the lower and upper disks which are defined in terms of the shear stresses in r-direction, τ_{zr} and θ-direction, $\tau_{z\theta}$. The skin friction coefficient which is of high engineering importance can therefore be defined in terms of the total shear stress at each of the rotating disks.

The total shear stress is given by:

$$\tau_w=\sqrt{\tau_{zr}^2+\tau_{z\theta}^2}$$

where:

$$\tau_{zr}=\left(\mu_{nf}\frac{\partial u}{\partial z}\right)_{z=0}=\frac{C_1\mu_f r\Omega_{LD}}{(h-a\sin t)^3}f''(0) \text{ and}$$

$$\tau_{zr}=\left(\mu_{nf}\frac{\partial u}{\partial z}\right)_{z=d(t)}=\frac{C_1\mu_f r\Omega_{LD}}{(h-a\sin t)^3}f''(1)$$

$$\tau_{z\theta}=\left(\mu_{nf}\frac{\partial v}{\partial z}\right)_{z=0}=\frac{C_1\mu_f r\Omega_{LD}}{(h-a\sin t)^3}g'(0) \text{ and}$$

$$\tau_{z\theta}=\left(\mu_{nf}\frac{\partial v}{\partial z}\right)_{z=d(t)}=\frac{C_1\mu_f r\Omega_{LD}}{(h-a\sin t)^3}g'(1)$$

Hence, the dimensionless skin drag coefficients on the surfaces of the disks can therefore be given as:

$$Cf_{LD}=\frac{(\tau_w)_{z=0}}{\rho_f(r\Omega_{LD})^2}=Re_\tau C_1\left(\sqrt{(f''(0))^2+(g'(0))^2}\right),$$

$$Cf_{UD}=\frac{(\tau_w)_{z=d(t)}}{\rho_f(r\Omega_{LD})^2}=Re_\tau C_1\left(\sqrt{(f''(1))^2+(g'(1))^2}\right)$$

where: $Re_\tau=\frac{r\Omega_{LD}(h-a\sin t)^3}{\nu_f}$ is the local squeezed rotating Reynold number.

Additional physical quantities of pertinent engineering interest for the current research work are the rates of heat transfer at the rotating disks, which are measured by the Nusselt numbers. The heat transfer coefficients on the surfaces of the disks can be expressed as:

$$Nur_{LD}=\left(\frac{q_w}{k_f(T_{LD}-T_{UD})}\right)_{z=0},$$

$$Nur_{UD}=\left(\frac{q_w}{k_f(T_{LD}-T_{UD})}\right)_{z=d(t)},$$

where, the wall heat flux, q_w in terms of the radiative heat flux is given by:

$$(q_w)_{z=0}=\left(-k_{nf}\frac{\partial T}{\partial z}\right)_{z=0}+(q_r)_{z=0},$$

$$(q_w)_{z=d(t)}=\left(-k_{nf}\frac{\partial T}{\partial z}\right)_{z=d(t)}+(q_r)_{z=d(t)},$$

And the radiative heat fluxes at the rotating disks are:

$$(q_r)_{z=0}=\left(-\frac{16\sigma^*T_{LD}^3}{3k^*}\frac{\partial T}{\partial z}\right)_{z=0},$$

$$(q_r)_{z=d(t)}=\left(-\frac{16\sigma^*T_{LD}^3}{3k^*}\frac{\partial T}{\partial z}\right)_{z=d(t)},$$

The dimensionless Nusselt numbers at the lower and upper rotating disks are given by:

$$Nur_{LD}=-\left(\frac{k_{nf}}{k_f}+R_{nd}\right)\theta'(0),$$

$$Nur_{UD}=-\left(\frac{k_{nf}}{k_f}+R_{nd}\right)\theta'(1)$$

3. Spectral quasilinearization method on overlapping grids

This solution method is an iterative one that involves the idea of breaking the solution domain into multi-domains of overlapping grids, quasilinearization, modified Chebyshev spectral collocation and Langrange interpolation with Gauss-Lobatto grid points. Spectral quasilinearization method (SQLM) guarantees better stability with few grid points, suitability, accuracy and minimum computation time in relations to the common numerical methods such as shooting method, Runge-Kutta method, Keller Box method, etc. Implementing SQLM on overlapping grids massively improves its performance in terms of stability for larger sub-domain with fewer grid points, accuracy and computation time. This is as a result of the fact that overlapping grid spectral quasilinearization method involves sparse coefficient matrices that makes matrix inversion and matrix-vector multiplication easier and faster. The method is implemented as follows:

First step is to split the solution domain into overlapping sub-domains. The finite domain for the current model is defined in terms of a curtailed distance of integration $I = [0, \eta]$, which is then partitioned into q-overlapping sub-domains defined as:

$$I_l = \left[\eta_0^l, \eta_{M_\eta}^l\right],\ l = 1,2,3,\ldots,q$$

The next step is the discretization of the subinterval, I_l into $M_\eta + 1$ collocation points takes place with the domain having a uniform length, given by

$$L = \frac{\eta}{q + (1-q)\frac{\left(1-cos\left(\frac{\pi}{M_\eta}\right)\right)}{2}}, \tag{17}$$

The end point which signifies the total length of the domain is obtained with the aid of the collocation points of Gauss-Lobatto given by $z_i = \cos\left(\frac{\pi i}{M_\eta}\right), i = 0,1,2,3,\ldots,M_\eta$, as $= \frac{L}{2}\left(1 - \cos\left(\frac{\pi}{M_\eta}\right)\right)(1-q) + qL,.$

For the current study, being a finite domain problem, $\eta = 1$.

The NE-ODEs (14), (9) and (11) are then solved in each subinterval, I_l. To obtain these solutions, we linearize the equations using quasilinearization technique as in regular SQLM with the variable coefficients given as:

$$a11_{0,r} = 2Ref_r''',\ a11_{2,r} = -C_2,$$

$$b22_{0,r} = -2Ref_r' - C_2\left(\frac{M_p\sigma_{nf}}{\sigma_f} + C_1k_p\right) + 2S_qRe,$$

$$b22_{1,r} = 2Ref_r + \eta ReS_q,\ b22_{2,r} = C_1C_2,$$

$$b11_{0,r} = 2Reg_r',\ b11_{1,r} = 2Reg_r,$$

$$a22_{1,r} = -2Reg_r,\ c33_{1,r} = \frac{1}{C_2}\left(2Ref_r + \eta S_q\right),$$

$$a33_{0,r} = 2C_3Re\theta_r',\ a33_{1,r} = \frac{2M_pE_k\sigma_{nf}}{\sigma_f}f_r',$$

$$b33_{0,r} = \frac{2M_pE_k\sigma_{nf}}{\sigma_f}g_r,\ c33_{2,r} = \frac{1}{P_r}\frac{k_{nf}}{k_f}(1+R_{nd}),$$

$$a11_{4,r} = C_1C_2,\ a22_{0,r} = 2Reg_r',$$

$$a11_{3,r} = 2Ref_r + \eta S_qRe\,.$$

We consider the transformation of each interval $I_l = [\eta_0^l, \eta_{M_\eta}^l]$ into $z \in [-1,1]$ by the use of the linear transformation $\eta_i^l = \frac{L}{2}(z_i + 1),\ z_i = \cos\left(\frac{\pi i}{M_\eta}\right)$. To apply the spectral collocation on the sub-intervals, we evaluate the first derivative defined as:

$$\frac{dF^l}{dz} = \sum_{j=0}^{M_\eta} \boldsymbol{D}_{i,j}^l \boldsymbol{F}^l(z_j),$$

where, $\boldsymbol{D}_{i,j}^l = \frac{2}{\eta_{M_\eta}^l - \eta_0^l}\tilde{\boldsymbol{D}}_{i,j},\ i = 0,1,2,\cdots,M$ and $\boldsymbol{F}^l(z_j) = \left[f^l(z_j), g^l(z_j),\ \theta^l(z_j)\right]$.

$\tilde{\boldsymbol{D}}_{i,j}$ represents the first order differential operator in a single domain $[-1,1]$. Similarly, we can obtain the nth order derivative at the sub-interval I_l as:

$$\frac{d^n\boldsymbol{F}^l}{dz^n} = \sum_{j=0}^{M_\eta}\left[\boldsymbol{D}_{i,j}^{(l)}\right]^n \boldsymbol{F}^l(z_j), i = 0,1,2,\cdots,M_\eta$$

Proceeding, we obtain the derivatives of the unknown functions in a system of equations given as:

$$\Delta_{\boldsymbol{11}}\tilde{\boldsymbol{f}}_{\boldsymbol{r+1}} + \Delta_{\boldsymbol{12}}\tilde{\boldsymbol{g}}_{\boldsymbol{r+1}} + \Delta_{\boldsymbol{13}}\tilde{\theta}_{\boldsymbol{r+1}} = \boldsymbol{R}_f^l$$

$$\Delta_{\boldsymbol{21}}\tilde{\boldsymbol{f}}_{\boldsymbol{r+1}} + \Delta_{\boldsymbol{22}}\tilde{\boldsymbol{g}}_{\boldsymbol{r+1}} + \Delta_{\boldsymbol{23}}\tilde{\theta}_{\boldsymbol{r+1}} = \boldsymbol{R}_g^l$$

$$\Delta_{\boldsymbol{31}}\tilde{\boldsymbol{f}}_{\boldsymbol{r+1}} + \Delta_{\boldsymbol{32}}\tilde{\boldsymbol{g}}_{\boldsymbol{r+1}} + \Delta_{\boldsymbol{33}}\tilde{\theta}_{\boldsymbol{r+1}} = \boldsymbol{R}_\theta^l \tag{18}$$

Each matrix, $\Delta_{\varrho,\varsigma}$ $(\varrho = 1,2,3; \varsigma = 1,2,3)$ is $(M+1)\times(M+1)$ order and $R_f^l,\ R_g^l$ and R_θ^l are vectors each of $(M+1)\times 1$ order.

We obtain a less dense matrix system after imposing the boundary conditions which is then solved with suitable initial guesses that also satisfy the boundary conditions. The suitable initial guesses for the current model are:

$$f_0(\eta) = \frac{2S_2e^{-1} - 4S_1e^{-1} + 2S_1 + S_qe^{-1}}{2(3e^{-1}-1)}\eta^2 + \frac{3S_1e^{-1} - 2S_1 - S_2 + S_q}{3e^{-1}-1}\eta + \frac{S_1 + S_2 - S_q}{3e^{-1}-1} + \frac{S_q + S_1 - S_2}{3e^{-1}-1}e^{-\eta},$$

$$g_0(\eta) = \Phi_1 + (\Phi_2 - \Phi_1)\eta,\ \theta_0(\eta) = 1 - \eta\,.$$

4. Validation of model and code

We establish that the results presented here are trustworthy by comparing the results from the model and code to the published results of the research works of Imtiaz et al. [48] and Tausif et al. [47]. The results here have been obtained via spectral quasilinearization method on overlapping grids using codes executed in MATLAB (see Table 1). We

Table 1 Thermophysics features of kerosene oil and SiO_2 (See Ref. [43]).

Physical properties	Kerosene oil	SiO_2
Density, ρ ($kg \cdot m^{-3}$)	783	2650
Heat capacitance, C_p ($J \cdot kg^{-1} \cdot K^{-1}$)	2090	730
Thermal conductivity, k ($W \cdot m^{-1} \cdot K^{-1}$)	0.15	1.5
Electrical conductivity, σ ($S \cdot m^{-1}$)	5×10^{-11}	1×10^{-18}

obtained the values of $f''(0)$ and $g'(0)$ for various values of Φ_2, which are as shown in Table 2. Excellent agreements were found for both research works, which gives clear indications of the correctness of the model and code.

5. Results and analysis

With validity of the model established, we put forward via tables and graphs the results of varying pertinent parameters on the drag forces at the surfaces, heat transfer rates at the surfaces, dimensionless velocity and heat profiles.

5.1. Dimensionless surface drag

Table 3 presents how the skin friction drag ranges at the rotating disks as consequences of the variations in the values of ϕ, S_q, S_1, S_2, Φ_1 and Φ_2. The Skin friction drag basically represents the force per unit area acting tangentially to the solid surface. It demonstrates the resistance of the fluid to flow along the surface boundary. In this case, the skin friction drag describes the hydrodynamic force at each of the disks, which can be seen from the table that, it is more evident at the lower disk as a result of the nanofluid fluid physical property and the increased fluid pressure resulting from the continuous oscillations of the upper disk. We observed overall increases in the drag forces at both disks as values of ϕ, S_1, S_2, Φ_1 and Φ_2 grow. However, in the case of squeezing parameter, S_q, a dynamic variation is seen, as the effect is more evident in the upper disk when it squeezes downwards, ($S_q < 0$), because the distance between the two disks significantly reduces and hence, the nanofluids are forced to flow along the disk surfaces with more resistance provided to the mobile disk and more evident in the disk at the bottom when the disk at the top is stationary, ($S_q = 0$) or stretches upwards, ($S_q > 0$).

Table 3 Numerical values of the skin friction coefficients at the lower and upper disks for different values of some pertinent parameters.

ϕ	S_1	S_2	Φ_1	Φ_2	S_q	$Re_r Cf_{LD}$	$Re_r Cf_{UD}$
0	0.7	0.8	0.5	0.8	0.5	5.63749749	2.30796034
0.1						7.01498802	2.98620125
0.2						8.73189516	3.95027382
0.3						11.00729068	5.45990595
0.2	0.1					5.06092601	2.81341409
	0.2					5.38504623	3.00879860
	0.5					7.11998496	3.57945927
	0.7	0.1				3.83896201	1.37010758
		0.2				4.55802535	1.45020756
		0.5				6.65699605	1.67750020
		0.7				8.03509004	1.81381835
		0.8	−0.2			10.82469940	2.82733788
			−0.1			10.75198725	2.91396190
			0.1			10.52139526	3.11027874
			0.2			10.36057085	3.21825575
			0.5	−0.2		7.54234786	2.82402008
				−0.1		7.23764266	2.87361613
				0.1		6.98725506	2.99375620
				0.2		7.05700428	3.06411464
				0.8	−0.2	8.71704807	13.32424373
					−0.1	8.83332170	10.81129392
					0	9.02963178	8.84954242
					0.1	9.25234139	7.31607696
					0.2	9.44977399	6.09188135

5.2. Dimensionless surface rate of heat transfer

The rates of heat transmission at the disks described by the Nusselt numbers have been analyzed for ranging values of ϕ, R_{nd} and S_q. We observed significant changes in the Nusselt number at the lower disk compare to the upper disk for ϕ and R_{nd}, while the reverse is the case for S_q, as the upper disk squeezes up and down. When the disk at the top squeezes upwards, this describes a situation where the molecules of the nanofluid are more away from it and hence, the less rate of heat transfer at its surface compare to the surface of the disk at the bottom. On contrary, when the disk at the top moves downwards, it closes the distance of the molecules resulting in higher rate of heat transfer at its surface in relation to other disk. Also we observed increasing trends in the overall heat transfer rates at both disks for ϕ and R_{nd}. However, the trends are in opposite direction for S_q in the disks as seen in Table 4.

Table 2 Comparison for validation with $\phi = S_1 = S_2 = S_q = 0$, $Re = 1.0$ and $\Phi_1 = 1.0$.

Φ_2	$f''(0)$ [48]	$-g'(0)$ [48]	$f''(0)$ [47]	$-g'^{(0)}$ [47]	$f''(0)$	$g'(0)$
−1.0	0.06666	2.00095	0.066663142	2.00095151	0.066663142	2.000952151
−0.8	0.08394	1.80259	0.083942072	1.802588473	0.083942072	1.802588482
−0.3	0.10395	1.30442	0.103950887	1.304423548	0.103950886	1.304423551
0	0.09997	1.00428	0.099972209	1.004277556	0.099972211	1.004277562
0.5	0.06663	0.50261	0.066634195	0.502613511	0.066634196	0.502613512

5.3. Dimensionless radial velocity distribution

Consequences of variations in ϕ, S_q, Re, S_1, S_2, Φ_1 and Φ_2 on the radial velocity of the nanofluid are displayed in Figures 2, 3, 4, 5, 6, 7, 8, and 9. Figure 2 shows how the fluid speeds up radially in the vicinity of the disk at the bottom and slows down radially in the vicinity of the disk at the top, owning to enhancement of ϕ in both cases. Similar patterns are demonstrated for varying values of S_1, as seen in Figure 6, Φ_1, as seen in Figure 8. In each case, increasing values of the parameters results to increased nanofluid pressure and hence, the nanofluid releases the increased pressure radially in the vicinity of the stationary disk. For $S_q < 0$, as the upper disk pushes downwards, fluid pressure increases and the fluid releases the pressure radially around mid-distance region between the two disks which makes the velocity to shoot up in radial direction around this region as seen in Figure 3. For S_q, as the upper disk moves up, fluid pressure reduces, hence the observed decrease in the fluid velocity in radial direction as seen in Figure 4. Figure 5 presents reduction in the velocity of the fluid radially around the disk at the bottom and increment in it around the disk at the top as the values of Re enhances owing to increased pressure that accompanies increased Re values which result to higher squeezing energy required at the top disk. Similar variations are observed for increasing values of S_2 and Φ_2 as seen in Figures 7 and 9.

5.4. Dimensionless axial velocity distribution

Figure 10 depicts how ϕ, influences the speed of the nanofluid in axial direction. Increasing SiO_2 nanoparticle percentage in this configuration reduces the based fluid viscosity and the pressure drop which influences the axial velocity of the nanofluid as opposition to the flow between the disks is greatly diminished. Hence, it can be observed that the nanofluid speed in the axial direction between the two rotating stretching disks becomes elevated for heightening in ϕ values. The patterns are the same in Figures 14 and 16 for increasing values of S_1 and Φ_1 respectively.

Table 4 Numerical values of the Nusselt numbers at the lower and upper disks for different values of some pertinent parameters.

ϕ	R_{nd}	S_q	Nur_{LD}	Nur_{UD}
0	0.5	0.5	8.14924570	0.01108030
0.05			8.73019689	0.01744920
0.1			9.42129297	0.04429902
0.2			11.00481634	0.50925930
0.2	0.5		10.74676439	0.70607173
	1.0		10.51851004	1.03126087
	1.5		10.40440755	1.61443750
	0.5	−0.2	4.82268587	10.91746896
		−0.1	5.27661533	8.86201695
		0	5.77618912	7.04526821
		0.1	6.33399424	5.46816441
		0.2	6.94731004	4.14031345

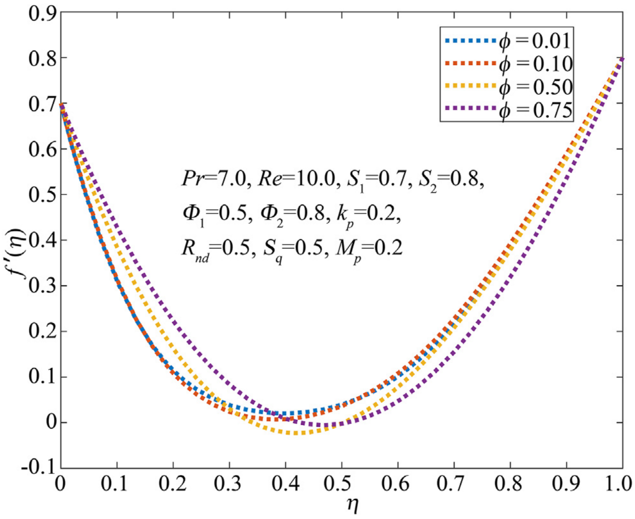

Figure 2 Implication of ϕ on $f'(\eta)$.

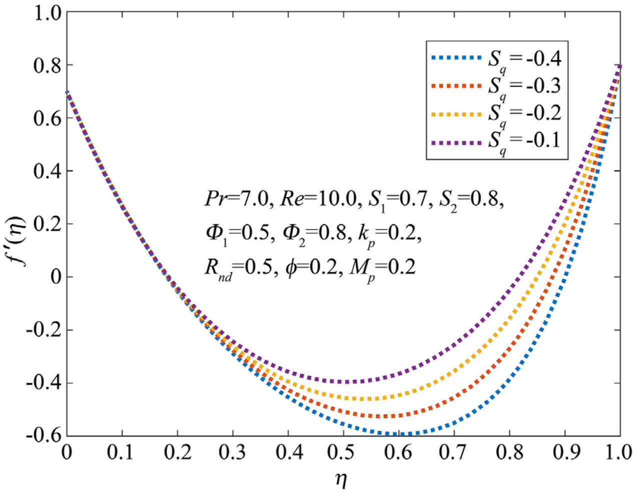

Figure 3 Implication of $S_q < 0$ on $f'(\eta)$.

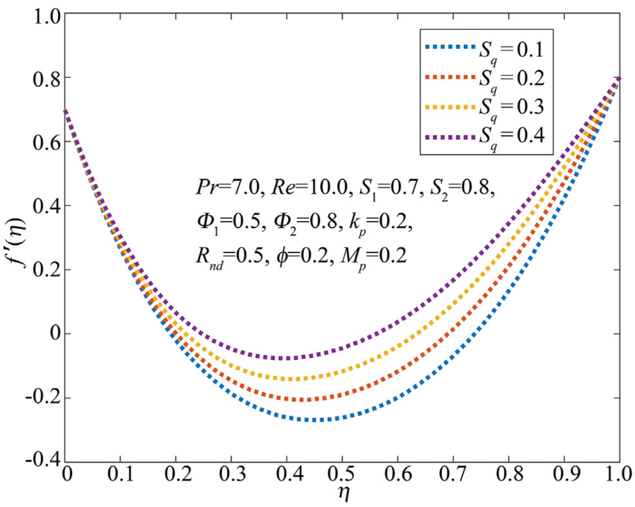

Figure 4 Implication of $S_q > 0$ on $f'(\eta)$.

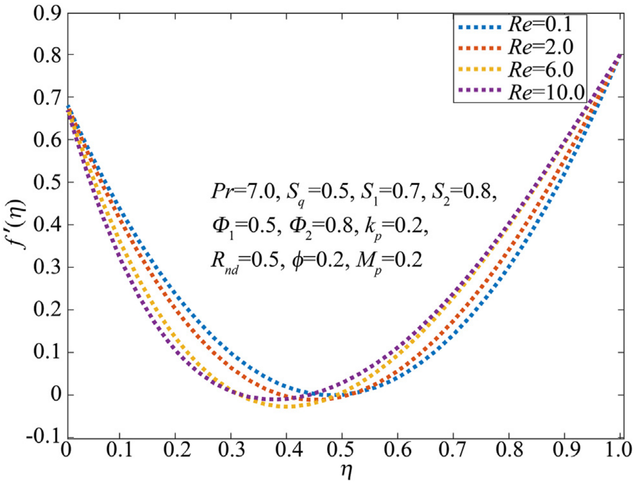

Figure 5 Implication of Re on $f'(\eta)$.

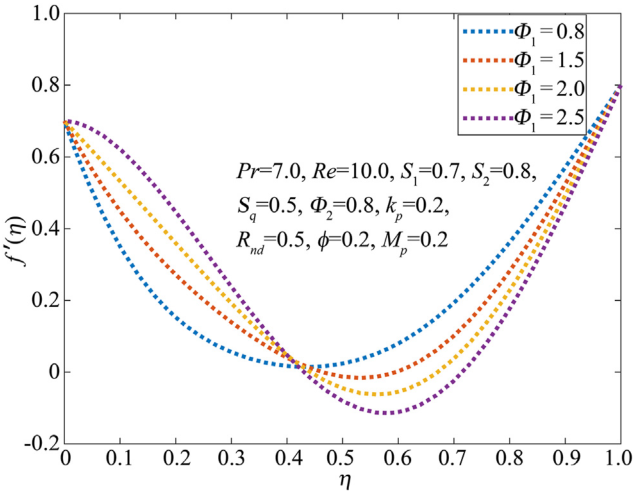

Figure 8 Implication of Φ_1 on $f'(\eta)$.

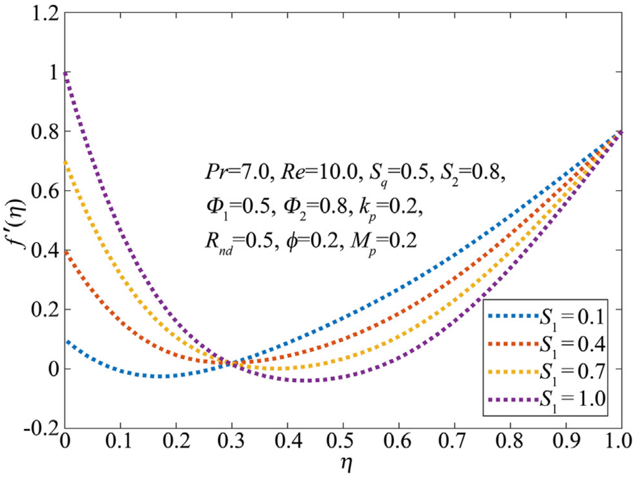

Figure 6 Implication of S_1 on $f'(\eta)$.

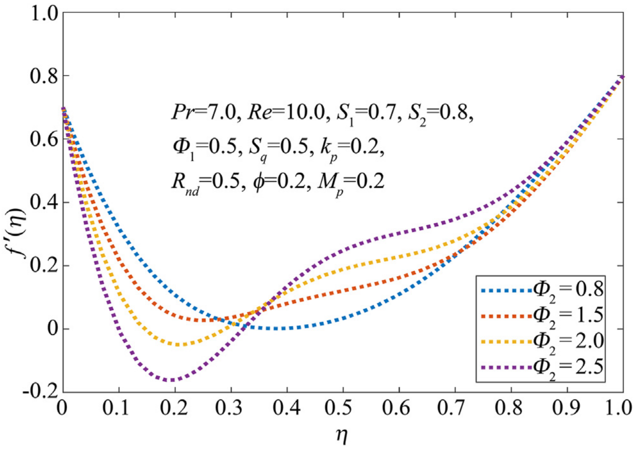

Figure 9 Implication of Φ_2 on $f'(\eta)$.

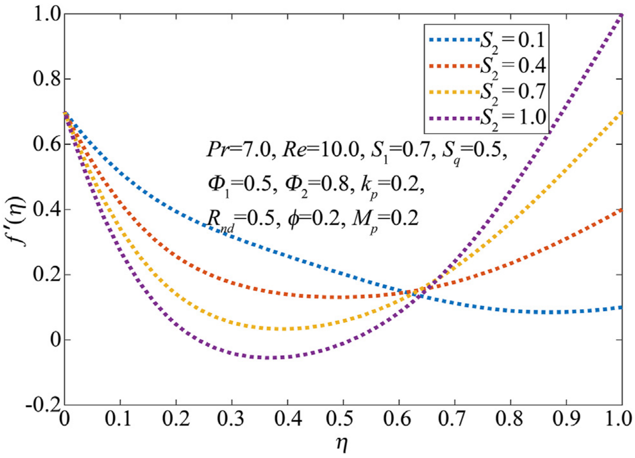

Figure 7 Implication of S_2 on $f'(\eta)$.

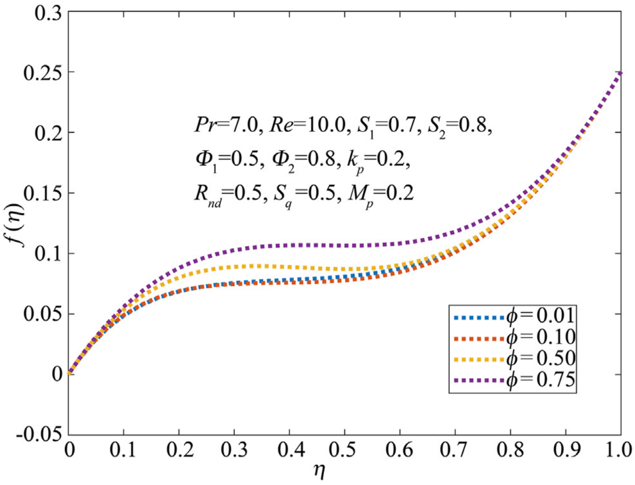

Figure 10 Implication of ϕ on $f(\eta)$.

For both cases of the squeezing parameter, S_q from Figures 11 and 12, the axial velocity profile increases as S_q increases, this is because the gaps between the disks continually fluctuates which results to increased pressure drop and hence increased axial velocity of the fluid. In Figures 13 and 15, we see overall decrease in the axial

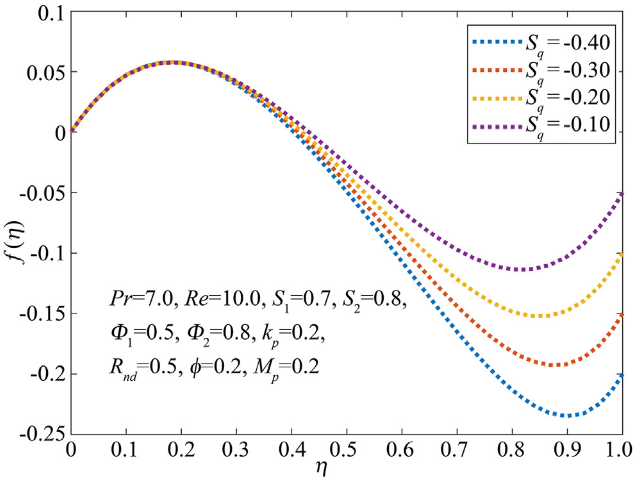

Figure 11 Implication of $S_q < 0$ on $f(\eta)$.

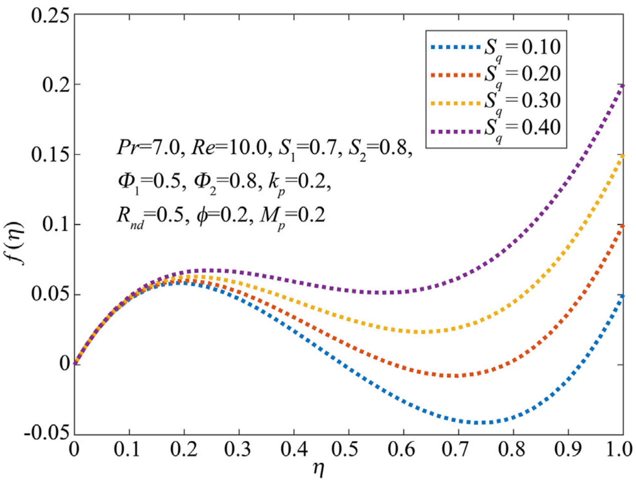

Figure 12 Implication of $S_q > 0$ on $f(\eta)$.

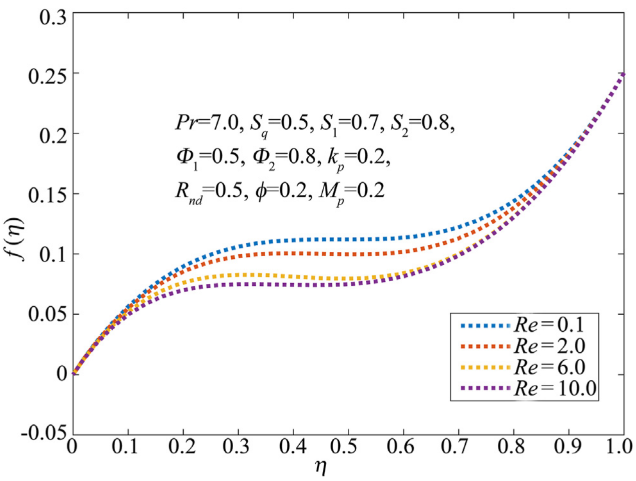

Figure 13 Implication of Re on $f(\eta)$.

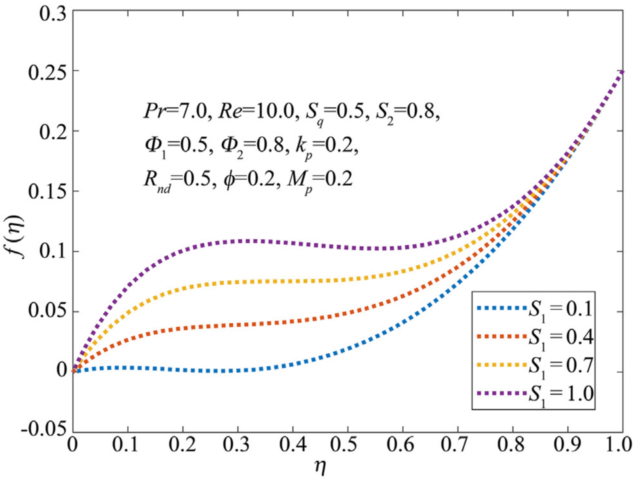

Figure 14 Implication of S_1 on $f(\eta)$.

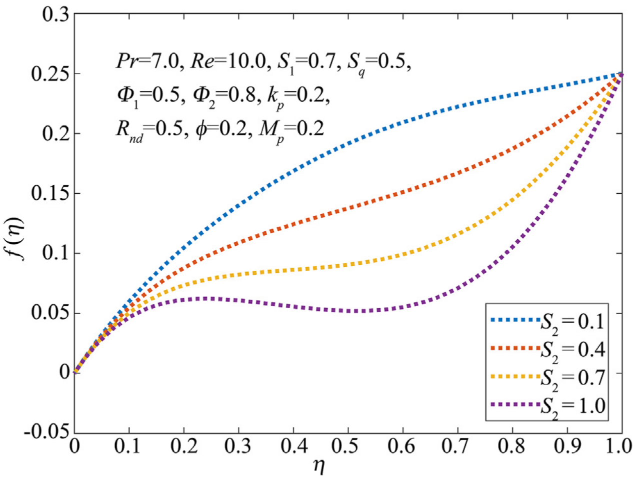

Figure 15 Implication of S_2 on $f(\eta)$.

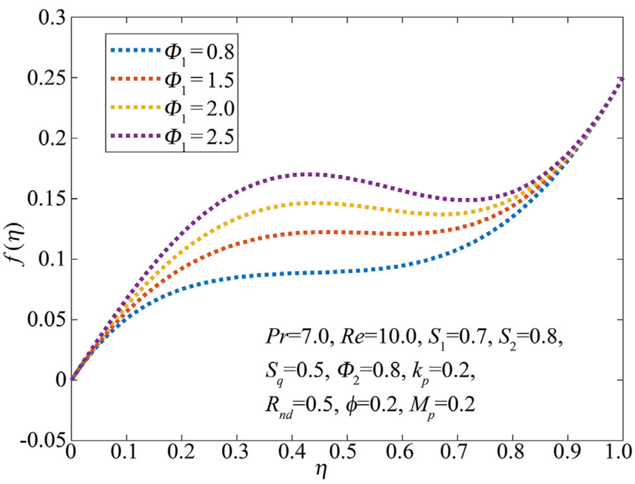

Figure 16 Implication of Φ_1 on $f(\eta)$.

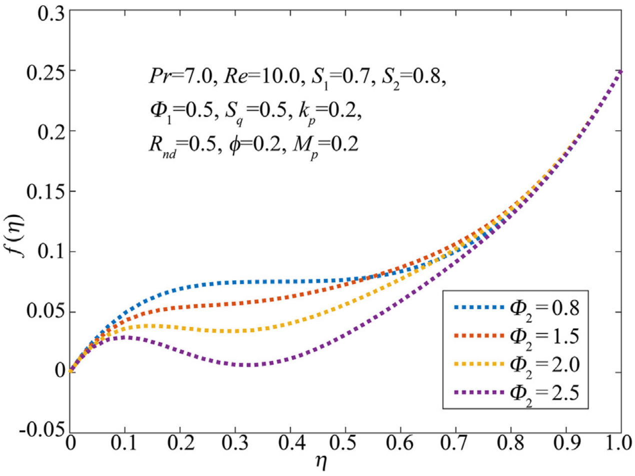

Figure 17 Implication of Φ_2 on $f(\eta)$.

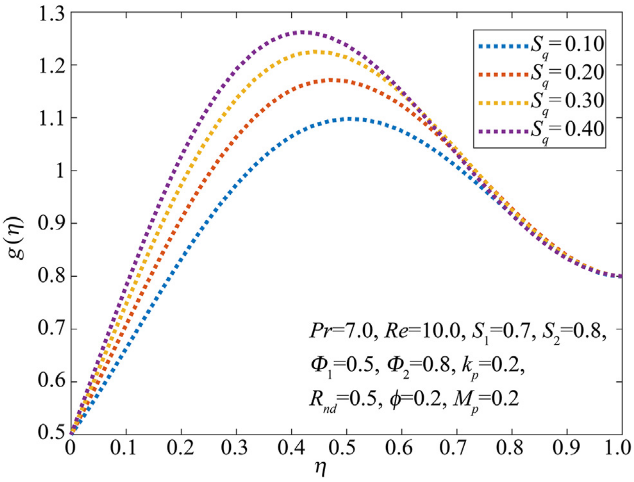

Figure 20 Implication of $S_q > 0$ on $g(\eta)$.

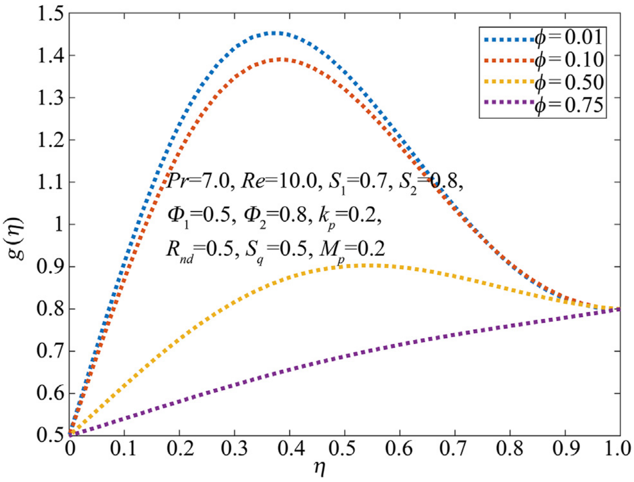

Figure 18 Implication of ϕ on $g(\eta)$.

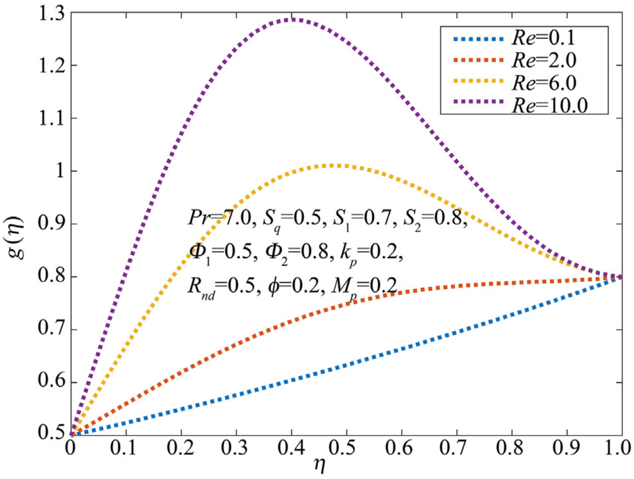

Figure 21 Implication of Re on $g(\eta)$.

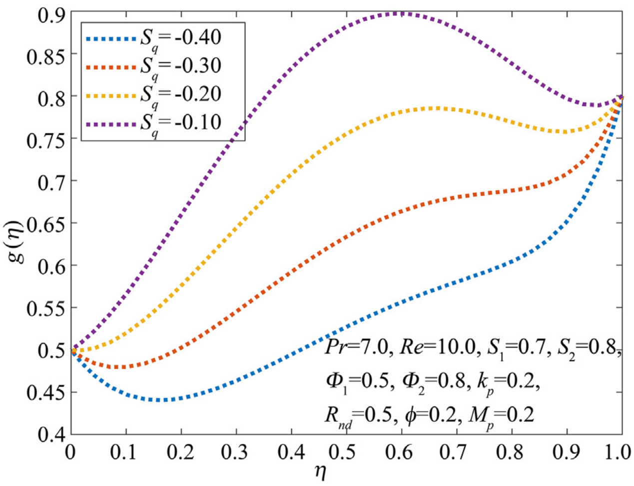

Figure 19 Implication of $S_q < 0$ on $g(\eta)$.

velocity distribution as Re and S_2 are enhanced. Figure 17 depicts how the speed of the nanofluid in axial direction depreciates around the disk at the bottom in the interval of $[0, 0.4)$ for improving values of Φ_2 and increases around the upper disk in the region of $0.4 \leq \eta \leq 1$, with the negative value of the velocity indicating relative difference in the speed of the disks, in particular it shows that the one at the top is moving faster relative to the bottom one.

5.5. Dimensionless tangential velocity distribution

Figures 21, 22, 24, and 25 present velocity distribution behaviour in response to the increasing value changes in Re, S_1, Φ_1 and Φ_2 respectively. An overall increasing trend in velocity distribution in tangential direction can be observed in these graphs. The squeeze parameter typically represents the distance between the rotating disks and their relative motion. As the squeeze, S_q parameter increases, meaning

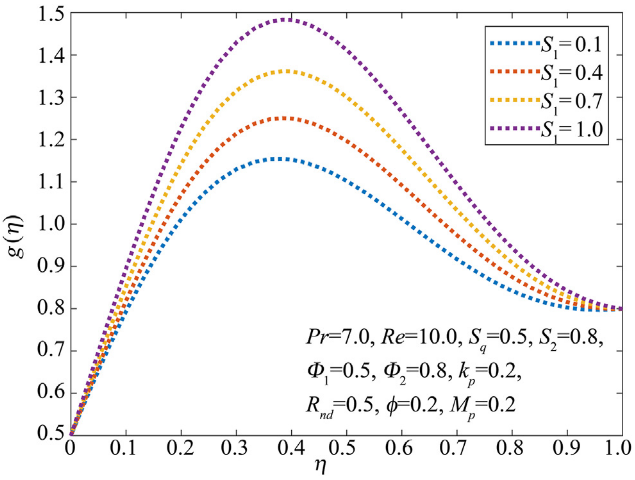

Figure 22 Implication of S_1 on $g(\eta)$.

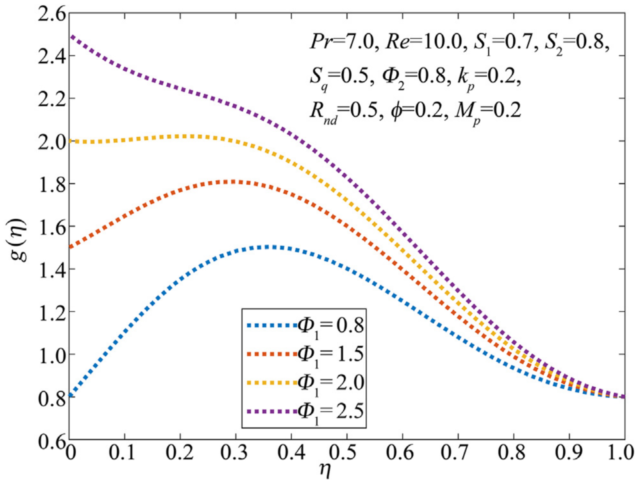

Figure 24 Implication of Φ_1 on $g(\eta)$.

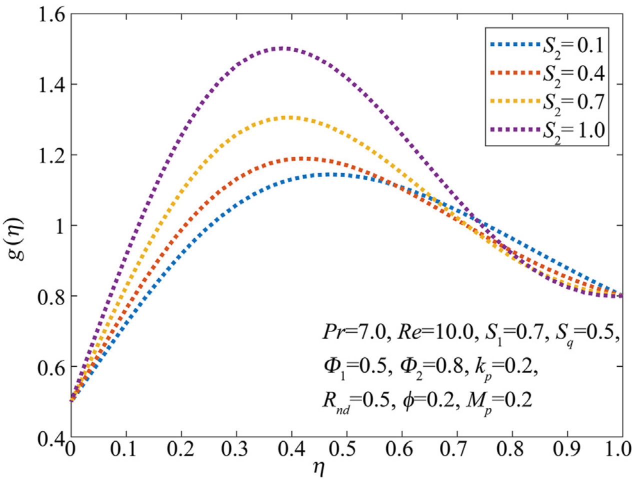

Figure 23 Implication of S_2 on $g(\eta)$.

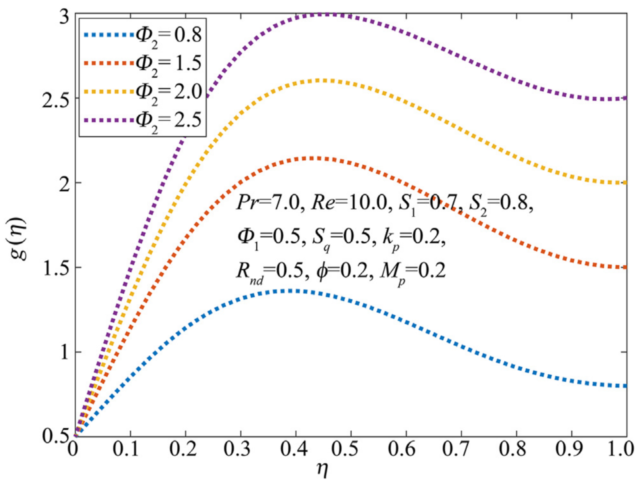

Figure 25 Implication of Φ_2 on $g(\eta)$.

that the gap between the rotating disks widens or the relative motion between the disks becomes less intense, the axial velocity is generally expected to increase. This is because a wider gap or reduced squeezing action allows for less opposition to fluid flow, enabling the fluid to flow more easily along the axial direction. This validates the observed trends in Figures 19 and 20. Figure 18 displays declining trend in the tangential velocity distribution as ϕ increases owing to the increased flow resistance as a result of higher pressure drop. Around the region $0 \leq \eta < 0.8$, Figure 20 exhibits increasing trend velocity distribution in tangential direction as S_2 appreciates and the trend reverses in the region $0.8 \leq \eta \leq 1$ as S_2 continually grows (see Figure 23).

5.6. Dimensionless temperature distribution

Enhancement in ϕ which means increasing ϕ brings about elevated temperature distribution of the fluid. This is because higher percentage of ϕ enhances thermal conductivity of the nanofluid and hence the temperature distribution is enhanced as seen in Figure 26. In Figures 27 and 28, observable declines can be seen in the distribution of the temperature as the S_q goes up showing reduction thermal profile of nanofluid, owing to the continuous squeezing by

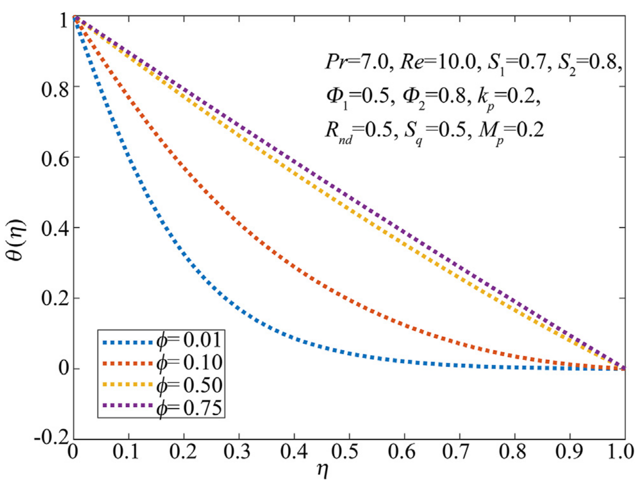

Figure 26 Implication of ϕ on $\theta(\eta)$.

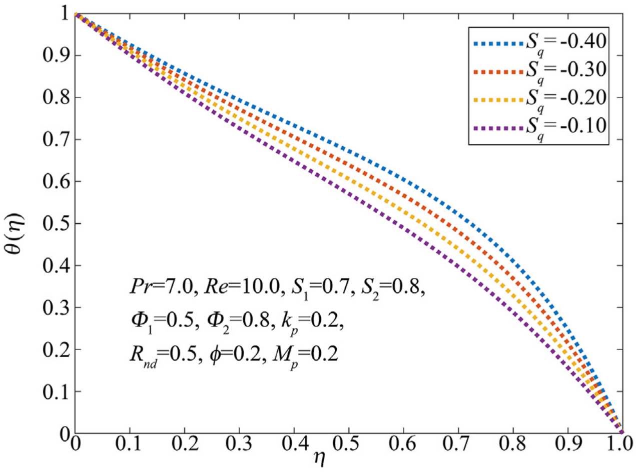

Figure 27 Implication of $S_q < 0$ on $\theta(\eta)$.

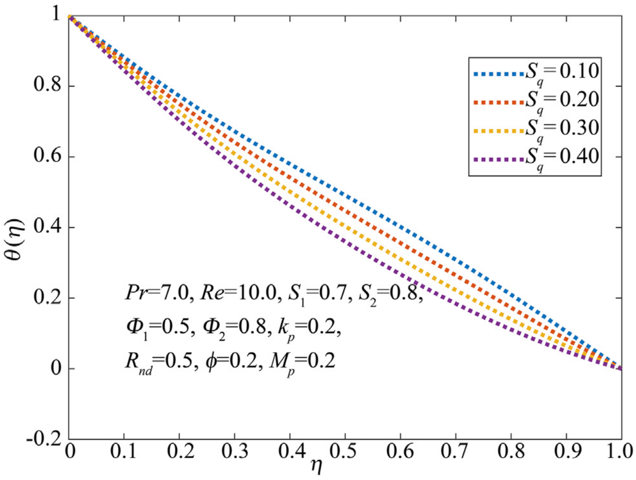

Figure 28 Implication of $S_q > 0$ on $\theta(\eta)$.

the top disk of the nanofluid. In Figure 29, we have noticed steady down fall of thermal distribution in reaction to enhancing Re, as a result of the less fluid motion and decreased convective heat transfer. Similar trends are noticeable in Figures 30 and 32 for S_1 and Φ_1. Increasing

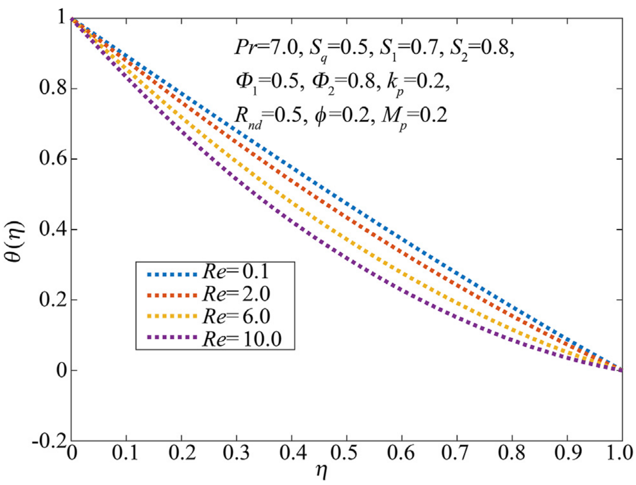

Figure 29 Implication of Re on $\theta(\eta)$.

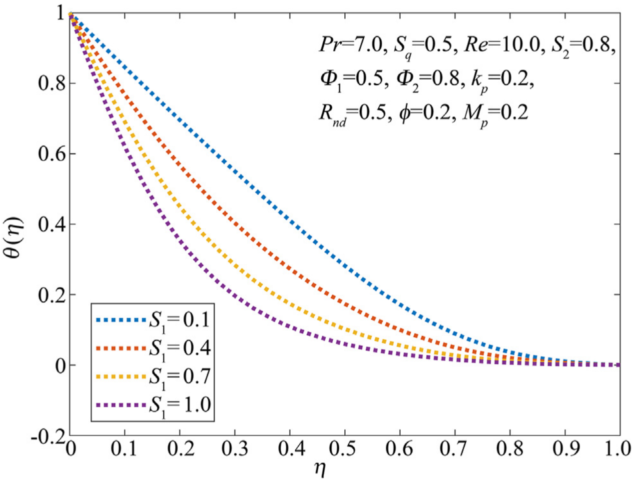

Figure 30 Implication of S_1 on $\theta(\eta)$.

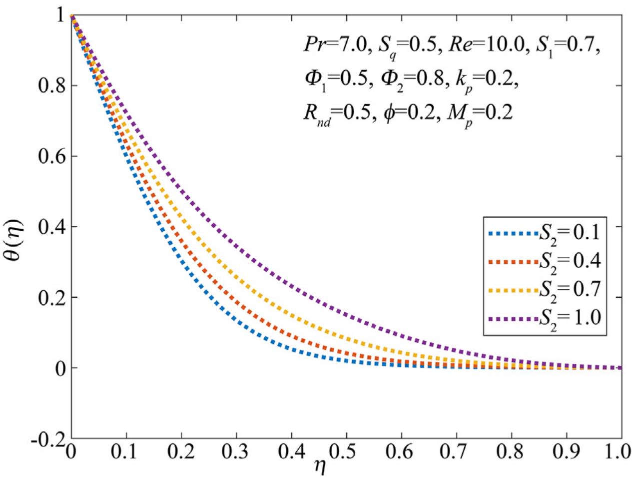

Figure 31 Implication of S_2 on $\theta(\eta)$.

R_{nd} influences reduction in the absorption coefficient which in turns elevates the radiative heat transfer rate, hence, we see observable increasing temperature profile trend of Figure 34. Similar trends are seen in Figures 31 and 33 for increasing S_2 and Φ_2.

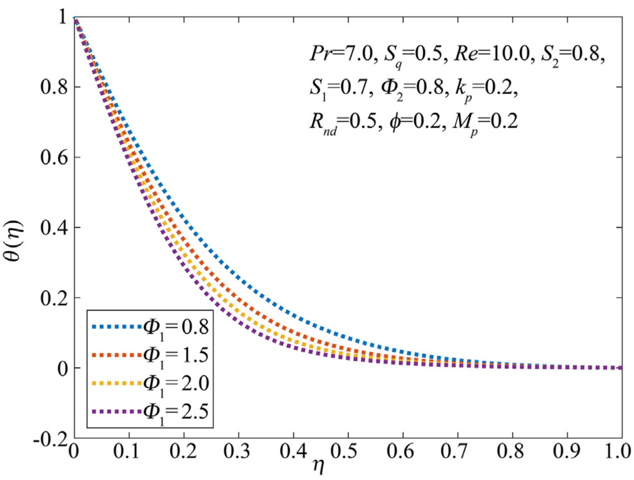

Figure 32 Implication of Φ_1 on $\theta(\eta)$.

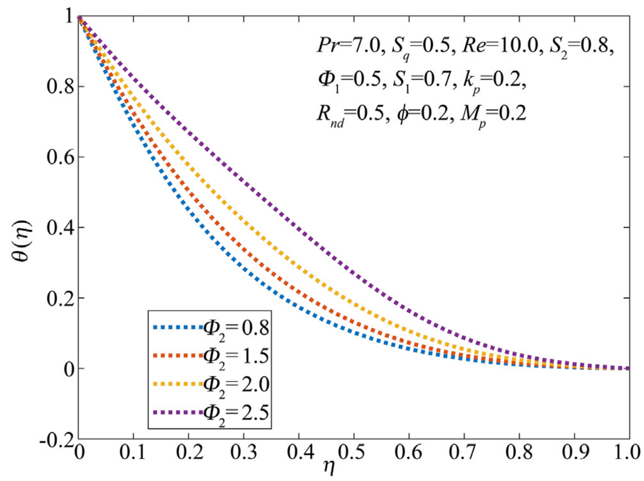

Figure 33 Implication of Φ_2 on $\theta(\eta)$.

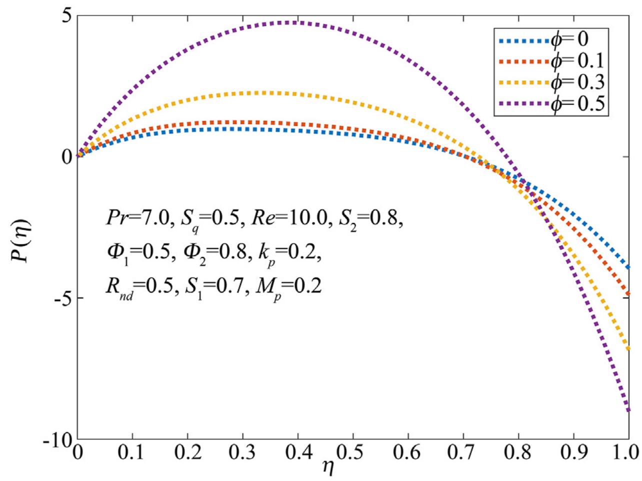

Figure 35 Implication of ϕ on $P(\eta)$.

5.7. Dimensionless pressure distribution

In Figure 35, we see how higher values of ϕ, which means elevating the nanoparticle volume percentage influences the pressure distribution at the two halves of the flow structure. The pressure distribution increases significantly at the lower half of the flow system as ϕ increases with respect to the larger presence of the nanofluid molecules in that vicinity of the flow compare to the top area of the flow structure where the pressure decreases rapidly. Similar trends are observed in Figure 36 with the reduction in the upper region more significant as a result of the relationship between Reynold number and the radial velocity of the fluid. Figure 38 displays the case when upper disk is controlling upwards ($S_q > 0$), the pressure distribution reduces steadily across the regions of the fluid structure because the widening gap between the disks and intensified relative motion reduce the resistance to fluid flow. We see in Figure 37 the fluid pressure in the lower region rises as the upper disk squeezes downwards, with reverse patterns in the upper region of the flow. The negative values in the pressure distribution describes the situation where the continuous rotating, stretching and squeezing of the disks creates in which the fluid pressure is relative to the atmospheric pressure is less, which has major engineering and medical applications.

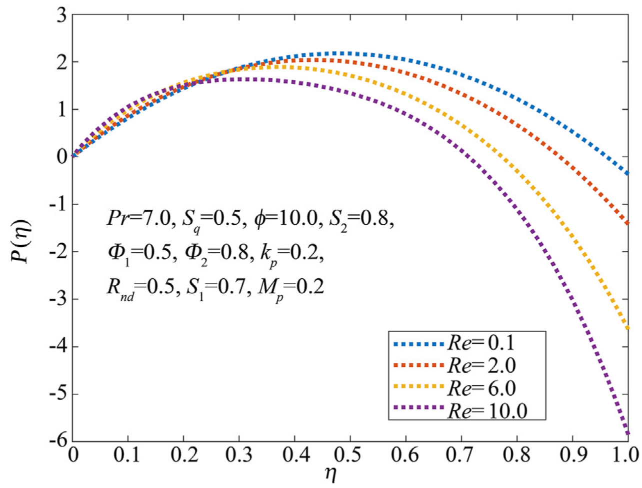

Figure 36 Implication of Re on $P(\eta)$.

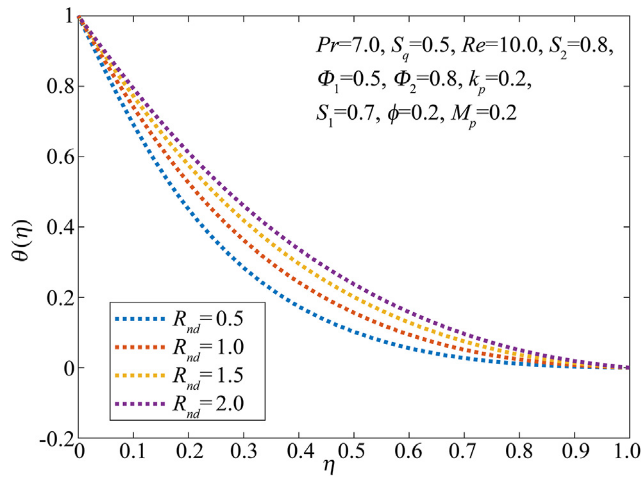

Figure 34 Implication of R_{nd} on $\theta(\eta)$.

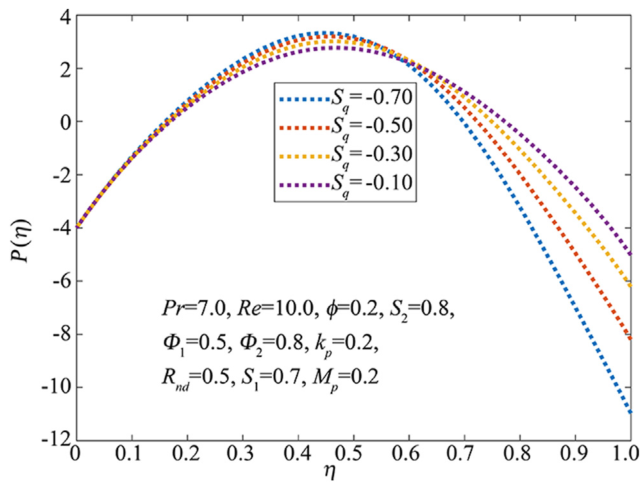

Figure 37 Implication of $S_q < 0$ on $P(\eta)$.

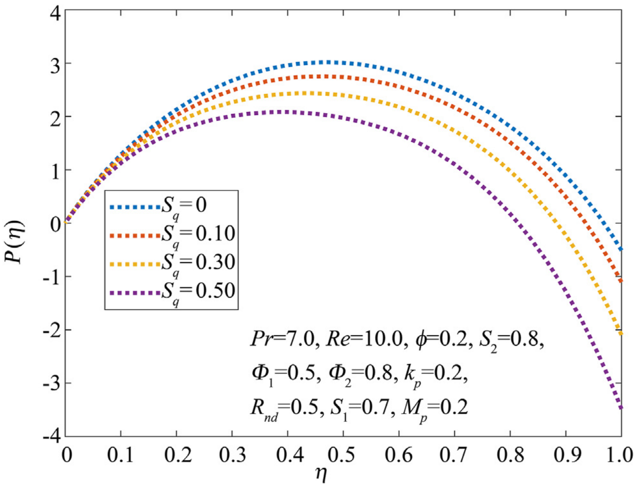

Figure 38 Implication of $S_q > 0$ on $P(\eta)$.

6. Conclusion

An unsteady compressing flow of SiO_2/kerosene oil nanofluid between stretchable spinning disks was reported in this study, with the disk at the top continually oscillating at a periodic velocity. The modeled PDEs that describe the flow are adjusted in such a way that system of ODEs is generated using appropriate similarity transformations, and then numerical solutions are obtained using the spectral quasilinearization method on overlapping grids through MATLAB codes.

The pressure, temperature and velocity distributions are analyzed and discussed graphically. The skin drag coefficient and heat transfer rate are tabulated and examined in detail. Based on the findings, we have reached the following concluding remarks:

1) The flow structure gives rise to a situation of negative pressure which has vast applications in engineering and medical sciences.
2) The fluid pressure improves in the lower region of the flow system and decreases in the upper region as ϕ and Re become greater. This is also the case when the upper disk squeezes downwards for $S_q < 0$.
3) The fluid pressure decreases steadily across regions when the top disk is moving upwards ($S_q > 0$).
4) The fluid temperature drops as the upper disk undergoes it vertical oscillatory motion. This is also the case for increasing values of Re, S_1 and Φ_1.
5) Improving ϕ, R_{nd}, S_2 and Φ_2 improves the fluid temperature distributions.
6) The nanofluid speed in the tangetial direction increases as S_q, Re, S_1, Φ_1 and Φ_2 are enhanced while it decreases with improving ϕ.
7) The tangential velocity changes it behaviour in different intervals of graphs as S_2. In the region $0 \leq \eta < 0.8$, it is increasing and then decreasing in the region of $0.8 \leq \eta \leq 1$.
8) The axial velocity of the nanofluid increases as ϕ, S_q, S_1 and Φ_1 increases, while it decreases for increasing Re and S_2.
9) Axial velocity distribution falls close to the surface of the disk at the bottom and increases in the domain of the disk at the top as Φ_2 grows.
10) Radially the nanofluid speeds up around the bottom disk and slows down around the top disk as ϕ, S_1 and Φ_1 go up. Reverse trends happen near the two disks as Re, S_2 and Φ_2 grow. The radial velocity distribution goes up in response to enhancements in S_q.
11) The drag force at each of the two disks goes down generally but more significantly at the lower disk for increasing values of ϕ, S_1, S_2, Φ_1 and Φ_2. A dynamic variation exist for S_q.
12) Thermal transfer rate moves up significantly as ϕ and R_{nd} enhances at the bottom disk compare to the top disk. Reverse behaviour occurs for the case of S_q.
13) The configuration used in this research work can be applied for fluid pumping in lab-on-a-chip devices, energy harvesting as the oscillating motion energy of the upper disk can be harnessed, cooling systems for spacecraft or aircraft components, enhancement of the cooling system of electronic components and so much more.

References

[1] H. Masuda, A. Ebata, K. Teramae, N. Hishinuma, Alteration of thermal conductivity and viscosity of liquid by dispersing ultra-fine particles, Netsu Bussei 7 (4) (1993) 227–233.
[2] S. Choi, J.A. Eastman, Enhancing thermal conductivity of fluids with nanoparticles, Asme Fed 231 (1) (1995) 99–105.
[3] J.A. Eastman, S. Choi, S. Li, W. Yu, L.J. Thompson, Anomalously increased effective thermal conductivities of ethylene glycol-based nanofluids containing copper nanoparticles, Appl. Phys. Lett. 78 (6) (2001) 718–720.
[4] R.K. Tiwari, M.K. Das, Heat transfer augmentation in a two-sided lid-driven differentially heated square cavity utilizing nanofluids, Int. J. Heat Mass Tran. 50 (9–10) (2007) 2002–2018.
[5] C. Zhang, L. Zheng, X. Zhang, G. Chen, MHD flow and radiation heat transfer of nanofluids in porous media with variable surface heat flux and chemical reaction, Appl. Math. Model. 39 (1) (2015) 165–181.
[6] M. Sheikholeslami, R. Ellahi, Electrohydrodynamic nanofluid hydrothermal treatment in an enclosure with sinusoidal upper wall, Appl. Sci. 5 (3) (2015) 294–306.
[7] M. Turkyilmazoglu, Analytical solutions of single and multi-phase models for the condensation of nanofluid film flow and heat transfer, Eur. J. Mech. B Fluid 53 (2015) 272–277.
[8] M. Sheikholeslami, D.D. Ganji, M.Y. Javed, R. Ellahi, Effect of thermal radiation on magnetohydrodynamics nanofluid flow and heat transfer by means of two-phase model, J. Magn. Magn Mater. 374 (2015) 36–43.
[9] T. Hayat, M. Imtiaz, A. Alsaedi, MHD 3D flow of nanofluid in presence of convective conditions, J. Mol. Liq. 212 (2015) 203–208.
[10] S. Rashidi, S. Akar, M. Bovand, R. Ellahi, Volume of fluid model to simulate the nanofluid flow and entropy generation in a single slope solar still, Renew. Energy 115 (2018) 400–410.
[11] S.A. Shehzad, Z. Abdullah, A. Alsaedi, F.M. Abbasi, T. Hayat, Thermally radiative three-dimensional flow of Jeffrey nanofluid with internal heat generation and magnetic field, J. Magn. Magn Mater. 397 (2016) 108–114.

[12] T. Hayat, M. Imtiaz, A. Alsaedi, M.A. Kutbi, MHD three-dimensional flow of nanofluid with velocity slip and nonlinear thermal radiation, J. Magn. Magn Mater. 396 (2015) 31–37.
[13] S. Salman, A.R. Talib, S. Saadon, M.T.H. Sultan, Hybrid nanofluid flow and heat transfer over backward and forward steps: a review, Powder Technol. 363 (2020) 448–472.
[14] X.L. Shi, P. Jaryani, A. Amiri, A. Rahimi, E.H. Malekshah, Heat transfer and nanofluid flow of free convection in a quarter cylinder channel considering nanoparticle shape effect, Powder Technol. 346 (2019) 160–170.
[15] M. Sheikholeslami, S. Abelman, Two-phase simulation of nanofluid flow and heat transfer in an annulus in the presence of an axial magnetic field, IEEE Trans. Nanotechnol. 14 (3) (2015) 561–569.
[16] M.H. Bahmani, G. Sheikhzadeh, M. Zarringhalam, O.A. Akbari, A.A. Alrashed, G.A.S. Shabani, M. Goodarzi, Investigation of turbulent heat transfer and nanofluid flow in a double pipe heat exchanger, Adv. Powder Technol. 29 (2) (2018) 273–282.
[17] A. Kasaeian, R. Daneshazarian, O. Mahian, L. Kolsi, A.J. Chamkha, S. Wongwises, I. Pop, Nanofluid flow and heat transfer in porous media: a review of the latest developments, Int. J. Heat Mass Tran. 107 (2017) 778–791.
[18] X.M. Wang, Y.X. Song, C.H. Li, Y.B. Zhang, H.M. Ali, S. Sharma, R.Z. Li, M. Yang, T. Gao, M.Z. Liu, X. Cui, Z. Said, Z.M. Zhou, Nanofluids application in machining: a comprehensive review. The International Journal of Advanced Manufacturing Technology (2023) https://doi.org/10.1007/s00170-022-10767-2.
[19] H. Younes, M. Mao, S.S. Murshed, D. Lou, H. Hong, G. P Peterson, Nanofluids: key parameters to enhance thermal conductivity and its applications, Appl. Therm. Eng. 207 (2022) 118202.
[20] T. Von Karman, Uber laminare und turbulente reibung, Zamm-Journal of Applied Mathematics and Mechanics/Zeitschrift fur Angewandte Mathematik und Mechanik 1 (4) (1921) 233–252.
[21] W.G. Cochran, The flow due to a rotating disc, Mathematical Proceedings of the Cambridge Philosophical Society, Cambridge University Press 30 (3) (1934) 365–375.
[22] K. Millsaps, K. Pohlhausen, Heat transfer by laminar flow from a rotating plate, J. Aeronaut. Sci. 19 (2) (1952) 120–126.
[23] S.S. Zhou, M. Bilal, M.A. Khan, T. Muhammad, Numerical analysis of thermal radiative maxwell nanofluid flow over-stretching porous rotating disk, Micromachines 12 (5) (2021) 540.
[24] N. Acharya, R. Bag, P.K. Kundu, Influence of hall current on radiative nanofluid flow over a spinning disk: a hybrid approach, Phys. E Lowdimens. Syst. Nanostruct. 111 (2019) 103–112.
[25] S. Saranya, Q.M. Al-Mdallal, Computational study on nanoparticle shape effects of Al_2O_3-silicon oil nanofluid flow over a radially stretching rotating disk, Case Stud. Therm. Eng. 25 (2021) 100943.
[26] A. Tassaddiq, S. Khan, M. Bilal, T. Gul, S. Mukhtar, Z. Shah, E. Bonyah, Heat and mass transfer together with hybrid nanofluid flow over a rotating disk, AIP Adv. 10 (5) (2020) 055317.
[27] M. Mustafa, MHD nanofluid flow over a rotating disk with partial slip effects: buongiorno model, Int. J. Heat Mass Tran. 108 (2017) 1910–1916.
[28] C. Yin, L. Zheng, C. Zhang, X. Zhang, Flow and heat transfer of nanofluids over a rotating disk with uniform stretching rate in the radial direction, Propuls. Power Res. 6 (1) (2017) 25–30.
[29] H. Waqas, R. Naseem, T. Muhammad, U. Farooq, Bioconvection flow of casson nanofluid by rotating disk with motile microorganisms, J. Mater. Res. Technol. 13 (2) (2021) 2392–2407.
[30] A. Tulu, W. Ibrahim, MHD slip flow of cntethylene glycol nanofluid due to a stretchable rotating disk with Cattaneo-Christov heat flux model, Math. Probl Eng. 2020 (2020) 1–13.
[31] M. Bilal, A. Saeed, T. Gul, I. Ali, W. Kumam, P. Kumam, Numerical approximation of microorganisms hybrid nanofluid flow induced by a wavy fluctuating spinning disc, Coatings 11 (9) (2021) 1–12.
[32] M.D. Shamshuddin, S.R. Mishra, O.A. Beg, A. Kadir, Numerical study of heat transfer and viscous flow in a dual rotating extendable disk system with a non-fourier heat flux model, Heat Tran. Asian Res. 48 (1) (2019) 435–459.
[33] J. Ahmed, M. Khan, L. Ahmad, MHD swirling flow and heat transfer in maxwell fluid driven by two coaxially rotating disks with variable thermal conductivity, Chin. J. Phys. 60 (2019) 22–34.
[34] S. Mosayebidorcheh, M. Hatami, Heat transfer analysis in carbon nanotube-water between rotating disks under thermal radiation conditions, J. Mol. Liq. 240 (2017) 258–267.
[35] D.C. Lu, Z.X. Li, M. Ramzan, A. Shafee, J.D. Chung, Unsteady squeezing carbon nanotubes-based nano-liquid flow with Cattaneo-Christov heat flux and homogeneous-heterogeneous reactions, Appl. Nanosci. 9 (2019) 169–178.
[36] M. Ramzan, S. Riasat, S. Kadry, P. Kuntha, Y.Y. Nam, F. Howari, Numerical analysis of carbon nanotube-based nanofluid unsteady flow amid two rotating disks with hall current coatings and homogeneous-heterogeneous reactions, Coatings 10 (1) (2020) 48–68.
[37] T. Hayat, S. Qayyum, M. Imtiaz, F. Alzahrani, A. Alsaedi, Partial slip effect in flow of magnetite-Fe_3O_4 nanoparticles between rotating stretchable disks, J. Magn. Magn Mater. 413 (2016) 39–48.
[38] M. Yaseen, S.K. Rawat, M. Kumar, Cattaneo-Christov heat flux model in Darcy-forchheimer radiative flow of MoS_2-SiO_2/kerosene oil between two parallel rotating disks, J. Therm. Anal. Calorim. 147 (19) (2022) 10865–10887.
[39] K.A.M. Alharbi, M. Rehman, M. Ramzan, N. Shahmir, S. Kadry, Insight into hall current impact in the hybrid squeezing nanofluid flow amid two rotating disks in a thermally stratified medium, Numer. Heat Tran., Part A: Applications (2023) 1–17.
[40] S. Bilal, I.A. Shah, M. Ramzan, K.S. Nisar, A. Elfasakhany, E. M Eed, H.A.S. Ghazwani, Significance of induced hybridized metallic and non-metallic nanoparticles in single-phase nano liquid flow between permeable disks by analyzing shape factor, Sci. Rep. 12 (1) (2022) 3342.
[41] Y. Zhang, N. Shahmir, M. Ramzan, H. Alotaibi, H.M. Aljohani, Upshot of melting heat transfer in a von karman rotating flow of gold-silver/engine oil hybrid nanofluid with cattaneochristov heat flux, Case Stud. Therm. Eng. 26 (2021) 101149.
[42] L.L. Chen, M. Tahir, S. Yasmin, T. Muhammad, M. Imran, F.H. Liu, Flow and melting thermal transfer enhancement analysis of alumina, titanium oxide-based maxwell nanofluid flow inside double rotating disks with finite element simulation, CMES Comput. Model. Eng. Sci 130 (3) (2022) 1771–1788.
[43] A. Rauf, M. Irfan, M. Omar, T. Mushtaq, S.A. Shehzad, M. N Bashir, Numerical study of micropolar nanofluid flow between two parallel permeable disks with thermophysical property and Arrhenius activation energy, Int. Commun. Heat Mass Tran. 137 (2022) 106272.
[44] S.K. Rawat, M. Yaseen, U. Khan, M. Kumar, S. M Eldin, A.M. Alotaibi, A.M. Galal, Significance of non-uniform heat source/sink and Cattaneo-Christov model on hybrid nanofluid flow in a Darcy-Forchheimer porous medium between two parallel rotating disks, Frontiers in Materials 9 (2023) 1097057.
[45] T. Hayat, S. Qayyum, M. Imtiaz, A. Alsaedi, Flow between two stretchable rotating disks with Cattaneo-Christov heat flux model, Results Phys. 7 (2017) 126–133.
[46] T. Gul, M. Usman, I. Khan, S. Nasir, A. Saeed, A. Khan, M. Ishaq, Magneto hydrodynamic and dissipated nanofluid flow over an unsteady turning disk, Adv. Mech. Eng. 13 (7) (2021) 1–11.
[47] M. Tausif, K. Das, P.K. Kundu, Unsteady nanofluid flow between two spinning expanding disks with continuous vertical motion under the influence of modified hall effect, Heat Transfer 51 (5) (2022) 4286–4305.
[48] M. Imtiaz, T. Hayat, A. Alsaedi, B. Ahmad, Convective flow of carbon nanotubes between rotating stretchable disks with thermal radiation effects, Int. J. Heat Mass Tran. 101 (2016) 948–957.

Chapter 5

Analysis of unsteady ternary hybrid nanofluid flow with magnetic dipole over an oscillatory stretching surface

The last three chapters show that the traditional SQLM and overlapping SQLM effectively deal with ODEs. The focus in this chapter shifts to the application of overlapping bivariate simple iteration method in the analysis of ternary hybrid nanofluid comprising blade-shaped SiO_2, cylinder-shaped MoS_2, and platelet-shaped copper nanoparticles dispersed in engine oil and water base fluids. The nanofluid's behaviour is analyzed within the influence of a magnetic dipole region over an oscillatory stretching surface to understand its potential applications in heat transfer and fluid dynamics. The chapter examines the effects of physical parameters on surface characteristics, including local skin drag, Nusselt number, and Sherwood number. The results are presented in tables and discussed in detail to elucidate the interplay between various parameters, such as nanoparticle shapes, magnetic dipole strength, and oscillation effects, on the nanofluid characteristics. Key insights from the analysis include how the magnetic dipole field influences the distribution and movement of nanoparticles within the nanofluid and how this, in turn, impacts heat transfer and fluid flow characteristics. The findings hold implications for various applications, including thermal management systems and advanced heat exchangers, by providing a deeper understanding of ternary hybrid nanofluid behaviour under complex conditions.

Analysis Of Unsteady Ternary Hybrid Nanofluid Flow With Magnetic Dipole Over An Oscillatory Stretching Surface Using the Bivariate Simple Iteration Method On Overlapping Grids

Folarin Oluwaseun [a], Sicelo Goqo [a], Hiranmoy Mondal [b]*, Sibonelo Nzama [a]

[a] *School of Mathematics, Statistics and Computer Science, University of KwaZulu-Natal, Private Bag X01, Scottsvile, Pietermaritzburg-3209, South Africa*

[b] *Department of Applied Mathematics, Maulana Abul Kalam Azad University of Technology, West Bengal, Kolkata-700064, India*

Abstract

Ternary hybrid nanofluids, consisting of nanoparticles of distinct shapes in relations to different base fluids have emerged as promising candidates for applications in heat transfer and fluid dynamics. In this study, we investigated the behavior of a ternary hybrid nanofluid consisting of blade-shaped SiO_2, cylinder-shaped MoS_2, platelet-shaped copper nanoparticles with engine oil and water as base fluids, within the influence of a magnetic dipole region over an oscillatory stretching surface. The transformed governing equations with the suitable boundary conditions are solved using the numerical technique of bivariate simple iteration on overlapping grids which offers robust numerical framework for the simulation and analysis. The effects of physical parameters on the flow surface characteristics are examined in form of the local skin drag, Nusselt number and Sherwood number, with the results presented in tables and discussed in detail. The current study is focused on exploring the insights into the interplay between various parameters, including nanoparticle shapes, strength of the magnetic dipole, and oscillation effects, on the nanofluid characteristics. Through this analysis, we seek to elucidate how the magnetic dipole field influences the distribution and movement of nanoparticles within the nanofluid, and how this, in turn, impacts heat transfer and fluid flow characteristics. Our findings may have implications for various applications, including thermal management systems and advanced heat exchangers.

Keywords: Ternary hybrid nanofluid, SiO_2, MoS_2, Cu, Engine oil, Water, Bivariate simple iteration method, magnetic dipole, Oscillatory stretching, nanopaticle shapes.

1. Introduction

The ultimate need for the enhancement of thermal conductivities of liquids has resulted in certain types of liquid called nanofluids. A typical nanofluid is formed by introducing microscopic amount of nanoparticles such as metallic alloys, non-metallic alloys or polymers into a based liquid like oils, water, ethylene glycol and so on. Main purpose of this deliberate alteration is to obtain a liquid that is significantly enhanced in its thermal conductivity ability and hence aiding heat transfer rate. Continuous rigorous numerical and experimental exploration of nanofluids has led to new types of liquid that are mostly used contemporarily owing to advancements in nanotechnology. The new liquids are hybrid nanofluids which possess better thermal conductivities and heat transfer rates in comparison to ordinary nanofluids and based fluids. Hybrid nanofluids are formed using two different microscopic nanoparticles with a based fluid. For further enhancements of hybrid nanofluids, additional microscopic nanoparticles can be added to form ternary hybrid nanofluids which are widely employed in modern biomedical, engineering and automotive industries especially in construction and operations of heat exchanger, ventilation system, cooling of nuclear system, cooling generator, electronic cooling, solar energy devices. These applications have inspired researchers into ongoing rigorous numerical and experimental investigations on trihybrid nanofluids properties in relation to different prescribing environments and

*Corresponding author.
Email address : hiranmoymondal@yahoo.co.in (H. Mondal)

Preprint submitted to Elsevier *January 3, 2024*

geometric orientations[15, 9, 11, 5, 23].
Gharami et al. [13] highlighted the numerical experimentation of tangent hyperbolic MHD of time-dependent trihybrid nanofluid flow with Duffour and Soret effects taken into account with a major result presented in the concentration of the trihybrid nanofluid. [35] demonstrated influences of loop aspect ratio and input power on mass transfer rate and entropy generation for a trihybrid nanofluid in both time - dependent and independent states. Safiei et al. [33] examined how the presence of trihybrid fluid of $SiO_2 - Al_2O_3 - ZrO_2$ in cutting zones of machines helps with surface finishing and temperature at cutting surfaces. They observed that minimum quantity lubrication and excellent trihybrid nanofluids can significantly up to about 76% upgrade surface roughness and lower cutting temperature. Kumar and Sahoo [24] presented the study of heat exchanger using trihybrid nanofluid with consideration of different geometrics for numerous methods. Arif et al. [6] showed that heat transfer rate becomes better even up to about 33.67% by using $Al_2O_3 - CNT - Graphene$ water based trihybrid nanofluid presenting interesting results with major applications in engineering. Ramzan et al. [30] examined three dimensional MHD flow of ternary nanofluid using Forchheimer model with Hall current and ion - slip, focusing on chemical reaction and entropy generation analyses. [4] analyzed computationally Darcy ternary nanofluid flow across a stretching cylinder taking into consideration magnetic induction.
Recently, researchers have shown interest in influence of magnetic dipole around trihybrid nanofluid flow which have led to many fascinating observations and results. Magnetic dipole basically measures magnetic strength and orientation in addition to all other magnetic generating forces [40, 37]. Vafai [42] described the combined effects of magnetic dipole, duffour, soret and radiation on Powell - Eyring fluid over a stretching sheet. Alfannakh [3] demonstrated effects of thermophoretic dust particle diffusion and magnetic dipole of fluid flow in the vicinity of stretchable sheet. Hayat et al. [18] presented contribution of magnetic dipole on radiative flow of ferromagnetic Williamson fluid. [16] examined how magnetic dipole impacts hybrid nanofluid flow over a spreading surface. Sajjad et al. [36] articulated numerical simulations of magnetic dipole over a nonlinear radiative Eyring - Powell nanofluid with viscous and ohmic dissipation effects. More researchers have explored the overall idea of magnetic dipole [8, 10, 20, 27].
Nanoparticle exact shape is a significant factor in heat transfer characteristics of nanofluids. Enhancing heat transfer rate of nanofluids can be achieved with more attention to the shape of the nanoparticle used. This realization is fast gaining ground and hence more results are being reported to further shed light on the area. Kandasmy et al. [22] described how nanoparticle shape affects squeezing MHD flow of Cu, Al_2O_3 and SWCNTs water based nanofluid over a porous sensor surface. Rashid et al.[31] demonstrated specifically effects of gold nanoparticle shape on squeezing fluid flow and heat transfer. [12] investigated 3D MHD flow and heat transfer of $Cu/C_2H_6O_2$ hybrid nanofluid in the vicinity of a porous vertical stretching sheet with emphasis on variable thermal conductivity, suction/injection process, solar radiation and nanoparticle shape factor. Using Runge - Kutta Fehlberg method, [25] analyzed impact of magnetic dipole on Maxwell nanofluid flow with single wall and multiple walls carbon nanotubes. More outstanding experimental and numerical results have been presented in the quest [19, 17, 44, 2, 7, 38].

2. Physical Simulation Of The Problem

Heat transition is examined here using time - dependent two - dimensional trihybrid nanofluid flowing over an oscillating stretching surface placed horizontally within positive y - axis $(y > 0)$ of a semi - finite porous region of influence of a magnetic dipole that is assumed to be centered and horizontally situated. Ternary hybrid nanofluids using engine oil and water as based fluids with molybdennum-disulfide (MoS_2), silicon-dioxide (SiO_2) and copper (Cu) as the nanoparticles are analyzed. Tables 1 and 2 elaborate the mathematical expressions and values of the thermophysical characteristics respectively. We operate on premise that the oscillating stretching surface does so with a periodic velocity; $u_w = \tilde{b}x \sin \tilde{\omega}t$, given $\tilde{b}$ and $\tilde{\omega}$ are stretching rate and oscillating frequency of the surface. Sheet is maintained at uniform temperature; $\tilde{T}_w$ and concentration; $\tilde{C}_w$, which are greater than temperature; $\tilde{T}_\infty$ and concentration; $\tilde{C}_\infty$ of the surrounding environment. Simulation is done with the components of the velocity are given by; $(\tilde{v}_1, \tilde{v}_2)$. The controlling equations based on these assumptions following [39, 24, 32] are

$$\frac{\partial \tilde{v}_1}{\partial x} + \frac{\partial \tilde{v}_2}{\partial y} = 0, \tag{1}$$

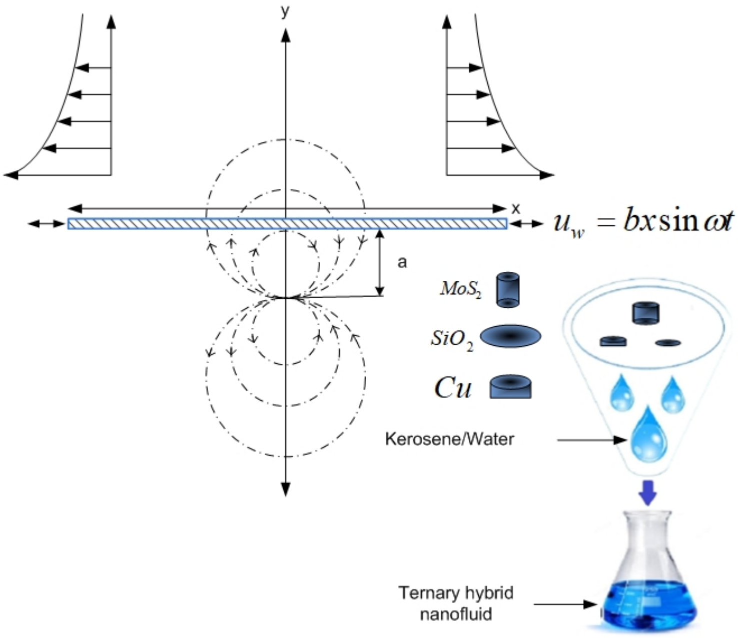

Figure 1: Flow Schematic Of The Model

$$\frac{\partial \tilde{v}_1}{\partial t} + \tilde{v}_1 \frac{\partial \tilde{v}_1}{\partial x} + \tilde{v}_2 \frac{\partial \tilde{v}_1}{\partial y} + \frac{1}{\rho_{thnf}} \frac{\partial P}{\partial x} + \left(\frac{\mu_{thnf}}{\rho_{thnf} k^+} + \frac{C_b}{\sqrt{k^+}} \tilde{v}_1 \right) \tilde{v}_1 = \frac{\mu_{thnf}}{\rho_{thnf}} \left(\frac{\partial^2 \tilde{v}_1}{\partial y^2} \right) + \frac{\mu_o}{\rho_{thnf}} M \frac{\partial H}{\partial x} + g\beta_{t^*}(\tilde{T} - \tilde{T}_\infty) + g\beta_{c^*}(\tilde{C} - \tilde{C}_\infty), \quad (2)$$

$$\frac{\partial \tilde{T}}{\partial t} + \tilde{v}_1 \frac{\partial \tilde{T}}{\partial x} + \tilde{v}_2 \frac{\partial \tilde{T}}{\partial y} = \frac{k_{thnf}}{(\rho C_p)_{thnf}} \left(\frac{\partial^2 \tilde{T}}{\partial y^2} \right) + \tau \left[D_B \frac{\partial \tilde{C}}{\partial y} \frac{\partial \tilde{T}}{\partial y} + \frac{D_T}{\tilde{T}_\infty} \left(\frac{\partial \tilde{T}}{\partial y} \right)^2 \right] + \frac{Q}{(\rho C_p)_{thnf}} (\tilde{T} - \tilde{T}_\infty) - \left(\tilde{v}_1 \frac{\partial H}{\partial x} + \tilde{v}_2 \frac{\partial H}{\partial y} \right) \frac{\mu_o \tilde{T}}{(\rho C_p)_{thnf}} \frac{\partial M}{\partial \tilde{T}}, \quad (3)$$

$$\frac{\partial \tilde{C}}{\partial t} + \tilde{v}_1 \frac{\partial \tilde{C}}{\partial x} + \tilde{v}_2 \frac{\partial \tilde{C}}{\partial y} = D_B \frac{\partial^2 \tilde{C}}{\partial y^2} + \frac{D_T}{\tilde{T}_\infty} \frac{\partial^2 \tilde{T}}{\partial y^2} - K_r(\tilde{C} - \tilde{C}_\infty) \quad (4)$$

Suitable limiting conditions are

$$\begin{aligned} &\tilde{v}_1 = u_w = \tilde{b}x \sin \tilde{\omega} t, \quad \tilde{v}_2 = \pm v_w, \quad \tilde{T} = \tilde{T}_w, \quad \tilde{C} = \tilde{C}_w, \quad at \quad y = 0, \quad t > 0, \\ &\tilde{v}_1 = 0, \quad \tilde{T} = \tilde{T}_\infty, \quad \tilde{C} = \tilde{C}_\infty, \quad as \quad y \to \infty. \end{aligned} \quad (5)$$

We observed the whole simulation in 2 - dimensional coordinates, (x, y), v_w describes suction/injection, β_{t^*} is thermal expansion coefficient, β_{c^*} is concentration expansion coefficient, C_b is drag coefficient, k^+ describes the porosity of the semi-finite space, K_r is chemical reaction coefficient, Q is coefficient of heat source/sink, D_T is thermophoretic diffusion coefficient, D_B is Brownian diffusion coefficient.
M represents the magnetization of the magnetic dipole and H denotes its intensity. The magnetic dipole is modeled with scalar potential given as:

$$\phi = \frac{x}{(y+a)^2 + x^2} \frac{a}{2\pi},$$

This allows fo the description of its intensity in x - direction and y - direction to be

$$\frac{\partial H}{\partial y} = -\frac{\partial \phi}{\partial y} = -\frac{2(y+a)x}{((y+a)^2 + x^2)^2} \frac{\gamma}{2\pi}, \quad \text{and} \quad \frac{\partial H}{\partial x} = -\frac{\partial \phi}{\partial x} = -\frac{(y+a) - x^2}{((y+a)^2 + x^2)^2} \frac{\gamma}{2\pi}.$$

Using the fact that the magnetic body force is directly proportional to the gradient of the magnitude of H which is given by:

$$H = \sqrt{\left(\frac{\partial \phi}{\partial y}\right)^2 + \left(\frac{\partial \phi}{\partial x}\right)^2}.$$

This results to

$$\frac{\partial H}{\partial y} = \left[\frac{4x^2}{(y+a)^5} - \frac{2}{(y+a)^3}\right]\frac{\gamma}{2\pi} \quad \text{and} \quad \frac{\partial H}{\partial x} = \left[-\frac{2x}{(y+a)^4}\right]\frac{\gamma}{2\pi}$$

We assume that the magnetic field intensity; H is sufficient to saturate the trihybrid nanofluid and that the magnetization; M is proportional to the fluid temperature; $\tilde{T}$ with the relationship is given by:

$$M = K_1(\tilde{T} - \tilde{T_\infty})$$

Table 1: Mathematical equations for the thermophysical characteristics of the ternary hybrid nanofluids [34, 17]

Physical characteristics	Ternary hybrid nanofluid
Density	$\rho_{thnf} = \phi_{SiO_2}\rho_1 + \phi_{MoS_2}\rho_2 + \phi_{Cu}\rho_3 + (1-\phi_{SiO_2}-\phi_{MoS_2}-\phi_{Cu})\rho_f$
Thermal capacity	$(\rho C_p)_{thnf} = \phi_{SiO_2}(\rho C_p)_1 + \phi_{MoS_2}(\rho C_p)_2 + \phi_{Cu}(\rho C_p)_3 + (1-\phi_{SiO_2}-\phi_{MoS_2}-\phi_{Cu})(\rho C_p)_f$
Dynamic viscosity	$\mu_{thnf} = \frac{(\mu_{NF1}\phi_{SiO_2}+\mu_{NF2}\phi_{MoS_2}+\mu_{NF3}\phi_{Cu})}{\phi}$
	$\mu_{NF1} = \mu_f(1+14.5\phi+123.3\phi^2)$
	$\mu_{NF2} = \mu_f(1+13.5\phi+904.4\phi^2)$
	$\mu_{NF3} = \mu_f(1+37.1\phi+612.6\phi^2)$
	$\phi = \phi_{SiO_2} + \phi_{MoS_2} + \phi_{Cu}$
Thermal conductivity	$k_{thnf} = \left(\frac{(k_{NF1}\phi_{SiO_2}+k_{NF2}\phi_{MoS_2}+k_{NF3}\phi_{Cu})}{\phi}\right)k_f$
	$k_{NF_i} = \left(\frac{(k_i+(s_p-1)k_f-(s_p-1)(k_f-k_i)\phi)}{k_i+(s_p-1)k_f-\phi(k_i-k_f)}\right)k_f$
	$s_p = \frac{3}{\psi}$ is shape factor parameter of nanoparticles
	For blade-shaped nanoparticles, $\psi = 0.36$
	For cylindrical-shaped nanoparticles, $\psi = 0.61$
	For platelet-shaped nanoparticles, $\psi = 0.52$

We invoke some self similarity transformations as used by [26, 45] to obtain the dimensionless forms of equations ($2-5$). These similarity variables are defined as

$$\begin{aligned}&\Psi(x,y,t) = \sqrt{\nu_\infty \tilde{b}}xf(\zeta,\varsigma), \quad \zeta = \sqrt{\frac{\tilde{b}}{\nu_\infty}}y, \quad \varsigma = t\omega, \quad \theta(\zeta,\varsigma) = \frac{\tilde{T}-\tilde{T_\infty}}{\tilde{T_w}-\tilde{T}_\infty}, \quad \varphi(\zeta,\varsigma) = \frac{\tilde{C}-\tilde{C}_\infty}{\tilde{C}_w-\tilde{C}_\infty},\\ &\tilde{v}_1 = \frac{\partial\Psi}{\partial y} = \tilde{b}xf'(\zeta,\varsigma), \quad \tilde{v}_2 = -\frac{\partial\Psi}{\partial x} = -\sqrt{\nu_\infty\tilde{b}}f(\zeta,\varsigma)\end{aligned} \tag{6}$$

With the implementation of these transformations, equations ($1-4$) become

$$\frac{1}{C_1^* C_2^*}f''' + ff'' - (1+F_r)f'^2 - \frac{\lambda^+}{C_1^* C_2^*}f' + M_{cp}(\theta + N\phi) - \frac{2\beta^*}{C_2^*(\zeta+\gamma^*)^4}\theta - S\frac{\partial f'}{\partial\varsigma} = 0, \tag{7}$$

$$\begin{aligned}\theta'' + \frac{C_T}{C_{T_1}}P_r f\theta' + \frac{P_r}{C_{T_1}}(N_b\theta'\phi' + N_t\theta'^2) + \frac{P_r}{C_{T_1}}G_t\theta + \frac{\beta^* E_c P_r}{C_{T_1}(\zeta+\gamma^*)^3}(\theta-\epsilon)f + \frac{\beta^* E_c P_r}{C_{T_1}}(\theta-\epsilon)\left[\frac{2f'}{(\zeta+\gamma^*)^4} + \frac{4f}{(\zeta+\gamma^*)^5}\right]\\ - \frac{SP_r C_T}{C_{T_1}}\frac{\partial\theta}{\partial\varsigma} = 0,\end{aligned} \tag{8}$$

$$\varphi'' + \frac{N_t}{N_b}\theta'' + S_c(f\varphi' - R_k\varphi) - S_c S\frac{\partial\varphi}{\partial\varsigma} = 0 \tag{9}$$

Now the corresponding nondimensional suitable limiting conditions are

$$\begin{aligned}&f'(0,\varsigma) = \sin\varsigma, \quad f(0,\varsigma) = f_w, \quad \theta(0,\varsigma) = 1, \quad \varphi(0,\varsigma) = 1,\\ &f'(\infty,\varsigma) = 0, \quad \theta(\infty,\varsigma) = 0, \quad \varphi(\infty,\varsigma) = 0.\end{aligned} \tag{10}$$

We define the dimensionless variables used above as follows $\beta^* = \frac{\mu_o k_1(T_w - T_\infty)\gamma_1\rho_f}{2\pi\mu_{2_\infty}}$ is the Ferrohydrodynamic interaction constant, $\gamma^* = \sqrt{\frac{bc^2}{\nu_\infty}}$ is the strength of the magnetic dipole, $F_r = \frac{C_b x}{\sqrt{k^+}}$ is

the local Forchheimer parameter, $M_{cp} = \frac{g\beta_{t^*}(T_w - T_\infty)x^3}{Re_x^2 \nu_\infty^2}$ is the parameter due to mixed convection, $N = \frac{\beta_{c^*}(C_c - C_\infty)}{\beta_{t^*}(T_w - T_\infty)}$ is the mass bouyancy parameter, $S_c = \frac{\nu_\infty}{D_B}$ is the Schmidt number, $E_c = \frac{x}{(rhoc_p)_f(T_w - T_\infty)}$ represents local Eckert constant, $P_r = \frac{\nu_\infty(\rho c_p)_f}{k_f}$ is the local Prandtl constant, $f_w = \frac{-v_w}{(\rho c_p)_f(T_w - T_\infty)}$ describes suction/injection number, $N_b = \frac{D_B(C_w - C_\infty)}{\nu_\infty(\rho c_p)_f}$ represents Brownian motion constant, $N_t = \frac{D_T(T_w - T_\infty)}{T_\infty \nu_\infty(\rho c_p)_f}$ is the local thermophoresis number, $R_k = \frac{k_r}{b}$ is the chemical reaction constant, $G_t = \frac{Q}{b(\rho c_p)_f}$ is the heat source or sink parameter, $\lambda^+ = \frac{\nu_f}{\rho_f k^+ b}$ is the local dimensionless constant.
The local surface skin drag (Cf_x), heat transfer rate (Nu_x) and mass transfer rate (Sh_x) are given by

$$Cf_x = \frac{\tau_w}{\rho_f u_w^2}, \qquad Nu_x = \frac{x\hat{q}_{hw}}{k_f(T_w - T_\infty)}, \qquad Sh_x = \frac{x\hat{q}_{mw}}{D_B(C_w - C_\infty)}. \tag{11}$$

where τ_w, $\hat{q}_{hw}$ and $\hat{q}_{mw}$ describe the shear stress, heat and mass fluxes respectively at the oscillating surface and they are defined as

$$\tau_w = \mu_{thnf} \frac{\partial u}{\partial y}\bigg|_{y=0}, \qquad \tilde{q}_w = -k_{thnf} \frac{\partial T}{\partial y}\bigg|_{y=0}, \qquad \tilde{q}_m = -D_B \frac{\partial C}{\partial y}\Big|_{y=0}. (12)$$

Implementing (6), the non-dimensional form of (11) is given by

$$Re_x^{\frac{1}{2}} Cf_x = \frac{1}{C_1^* C_2^*} f''(0,\varsigma), \qquad Re_x^{-\frac{1}{2}} Nu_x = K_2 \theta'(0,\varsigma), \qquad Re_x^{-\frac{1}{2}} Sh_x = -\varphi'(0,\varsigma) \tag{13}$$

where $Re_x = \frac{xu_w}{\nu_f}$ is the local Reynolds number.

Table 2: Numerical values of thermophysical characteristics of the nanomaterials and based fluids [1, 21]

Based fluids and nanoparticles	ρ	C_p	k	Shape
Water	997.1	4179	0.613	-
Engine oil	884	1910	0.144	-
SiO_2	2270	730	1.4013	8.3
MoS_2	5060	397.746	34.5	4.9
Cu	8933	385	401	5.8

3. Numerical Solution

This section elucidate the procedural implementation of the proposed solution technique of overlapping grid bivariate simple iteration method (BSIM) for the solution of the non - linear PDEs (7 – 9) subject to the associated boundary conditions (10). The method begins with the partitioning of the space and solution domains into overlapping sub - intervals [26]. The semi-finite, $I = [0, \infty)$ space domain is first replaced with a truncated finite domain $I = [0, \zeta_\infty]$ for easy implementation of the method at ∞. $I = [0, \zeta_\infty]$ and $J = [0, \varsigma_f]$ space and time domains are then partitioned into p and q overlapping sub-interval respectively that can be defined as

$$I_\varrho = [\zeta_0^\varepsilon, \zeta_{M_\zeta}^\varepsilon], \qquad \varrho = 1, 2, 3, \cdots, p$$

$$J_\varepsilon = [\varsigma_0^\varrho, \varsigma_{M_\varsigma}^\varrho], \qquad \varepsilon = 1, 2, 3, \cdots, q$$

Next, using Chebyshev-Gauss-Lobatto collocation points, we carry out the discretization of each subinterval of I_ε and J_ϱ into $M_\zeta + 1$ and $M_\varsigma + 1$ collocation points respectively with the domains having uniform lengths defined as

$$L_\zeta = \frac{\zeta_\infty}{p + (1-p)\left(\frac{1 - \cos\left(\frac{\pi}{M_\zeta}\right)}{2}\right)}$$

$$L_\varsigma = \frac{\varsigma_f}{q+(1-q)\left(\frac{1-\cos\left(\frac{\pi}{M_\varsigma}\right)}{2}\right)}$$

The bivariate simple iteration method is then used,that requires performing relaxation on a nonlinear system of equations. This is accomplished by presuming that all linear functions are unknown and that non-linear functions are combinations of known (from a previously established starting solution that fulfills the boundary conditions) and unknown functions [14]. Proceeding thus, we obtain

$$\wedge_{11}^{(\varepsilon,\varrho)} f'''^{(\varepsilon,\varrho)}_{r+1} + \wedge_{12}^{(\varepsilon,\varrho)} f''^{(\varepsilon,\varrho)}_{r+1} + \wedge_{13}^{(\varepsilon,\varrho)} f'^{(\varepsilon,\varrho)}_{r+1} = S\frac{\partial f'^{(\varepsilon,\varrho)}_{r+1}}{\partial\varsigma} + a_1^{(\varepsilon,\varrho)}, \tag{14}$$

$$\wedge_{21}^{(\varepsilon,\varrho)} \theta''^{(\varepsilon,\varrho)}_{r+1} + \wedge_{22}^{(\varepsilon,\varrho)} \theta'^{(\varepsilon,\varrho)}_{r+1} + \wedge_{23}^{(\varepsilon,\varrho)} \theta^{(\varepsilon,\varrho)}_{r+1} = \frac{SP_rC_T}{C_{T_1}}\frac{\partial \theta^{(\varepsilon,\varrho)}_{r+1}}{\partial\varsigma} + a_2^{(\varepsilon,\varrho)}, \tag{15}$$

$$\wedge_{31}^{(\varepsilon,\varrho)} \varphi''^{(\varepsilon,\varrho)}_{r+1} + \wedge_{32}^{(\varepsilon,\varrho)} \varphi'^{(\varepsilon,\varrho)}_{r+1} + \wedge_{23}^{(\varepsilon,\varrho)} \varphi^{(\varepsilon,\varrho)}_{r+1} = S_cS\frac{\partial \varphi^{(\varepsilon,\varrho)}_{r+1}}{\partial\varsigma} + a_3^{(\varepsilon,\varrho)}. \tag{16}$$

where

$$\wedge_{11}^{(\varepsilon,\varrho)} = \frac{1}{C_1^*C_2^*}, \quad \wedge_{12}^{(\varepsilon,\varrho)} = f_r^{(\varepsilon,\varrho)}, \quad \wedge_{13}^{(\varepsilon,\varrho)} = -(1+F_r)f'^{(\varepsilon,\varrho)}_r - \frac{\lambda^+}{C_1^*C_2^*}, \quad a_1^{(\varepsilon,\varrho)} = -M_{cp}(\theta_r^{(\varepsilon,\varrho)} + N\varphi_r^{(\varepsilon,\varrho)}) + \frac{2\beta^*}{C_2^*(\zeta+\gamma^*)^4}\theta_r^{(\varepsilon,\varrho)},$$

$$\wedge_{22}^{(\varepsilon,\varrho)} = \frac{C_T}{C_{T_1}}P_rf_r^{(\varepsilon,\varrho)} + \frac{P_r}{C_{T_1}}(N_b\varphi'^{(\varepsilon,\varrho)}_r + N_t\theta'^{(\varepsilon,\varrho)}_r), \qquad \wedge_{32}^{(\varepsilon,\varrho)} = S_cf_r^{(\varepsilon,\varrho)}, \quad \wedge_{33}^{(\varepsilon,\varrho)} = -S_cR_k,$$

$$\wedge_{21}^{(\varepsilon,\varrho)} = 1, \quad a_2^{(\varepsilon,\varrho)} = \frac{\beta^*E_cP_r\epsilon}{C_{T_1}(\zeta+\gamma^*)^3}f_r^{(\varepsilon,\varrho)} + \frac{\beta^*E_cP_r\epsilon}{C_{T_1}}\left[\frac{2f'^{(\varepsilon,\varrho)}_r}{(\zeta+\gamma^*)^4} + \frac{4f_r^{(\varepsilon,\varrho)}}{(\zeta+\gamma^*)^5}\right], \quad \wedge_{31}^{(\varepsilon,\varrho)} = 1,$$

$$\wedge_{23}^{(\varepsilon,\varrho)} = \frac{P_r}{C_{T_1}}G_t + \frac{\beta^*E_cP_r}{C_{T_1}(\zeta+\gamma^*)^3}f_r^{(\varepsilon,\varrho)} + \frac{\beta^*E_cP_r}{C_{T_1}}\left[\frac{2f'^{(\varepsilon,\varrho)}_r}{(\zeta+\gamma^*)^4} + \frac{4f_r^{(\varepsilon,\varrho)}}{(\zeta+\gamma^*)^5}\right], \quad a_3^{(\varepsilon,\varrho)} = \frac{N_t}{N_b}\theta''^{(\varepsilon,\varrho)}.$$

With the knowledge that spectral collocation is only applicable in [-1,1], we therefore convert spatial and time domains to the form [-1,1] using the linear transformations given by

$$\zeta_i^\varrho = \frac{L_\zeta}{2}(\hat{\zeta}_i+1), \qquad \hat{\zeta}_{i=0}^{M_\zeta} = \cos\left(\frac{\pi i}{M_\zeta}\right) \tag{17}$$

$$\varsigma_j^\epsilon = \frac{L_\varsigma}{2}(\hat{\varsigma}_j+1), \qquad \hat{\varsigma}_{i=0}^{M_\varsigma} = \cos\left(\frac{\pi j}{M_\varsigma}\right) \tag{18}$$

Working in the premise that the solution can be approximated to $f(\zeta,\varsigma)$, $\theta(\zeta,\varsigma)$, and $\varphi(\zeta,\varsigma)$ at each sub - domain, using the well established bivariate Lagrange interpolation polynomial given by

$$f(\zeta,\varsigma) \approx \sum_{k=0}^{M_\zeta}\sum_{l=0}^{M_\varsigma} f(\zeta_k,\varsigma_l)L_k(\zeta)L_l(\varsigma), \tag{19}$$

$$\theta(\zeta,\varsigma) \approx \sum_{k=0}^{M_\zeta}\sum_{l=0}^{M_\varsigma} \theta(\zeta_k,\varsigma_l)L_k(\zeta)L_l(\varsigma), \tag{20}$$

$$\varphi(\zeta,\varsigma) \approx \sum_{k=0}^{M_\zeta}\sum_{l=0}^{M_\varsigma} \varphi(\zeta_k,\varsigma_l)L_k(\zeta)L_l(\varsigma). \tag{21}$$

where functions $L_k(\zeta)$ and $L_l(\varsigma)$ are the well-known characteristic Lagrange cardinal polynomial based on the Chebyshev-Gauss-Lobatto points [41]. We employed the differential matrices for collocation that are of the form

$$\left[\frac{\partial f^{(\epsilon,\varrho)}_{r+1}}{\partial \zeta}\right|_{(\zeta=\zeta_i,\varsigma=\varsigma_j)} = \sum_{k=0}^{M_\zeta} \hat{D}^{(\varepsilon)}_{i,k} F^{(\varepsilon,\varrho)}_{r+1}(\hat{\zeta}_k,\hat{\varsigma}_j) = \boldsymbol{D}\boldsymbol{F}_{j,r+1},$$

$$\left[\frac{\partial f^{(\varepsilon,\varrho)}_{r+1}}{\partial \varsigma}\right|_{(\zeta=\zeta_i,\varsigma=\varsigma_j)} = \left(\frac{2}{\varsigma^{\varrho}_{M_\varsigma}-\varsigma^{\varrho}_0}\right)\sum_{l=0}^{M_\varsigma} \hat{d}^{(\varrho)}_{j,l} F^{(\varepsilon,\varrho)}_{r+1}(\hat{\zeta}_i,\hat{\varsigma}_l) = \sum_{l=0}^{M_\varsigma} d_{j,l}\boldsymbol{F}_{l,r+1},$$

$$\left[\frac{\partial \theta^{(\epsilon,\varrho)}_{r+1}}{\partial \zeta}\right|_{(\zeta=\zeta_i,\varsigma=\varsigma_j)} = \sum_{k=0}^{M_\zeta} \hat{D}^{(\varepsilon)}_{i,k} \Theta^{(\varepsilon,\varrho)}_{r+1}(\hat{\zeta}_k,\hat{\varsigma}_j) = \boldsymbol{D}\boldsymbol{\Theta}_{j,r+1},$$

$$\left[\frac{\partial \theta^{(\varepsilon,\varrho)}_{r+1}}{\partial \varsigma}\right|_{(\zeta=\zeta_i,\varsigma=\varsigma_j)} = \left(\frac{2}{\varsigma^{\varrho}_{M_\varsigma}-\varsigma^{\varrho}_0}\right)\sum_{l=0}^{M_\varsigma} \hat{d}^{(\varrho)}_{j,l} \Theta^{(\varepsilon,\varrho)}_{r+1}(\hat{\zeta}_i,\hat{\varsigma}_l) = \sum_{l=0}^{M_\varsigma} d_{j,l}\boldsymbol{\Theta}_{l,r+1},$$

$$\left[\frac{\partial \varphi^{(\epsilon,\varrho)}_{r+1}}{\partial \zeta}\right|_{(\zeta=\zeta_i,\varsigma=\varsigma_j)} = \sum_{k=0}^{M_\zeta} \hat{D}^{(\varepsilon)}_{i,k} \Phi^{(\varepsilon,\varrho)}_{r+1}(\hat{\zeta}_k,\hat{\varsigma}_j) = \boldsymbol{D}\boldsymbol{\Phi}_{j,r+1},$$

$$\left[\frac{\partial \varphi^{(\varepsilon,\varrho)}_{r+1}}{\partial \varsigma}\right|_{(\zeta=\zeta_i,\varsigma=\varsigma_j)} = \left(\frac{2}{\varsigma^{\varrho}_{M_\varsigma}-\varsigma^{\varrho}_0}\right)\sum_{l=0}^{M_\varsigma} \hat{d}^{(\varrho)}_{j,l} \Phi^{(\varepsilon,\varrho)}_{r+1}(\hat{\zeta}_i,\hat{\varsigma}_l) = \sum_{l=0}^{M_\varsigma} d_{j,l}\boldsymbol{\Phi}_{l,r+1}. \quad (22)$$

where $\hat{D}^{(\varepsilon)}_{i,k} = \frac{2}{\zeta^{\varepsilon}_{M_\zeta}-\zeta^{\varepsilon}_0} D_{i,k}(i,k = 0,1,2,\cdots M_\zeta)$, with $D_{i,k}$ represents typical first order Chebyshev - Gauss - Lobatto differentiation matrix of size $(M_\varsigma+1)\times(M_\varsigma+1)$ as defined by [41], and $\hat{d}^{\varrho}_{j,l} = \frac{\varsigma^{\varrho}_{M_\varsigma}-\varsigma^{\varrho}_0}{2} d_{j,l}(j,l = 0,1,2,\cdots,M_\varsigma)$ describe the typical first order Chebyshev differentiation matrices of size $(M_\varsigma+1)\times(M_\varsigma+1)$ as used by [26]. $\boldsymbol{F}_j$, $\boldsymbol{\Theta}_j$ and $\boldsymbol{\Phi}_j$ are vectors of the form

$$\boldsymbol{F}_j = [f^{(\varepsilon,\varrho)}(\zeta_0,\varsigma_j), f^{(\varepsilon,\varrho)}(\zeta_1,\varsigma_j),\cdots, f^{(\varepsilon,\varrho)}(\zeta_{M_\zeta},\varsigma_j)]^T, \quad (23)$$

$$\boldsymbol{\Theta}_j = [\theta^{(\varepsilon,\varrho)}(\zeta_0,\varsigma_j), \theta^{(\varepsilon,\varrho)}(\zeta_1,\varsigma_j),\cdots, \theta^{(\varepsilon,\varrho)}(\zeta_{M_\zeta},\varsigma_j)]^T, \quad (24)$$

$$\boldsymbol{\Phi}_j = [\varphi^{(\varepsilon,\varrho)}(\zeta_0,\varsigma_j), \varphi^{(\varepsilon,\varrho)}(\zeta_1,\varsigma_j),\cdots, \varphi^{(\varepsilon,\varrho)}(\zeta_{M_\zeta},\varsigma_j)]^T. \quad (25)$$

With consideration to the overlapping last two points in the $\varepsilon-th$ sub-interval and the first two points in the $(\varepsilon+1)th$ sub - interval, the differentiation matrix, $\boldsymbol{D}$ for the overlapping grid in each case is assembled carefully, discarding the rows corresponding to the recurrent points, see [26] for the structure of this matrix.
Implementing the representations given by $(23-25)$ on the decoupled system $(14-16)$, we get

$$[\wedge^{(\varepsilon,\varrho)}_{11}\boldsymbol{D}^3 + \wedge^{(\varepsilon,\varrho)}_{12}\boldsymbol{D}^2 + \wedge^{(\varepsilon,\varrho)}_{13}\boldsymbol{D}]\boldsymbol{F}_{i,r+1} - S\sum_{j=0}^{m} d_{(i,j)}\boldsymbol{D}\boldsymbol{F}_{j,r+1} = R^{i}_{1,r}, \quad (26)$$

$$[\wedge^{(\varepsilon,\varrho)}_{21}\boldsymbol{D}^2 + \wedge^{(\varepsilon,\varrho)}_{22}\boldsymbol{D} + \wedge^{(\varepsilon,\varrho)}_{23}\boldsymbol{I}]\boldsymbol{\Theta}_{i,r+1} - \frac{SP_rC_T}{C_{T_1}}\sum_{j=0}^{m} d_{(i,j)}\boldsymbol{\Theta}_{j,r+1} = R^{i}_{2,r}, \quad (27)$$

$$[\wedge^{(\varepsilon,\varrho)}_{31}\boldsymbol{D}^2 + \wedge^{(\varepsilon,\varrho)}_{32}\boldsymbol{D} + \wedge^{(\varepsilon,\varrho)}_{33}\boldsymbol{I}]\boldsymbol{\Phi}_{i,r+1} - S_cS\sum_{j=0}^{m} d_{(i,j)}\boldsymbol{\Phi}_{j,r+1} = R^{i}_{3,r}. \quad (28)$$

where $\boldsymbol{I}$; is an identity matrix, $m = M_\varsigma + (M_\varsigma)\times(q-1)$ is the overall collocations in the whole time domain and

$$R^{i}_{1,r} = a^{(\varepsilon,\varrho)}_1,\quad R^{i}_{2,r} = a^{(\varepsilon,\varrho)}_2,\quad R^{i}_{3,r} = a^{(\varepsilon,\varrho)}_3.$$

4. Results And Analysis

The system of non - linear PDEs ($7-9$) with respect to the limiting conditions (10) was solved using Bivariate Simple Iteration Method (BSIM) on overlapping grids. The parameter values used here were chosen from existing similar research works [1, 17, 21, 34] and were found to be sufficiently modified to obtain accurate and consistent solutions. Throughout the numerical computational procedure, the parameter values were chosen as : $F_r = 0.1$, $\beta^* = 0.5$, $\gamma^* = 0.5$, $P_r = 0.7$, $E_c = 0.2$, $N_b = 0.2$, $N_t = 0.1$, $M_{cp} = 0.5$, $N = 0.1$, $\lambda^+ = 0.2$, $S = 0.5$, $S_c = 0.2$, $f_w = 1.0$, $R_k = 0.3$, $G_t = 0.2$, $\epsilon = 0.1$, $\phi_1 = 0.1$, $\phi_2 = 0.2$ and $\phi_3 = 0.3$. With accuracy and consistency in mind, we chose the sufficient values of $M_\eta = 20$ and $M_\varsigma = 10$ for the collocation points in space and time respectively with $p = 3$ and $q = 20$ sub - intervals in space and time respectively. The spatial domain was truncated at $\eta_\infty = 25$ and $[0, 10\pi]$ used as time domain. All these values were kept the same except when varied as stated in the various figures and tables.
We established the reliability of the results reported in this study by comparing them to the published results of [28], [43], [25] and [29] as seen in Table 3. All these results are observed to be excellently in agreement. Current results are further validated with the aid of residual errors. Residual errors are typically calculated as the difference between approximate solutions at each iteration and exact solutions. They indicate how far off the numerical solutions are from the exact solutions. In particular, we define the residual error in this study as follows :

$$Res(v) = ||\Delta_v[F_{r+1,j}, \Theta_{r+1,j}, \Phi_{r+1,j}]||_\infty, \qquad v = [f, \theta, \varphi]$$

Where; Δ_v represents the non - linear PDEs ($7-9$), F_j, Θ_j and Φ_j are the approximate solutions. Figures 2, 3 and 4, display the residual errors in the velocity, temperature and concentration solutions plotted against the scaled time parameter, ς. We observed very low residual error values that are very consistent across the time ς, indicating highly accurate numerical results and hence, comprehensively validating the model.

Dimensionless Surface Drag Force

Table 4 lays out numerically simulated dimensionless skin friction coefficient responses to incremental variations in f_w, β^*, γ^*,ϕ_{SiO_2}, ϕ_{MoS_2}, ϕ_{cu} and M_{cp}. We observed decreasing trend in the skin friction coefficient as the values of f_w and β^* go up. The Ferrohydrodynamic interaction parameter, β^* describes the influence of the magnetic dipole region on the nanofluid. Increasing β^* signifies stronger magnetic dipole region influence which directly results into more significant alignment of the nanoparticles. The nanoparticle alignment produces increment in the fluid viscosity and hence reduction in the skin friction coefficient at the oscillating surface. Positive values of f_w have been considered which represents injection of the nanofluid. Increasing positive values of f_w results to extra momentum imparted to the fluid and hence reduction in the surface drag. As the values of γ^*, ϕ_{SiO_2}, ϕ_{MoS_2}, ϕ_{cu} and M_{cp} get larger, the surface skin drag appreciates. In the presence of a magnetic field, when the magnetic dipole strength is increased, the Lorentz force experienced by the nanofluid becomes stronger. The force acts perpendicular to both the magnetic field and the direction of fluid motion and as such it increases the resistance to flow near the surface. As a result, the fluid motion is impeded, and the skin friction coefficient tends to increase. The surface drag increases with an increasing value of the mixed convective parameter M_{cp} because mixed convection introduces complex flow patterns, temperature gradients, and enhanced mixing effects in the nanofluid which disrupts the boundary layer and increases the resistance to fluid flow near the surface, leading to a higher skin friction coefficient. Similar enhancements are observed for increasing values of the nanoparticles fractions. As the nanoparticle fraction increases, there are more solid particles present in the nanofluid. These nanoparticles lead to increased friction at the fluid-solid interface. The presence of nanoparticles disrupts the smooth flow of the base fluid, leading to a rougher surface interaction. This results in a higher skin friction coefficient due to increased viscous drag and frictional resistance.

Dimensionless rate of heat transfer

Table 5 displays how P_r, β^*, γ^*, ϕ_{SiO_2}, ϕ_{MoS_2}, ϕ_{cu} and N_t influence the Nusselt number. It can be seen that the Nusselt number decreases with increasing Ferrphhydrodynamic parameter β^* which is primarily attributed to the disruptive effects of magnetic forces on flow patterns, particle clustering, and the reduction in effective thermal conductivity, consequently leading to less efficient convective heat transfer near the oscillating surface, hence, lowering the Nusselt number. Similar trend is observed as P_r

increases. Increase in the differently shaped nanoparticle percentages can be seen to improve the Nusselt number due to the better dispersion of heat by the nanoparticles owing to higher surface area. This allows for effective heat transfer rate within the magnetic dipole region close to the oscillating surface. As γ^* goes up the combined effects of the magnetized nanoparticles and the associated magnetic forces enhances heat transfer through improved thermal conductivity and more efficient heat conduction, hence, increasing the Nusselt number. Enhancing N_t also improves the Nusselt number. The thermophoretic parameter, N_t characterizes the ability of the nanoparticles in the fluid to move due to temperature gradients. A higher thermophoretic parameter indicates stronger thermophoresis. In this context, it implies that the nanoparticles are more responsive to temperature differences within the fluid. Increased N_t suggests that the thermal variation is significant. This enhanced temperature gradient promotes more efficient heat transfer. As nanoparticles move with respect to the temperature differences, they can carry heat around the different regions of the fluid especially at the oscillating surface and this, in turn, enhances the heat transfer process and increase the Nusselt number.

Table 3: Comparison for validation with $C_1 = C_2 = K_1 = K_2 = M_{cp} = f_w = 1.00$, $\beta^* = \gamma^* = N = 0$, $P_r = 2.0$

Published Results	[28]	[43]	[25]	[29]	Present Result
$-f''(0)$	0.6058427	0.6058427	0.6069352	0.615066	0.61543537

Dimensionless surface mass transfer

Sherwood number basically describes the convective mass transfer boundary layer characteristics of the fluid flow. Improving the nanoparticle fraction for each of the nanoparticles makes the fluid to become denser with solid particles. These nanoparticles inhibit the mass movement, by physically obstructing the transport of molecules between the fluid and the surrounding environment. The presence of more nanoparticles decrease the mass transfer rate by acting as barriers to molecular diffusion. This explains the trends in Table 6 as ϕ_{SiO_2}, ϕ_{MoS_2} and ϕ_{cu} are increased. Increasing N_t also increases the Sherwood number because thermophoresis causes nanoparticles to move and concentrate in regions with temperature gradients. This concentration of nanoparticles near the oscillating surface enhances their involvement in mass transfer processes, resulting in improved convective mass transfer efficiency and a higher Sherwood number. Increasing N_b values significantly reduces the sherwood number because more vigorous Brownian motion leads to wider nanoparticle dispersion and reduced concentration gradients which results to reduced convective mass transfer efficiency and hence, lowering the Sherwood number. Reduction in Sherwood number values is also observed for increasing γ^*. This is because a stronger magnetic field restricts the mobility of the nanoparticles and results to nanoparticle alignment along the field lines, reducing their random motion and mixing within the fluid. This constrained mobility limits the interaction of the particles with the surface and decreases the surface mass transfer.

Dimensionless velocity distribution

The fluid velocity is significantly influenced by increasing value of injection parameter, f_w, as seen in Figure 5. It can be seen that the velocity profile declines as f_w grows. This is because the injection parameter introduces external fluid into the boundary layer, which disrupts the existing flow pattern, increases the boundary layer thickness, reduces the velocity near the surface, and declines the overall velocity profile. In Figure 6, we see how the velocity profile depreciates close to the oscillating surface within the strong magnetic dipole region as β^* increases and goes up further away from this region. This is in line with what is expected as higher β^* values increase the effective viscosity and nanoparticle alignment within the magnetic dipole region close to the surface and hence, reduction in the velocity profile as observed. Further away from this region, this influence drastically reduce which leads to increased nanofluid speed. Reverse trend is observed in Figure 8 for increasing values of γ^* owing to the pronounced interaction of the magnetic nanoparticle (platelet-shaped copper) in the ternary fluid. In Figure 7, we see that the velocity distribution improves as M_{cp} value grows. This is because the forced convection become more dominance over the natural convection resulting from the combined effects of the oscillatory stretching surface, temperature gradients, and the potential influence of the magnetic field, hence, causing an increase in fluid velocity near the surface and, consequently, an overall significant increase in

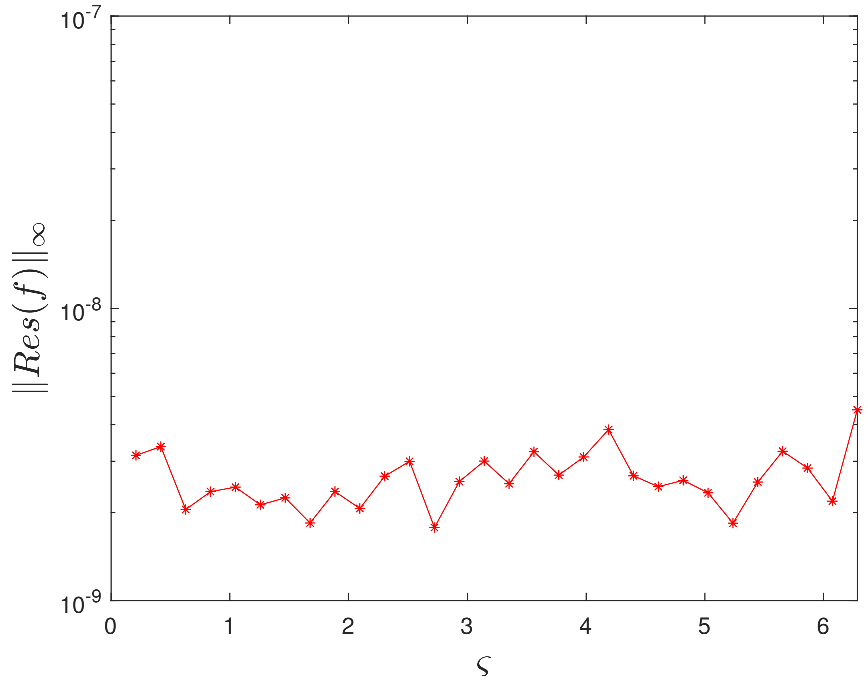

Figure 2: Residual error for velocity

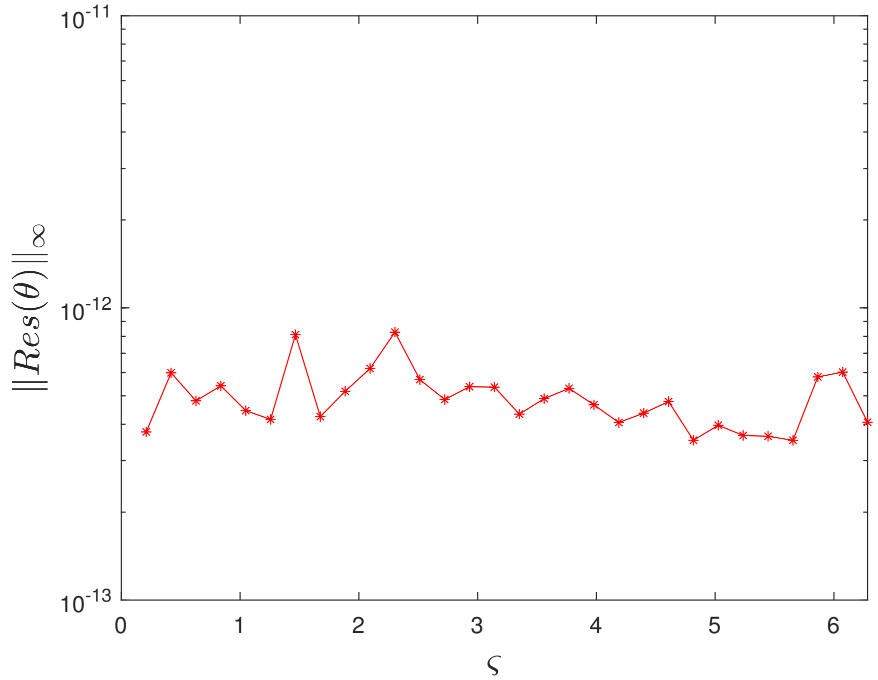

Figure 3: Residual error for temperature

the velocity profile. Generally, addition of nanoparticles to the base fluid can significantly increase the fluid's viscosity, especially if the nanoparticle fractions are high (in this case, we have considered up to 40 $\perp$ nanoparticle fraction in each). As the viscosity of the fluid increases, the resistance to flow also increases, resulting in a decrease in velocity profile. This explains the observations in Figures 9, 10 and 11.

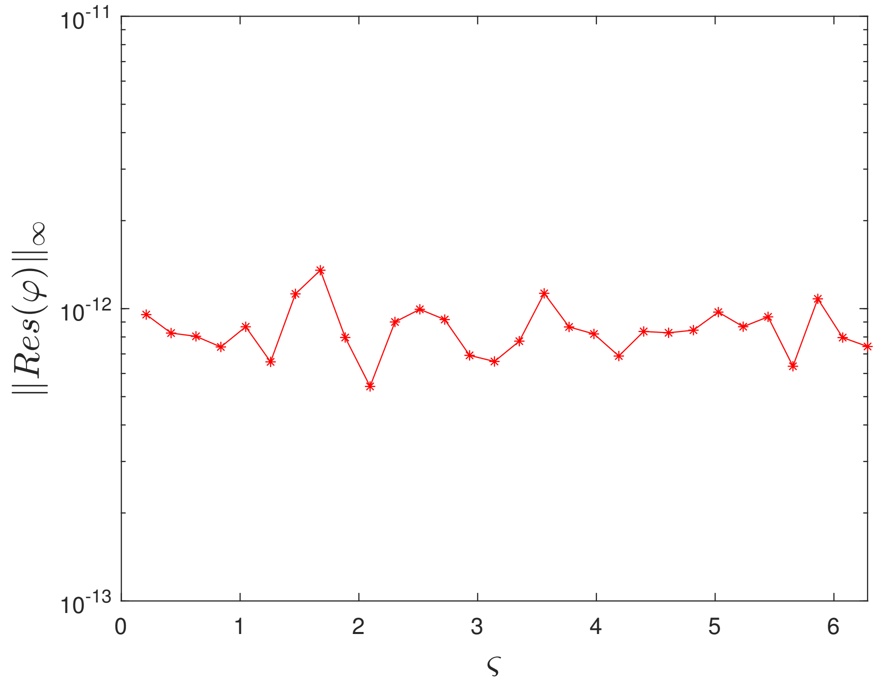

Figure 4: Residual error for concentration

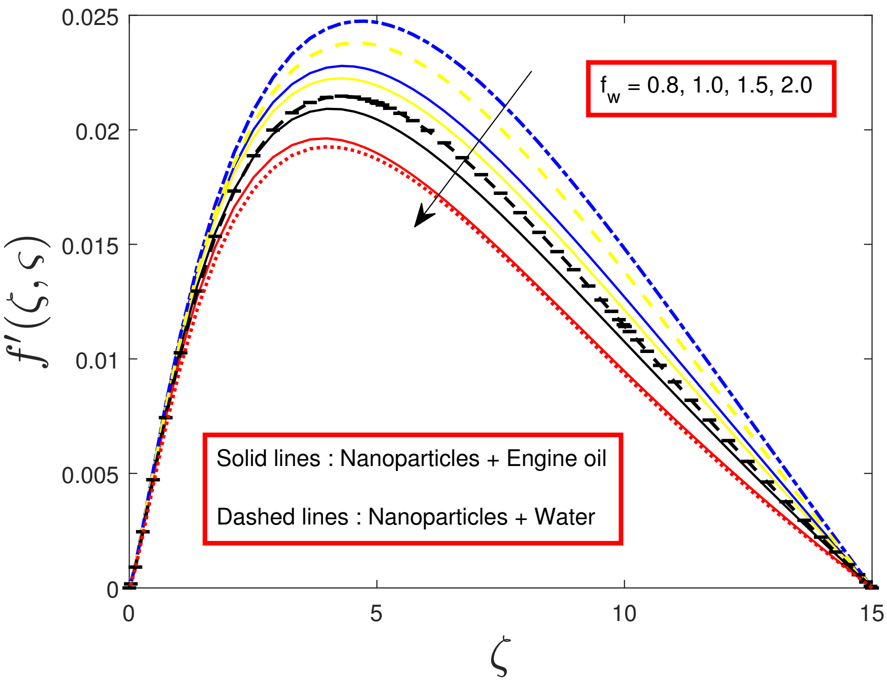

Figure 5: Influence of suction parameter on ternary fluid velocity

Table 4: Numerical values of the skin friction coefficient for different values of some pertinent parameters when $\varsigma = \frac{\pi}{2}$

f_w	β^*	γ^*	ϕ_{SiO_2}	ϕ_{MoS_2}	ϕ_{cu}	M_{cp}	$(Re_x)^{\frac{1}{2}}Cf_x$ - Engine oil based	$(Re_x)^{\frac{1}{2}}Cf_x$ - Water based
0.8	0.5	0.5	0.1	0.2	0.3	0.5	0.40400398	0.41984282
1.0							0.39638215	0.40504410
1.5							0.37634416	0.36546454
2.0							0.35521265	0.32365594
	0.5						0.39638215	0.40504410
	1.0						-0.25642602	-0.32793679
	3.0						-2.94356200	-3.46634169
	5.0						-5.76011545	-6.99431067
		0.5					0.39638215	0.40504410
		1.0					0.96806826	1.03857772
		3.0					1.03995276	1.11745807
		5.0					1.04159428	1.11916577
			0.1				0.39638215	0.38995499
			0.2				0.40496407	0.40504410
			0.3				0.41229644	0.41008746
			0.4				0.41772884	0.41373990
				0.1			0.29835965	0.30208386
				0.2			0.39638215	0.40504410
				0.3			0.44059366	0.43608034
				0.4			0.44908185	0.42096107
					0.1		0.26499304	0.29756435
					0.2		0.33698592	0.35459605
					0.3		0.39638215	0.40504410
					0.4		0.44627184	0.44774982
						0.5	0.39638215	0.40504410
						1.5	2.46137761	2.61046192
						2.5	4.47859936	4.72332475
						3.5	6.45347379	6.76272367

Dimensionless temperature distribution

As ferrohydrodynamic parameter, β^* increases, the magnetic dipole region becomes more influential leading to increased alignment of nanoparticles and changes in the effective thermal conductivity and as such the heat transfer within the nanofluid is enhanced as depicted in Figure 12. Reverse is the case as γ^* increases as seen in Figure 13 owing to the paramagnetic nature of the platelet-shaped copper in the fluid. In Figure 14, it can be seen that the thermal distribution declines as f_w heightens due to the introduction of cooler fluid into the boundary layer near the surface, which disrupts the existing temperature distribution and leads to mixing and dilution of the warmer fluid which results to overall reduction in the thermal profile. As earlier stated, thermophoresis parameter, N_t, measures the ability of particles in a fluid to move due to temperature gradients. Increasing N_t introduces effective temperature gradients within the nanofluid. These temperature gradients create fluid motion, which leads to improved heat transfer. The effective temperature gradients also increase the convective heat transfer effectiveness, contributing to the rise in the temperature profile as displayed in Figure 15. Enhanced values of M_{cp} enhances the fluid motion which promotes fluid agitation and mixing, disrupting the thermal boundary layer and contributing to the cooling effect. This explains what Figure 16 depicts. We observed similar trends in Figures 18 and 19 as the fractions of SiO_2 and MoS_2 increase. Prandtl number is a dimensionless parameter that represents the ratio of momentum diffusivity to thermal diffusivity. A higher Prandtl number indicates that momentum diffuses more slowly compared to thermal. Higher Prandtl number in this case results to slower diffusion of momentum and thicker thermal boundary layer owing to the differently shaped nanoparticles in the based fluid. The combined effects of the slower momentum diffusion and thicker thermal boundary layer lead to significant increase in the thermal profile of the fluid as seen in Figure 17. Increasing the fraction of copper nanoparticles in the nanofluid leads to a higher concentration of nanoparticles near the surface and copper nanoparticles being typically of higher

Table 5: Numerical values of the Nusselt number for different values of some pertinent parameters when $\varsigma = \frac{\pi}{2}$

P_r	β^*	γ^*	ϕ_{SiO_2}	ϕ_{MoS_2}	ϕ_{cu}	N_t	$(Re_x)^{-\frac{1}{2}}Nu_x$ - Engine oil based	$(Re_x)^{-\frac{1}{2}}Nu_x$ - Water based
0.5	0.5	0.5	0.1	0.2	0.3	0.5	0.20743367	-0.64208525
1.0							-0.82617786	-2.12092994
1.5							-1.88775750	-4.09526743
2.0							-2.95992084	-6.57858721
	0.5						-0.20189422	-1.18865188
	1.0						-1.33964274	-2.37961682
	3.0						-6.00913058	-7.46577860
	5.0						-10.87936411	-13.15731298
		0.5					0.39638215	0.40504410
		1.0					0.96806826	1.03857772
		3.0					1.03995276	1.11745807
		5.0					1.04159428	1.11916577
			0.1				-0.20189422	-1.18865188
			0.2				-0.13243221	-1.17708757
			0.3				0.03114528	-1.07811056
			0.4				0.44692120	-0.74606040
				0.1			-0.24086920	-1.22626018
				0.2			-0.20189422	-1.18865188
				0.3			-0.07423008	-1.04784967
				0.4			0.23213462	-0.73049872
					0.1		-0.81237859	-1.42941574
					0.2		-0.50448046	-1.30368675
					0.3		-0.20189422	-1.18865188
					0.4		0.12812850	-1.06704427
						0.5	-0.21392890	-1.20538220
						1.0	-0.22888407	-1.22633751
						1.5	-0.24374329	-1.24736683
						2.0	-0.25850779	-1.26850108

thermal conductivity compared to the base fluids contributes to a thicker thermal boundary layer near the surface. The thicker thermal boundary layer and higher thermal conductivity facilitate more efficient heat transfer from the solid surface to the fluid. This results to a decrease in the temperature near the surface and increase in temperature within the fluid further away from the surface as demonstrated in Figure 20. Eckert number characterizes the ratio of kinetic energy to enthalpy within a fluid flow and a higher Eckert number indicates that kinetic energy is more dominant compared to enthalpy, signifying a larger amount of kinetic energy within the flow. This enhanced kinetic energy leads to more vigorous fluid motion, especially near the oscillatory stretching surface which results to more efficient heat removal from the solid surface and, consequently, an increase in the temperature profile as depicted in Figure 22. Similar trend is observed in Figure 21 for increasing values of N_b.

Dimensionless ternary fluid concentration distribution

In Figure 23, we observed steady decline in the concentration profile as f_w increases. This is because introduction of fresh fluid into the boundary layer near the surface disrupts the existing concentration gradients and creates variations in nanoparticle distribution and hence creating reduction in the concentration profile. Figure 24 displays the concentration profile decline with increasing values of the thermophoresis parameter, N_t as a result of the motion of the differently-shaped nanoparticles in response to temperature gradients. Figures 25 and 28 showcase increasing fluid concentration profiles with increasing nanoparticle fractions of SiO_2 and MoS_2. Higher nanoparticle fraction in each case stimulates the near wall accumulation effect and mobility of the nanoparticles with the interaction to the magnetic dipole which results to a surge in the concentration profile. We observed similar trend in Figure 26 for increasing fraction of copper nanoparticles. However, in this case, as the fluid flow away from the surface, the copper nanoparticles have more space and are less influenced by the surface's temperature

Table 6: Numerical values of the Sherwood number for different values of some pertinent parameters when $\varsigma = \frac{\pi}{2}$

N_b	β^*	γ^*	ϕ_{SiO_2}	ϕ_{MoS_2}	ϕ_{cu}	N_t	$(Re_x)^{-\frac{1}{2}}Sh_x$ - Engine oil based	$(Re_x)^{-\frac{1}{2}}Sh_x$ - Water based
0.1	0.5	0.5	0.1	0.2	0.3	0.5	0.44215714	0.56250936
0.5							0.38291322	0.40705452
1.0							0.37551232	0.38763021
1.5							0.37304859	0.38115853
	0.5						0.40512717	0.46534286
	1.0						0.43580533	0.53656604
	3.0						0.56167641	0.84046523
	5.0						0.69290583	1.18006694
		0.5					0.40512788	0.46534350
		1.0					0.37714381	0.40146031
		3.0					0.37484199	0.39606148
		5.0					0.37477835	0.39589925
			0.1				0.40512788	0.46534286
			0.2				0.40262162	0.46100139
			0.3				0.39825198	0.44773488
			0.4				0.39691115	0.42156589
				0.1			0.40723453	0.47521856
				0.2			0.40512855	0.46534286
				0.3			0.40075017	0.44559941
				0.4			0.3938349	0.42041700
					0.1		0.44688291	0.53689046
					0.2		0.41856766	0.49001246
					0.3		0.40512788	0.46534286
					0.4		0.39650140	0.4775898
						0.5	0.55509907	0.85805048
						1.0	0.74517788	1.35671119
						1.5	0.93812536	1.86401053
						2.0	1.13390219	2.37998010

gradients. This leads to a decrease in the concentration profile. In Figure 27, improving values of β^* declines the concentration profile. As the β^* grows, the dynamic interaction between the magnetic field of the magnetic dipole and the differently shaped nanoparticle stimulates nanoparticle redistribution within the fluid which in turn influence steady decline in the concentration profile. Similar trend can seen for increasing values of R_k in Figure 30. As earlier stated higher Eckert number signifies more kinetic energy to the flow, which can be associated with more vigorous fluid flow. The vigorous fluid flow associated with the higher Eckert number promotes better dispersion of nanoparticles, preventing their agglomeration and ensuring a more even distribution which reflects in the significant decline of the concentration profile seen in Figure 29.

In general, in the comparison of the base fluid performance, we see water outperform engine oil due to its higher thermal conductivity, specific heat capacity, lower viscosity and ease of mixing and dispersion. However, altering the shapes of the nanoparticles and the interaction of the magnetic dipole narrows this gap in most cases. Nevertheless, it is worthy of note that the choice of base fluid also depends on the specific requirements of particular application area of this configuration. Engine oil may be preferred in certain cases where higher temperature stability and lubrication properties are essential factors. In contrast, water is better suited for scenarios where heat transfer, cooling, and biodegradability are critical factors.

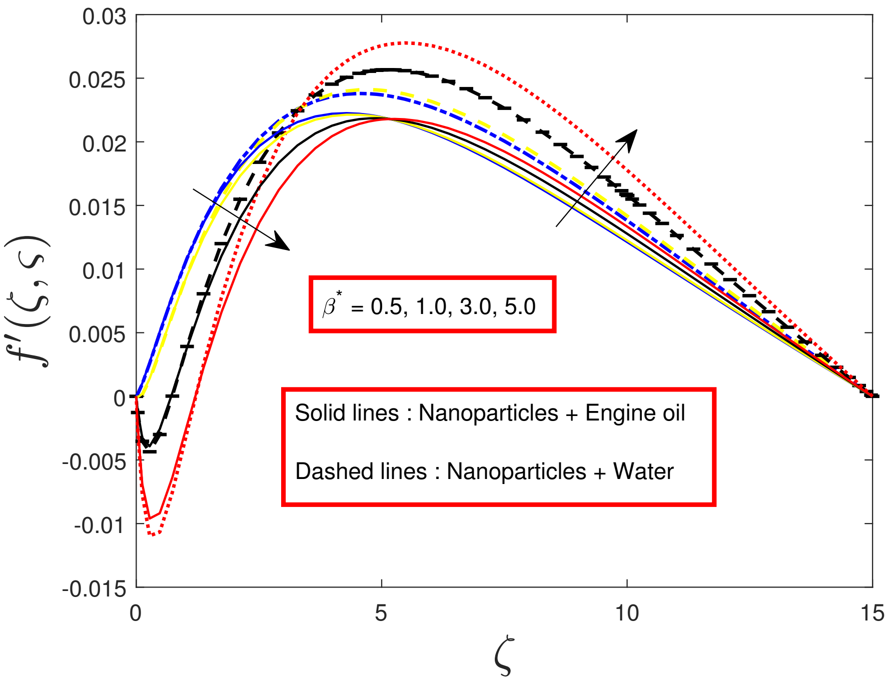

Figure 6: Influence of Ferrohydrodynamic parameter on ternary fluid velocity

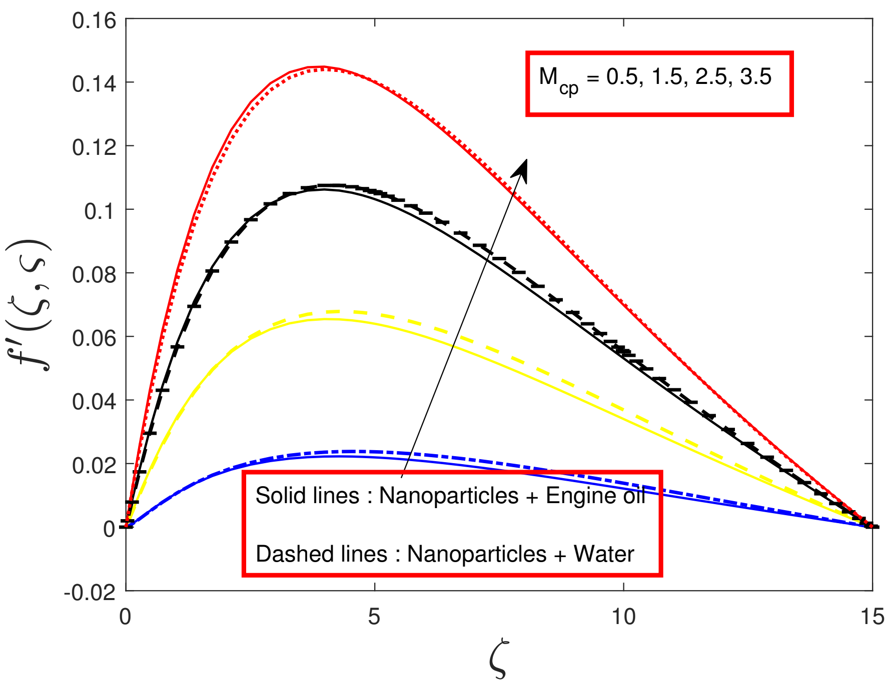

Figure 7: Influence of mixed convection parameter on ternary fluid velocity

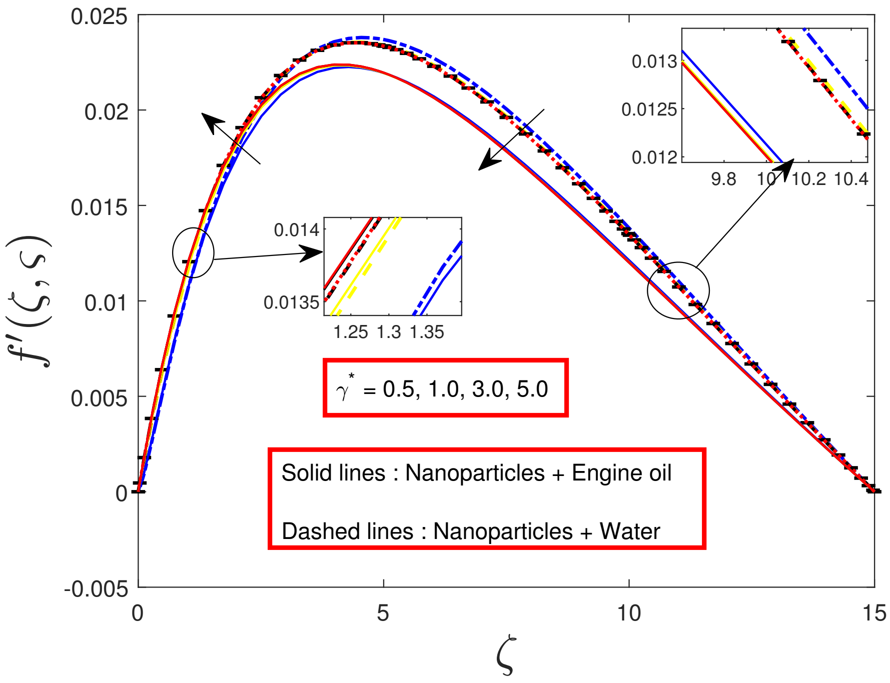

Figure 8: Influence of magnetic dipole strength on ternary fluid velocity

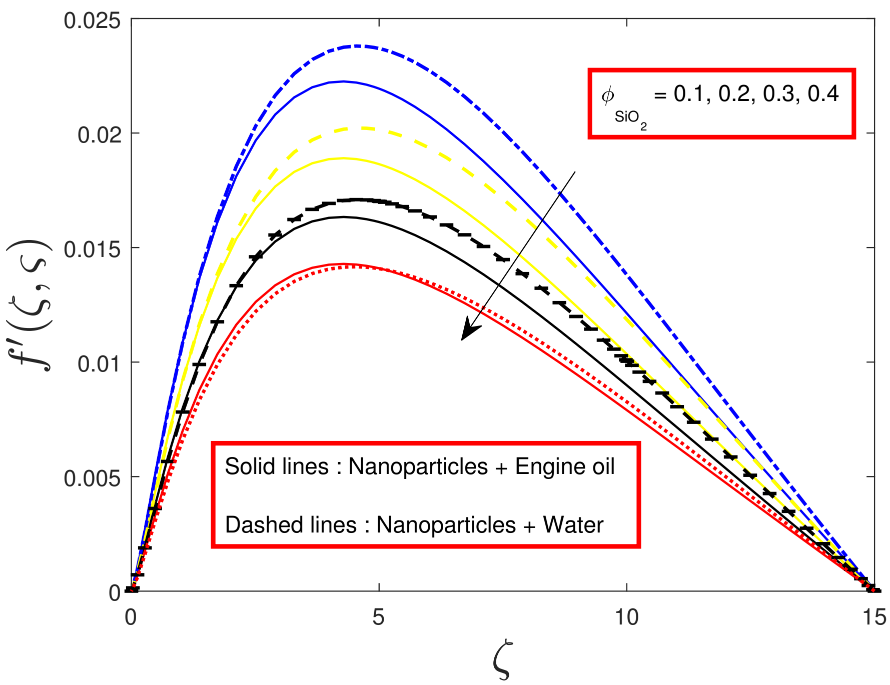

Figure 9: Influence of SiO_2 percentage on ternary fluid velocity

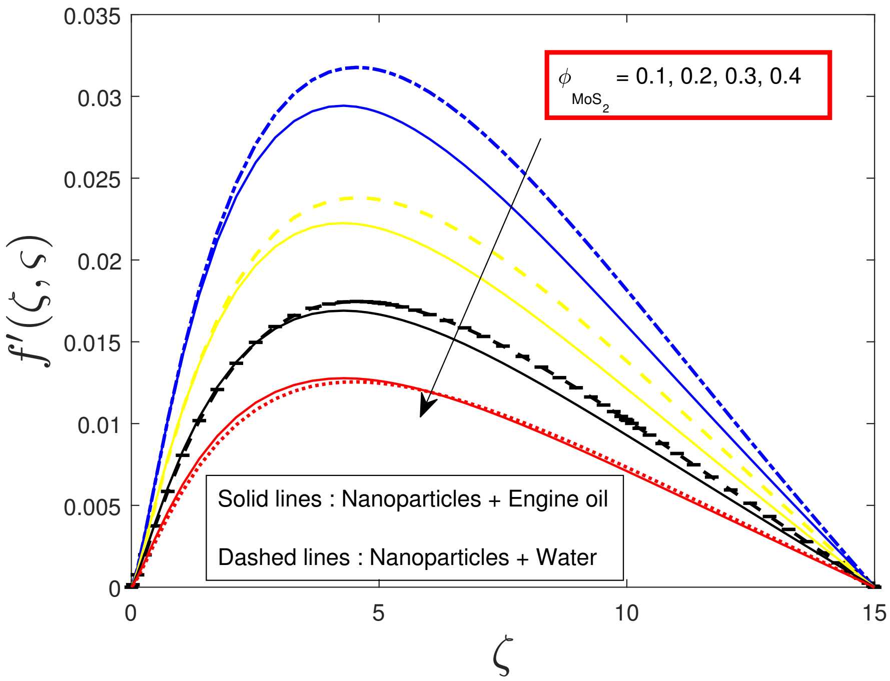

Figure 10: Influence of MoS_2 percentage on ternary fluid velocity

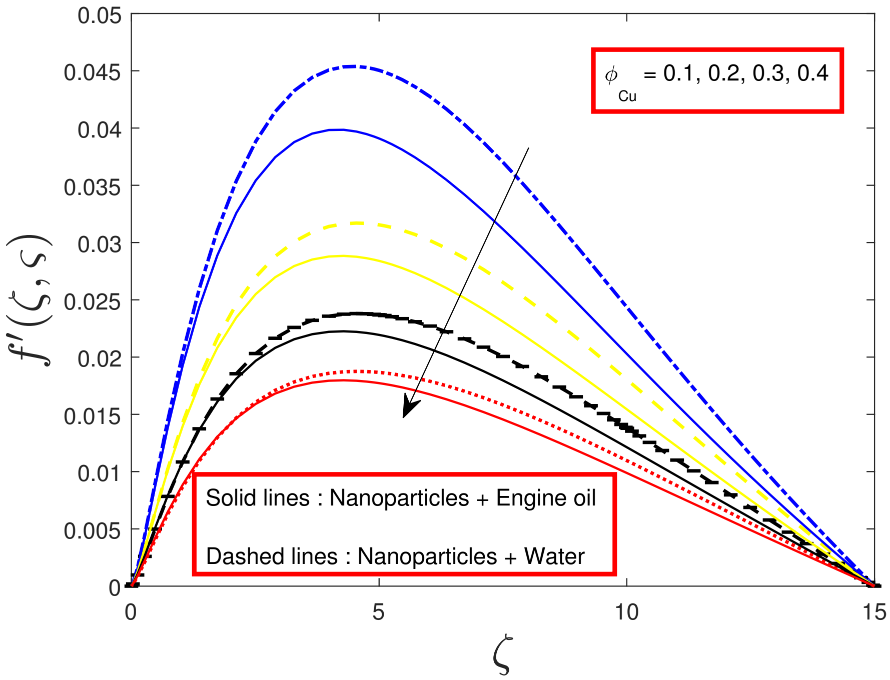

Figure 11: Influence of copper percentage on ternary fluid velocity

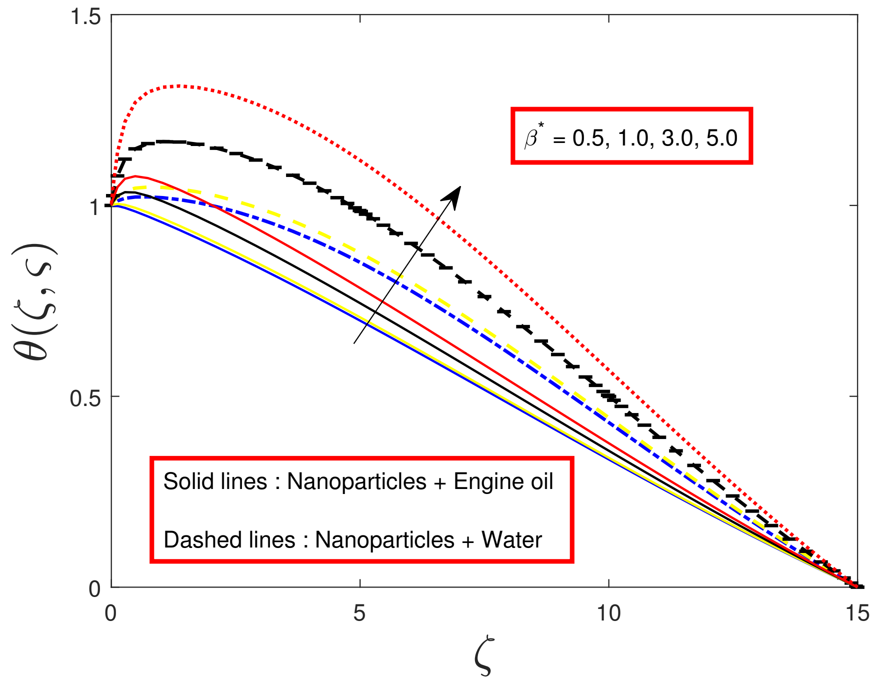

Figure 12: Influence of Ferrohydrodynamic interaction constant on ternary fluid temperature

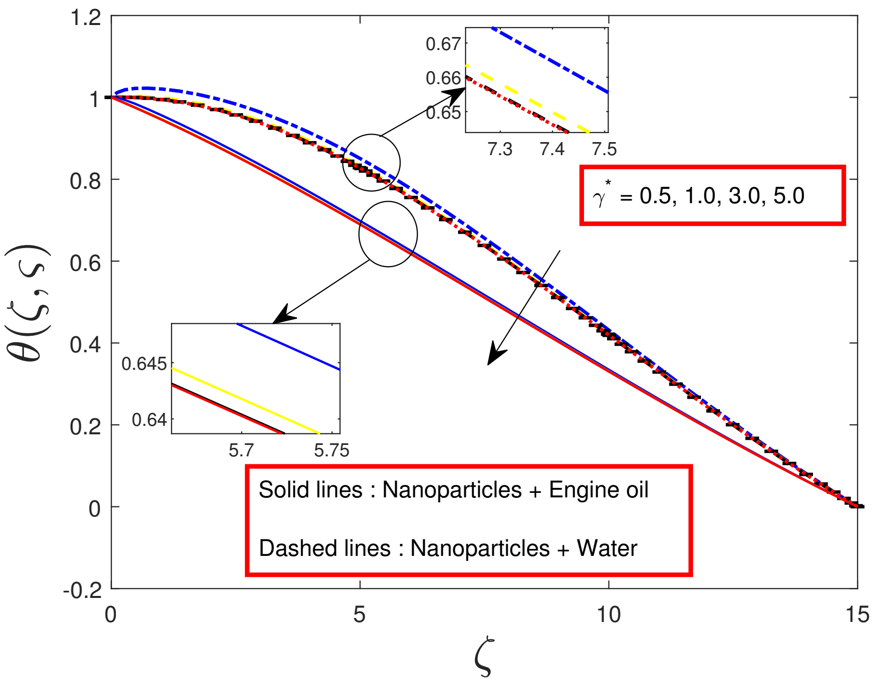

Figure 13: Influence of magnetic dipole strength on ternary fluid temperature

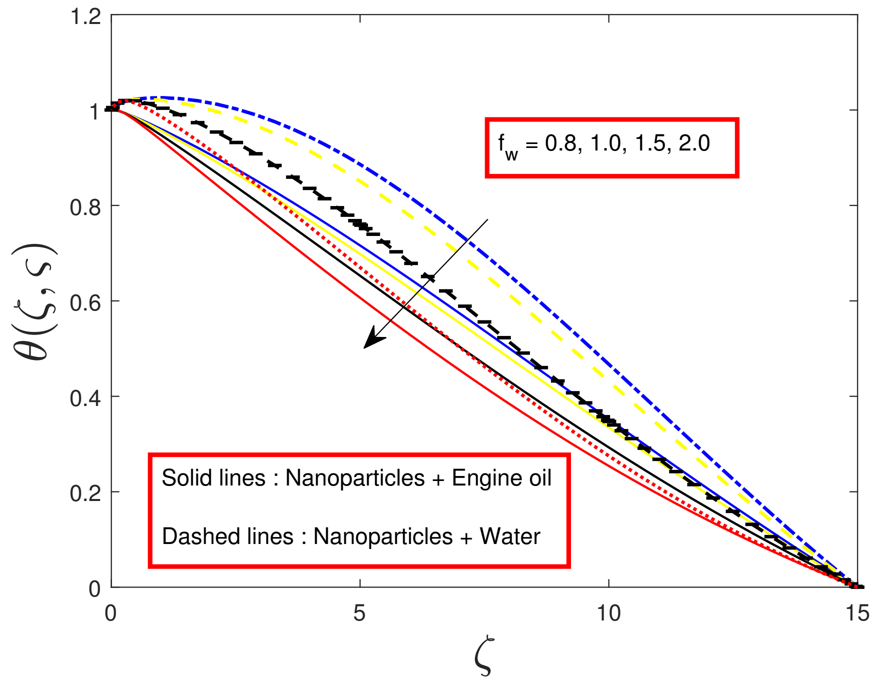

Figure 14: Influence of suction parameter on ternary fluid temperature

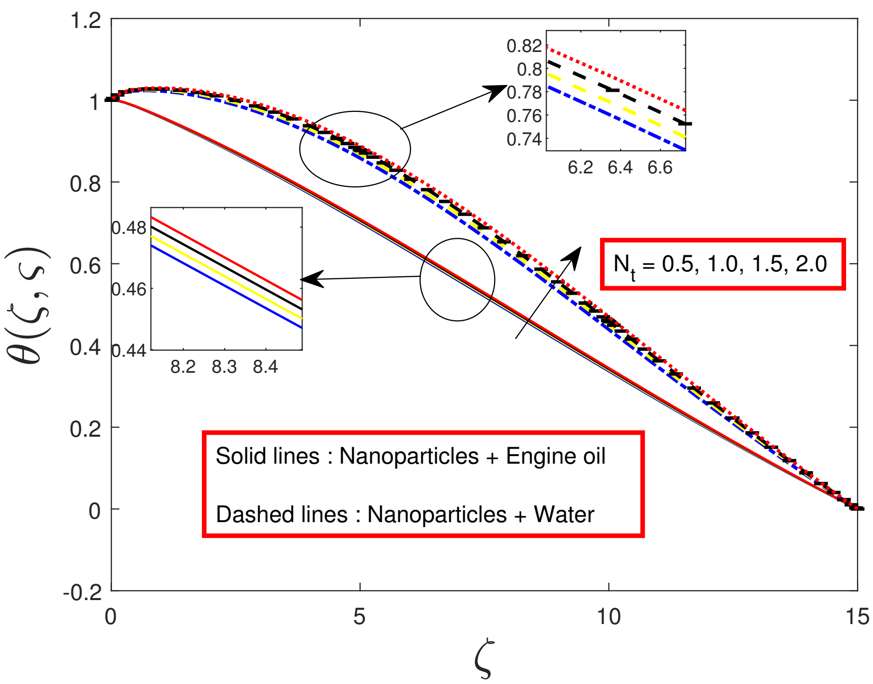

Figure 15: Influence of thermophoresis parameter on ternary fluid temperature

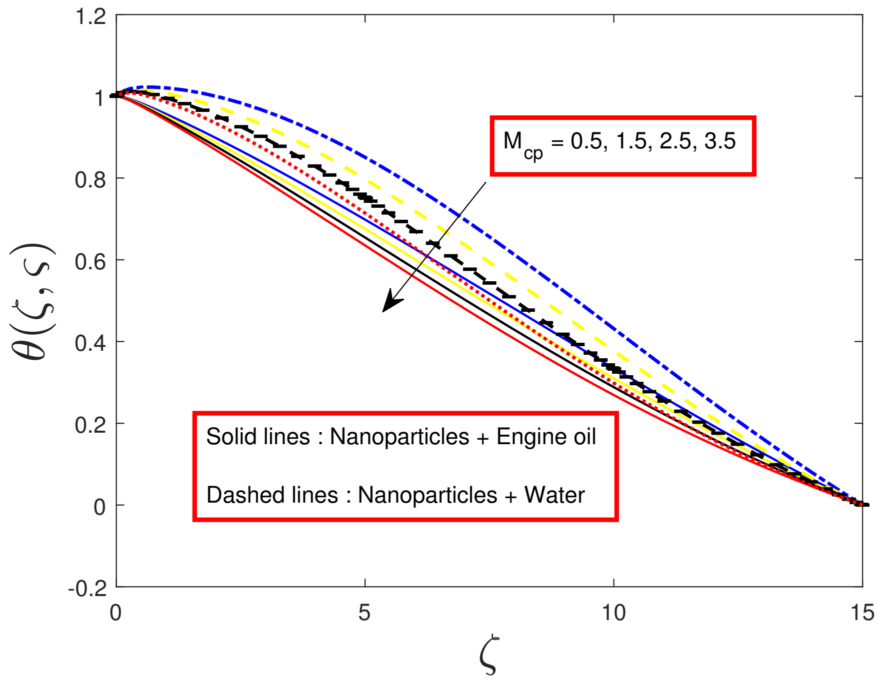

Figure 16: Influence of mixed convection parameter on ternary fluid temperature

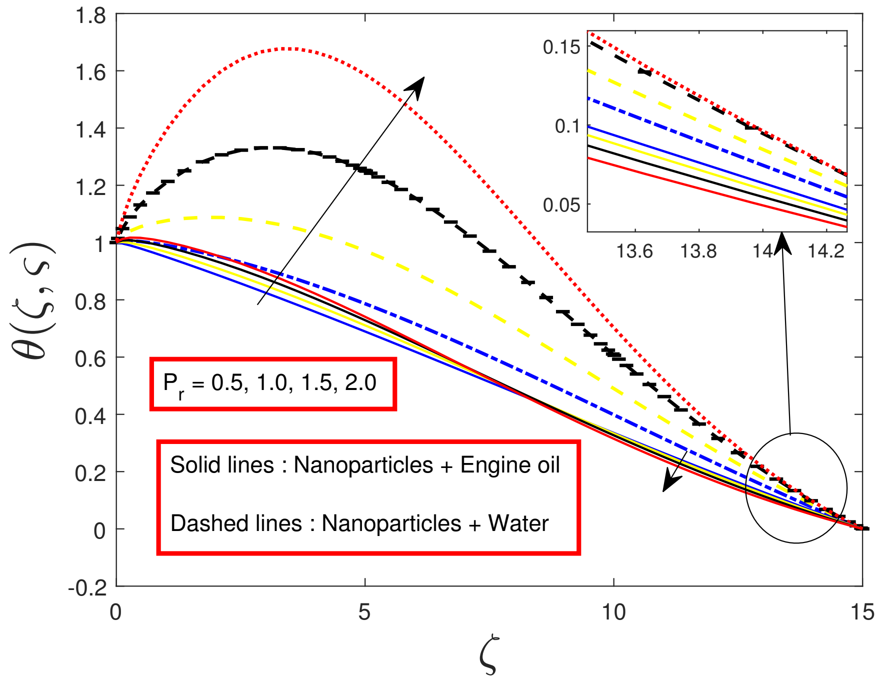

Figure 17: Influence of Prandtl number on ternary fluid temperature

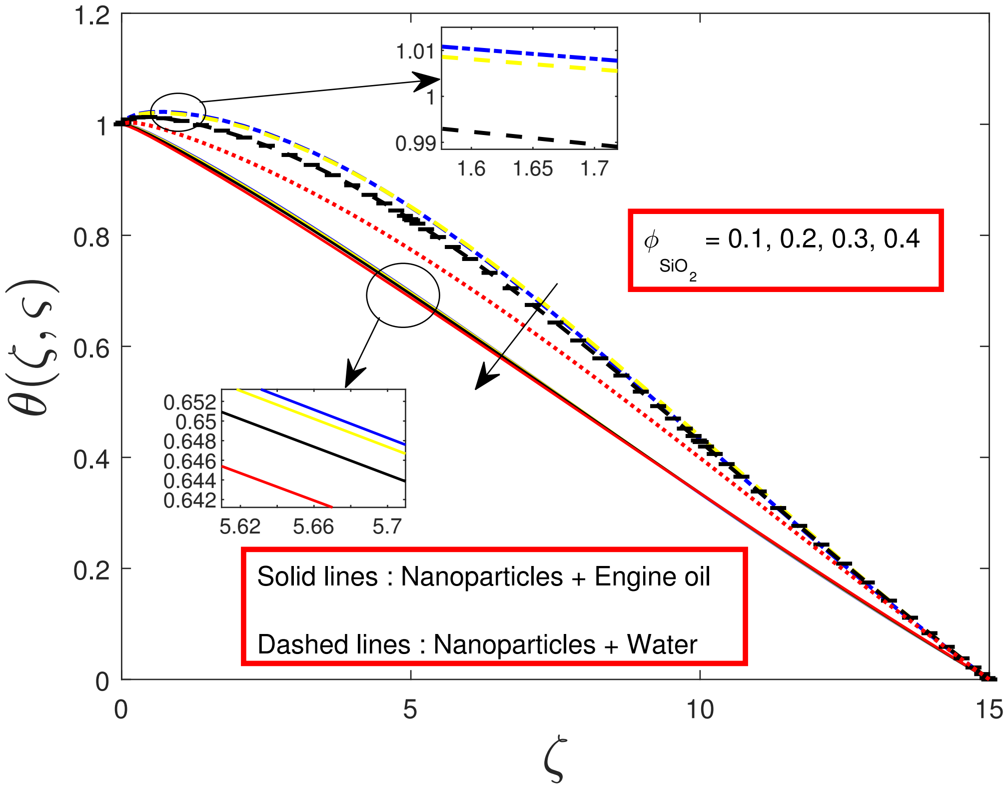

Figure 18: Influence of SiO_2 percentage on ternary fluid temperature

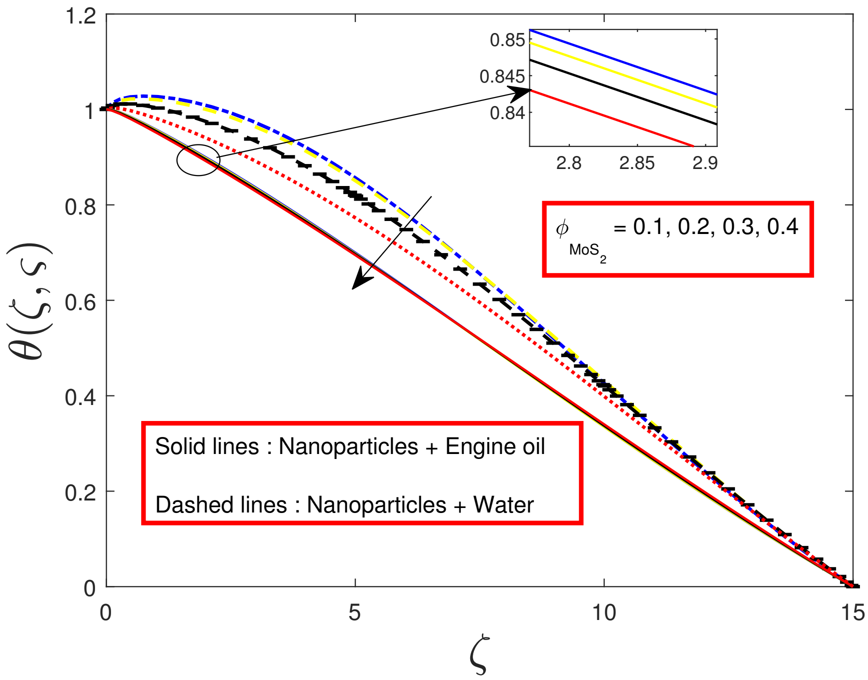

Figure 19: Influence of MoS_2 percentage on ternary fluid temperature

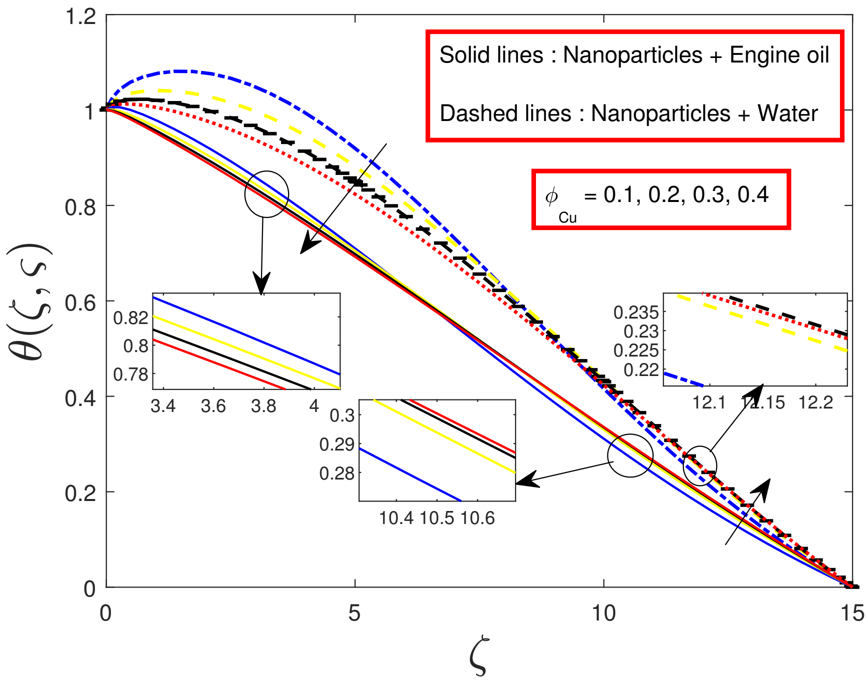

Figure 20: Influence of copper percentage on ternary fluid temperature

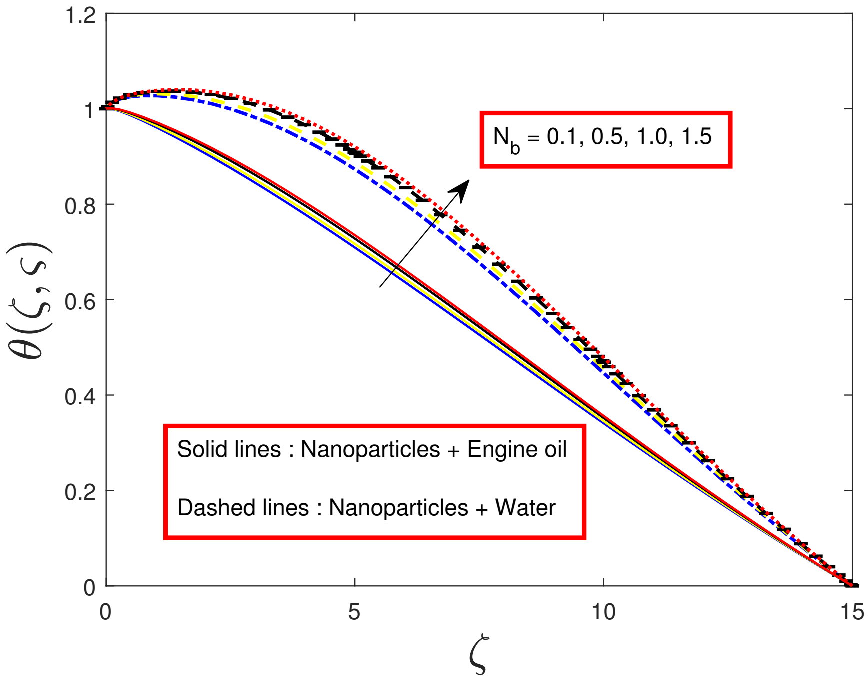

Figure 21: Influence of Brownian motion number on ternary fluid temperature

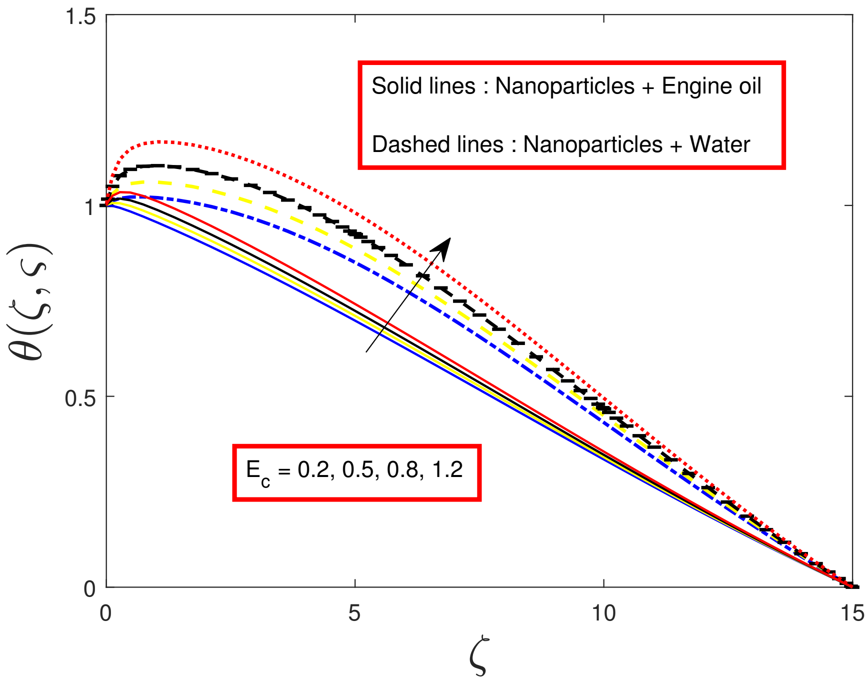

Figure 22: Influence of Eckert number on ternary fluid temperature

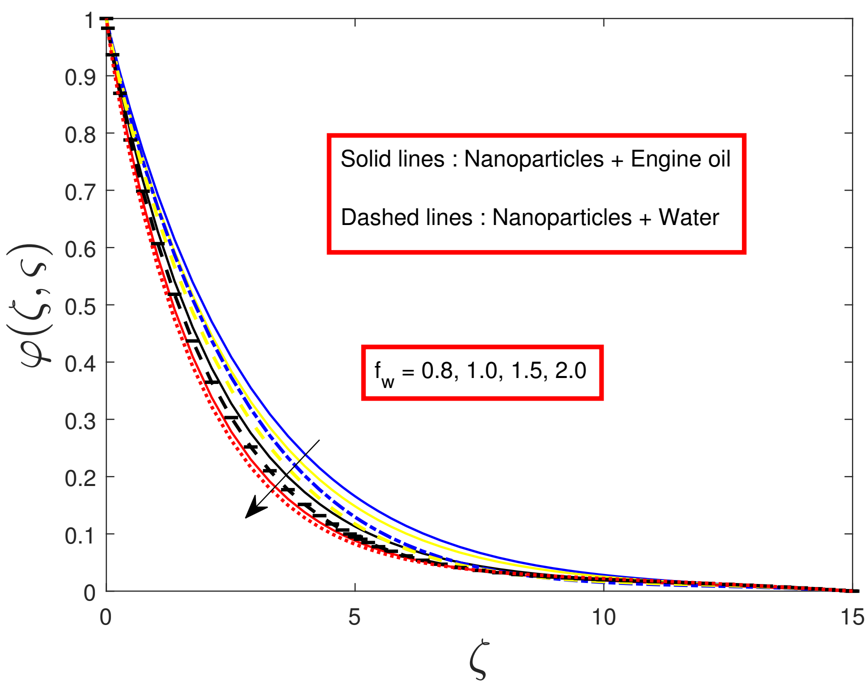

Figure 23: Influence of suction parameter on ternary fluid concentration

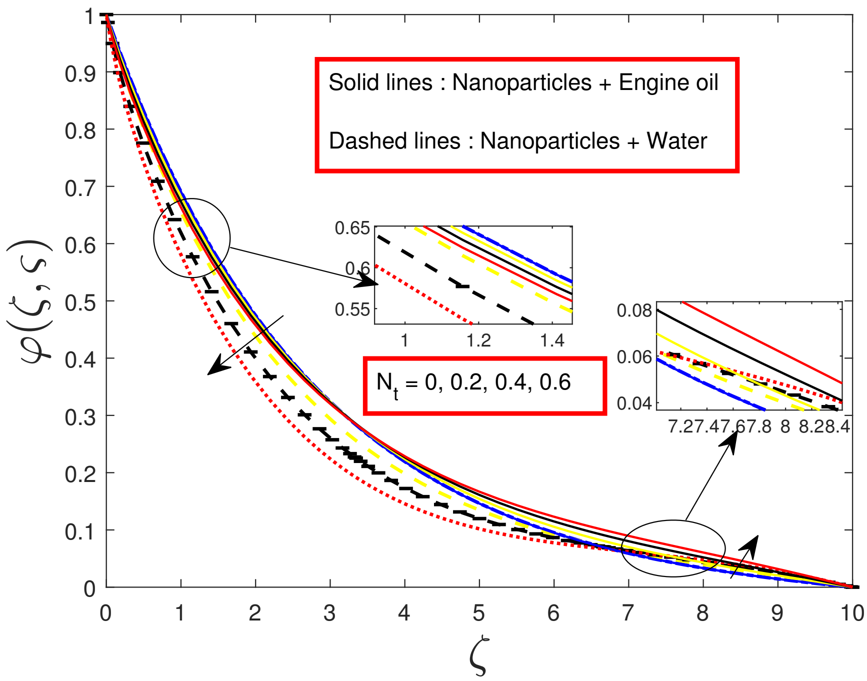

Figure 24: Influence of local thermophoresis number on ternary fluid concentration

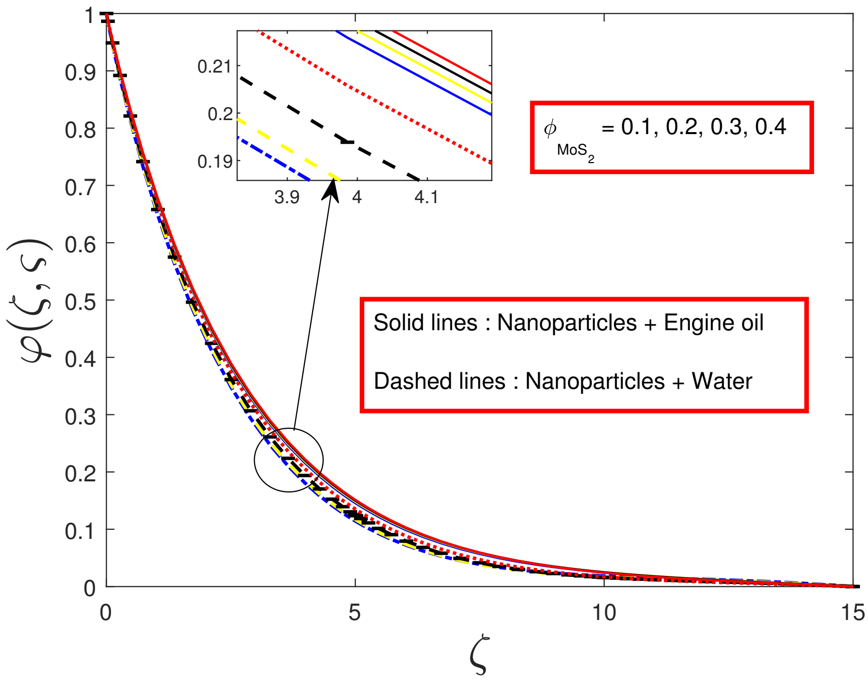

Figure 25: Influence of MoS_2 percentage on ternary fluid concentration

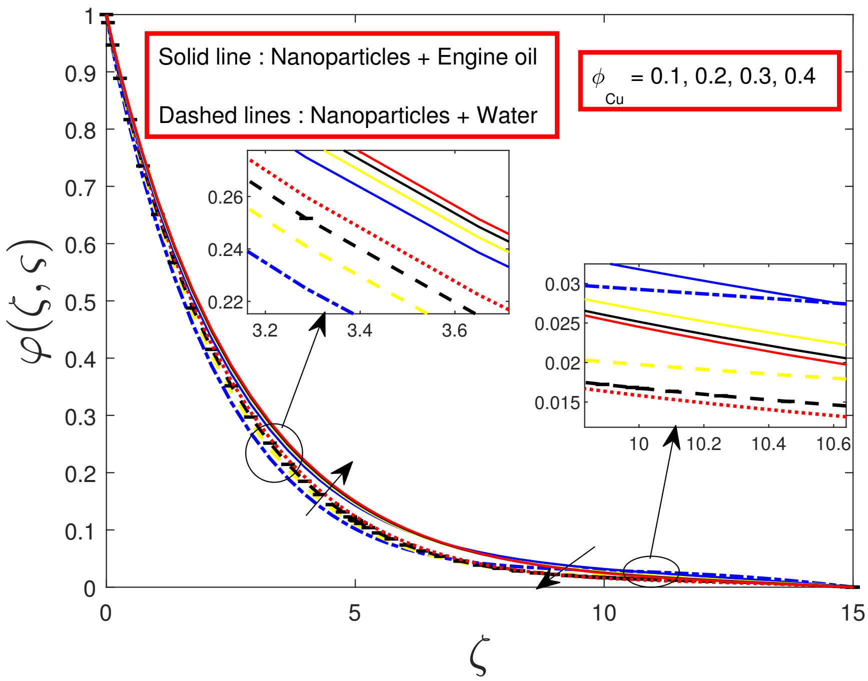

Figure 26: Influence of copper percentage on ternary fluid concentration

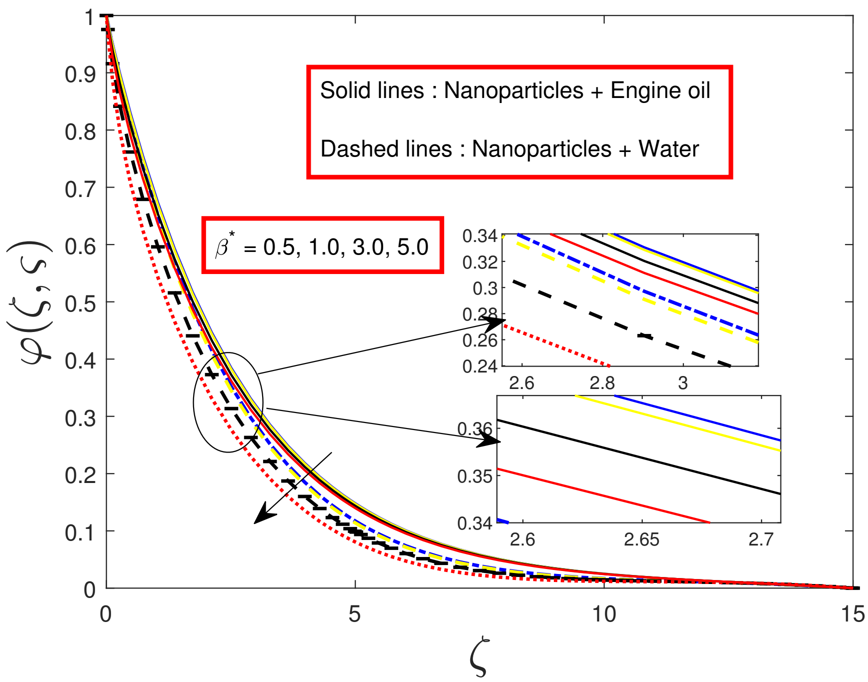

Figure 27: Influence of Ferrohydrodynamic interaction parameter on ternary fluid concentration

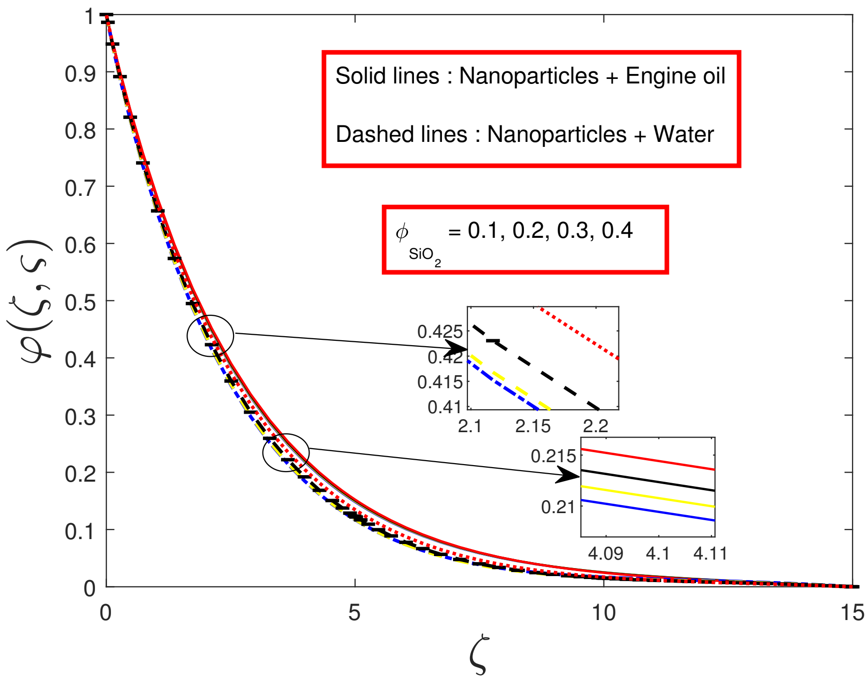

Figure 28: Influence of SiO_2 percentage on ternary fluid concentration

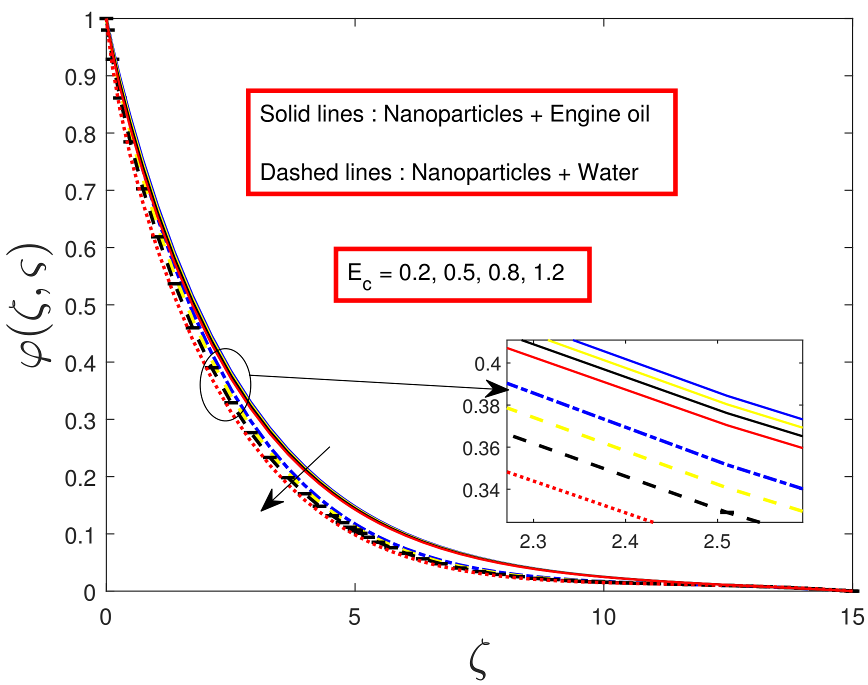

Figure 29: Influence of Eckert number on ternary fluid concentration

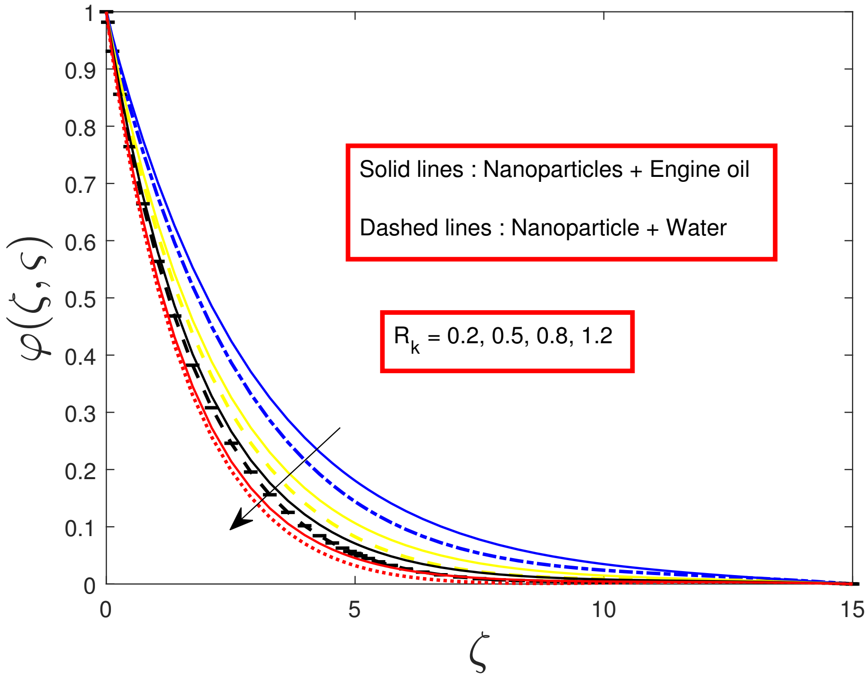

Figure 30: Influence of chemical reaction parameter on ternary fluid concentration

5. Conclusion

The flow, mass and heat transfers comparison of engine oil and water based ternary hybrid nanofluids containing differently shaped nanoparticles of SiO_2, MoS_2 and Cu over an oscillatory stretching sheet within magnetic dipole region of influence is numerically examined in this research work. The governing non - linear PDEs after some suitable transformations are solved via the numerical method of bivariate simple iteration on overlapping grids. Our analysis sheds light on how the varying shapes of SiO_2, MoS_2, and copper nanoparticles respond to the magnetic dipole field, elucidating their impact on heat transfer and fluid flow characteristics. The findings from this study hold immense promise for applications in advanced thermal management systems, nanoengineering, and innovative heat exchanger designs. The mass transfer, temperature, and velocity distributions are analyzed and discussed graphically. The skin drag coefficient, heat transfer rate and Sherwood number are tabulated and examined in detail. Based on the findings, we have reached the following concluding remarks

- Escalating the nanoparticle fractions of the differently shaped nanoparticles improves the surface skin drag.
- Enhancing magnetic dipole strength and mixed convection parameter increases the surface skin drag.
- The skin friction at the surface of oscillatory stretching sheet is reduced by increasing values of ferrohydrodynamic and suction parameters.
- Increasing ferrohydrodynamic parameter, speeds up the ternary hybrid nanofluid close to the oscillating surface and strong influence of the magnetic dipole and the fluid slows down farther away. Reverse is the case for increasing values of magnetic dipole strength.
- Enhancing the nanoparticle fractions and suction have diminishing effects on the ternary hybrid nanofluid velocity.
- Improving values of mixed convection parameter enhances the fluid velocity.
- Heat transfer rate at the surface increases as the values of magnetic dipole strength and the nanoparticle fractions of SiO_2, MoS_2 and copper grow.
- The Nusselt number depreciates as ferrohydrodynamic parameter, Prandtl number and thermophoresis parameter improve.
- Improving magnetic dipole strength and thermophoresis heightens the mass transfer at the oscillating surface.
- The local Sherwood number decreases with improving values of Brownian motion number, magnetic dipole strength and the nanoparticle fractions of SiO_2, MoS_2 and copper.
- The ternary hybrid nanofluid concentration declines as ferrohydrodynamic parameter, Eckert number and chemical reaction parameter improve.
- Enhancing nanoparticle fractions produce overall increments in the concentration of the ternary hybrid nanofluid.
- Thermal distribution of the fluid improves as ferrohydrodynamic parameter, Prandtl number, Eckert number and the nanoparticle fractions of SiO_2 and MoS_2 grow.
- Enhancing the nanoparticle of copper in the fluid produces a dynamic variation as it declines close to the oscillating surface and improves further away from it.
- Fluid temperature drops as the magnetic dipole strength and mixed convection parameter go up.
- Water performs better compare to engine oil in this configuration.

References

[1] Nomana Abid, Muhammad Ramzan, Jae Dong Chung, Seifedine Kadry, and Yu-Ming Chu. Comparative analysis of magnetized partially ionized copper, copper oxide–water and kerosene oil nanofluid flow with cattaneo–christov heat flux. *Scientific Reports*, 10(1):19300, 2020.

[2] Humphrey Adun, Michael Adedeji, Mustafa Dagbasi, and Akinola Babatunde. Amelioration of thermodynamic performance and environmental analysis of an integrated solar power generation system with storage capacities using optimized ternary hybrid nanofluids. *Journal of Energy Storage*, 51:104531, 2022.

[3] Huda Alfannakh. Significances of magnetic dipole flow and melting heat transfer over suspended dust particles along with carbon nanotubes. *Frontiers in Energy Research*, 10:935108, 2022.

[4] Khalid Abdulkhaliq M Alharbi, Ahmed El-Sayed Ahmed, Maawiya Ould Sidi, Nandalur Ameer Ahammad, Abdullah Mohamed, Mohammed A El-Shorbagy, Muhammad Bilal, and Riadh Marzouki. Computational valuation of darcy ternary-hybrid nanofluid flow across an extending cylinder with induction effects. *Micromachines*, 13(4):588, 2022.

[5] Awatif Alhowaity, Haneen Hamam, Muhammad Bilal, and Aatif Ali. Numerical study of williamson hybrid nanofluid flow with thermal characteristics past over an extending surface. *Heat transfer*, 51(7):6641–6655, 2022.

[6] Muhammad Arif, Poom Kumam, Wiyada Kumam, and Zaydan Mostafa. Heat transfer analysis of radiator using different shaped nanoparticles water-based ternary hybrid nanofluid with applications: A fractional model. *Case Studies in Thermal Engineering*, 31:101837, 2022.

[7] Subhash C Ayirala and Dandina N Rao. Solubility, miscibility and their relation to interfacial tension in ternary liquid systems. *Fluid phase equilibria*, 249(1-2):82–91, 2006.

[8] Assad Ayub, Zulqurnain Sabir, Salem Ben Said, Haci Mehmet Baskonus, R Sadat, and Mohamed R Ali. Nature analysis of cross fluid flow with inclined magnetic dipole. *Microsystem Technologies*, 29(5):697–714, 2023.

[9] Muhammad Bilal, Hamdi Ayed, Anwar Saeed, Ameni Brahmia, Taza Gul, and Poom Kumam. The parametric computation of nonlinear convection magnetohydrodynamic nanofluid flow with internal heating across a fixed and spinning disk. *Waves in Random and Complex Media*, pages 1–16, 2022.

[10] G Bognár and K Hriczó. Ferrofluid flow in the presence of magnetic dipole. *Technische Mechanik-European Journal of Engineering Mechanics*, 39(1):3–15, 2019.

[11] Samia Elattar, Maha M Helmi, Mohamed Abdelghany Elkotb, MA El-Shorbagy, Anas Abdelrahman, Muhammad Bilal, and Aatif Ali. Computational assessment of hybrid nanofluid flow with the influence of hall current and chemical reaction over a slender stretching surface. *Alexandria Engineering Journal*, 61(12):10319–10331, 2022.

[12] SS Ghadikolaei and M Gholinia. Terrific effect of h2 on 3d free convection mhd flow of c2h6o2h2o hybrid base fluid to dissolve cu nanoparticles in a porous space considering the thermal radiation and nanoparticle shapes effects. *International Journal of Hydrogen Energy*, 44(31):17072–17083, 2019.

[13] Partha Protim Gharami, Md Alamin Gazi, Samsun Nahar Ananna, Sarder Firoz Ahmmed, et al. Numerical exploration of mhd unsteady flow of thnf passing through a moving cylinder with soret and dufour effects. *Partial Differential Equations in Applied Mathematics*, 6:100463, 2022.

[14] S Goqo, O Otegbeye, Singh TP, Trivedi M, and Ansari S. Unsteady flow of jeffrey nanofluid: a numerical simulation by bivariate simple iteration method. *Advances and Applications in Mathematical Sciences*, 19:1279 – 1307, 2020.

[15] Taza Gul, Muhammad Bilal, Muhammad Shuaib, Safyan Mukhtar, and Phatiphat Thounthong. Thin film flow of the water-based carbon nanotubes hybrid nanofluid under the magnetic effects. *Heat Transfer*, 49(6):3211–3227, 2020.

[16] Taza Gul, Abbas Khan, Muhammad Bilal, Nasser Aedh Alreshidi, Safyan Mukhtar, Zahir Shah, and Poom Kumam. Magnetic dipole impact on the hybrid nanofluid flow over an extending surface. *Scientific Reports*, 10(1):8474, 2020.

[17] Jafar Hasnain and Nomana Abid. Numerical investigation for thermal growth in water and engine oil-based ternary nanofluid using three different shaped nanoparticles over a linear and nonlinear stretching sheet. *Numerical Heat Transfer, Part A: Applications*, 83(12):1365–1376, 2023.

[18] T Hayat, Salman Ahmad, M Ijaz Khan, and A Alsaedi. Exploring magnetic dipole contribution on radiative flow of ferromagnetic williamson fluid. *Results in physics*, 8:545–551, 2018.

[19] Saman Hosseinzadeh and Davood Domiri Ganji. A novel approach for assessment of mhd mixed fluid around two parallel plates by consideration hybrid nanoparticles and shape factor. *Alexandria Engineering Journal*, 61(12):9779–9793, 2022.

[20] Michael Iyoko and Bakai Ishola Olajuwon. Study on impact of magnetic dipole and thermal radiation on flow/heat transfer of jeffery fluid over stretching sheet with suction/injection. *Journal of Advanced Research in Fluid Mechanics and Thermal Sciences*, 104(1):65–83, 2023.

[21] Wasim Jamshed, Nor Ain Azeany Mohd Nasir, Siti Suzilliana Putri Mohamed Isa, Rabia Safdar, Faisal Shahzad, Kottakkaran Sooppy Nisar, Mohamed R Eid, Abdel-Haleem Abdel-Aty, and IS Yahia. Thermal growth in solar water pump using prandtl–eyring hybrid nanofluid: a solar energy application. *Scientific reports*, 11(1):18704, 2021.

[22] Ramasamy Kandasamy, Nur Atikah bt Adnan, and Radiah Mohammad. Nanoparticle shape effects on squeezed mhd flow of water based cu, al2o3 and swcnts over a porous sensor surface. *Alexandria engineering journal*, 57(3):1433–1445, 2018.

[23] Umar Khan, Adnan, Naveed Ahmed, and Syed Tauseef Mohyud-Din. Surface thermal investigation in water functionalized al 2 o 3 and γal 2 o 3 nanomaterials-based nanofluid over a sensor surface. *Applied Nanoscience*, pages 1–11, 2020.

[24] V Kumar and RR Sahoo. Performance analysis of air heat exchanger equipped with various twisted turbulator inserts utilizing ternary hybrid nanomaterials. *Alex. Eng. J.*, 61(7):5033–5050, 2022.

[25] Varun Kumar, JK Madhukesh, AM Jyothi, BC Prasannakumara, M Ijaz Khan, and Yu-Ming Chu. Analysis of single and multi-wall carbon nanotubes (swcnt/mwcnt) in the flow of maxwell nanofluid with the impact of magnetic dipole. *Computational and Theoretical Chemistry*, 1200:113223, 2021.

[26] MP Mkhatshwa, SS Motsa, and P Sibanda. Mhd mixed convection flow of couple stress fluid over an oscillatory stretching sheet with thermophoresis and thermal diffusion using the overlapping multi-domain spectral relaxation approach. *International Journal of Applied and Computational Mathematics*, 7(3):93, 2021.

[27] S Odenbach. Magnetic fluids-suspensions of magnetic dipoles and their magnetic control. *Journal of physics: condensed matter*, 15(15):S1497, 2003.

[28] PO Olanrewaju. Effects of internal heat generation on hydromagnetic non-darcy flow and heat transfer over a stretching sheet in the presence of thermal radiation and ohmic dissipation. *World Applied Sciences Journal*, 16:37–45, 2012.

[29] Dulal Pal and Hiranmoy Mondal. Hydromagnetic non-darcy flow and heat transfer over a stretching sheet in the presence of thermal radiation and ohmic dissipation. *Communications in Nonlinear Science and Numerical Simulation*, 15(5):1197–1209, 2010.

[30] Muhammad Ramzan, Abdullah Dawar, Anwar Saeed, Poom Kumam, Kanokwan Sitthithakerngkiet, and Showkat Ahmad Lone. Analysis of the partially ionized kerosene oil-based ternary nanofluid flow over a convectively heated rotating surface. *Open Physics*, 20(1):507–525, 2022.

[31] Umair Rashid, Thabet Abdeljawad, Haiyi Liang, Azhar Iqbal, Muhammad Abbas, and Mohd Junaid Siddiqui. The shape effect of gold nanoparticles on squeezing nanofluid flow and heat transfer between parallel plates. *Mathematical Problems in Engineering*, 2020:1–12, 2020.

[32] Muhammad Rooman, Anwar Saeed, Zahir Shah, Ahmed Alshehri, Saeed Islam, Poom Kumam, and Panawan Suttiarporn. Electromagnetic trihybrid ellis nanofluid flow influenced with a magnetic dipole and chemical reaction across a vertical surface. *ACS omega*, 7(41):36611–36622, 2022.

[33] Wahaizad Safiei, MM Rahman, Ahmad Razlan Yusoff, MN Arifin, and W Tasnim. Effects of sio 2-al 2 o 3-zro 2 tri-hybrid nanofluids on surface roughness and cutting temperature in end milling process of aluminum alloy 6061-t6 using uncoated and coated cutting inserts with minimal quantity lubricant method. *Arabian Journal for Science and Engineering*, 46:7699–7718, 2021.

[34] Rashmi Rekha Sahoo. Heat transfer and second law characteristics of radiator with dissimilar shape nanoparticle-based ternary hybrid nanofluid. *Journal of Thermal Analysis and Calorimetry*, 146(2):827–839, 2021.

[35] Mayaram Sahu, Jahar Sarkar, and Laltu Chandra. Steady-state and transient hydrothermal analyses of single-phase natural circulation loop using water-based tri-hybrid nanofluids. *AIChE Journal*, 67(6):e17179, 2021.

[36] R Sajjad, M Mushtaq, S Farid, K Jabeen, and RMA Muntazir. Numerical simulations of magnetic dipole over a nonlinear radiative eyring–powell nanofluid considering viscous and ohmic dissipation effects. *Mathematical Problems in Engineering*, 2021:1–16, 2021.

[37] Franz E Schunck. Magnetic dipole moment of the electron. *arXiv preprint arXiv:0809.2770*, 2008.

[38] M Shanmugapriya, R Sundareswaran, P Senthil Kumar, and Gayathri Rangasamy. Impact of nanoparticle shape in enhancing heat transfer of magnetized ternary hybrid nanofluid. *Sustainable Energy Technologies and Assessments*, 53:102700, 2022.

[39] Ram Prakash Sharma, JK Madhukesh, Sunendra Shukla, and BC Prasannakumara. Numerical and levenberg–marquardt backpropagation neural networks computation of ternary nanofluid flow across parallel plates with nield boundary conditions. *The European Physical Journal Plus*, 138(1):63, 2023.

[40] Charles M Sommerfield. Magnetic dipole moment of the electron. *Physical Review*, 107(1):328, 1957.

[41] Lloyd N Trefethen. *Spectral methods in MATLAB*. SIAM, 2000.

[42] K Vafai, Ambreen A Khan, G Fatima, Sadiq M Sait, and R Ellahi. Dufour, soret and radiation effects with magnetic dipole on powell-eyring fluid flow over a stretching sheet. *International Journal of Numerical Methods for Heat & Fluid Flow*, 31(4):1085–1103, 2021.

[43] A Zeeshan and A Majeed. Effect of magnetic dipole on radiative non-darcian mixed convective flow over a stretching sheet in porous medium. *Journal of Nanofluids*, 5(4):617–626, 2016.

[44] Chun-Yu Zhang, Hang Ding, Peng Gao, and Yan-Ling Wu. Diffuse interface simulation of ternary fluids in contact with solid. *Journal of Computational Physics*, 309:37–51, 2016.

[45] Lian-Cun Zheng, Xin Jin, Xin-Xin Zhang, and Jun-Hong Zhang. Unsteady heat and mass transfer in mhd flow over an oscillatory stretching surface with soret and dufour effects. *Acta Mechanica Sinica*, 29(5):667–675, 2013.

Chapter 6

Exploring Numerical Analysis Of Unsteady Casson Ternary Nanofluid Flow Over A Bidirectionally Stretching Surface with Motile Gyrotactic Microorganisms And Nanoparticle Shape Factor

Chapter 6 introduces another power numerical technique for solving highly non-linear PDEs. In this chapter, we apply the overlapping BSQLM in the comprehensive analysis of the unsteady magnetohydrodynamic (MHD) flow of Casson ternary hybrid nanofluid, offering valuable insights into the complex interactions among magnetic fields, nanoparticle dispersion, gyrotactic microorganisms, and dissimilar nanoparticle shapes. The chapter examines the effects of physical parameters on flow surface characteristics, including local skin drags, Nusselt numbers, Sherwood numbers, and motile density numbers. The results are presented in tables and discussed in detail, shedding light on bioconvection patterns driven by the influence of nanoparticles on the temperature field, guiding the movement of microorganisms, velocity profile, thermal distribution, mass flux, and motile density profiles. Key findings from the analysis underscore the superiority of ternary hybrid nanofluids featuring diverse nanoparticle shapes compared to fluids with fewer components. The Casson parameter is key in optimizing nanofluid flow, heat, mass, and motile transfers. The numerically modelled problem holds significant implications for various applications, including environmental remediation, bioremediation, tissue engineering, food processing, textile processing, and industrial processes.

Exploring Numerical Analysis Of Unsteady Casson Ternary Nanofluid Flow Over A Bidirectionally Stretching Surface with Motile Gyrotactic Microorganisms And Nanoparticle Shape Factor

Folarin Oluwaseun [a], Sicelo Goqo [a], Hiranmoy Mondal [b*]

[a] *School of Mathematics, Statistics and Computer Science, University of KwaZulu-Natal, Private Bag X01, Scottsvile, Pietermaritzburg-3209, South Africa*

[b] *Department of Applied Mathematics, Maulana Abul Kalam Azad University of Technology, West Bengal, Kolkata-700064, India*

Abstract

This analysis contributes valuable insights into the unsteady MHD flow of Casson ternary hybrid nanofluid, offering a nuanced perspective on the interactions of magnetic fields, nanoparticle dispersion, gyrotactic microorganisms, and dissimilar nanoparticle shapes. The transformed governing equations with the suitable boundary conditions are solved using the numerical technique of overlapping bivariate spectral quasi-linearization method which offers robust numerical framework for the simulation and analysis. The effects of physical parameters on the flow surface characteristics are examined in form of the local skin drags, Nusselt number, Sherwood number, and motile density number with the results presented in tables and discussed in detail. In this current study, we explored bioconvection patterns, driven by the nanoparticles' influence on the temperature field: guiding the movement of microorganisms, velocity profile, thermal distribution, mass flux and motile density profiles. The ternary hybrid nanofluid, featuring diverse nanoparticle shapes, highlighted its superiority compared to hybrid fluids and nanofluids with fewer components and Casson parameter is established as a key factor in the optimization of nanofluid flow, heat, mass and motile transfers. The numerically modeled problem easily finds applications in the environmental remediation, bioremediation, tissue engineering, food processing, text processing, and industrial processes.

Keywords: Ternary hybrid nanofluid, Al_2O_3, TiO_2, Cu,Water, overlapping bivariate spectral quasi-linearization, bidirectionally stretching, nanopaticle shapes.

---

1. Introduction

In recent years, dynamic interplay of various physical and chemical phenomena in complex fluid flow scenarios has been a central focus of research due to its wide-ranging applications in various industrial, engineering, bio-engineering, and environmental processes. One such intricate scenario involves the Casson ternary hybrid nanofluid flow over a bidirectionally stretching surface, which embodies a multitude of forces that shape the fluid's behavior. Tri-hybrid nanofluids, characterized by the dispersion of nanoparticles in conventional fluids, exhibit remarkable thermal conductivity and enhanced heat transfer properties. The Casson fluid model, recognized for its non-Newtonian behavior, is particularly suited for modeling the flow of such nanofluids. Nadeem et al. [22] presented a model of 3D-MHD Casson fluid traveling in two lateral directions across a linearly extending porous surface. Shatnawi et al. [29] carried out the comparative analysis of Casson hybrid nanofluid models with induced magnetic radiative flow across a vertical permeable exponentially stretching sheet. Nandi et al. [23] recently examined the computational analysis of MHD Carreau tri-hybrid nano-liquid flow along an elongating surface with entropy generation.

The flow through porous media, often encountered in geological formations and industrial processes, has been a subject of considerable interest. Non-Darcy effects, describing deviations from Darcy's law in

*Corresponding author.

Email address : hiranmoymondal@yahoo.co.in (H. Mondal)

Preprint submitted to journal *February 1, 2024*

fluid flow through porous media, have been studied extensively. Kundu et al. [14] presented experimental and numerical investigation of fluid flow hydrodynamics in porous media with characterization into pre-Darcy, Darcy and non-Darcy flow regimes. Ibrahim et al. [9] examined the activation energy and chemical reaction effects on MHD Bingham nanofluid flow through a non-Darcy porous media. Mishra et al. [19] explored non-darcy model approach for the numerical investigation of MHD flow of williamson nanofluid with variable viscosity pasting a wedge within porous media. More interesting researches have been around the general idea of non-Darcy effects (See [6, 8, 21, 24]).
Ternary hybrid nanofluids, composed of a base fluid, nanoparticles, and microorganisms, are gaining recognition for their potential to enhance thermal conductivity and fluid properties. Slip flow, which occurs at the fluid-solid interface and is characterized by significant velocity gradients, plays a critical role in various industrial and biomedical applications. Muhammad et al. [32] recently presented ternary hybrid nanofluid slip flow on an inclined rotating disk with thermal radiation and viscous dissipation effects. Mahmood et al. [18] described ternary hybrid nanofluid near a stretching/shrinking sheet with heat generation/absorption and velocity slip on unsteady stagnation point flow. Impact of exponential form of internal heat generation on water-based ternary hybrid nanofluid flow by capitalizing non-Fourier heat flux model was critically examined by [28]. Ramzan et al. [25] carried out the computational assessment of Carreau ternary hybrid nanofluid influenced by MHD flow for entropy generation. Investigation of thermal performance of ternary hybrid nanofluid flow in a permeable inclined cylinder/plate was done by Madhukesh et al. [16]. The concept of nanoparticle shape factor, which characterizes the geometry and thermodynamic properties of nanoparticles, offers a novel perspective on the behavior of nanofluids. The shape factor can significantly influence the flow and heat transfer characteristics, but its role in the described scenario is yet to be fully explored (see [4, 10, 12, 13, 15]). However, some interesting experimental and numerical studies have been carried out. Waqas et al. [33] presented the importance of shape factor in Sisko nanofluid flow considering gold nanoparticles. Computational examination of Casson nanofluid due to a non-linear stretching sheet subjected to particle shape factor was presented by Jamshed et al. [11]. Soumya et al. [30] used Hamilton and Crosser's model to study the effects of NP shapes on Fe_3O_4-Ag/kerosene and Fe_3O_4-Ag/water hybrid nanofluid flow in suction/injection process with nonlinear-thermal-radiation and slip condition. Insight into the motion of water conveying three kinds of nanoparticles shapes on a horizontal surface was examined by Saleem et al. [27]. Arif et al. [2] discussed heat transfer analysis of fractional model of couple stress Casson tri-hybrid nanofluid using dissimilar shape nanoparticles in blood with biomedical applications.
Following the extensive literature, no study has been carried out on unsteady Casson ternary hybrid nanofluid flow over a bidirectionally stretching surface with motile gyrotactic microorganisms and nanoparticle shape factor. Therefore, this research work seeks to present the amalgamation of Casson ternary hybrid nanofluids, flow over bidirectional stretchable surface, motile gyrotactic microorganisms, and nanoparticle shape factor. The novelties and scientific contributions of our research work are thus presented:

- Presenting holistic approach to understanding a multifaceted problem by integrating various complex factors and providing insights into the behavior of unsteady Casson ternary nanofluid of copper(Cu), aluminium oxide(Al_2O_3) and titanium oxide(TiO_2) nanoparticles in water base fluid.
- Understanding how the microorganisms move in response to complex flow fields and gradients.
- Incorporating nanoparticle shape factor analysis which represents a cutting-edge dimension in heat transfer.
- The findings of the study can have direct implications in various practical applications, such as environmental remediation, bioremediation, tissue engineering, food processing, text processing, and industrial processes, making it a valuable contribution to applied research.

2. Physical Simulation Of The Problem

This study addresses the unsteady MHD flow of Casson ternary hybrid nanofluid, influenced by magnetic field, and the dispersion of nanoparticles, with motile gyrotactic microorganisms mixed into the fluid. Flow is assumed over a bidirectional stretching sheet and it is analyzed with respect to thermal radiation, chemical reaction, and nanoparticle shape factor. The stretching sheet is situated at $z = 0$ and it is extending with velocities $v_{1w} = \tilde{a}x$ and $v_{2w} = \tilde{b}y$ in x and y directions respectively. The flow is restricted to $z \geq 0$ and the based fluid of the ternary hybrid nanofluid is assumed to possess a uniform velocity with the dispersed nanoparticles and microorganism so that the directions of the swimming microorganisms are independent of the nanoparticles. The velocity components $(\tilde{v}_1, \tilde{v}_2, \tilde{v}_3)$ is taken in x, y and z-direction respectively. Uniform magnetic field, B is applied along z-direction and the magnetic Reynold number is assumed infinitesimally small so that the the induced magnetic field can be ignored. The geometry of the flow can be observed in Figure 1 and the mathematical simulation of the flow as modeled by [17, 35, 36] are

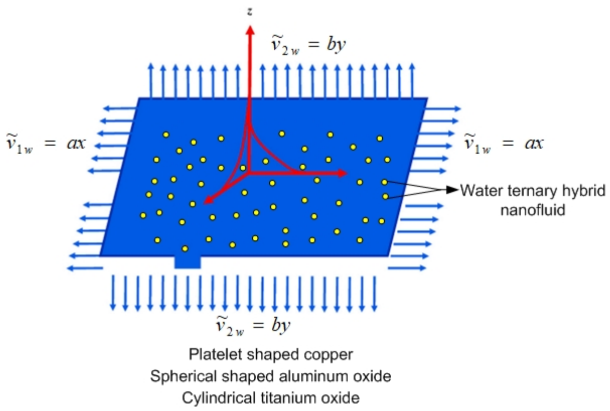

Figure 1: Flow Schematic Of The Model

$$\frac{\partial \tilde{v}_1}{\partial x} + \frac{\partial \tilde{v}_2}{\partial y} + \frac{\partial \tilde{v}_3}{\partial z} = 0, \tag{1}$$

$$\frac{\partial \tilde{v}_1}{\partial t} + \tilde{v}_1 \frac{\partial \tilde{v}_1}{\partial x} + \tilde{v}_2 \frac{\partial \tilde{v}_1}{\partial y} + \tilde{v}_3 \frac{\partial \tilde{v}_1}{\partial z} = \nu_{thnf} \left(1 + \frac{1}{\beta}\right) \left(\frac{\partial^2 \tilde{v}_1}{\partial z^2}\right) - \frac{\sigma_{thnf} B^2}{\rho_{thnf}} \tilde{v}_1 - \frac{\nu_{thnf}}{k^+} \tilde{v}_1, \tag{2}$$

$$\frac{\partial \tilde{v}_2}{\partial t} + \tilde{v}_1 \frac{\partial \tilde{v}_2}{\partial x} + \tilde{v}_2 \frac{\partial \tilde{v}_2}{\partial y} + \tilde{v}_3 \frac{\partial \tilde{v}_2}{\partial z} = \nu_{thnf} \left(1 + \frac{1}{\beta}\right) \left(\frac{\partial^2 \tilde{v}_2}{\partial z^2}\right) - \frac{\sigma_{thnf} B^2}{\rho_{thnf}} \tilde{v}_2 - \frac{\nu_{thnf}}{k^+} \tilde{v}_2, \tag{3}$$

$$\frac{\partial \tilde{T}}{\partial t} + \tilde{v}_1 \frac{\partial \tilde{T}}{\partial x} + \tilde{v}_2 \frac{\partial \tilde{T}}{\partial y} + \tilde{v}_3 \frac{\partial \tilde{T}}{\partial z} = \frac{k_{thnf}}{(\rho C_p)_{thnf}} \frac{\partial^2 \tilde{T}}{\partial z^2} - \frac{1}{(\rho C_p)_{thnf}} \frac{\partial \tilde{q}_r}{\partial z} + \tau^* \left[D_B \frac{\partial \tilde{C}}{\partial z} \frac{\partial \tilde{T}}{\partial z} + \frac{D_T}{\tilde{T}_\infty} \left(\frac{\partial \tilde{T}}{\partial z}\right)^2 \right], \tag{4}$$

$$\frac{\partial \tilde{C}}{\partial t} + \tilde{v}_1 \frac{\partial \tilde{C}}{\partial x} + \tilde{v}_2 \frac{\partial \tilde{C}}{\partial y} + \tilde{v}_3 \frac{\partial \tilde{C}}{\partial z} = D_B \frac{\partial^2 \tilde{C}}{\partial z^2} - k_{chr}(\tilde{C} - \tilde{C}_\infty) + \frac{D_T}{\tilde{T}_\infty} \frac{\partial^2 \tilde{T}}{\partial z^2}, \tag{5}$$

$$\frac{\partial \tilde{N}}{\partial t} + \tilde{v}_1 \frac{\partial \tilde{N}}{\partial x} + \tilde{v}_2 \frac{\partial \tilde{N}}{\partial y} + \tilde{v}_3 \frac{\partial \tilde{N}}{\partial z} + \frac{b^{**} W_b}{(\tilde{C}_w - \tilde{C}_\infty)} \left[\frac{\partial}{\partial z} \left(\tilde{N} \frac{\partial \tilde{C}}{\partial z} \right) \right] = D_m \frac{\partial^2 \tilde{N}}{\partial z^2}, \tag{6}$$

Suitable limiting conditions following are [35, 36]:

$$\begin{aligned}
&t < 0: \quad \tilde{v}_1 = 0, \quad \tilde{v}_2 = 0, \quad \tilde{T} = \tilde{T}_\infty, \quad \tilde{C} = \tilde{C}_\infty, \quad \tilde{N} = \tilde{N}_\infty, \quad \text{at} \quad z = 0, \\
&t \geq 0: \quad \tilde{v}_1 = v_{1w} = \tilde{a}x, \quad \tilde{v}_2 = v_{2w} = \tilde{b}y, \quad \tilde{T} = \tilde{T}_w, \quad \tilde{C} = \tilde{C}_w, \quad \tilde{N} = \tilde{N}_w, \quad \text{at} \quad z = 0, \\
&t \geq 0: \quad \tilde{v}_1 \to 0, \quad \tilde{v}_2 \to 0, \quad \tilde{T} \to \tilde{T}_\infty, \quad \tilde{C} \to \tilde{C}_\infty, \quad \tilde{N} \to \tilde{N}_\infty, \quad \text{as} \quad z \to \infty.
\end{aligned} \tag{7}$$

Proceeding from equation (1-8), we have that $(\tilde{T}_w, \tilde{C}_w, \tilde{N}_w)$ are respectively the temperature, concentration and microorganism density at the stretching surface, $(\tilde{T}_\infty, \tilde{C}_\infty, \tilde{N}_\infty)$ are the respective temperature, concentration and microorganism density in relations to the surroundings. $(\tilde{T}, \tilde{C}, \tilde{N})$ describe the fluid temperature, concentration and microorganism density within the flow region. k_{thnf}, ρ_{thnf}, μ_{thnf}, σ_{thnf} and $(\rho Cp)_{thnf}$ are respectively the ternary nanofluid thermal conductivity, density, dynamic viscosity, electrical conductivity and specific heat capacity, which are defined as follows [1, 7]:

$$\frac{\rho_{thnf}}{\rho_f} = (1 - \phi_2) \left[(1 - \phi_1) \left\{ (1 - \phi_3) + \phi_3 \left(\frac{\rho_3}{\rho_f} \right) \right\} + \phi_2 \left(\frac{\rho_2}{\rho_f} \right) \right] + \phi_1 \left(\frac{\rho_1}{\rho_f} \right),$$

$$\frac{(\rho Cp)_{thnf}}{(\rho Cp)_f} = (1-\phi_2)\left[(1-\phi_1)\left\{(1-\phi_3)+\phi_3\left(\frac{(\rho Cp)_3}{(\rho Cp)_f}\right)\right\}+\phi_2\left(\frac{(\rho Cp)_2}{(\rho Cp)_f}\right)\right]+\phi_1\left(\frac{(\rho Cp)_1}{(\rho Cp)_f}\right),$$

$$\frac{\sigma_{nf}}{\sigma_f} = \left[1+\frac{3\left(\frac{\sigma_1}{\sigma_f}-1\right)\varphi_1}{\left(\frac{\sigma_1}{\sigma_f}+2\right)-\left(\frac{\sigma_1}{\sigma_f}-1\right)\varphi_1}\right], \quad \frac{\sigma_{hnf}}{\sigma_{nf}} = \left[1+\frac{3\left(\frac{\sigma_2}{\sigma_{nf}}-1\right)\phi_2}{\left(\frac{\sigma_2}{\sigma_{nf}}+2\right)-\left(\frac{\sigma_2}{\sigma_{nf}}-1\right)\phi_2}\right],$$

$$\frac{\sigma_{thnf}}{\sigma_{hnf}} = \left[1+\frac{3\left(\frac{\sigma_3}{\sigma_{hnf}}-1\right)\phi_3}{\left(\frac{\sigma_3}{\sigma_{hnf}}+2\right)-\left(\frac{\sigma_3}{\sigma_{hnf}}-1\right)\phi_3}\right].$$

In defining the effective viscosity and thermal conductivity, we must consider the nanoparticle shapes as the nanodfluid viscosity and thermal conductivity are significantly influenced by the shape. The effective thermal conductivity and viscosity can therefore be evaluated via the Maxwell Garnet model, mixture model, and interpolation as follows [3, 5, 26].
The thermal conductivity of nanofluid having similar nnoparticles of any shape is given by

$$k_{nf} = \frac{k_p+(m-1)k_f-(m-1)\phi(k_p-k_f)}{k_p+(m-1)k_f+\phi(k_p-k_f)},$$

So, for the spherical shape nanoparticle, we have

$$\frac{\mu_{nf1}}{\mu_f} = 1+2.5\phi+6.2\phi^2, \quad \frac{k_{nf1}}{k_f} = \frac{k_1+2k_f-2\phi(k_1-k_f)}{k_1+2k_f+\phi(k_1-k_f)},$$

For platelet shape nanoparticle

$$\frac{\mu_{nf2}}{\mu_f} = 1+13.5\phi+904.4\phi^2, \quad \frac{k_{nf2}}{k_f}k_{nf2} = \frac{k_2+3.9k_f-3.9\phi(k_2-k_f)}{k_2+3.9k_f+\phi(k_2-k_f)},$$

For cylindrical shape nanoparticle

$$\frac{\mu_{nf3}}{\mu_f} = 1+37.1\phi+612.6\phi^2, \quad \frac{k_{nf3}}{k_f} = \frac{k_3+4.8k_f-4.8\phi(k_3-k_f)}{k_3+4.8k_f+\phi(k_3-k_f)},$$

The effective ternary hybrid nanofluid viscosity and thermal conductivity are therefore given by

$$\mu_{thnf} = \frac{\mu_{nf1}\phi_1+\mu_{nf2}\phi_2+\mu_{nf3}\phi_3}{\phi}, \quad k_{thnf} = \frac{k_{nf1}\phi_1+k_{nf2}\phi_2+k_{nf3}\phi_3}{\phi},$$

where, $\phi = \phi_1+\phi_2+\phi_3$, ϕ_1, ϕ_2, ϕ_3, are the nanoparticle volume fractions of aluminium oxide(Al_2O_3), copper(Cu), and titanium oxide(TiO_2) in that order. The shape factor of the nanoparticles is represented with $m = \frac{3}{\Psi}$, Ψ is the sphericity. For spherical shaped nanoparticle, $\Psi = 1$, so $m = 3$. For cylindrical shape, $\Psi = 0.52$, so $m = 5.8$. For platelet shape, $\Psi = 0.612$, so $m = 4.9$.
Table 2 depicts the numerical values of the thermophysical properties of the based fluid and the nanoparticles with shape used for each explicitly stated. The ternary nanofluid here comprises of water as based fluid, copper, aluminium oxide and titanium nanoparticles. The hybrid nanofluid used is a mixture of aluminium oxide and copper in water and the nanofluid consist of copper nanoparticles and water.
$\tilde{q_r}$ represents the radiative heat flux which following the Rosseland approximation can be defined as:

$$\tilde{q}_r = -\frac{4\sigma^*}{3k^*}\frac{\partial \tilde{T}^4}{\partial z},$$

where σ^* is the Stephan Boltzmann constant, k^* is the mean absorption coefficient, and $\tilde{T}^4$ can be expressed in expanded form using truncated Taylor's series about $\tilde{T}_\infty$ as :

$$\tilde{T}^4 = \tilde{T}_\infty^4 + 4\tilde{T}_\infty^3(\tilde{T}-\tilde{T}_\infty) + 6\tilde{T}_\infty^2(\tilde{T}-\tilde{T}_\infty)^2 + \cdots$$

Ignoring second and higher order terms, $\tilde{T}^4$ can be approximated as:

$$\tilde{T}^4 \approxeq 4\tilde{T}_\infty^3\tilde{T} - 3\tilde{T}_\infty^4$$

So;

$$\tilde{q}_r = -\frac{16\sigma^* \tilde{T}_\infty^3}{3k^*}\frac{\partial^2 \tilde{T}}{\partial z^2}$$

The PDEs (1-7) can be modified into non-dimensional form via the introduction of some self similarity transformations defined as follows (see [35])

$$\eta = z\sqrt{\frac{\tilde{a}}{\zeta\nu_f}}, \quad \tilde{v}_1 = \tilde{a}xf'(\eta,\zeta), \quad \tilde{v}_2 = \tilde{b}yg'(\eta,\zeta), \quad \tilde{v}_3 = -\sqrt{\tilde{a}\nu_f}[f(\eta,\zeta)+cg(\eta,\zeta)], \quad \zeta = 1-e^{-at},$$

$$\theta(\eta,\zeta) = \frac{\tilde{T}-\tilde{T}_\infty}{\tilde{T}_w-\tilde{T}_\infty}, \quad \varphi(\eta,\zeta) = \frac{\tilde{C}-\tilde{C}_\infty}{\tilde{C}_w-\tilde{C}_\infty}, \quad M(\eta,\zeta) = \frac{\tilde{N}-\tilde{N}_\infty}{\tilde{N}_w-\tilde{N}_\infty}, \quad c = \frac{b}{a}. \tag{8}$$

Implementing (8) on (1-7), we obtain the equations:

$$\frac{\nu_{thnf}}{\nu_f}\left(1+\frac{1}{\beta}\right)f'''(\eta,\zeta)+\zeta[f(\eta,\zeta)+cg(\eta,\zeta)]f''(\eta,\zeta)-\zeta f'^2(\eta,\zeta)-\zeta\left(\frac{\sigma_{thnf}}{\sigma_f}\frac{\rho_f}{\rho_{thnf}}+\frac{\nu_{thnf}}{\nu_f}\lambda_*\right)f'(\eta,\zeta)$$
$$+\frac{\eta}{2}(1-\zeta)f''(\eta,\zeta)-\zeta(1-\zeta)\frac{\partial^2 f}{\partial\eta\partial\zeta}=0, \tag{9}$$

$$\frac{\nu_{thnf}}{\nu_f}\left(1+\frac{1}{\beta}\right)g'''(\eta,\zeta)+\zeta[f(\eta,\zeta)+cg(\eta,\zeta)]g''(\eta,\zeta)-\zeta cg'^2(\eta,\zeta)-\zeta\left(\frac{\sigma_{thnf}}{\sigma_f}\frac{\rho_f}{\rho_{thnf}}+\frac{\nu_{thnf}}{\nu_f}\lambda_*\right)g'(\eta,\zeta)$$
$$\frac{\eta}{2}(1-\zeta)g''(\eta,\zeta)-\zeta(1-\zeta)\frac{\partial^2 g}{\partial\eta\partial\zeta}=0, \tag{10}$$

$$\frac{(\rho Cp)_f}{(\rho Cp)_{thnf}}\left\{\frac{k_{thnf}}{k_f}+N_r\right\}\theta''(\eta,\zeta)+P_r\zeta[f(\eta,\zeta)+cg(\eta,\zeta)]\theta'(\eta,\zeta)+\frac{\eta}{2}(1-\zeta)\theta'(\eta,\zeta)+P_rN_b\varphi'(\eta,\zeta)\theta'(\eta,\zeta)$$
$$+P_rN_t\theta'^2(\eta,\zeta)-P_r\zeta(1-\zeta)\frac{\partial\theta}{\partial\zeta}=0, \tag{11}$$

$$\varphi''(\eta,\zeta)+Le\frac{N_t}{N_b}\theta''(\eta,\zeta)+\zeta Le[f(\eta,\zeta)+cg(\eta,\zeta)]\varphi'(\eta,\zeta)-\zeta LeR_k\varphi(\eta,\zeta)+\frac{\eta}{2}Le(1-\zeta)\varphi'(\eta,\zeta)-Le\zeta(1-\zeta)\frac{\partial\varphi}{\partial\zeta}=0, \tag{12}$$

$$M''(\eta,\zeta)+\zeta Lb[f(\eta,\zeta)+cg(\eta,\zeta)]M'(\eta,\zeta)-Pe[M(\eta,\zeta)+R_{mb}]\varphi''(\eta,\zeta)-PeM'(\eta,\zeta)\varphi'(\eta,\zeta)$$
$$+\frac{\eta}{2}Lb(1-\zeta)M'(\eta,\zeta)-Lb\zeta(1-\zeta)\frac{\partial M}{\partial\zeta}=0. \tag{13}$$

Now the corresponding nondimensional suitable limiting conditions are

$$f(0,\zeta)=0, \quad f'(0,\zeta)=1, \quad g(0,\zeta)=0, \quad g'(0,\zeta)=c \quad \theta(0,\zeta)=1, \quad \varphi(0,\zeta)=1, \quad M(0,\zeta)=1, \quad \zeta\geq 0, \quad \text{at } \eta=0,$$
$$f'(\infty,\zeta)\to 0, \quad g'(\infty,\zeta)\to 0, \quad \theta(\infty,\zeta)\to 0, \quad \varphi(\infty,\zeta)\to 0, \quad M(\infty,\zeta)\to 0, \quad \zeta\geq 0 \quad \text{as } \eta\to\infty. \tag{14}$$

We have defined the dimensionless variables used above as follows

$H_h = \frac{B^2\sigma_f}{a\rho_f}$, is the magnetic parameter, $\lambda_* = \frac{\nu_f}{ak^+}$, is the porosity parameter,

$N_b = \frac{\tau^* D_B(\tilde{C}_w-\tilde{C}_\infty)}{\nu_f}$, is the Brownian motion parameter, $P_r = \frac{(\rho Cp)_f\nu_f}{k_f}$, is Prandtl number,

$N_t = \frac{\tau^* D_T(\tilde{T}_w-\tilde{T}_\infty)}{\nu_f\tilde{T}_\infty}$, is the thermophoresis parameter, $R_k = \frac{k_r^2}{b}$, is the chemical reaction parameter,

$Le = \frac{\nu_f}{D_B}$, is the Lewis number, $Pe = \frac{b^{**}W_c}{D_m}$, is the bioconvection Peclet number,

5

$$R_{mb} = \frac{\tilde{N}_{mb}}{\tilde{N}_w - \tilde{N}_\infty}, \text{ is motile density ratio,} \quad N_r = \frac{16\sigma^* T_\infty^3}{3k_f k^*}, \text{ is the thermal radiation number,}$$

$$Lb = \frac{\nu_f}{D_m}, \text{ is bioconvection Lewis number,}$$

Engineering quantities of particular interest are the skin friction coefficient, Nusselt number, Sherwood number and motile microorganism density number which are locally defined as follows

$$C_{fx} = \frac{\mu_{thnf}}{\rho_f v_{1w}^2}\left(\frac{\partial \tilde{v}_1}{\partial z}\right)_{z=0}, \quad C_{gy} = \frac{\mu_{thnf}}{\rho_f v_{2w}^2}\left(\frac{\partial \tilde{v}_2}{\partial z}\right)_{z=0}, \quad Nu_x = \frac{-x}{k_f(\tilde{T}_w - \tilde{T}_\infty)}\left\{k_{thnf} + \frac{16\sigma^* T_\infty^3}{3k^*}\right\}\left(\frac{\partial \tilde{T}}{\partial z}\right)_{z=0},$$

$$Sh_x = \frac{-x}{(\tilde{C}_w - \tilde{C}_\infty)}\left(\frac{\partial \tilde{C}}{\partial z}\right)_{z=0}, \quad Nh_x = \frac{-x}{(\tilde{N}_w - \tilde{N}_\infty)}\left(\frac{\partial \tilde{N}}{\partial z}\right)_{z=0}. \tag{15}$$

These physical quantities in dimensionless forms are given by:

$$Re_x^{\frac{1}{2}}\zeta^{-\frac{1}{2}}C_{fx} = \frac{\mu_{thnf}}{\rho_f \nu_f} f''(0,\zeta), \quad Re_y^{\frac{1}{2}}\zeta^{-\frac{1}{2}}C_{gy} = \frac{\mu_{thnf}}{c\rho_f \nu_f} g''(0,\zeta), \quad Re_x^{-\frac{1}{2}}\zeta^{-\frac{1}{2}}Nu_x = -\left(\frac{k_{thnf}}{k_f} + N_r\right)\theta'(0,\zeta),$$

$$Re_x^{-\frac{1}{2}}\zeta^{-\frac{1}{2}}Sh_x = -\varphi'(0,\zeta), \quad Re_x^{-\frac{1}{2}}\zeta^{-\frac{1}{2}}Nh_x = -M'(0,\zeta). \tag{16}$$

where, $Re_x^{\frac{1}{2}} = \frac{a^{\frac{1}{2}}x}{\nu_f^{\frac{1}{2}}}$ and $Re_y^{\frac{1}{2}} = \frac{a^{\frac{1}{2}}y}{\nu_f^{\frac{1}{2}}}$ are the Reynolds numbers along x- and y-directions respectively.

Table 1: Numerical values of thermophysical characteristics of the nanomaterials and based fluids [26, 34, 32]

Material	$\rho(Kgm^{-3})$	$C_p(JKg^{-1}K^{-1})$	$k(Wm^{-1}K^{-1})$	$\beta(K^{-1})$	$\sigma(Sm^{-1})$	Nanoparticle shape
Water	997.1	4179	0.613	21×10^{-5}	5.5×10^{-6}	-
Copper	8933	385	401	51×10^{-6}	5.96×10^{7}	Platelet
Al_2O_3	4907	765	3.7	5.08×10^{-5}	1×10^{-9}	Spherical
TiO_2	4250	686.2	8.9538	2.4×10^{-5}	2.38×10^{6}	Cylindrical

3. Numerical Solution

The system of non-linear partial differential equations (9 − 13) subjects to the boundary conditions (14) is solved via the overlapping bivariate spectral quasi-linearization method (OBSQLM). The main principle of this method involves partitioning of the solution domain into overlapping sub-grids, implementing at each sub-interval the bivariate spectral collocations and quasi-linearization [20]. The semi-finite, $I = [0, \infty)$ space domain is first replaced with a truncated finite domain $I = [0, \eta_\infty]$ for easy implementation of the method at ∞. $I = [0, \eta_\infty]$ and $J = [0, \zeta_f]$ space and time domains are then partitioned into p and q overlapping sub-interval respectively that can be defined as

$$I_\varrho = [\eta_0^\varepsilon, \eta_{N_\eta}^\varepsilon], \qquad \varrho = 1, 2, 3, \cdots, p$$

$$J_\varepsilon = [\zeta_0^\varrho, \zeta_{N_\zeta}^\varrho], \qquad \varepsilon = 1, 2, 3, \cdots, q$$

Next, using Chebyshev-Gauss-Lobatto collocation points, we carry out the discretization of each sub-interval of I_ε and J_ϱ into $N_\eta + 1$ and $N_\zeta + 1$ collocation points respectively with the domains having uniform lengths defined as

$$L_\eta = \frac{\eta_\infty}{p + (1-p)\left(\frac{1-\cos\left(\frac{\pi}{N_\eta}\right)}{2}\right)}$$

$$L_\zeta = \frac{\zeta_f}{q + (1-q)\left(\frac{1-\cos\left(\frac{\pi}{N_\zeta}\right)}{2}\right)}$$

Next we apply the quasi-linearization technique at subintervals I_ϱ and J_ε to transform the non-linear PDEs into linear PDEs as follows:

$$\wedge_{11}^{(\varepsilon,\varrho)} f_{r+1}'''^{(\varepsilon,\varrho)} + \wedge_{12}^{(\varepsilon,\varrho)} f_{r+1}''^{(\varepsilon,\varrho)} + \wedge_{13}^{(\varepsilon,\varrho)} f_{r+1}'^{(\varepsilon,\varrho)} + \wedge_{14}^{(\varepsilon,\varrho)} f_{r+1}^{(\varepsilon,\varrho)} = \zeta(1-\zeta)\frac{\partial f_{r+1}'^{(\varepsilon,\varrho)}}{\partial\zeta} + a_1^{(\varepsilon,\varrho)}, \tag{17}$$

$$\wedge_{21}^{(\varepsilon,\varrho)} g_{r+1}'''^{(\varepsilon,\varrho)} + \wedge_{22}^{(\varepsilon,\varrho)} g_{r+1}''^{(\varepsilon,\varrho)} + \wedge_{23}^{(\varepsilon,\varrho)} g_{r+1}'^{(\varepsilon,\varrho)} + \wedge_{24}^{(\varepsilon,\varrho)} g_{r+1}^{(\varepsilon,\varrho)} = \zeta(1-\zeta)\frac{\partial g_{r+1}'^{(\varepsilon,\varrho)}}{\partial\zeta} + a_2^{(\varepsilon,\varrho)}, \tag{18}$$

$$\wedge_{31}^{(\varepsilon,\varrho)} \theta_{r+1}''^{(\varepsilon,\varrho)} + \wedge_{32}^{(\varepsilon,\varrho)} \theta_{r+1}'^{(\varepsilon,\varrho)} + \wedge_{33}^{(\varepsilon,\varrho)} \theta_{r+1}^{(\varepsilon,\varrho)} = P_r\zeta(1-\zeta)\frac{\partial\theta_{r+1}^{(\varepsilon,\varrho)}}{\partial\varsigma} + a_3^{(\varepsilon,\varrho)}, \tag{19}$$

$$\wedge_{41}^{(\varepsilon,\varrho)} \varphi_{r+1}''^{(\varepsilon,\varrho)} + \wedge_{42}^{(\varepsilon,\varrho)} \varphi_{r+1}'^{(\varepsilon,\varrho)} + \wedge_{43}^{(\varepsilon,\varrho)} \varphi_{r+1}^{(\varepsilon,\varrho)} = Le\zeta(1-\zeta)\frac{\partial\varphi_{r+1}^{(\varepsilon,\varrho)}}{\partial\zeta} + a_4^{(\varepsilon,\varrho)}. \tag{20}$$

$$\wedge_{51}^{(\varepsilon,\varrho)} M_{r+1}''^{(\varepsilon,\varrho)} + \wedge_{52}^{(\varepsilon,\varrho)} M_{r+1}'^{(\varepsilon,\varrho)} + \wedge_{53}^{(\varepsilon,\varrho)} M_{r+1}^{(\varepsilon,\varrho)} = Lb\zeta(1-\zeta)\frac{\partial M_{r+1}^{(\varepsilon,\varrho)}}{\partial\zeta} + a_5^{(\varepsilon,\varrho)}. \tag{21}$$

where

$$\wedge_{11}^{(\varepsilon,\varrho)} = \frac{\nu_{thnf}}{\nu_f}\left(1+\frac{1}{\beta}\right), \quad \wedge_{12}^{(\varepsilon,\varrho)} = \zeta(f_r^{(\varepsilon,\varrho)}+cg_r^{(\varepsilon,\varrho)})+\frac{1}{2}(1-\zeta)\eta, \quad \wedge_{13}^{(\varepsilon,\varrho)} = -2\zeta f_r'^{(\varepsilon,\varrho)}-\zeta\left(\frac{\sigma_{thnf}}{\sigma_f}\frac{\rho_f}{\rho_{thnf}}H_h+\left(\frac{\nu_{thnf}}{\nu_f}\right)\lambda_*\right),$$

$$\wedge_{14}^{(\varepsilon,\varrho)} = \zeta f_r''^{(\varepsilon,\varrho)}, \quad a_1^{(\varepsilon,\varrho)} = \zeta(f_r^{(\varepsilon,\varrho)} f_r''^{(\varepsilon,\varrho)}-f_r'^{2(\varepsilon,\varrho)}), \quad \wedge_{21}^{(\varepsilon,\varrho)} = \frac{\nu_{thnf}}{\nu_f}\left(1+\frac{1}{\beta}\right), \quad \wedge_{22}^{(\varepsilon,\varrho)} = \zeta(f_r^{(\varepsilon,\varrho)}+cg_r^{(\varepsilon,\varrho)})+\frac{1}{2}(1-\zeta)\eta,$$

$$\wedge_{23}^{(\varepsilon,\varrho)} = -2c\zeta g_r'^{(\varepsilon,\varrho)}-\zeta\left(\frac{\sigma_{thnf}}{\sigma_f}\frac{\rho_f}{\rho_{thnf}}H_h+\left(\frac{\nu_{thnf}}{\nu_f}\right)\lambda_*\right), \quad \wedge_{24}^{(\varepsilon,\varrho)} = \zeta c g_r''^{(\varepsilon,\varrho)}, \quad a_2^{(\varepsilon,\varrho)} = c\zeta(g_r^{(\varepsilon,\varrho)} g_r''^{(\varepsilon,\varrho)}-g_r'^{2(\varepsilon,\varrho)}),$$

$$\wedge_{31}^{(\varepsilon,\varrho)} = \frac{(\rho Cp)_f}{(\rho Cp)_{thnf}}\left(\frac{k_{thnf}}{k_f}+N_r\right), \quad \wedge_{32}^{(\varepsilon,\varrho)} = P_r\zeta(f_r^{(\varepsilon,\varrho)}+cg_r^{(\varepsilon,\varrho)})+\frac{1}{2}P_r(1-\zeta)\eta+P_rN_b\varphi_r'^{(\varepsilon,\varrho)}+P_rN_t\theta_r'^{(\varepsilon,\varrho)},$$

$$a_3^{(\varepsilon,\varrho)} = P_rN_t\theta_r'^{2(\varepsilon,\varrho)}, \quad \wedge_{41}^{(\varepsilon,\varrho)} = 1, \quad \wedge_{42}^{(\varepsilon,\varrho)} = Le\zeta(f_r^{(\varepsilon,\varrho)}+cg_r^{(\varepsilon,\varrho)})+\frac{1}{2}Le(1-\zeta)\eta, \quad \wedge_{43}^{(\varepsilon,\varrho)} = -Le\zeta R_k,$$

$$a_4^{(\varepsilon,\varrho)} = -\frac{N_t}{N_b}Le\theta_r''^{(\varepsilon,\varrho)}, \quad \wedge_{51}^{(\varepsilon,\varrho)}=1, \quad \wedge_{52}^{(\varepsilon,\varrho)}=Lb\zeta(f_r^{(\varepsilon,\varrho)}+cg_r^{(\varepsilon,\varrho)})+\tfrac{1}{2}Le(1-\zeta)\eta-Pe\varphi_r'^{(\varepsilon,\varrho)}, \quad \wedge_{53}^{(\varepsilon,\varrho)}=-Pe\varphi_r''^{(\varepsilon,\varrho)}, \quad a_5^{(\varepsilon,\varrho)}=-PeR_{mb}\varphi_r''^{(\varepsilon,\varrho)}$$

With the knowledge that spectral collocation is only applicable in [-1,1], we therefore convert spatial and time domains to the form [-1,1] using the linear transformations given by

$$\eta_i^\varrho = \frac{L_\eta}{2}(\hat{\eta}_i+1), \qquad \hat{\eta}_{i=0}^{N_\eta} = \cos\left(\frac{\pi i}{N_\eta}\right) \tag{22}$$

$$\zeta_j^\epsilon = \frac{L_\zeta}{2}(\hat{\zeta}_j+1), \qquad \hat{\zeta}_{i=0}^{N_\zeta} = \cos\left(\frac{\pi j}{N_\zeta}\right) \tag{23}$$

Working in the premise that the solution can be approximated to $f(\eta,\zeta)$, $g(\eta,\zeta)$, $\theta(\eta,\zeta)$, $\varphi(\eta,\zeta)$, and $M(\eta,\zeta)$ at each sub - domain, using the well established bivariate Lagrange interpolation polynomial given by

$$f(\eta,\zeta) \approx \sum_{k=0}^{N_\eta}\sum_{l=0}^{N_\zeta} f(\eta_k,\zeta_l)L_k(\eta)L_l(\zeta), \tag{24}$$

$$g(\eta,\zeta) \approx \sum_{k=0}^{N_\eta}\sum_{l=0}^{N_\zeta} g(\eta_k,\zeta_l)L_k(\eta)L_l(\zeta), \tag{25}$$

$$\theta(\eta,\zeta) \approx \sum_{k=0}^{N_\eta}\sum_{l=0}^{N_\zeta} \theta(\eta_k,\zeta_l) L_k(\eta) L_l(\zeta), \tag{26}$$

$$\varphi(\eta,\zeta) \approx \sum_{k=0}^{M_\eta}\sum_{l=0}^{M_\zeta} \varphi(\eta_k,\zeta_l) L_k(\eta) L_l(\zeta). \tag{27}$$

$$M(\eta,\zeta) \approx \sum_{k=0}^{N_\eta}\sum_{l=0}^{N_\zeta} N(\eta_k,\zeta_l) L_k(\eta) L_l(\zeta). \tag{28}$$

where functions $L_k(\eta)$ and $L_l(\zeta)$ are the well-known characteristic Lagrange cardinal polynomial based on the Chebyshev-Gauss-Lobatto points [31]. We employed the differential matrices for collocation that are of the form

$$\left[\frac{\partial f_{r+1}^{(\epsilon,\varrho)}}{\partial \zeta}\right|_{(\eta=\eta_i,\zeta=\zeta_j)} = \sum_{k=0}^{N_\zeta} \hat{D}_{i,k}^{(\varepsilon)} F_{r+1}^{(\varepsilon,\varrho)}(\hat{\eta}_k,\hat{\zeta}_j) = \boldsymbol{D}\boldsymbol{F}_{j,r+1},$$

$$\left[\frac{\partial f_{r+1}^{(\varepsilon,\varrho)}}{\partial \zeta}\right|_{(\eta=\eta_i,\zeta=\zeta_j)} = \left(\frac{2}{\eta_{N_\zeta}^{\varrho} - \zeta_0^{\varrho}}\right) \sum_{l=0}^{N_\zeta} \hat{d}_{j,l}^{(\varrho)} F_{r+1}^{(\varepsilon,\varrho)}(\hat{\eta}_i,\hat{\zeta}_l) = \sum_{l=0}^{N_\zeta} d_{j,l}\boldsymbol{F}_{l,r+1},$$

$$\left[\frac{\partial g_{r+1}^{(\epsilon,\varrho)}}{\partial \zeta}\right|_{(\eta=\eta_i,\zeta=\zeta_j)} = \sum_{k=0}^{N_\zeta} \hat{D}_{i,k}^{(\varepsilon)} G_{r+1}^{(\varepsilon,\varrho)}(\hat{\eta}_k,\hat{\zeta}_j) = \boldsymbol{D}\boldsymbol{G}_{j,r+1},$$

$$\left[\frac{\partial g_{r+1}^{(\varepsilon,\varrho)}}{\partial \zeta}\right|_{(\eta=\eta_i,\zeta=\zeta_j)} = \left(\frac{2}{\eta_{N_\zeta}^{\varrho} - \zeta_0^{\varrho}}\right) \sum_{l=0}^{N_\zeta} \hat{d}_{j,l}^{(\varrho)} G_{r+1}^{(\varepsilon,\varrho)}(\hat{\eta}_i,\hat{\zeta}_l) = \sum_{l=0}^{N_\zeta} d_{j,l}\boldsymbol{G}_{l,r+1},$$

$$\left[\frac{\partial \theta_{r+1}^{(\epsilon,\varrho)}}{\partial \zeta}\right|_{(\eta=\eta_i,\zeta=\zeta_j)} = \sum_{k=0}^{N_\eta} \hat{D}_{i,k}^{(\varepsilon)} \Theta_{r+1}^{(\varepsilon,\varrho)}(\hat{\eta}_k,\hat{\zeta}_j) = \boldsymbol{D}\boldsymbol{\Theta}_{j,r+1},$$

$$\left[\frac{\partial \theta_{r+1}^{(\varepsilon,\varrho)}}{\partial \zeta}\right|_{(\eta=\eta_i,\zeta=\zeta_j)} = \left(\frac{2}{\zeta_{N_\zeta}^{\varrho} - \zeta_0^{\varrho}}\right) \sum_{l=0}^{N_\zeta} \hat{d}_{j,l}^{(\varrho)} \Theta_{r+1}^{(\varepsilon,\varrho)}(\hat{\eta}_i,\hat{\zeta}_l) = \sum_{l=0}^{N_\zeta} d_{j,l}\boldsymbol{\Theta}_{l,r+1},$$

$$\left[\frac{\partial \varphi_{r+1}^{(\epsilon,\varrho)}}{\partial \zeta}\right|_{(\eta=\eta_i,\zeta=\zeta_j)} = \sum_{k=0}^{N_\eta} \hat{D}_{i,k}^{(\varepsilon)} \Phi_{r+1}^{(\varepsilon,\varrho)}(\hat{\eta}_k,\hat{\zeta}_j) = \boldsymbol{D}\boldsymbol{\Phi}_{j,r+1},$$

$$\left[\frac{\partial \varphi_{r+1}^{(\varepsilon,\varrho)}}{\partial \varsigma}\right|_{(\eta=\eta_i,\zeta=\zeta_j)} = \left(\frac{2}{\zeta_{N_\zeta}^{\varrho} - \zeta_0^{\varrho}}\right) \sum_{l=0}^{N_\zeta} \hat{d}_{j,l}^{(\varrho)} \Phi_{r+1}^{(\varepsilon,\varrho)}(\hat{\eta}_i,\hat{\zeta}_l) = \sum_{l=0}^{N_\zeta} d_{j,l}\boldsymbol{\Phi}_{l,r+1}.$$

$$\left[\frac{\partial M_{r+1}^{(\epsilon,\varrho)}}{\partial \zeta}\right|_{(\eta=\eta_i,\zeta=\zeta_j)} = \sum_{k=0}^{N_\eta} \hat{D}_{i,k}^{(\varepsilon)} M_{r+1}^{(\varepsilon,\varrho)}(\hat{\eta}_k,\hat{\zeta}_j) = \boldsymbol{D}\boldsymbol{M}_{j,r+1},$$

$$\left[\frac{\partial M_{r+1}^{(\varepsilon,\varrho)}}{\partial \varsigma}\right|_{(\eta=\eta_i,\zeta=\zeta_j)} = \left(\frac{2}{\zeta_{N_\zeta}^{\varrho} - \zeta_0^{\varrho}}\right) \sum_{l=0}^{N_\zeta} \hat{d}_{j,l}^{(\varrho)} M_{r+1}^{(\varepsilon,\varrho)}(\hat{\eta}_i,\hat{\zeta}_l) = \sum_{l=0}^{N_\zeta} d_{j,l}\boldsymbol{M}_{l,r+1}. \tag{29}$$

where $\hat{D}_{i,k}^{(\varepsilon)} = \frac{2}{\eta_{N_\eta}^{\varepsilon} - \eta_0^{\varepsilon}} D_{i,k}(i,k = 0,1,2,\cdots N_\eta)$, with $D_{i,k}$ represents typical first order Chebyshev - Gauss - Lobatto differentiation matrix of size $(N_\eta + 1) \times (N_\eta + 1)$ as defined by [31], and $\hat{d}_{j,l}^{\varrho} =$

$\frac{\zeta^{\varrho}_{N_\zeta}-\zeta^{\varrho}_0}{2}d_{j,l}(j,l = 0,1,2,\cdots,N_\zeta)$ describe the typical first order Chebyshev differentiation matrices of size $(N_\eta+1)\times(N_\zeta+1)$ as used by [20]. $\boldsymbol{F}_j$, $\boldsymbol{G}_j$, $\boldsymbol{\Theta}_j$, $\boldsymbol{\Phi}_j$, and $\boldsymbol{M}_j$, are vectors of the form

$$\boldsymbol{F}_j = [f^{(\varepsilon,\varrho)}(\eta_0,\zeta_j), f^{(\varepsilon,\varrho)}(\eta_1,\zeta_j),\cdots, f^{(\varepsilon,\varrho)}(\zeta_{N_\eta},\zeta_j)]^T, \tag{30}$$

$$\boldsymbol{G}_j = [g^{(\varepsilon,\varrho)}(\eta_0,\zeta_j), g^{(\varepsilon,\varrho)}(\eta_1,\zeta_j),\cdots, g^{(\varepsilon,\varrho)}(\zeta_{N_\eta},\zeta_j)]^T, \tag{31}$$

$$\boldsymbol{\Theta}_j = [\theta^{(\varepsilon,\varrho)}(\eta_0,\zeta_j), \theta^{(\varepsilon,\varrho)}(\eta_1,\zeta_j),\cdots, \theta^{(\varepsilon,\varrho)}(\eta_{M_\eta},\zeta_j)]^T, \tag{32}$$

$$\boldsymbol{\Phi}_j = [\varphi^{(\varepsilon,\varrho)}(\eta_0,\zeta_j), \varphi^{(\varepsilon,\varrho)}(\eta_1,\zeta_j),\cdots, \varphi^{(\varepsilon,\varrho)}(\eta_{N_\eta},\zeta_j)]^T. \tag{33}$$

$$\boldsymbol{M}_j = [M^{(\varepsilon,\varrho)}(\eta_0,\zeta_j), M^{(\varepsilon,\varrho)}(\eta_1,\zeta_j),\cdots, M^{(\varepsilon,\varrho)}(\zeta_{N_\eta},\zeta_j)]^T, \tag{34}$$

With consideration to the overlapping last two points in the $\varepsilon - th$ sub-interval and the first two points in the $(\varepsilon+1)th$ sub - interval, the differentiation matrix, $\boldsymbol{D}$ for the overlapping grid in each case is assembled carefully, discarding the rows corresponding to the recurrent points, see [20] for the structure of this matrix.
The decoupled system becomes:

$$[\wedge^{(\varepsilon,\varrho)}_{11}\boldsymbol{D}^3 + \wedge^{(\varepsilon,\varrho)}_{12}\boldsymbol{D}^2 + \wedge^{(\varepsilon,\varrho)}_{13}\boldsymbol{D} + \wedge^{(\varepsilon,\varrho)}_{14}\boldsymbol{I}]\boldsymbol{F}_{i,r+1} - \zeta(1-\zeta)\sum_{j=0}^{m} d_{(i,j)}\boldsymbol{D}\boldsymbol{F}_{j,r+1} = R^{i}_{1,r}, \tag{35}$$

$$[\wedge^{(\varepsilon,\varrho)}_{21}\boldsymbol{D}^3 + \wedge^{(\varepsilon,\varrho)}_{22}\boldsymbol{D}^2 + \wedge^{(\varepsilon,\varrho)}_{23}\boldsymbol{D} + \wedge^{(\varepsilon,\varrho)}_{24}\boldsymbol{I}]\boldsymbol{G}_{i,r+1} - \zeta(1-\zeta)\sum_{j=0}^{m} d_{(i,j)}\boldsymbol{D}\boldsymbol{F}_{j,r+1} = R^{i}_{2,r}, \tag{36}$$

$$[\wedge^{(\varepsilon,\varrho)}_{31}\boldsymbol{D}^2 + \wedge^{(\varepsilon,\varrho)}_{32}\boldsymbol{D}]\boldsymbol{\Theta}_{i,r+1} - P_r\zeta(1-\zeta)\sum_{j=0}^{m} d_{(i,j)}\boldsymbol{\Theta}_{j,r+1} = R^{i}_{3,r}, \tag{37}$$

$$[\wedge^{(\varepsilon,\varrho)}_{41}\boldsymbol{D}^2 + \wedge^{(\varepsilon,\varrho)}_{42}\boldsymbol{D} + \wedge^{(\varepsilon,\varrho)}_{43}\boldsymbol{I}]\boldsymbol{\Phi}_{i,r+1} - Le\zeta(1-\zeta)\sum_{j=0}^{m} d_{(i,j)}\boldsymbol{\Phi}_{j,r+1} = R^{i}_{4,r}. \tag{38}$$

$$[\wedge^{(\varepsilon,\varrho)}_{51}\boldsymbol{D}^2 + \wedge^{(\varepsilon,\varrho)}_{52}\boldsymbol{D} + \wedge^{(\varepsilon,\varrho)}_{53}\boldsymbol{I}]\boldsymbol{M}_{i,r+1} - Lb\zeta(1-\zeta)\sum_{j=0}^{m} d_{(i,j)}\boldsymbol{M}_{j,r+1} = R^{i}_{5,r}. \tag{39}$$

where $\boldsymbol{I}$; is an identity matrix, $m = N_\zeta + (N_\zeta)\times(q-1)$ is the overall collocations in the whole time domain and

$$R^{i}_{1,r} = a^{(\varepsilon,\varrho)}_1,\;\; R^{i}_{2,r} = a^{(\varepsilon,\varrho)}_2,\;\; R^{i}_{3,r} = a^{(\varepsilon,\varrho)}_3,\;\; R^{i}_{4,r} = a^{(\varepsilon,\varrho)}_4,\;\; R^{i}_{5,r} = a^{(\varepsilon,\varrho)}_5.$$

4. Results And Analysis

This study presents a comprehensive numerical simulation of unsteady Casson ternary nanofluid flow over a bidirectionally stretching surface, incorporating motile gyrotactic microorgamisms, chemical reactions, and nanoparticle shape factor. To facilitate the analysis, the governing equations are non-dimensionalized via appropriate self similarity transformations, and the resulting system is numerically solved using overlapping bivariate spectral quasi-linearization method (OBSQLM). To rigorously validate the computational framework and instill confidence in the findings, a meticulous code verification process was done by computing the local skin friction coefficient and comparing with the established results of Yanala et al. [35] and Yousif et al. [36] under specific conditions: thermal radiation number N_r, magnetic parameter H_h, Prandtl number P_r, chemical reaction parameter R_k, nanoparticle fractions φ_i, Lewis number Le, bioconvection Peclet number Pe, motile density ratio, bioconvection Lewis number, and thermophoresis parameter N_t were all set to zero, while c and β were maintained at 0.5 and 1.0, respectively and $\zeta = 1.0$ (which denotes the steady case of our current problem). The porosity parameter (λ_*) was systematically varied and Table 2 presents a comprehensive juxtaposition of the computed results alongside those of Yanala et al [35] and Yousif et al. [36], revealing a remarkable degree of consensus. This profound agreement between independent numerical simulations serves as a potent testament to the unwavering validity of the present study, laying a robust foundation for subsequent analyses and interpretations. We have the following values constant except when stated otherwise: $H_h = 0.5$, $N_b = 1.5$, $\lambda_* = 0.5$, $\phi_1 = \phi_2 = \phi_3 = 0.01$, $c = 0.5$, $N_t = 1.2$, $Le = 0.5$, $P_r = 6.2$, $\beta = 1.0$, $R_k = 0.2$, $N_r = 2.0$, $R_{mb} = 0.2$, $Lb = 0.5$, $Pe = 0.5$. Table 3 displays the variations in the skin friction

Table 2: Comparison for validation with $\phi_1 = \phi_2 = \phi_3 = 0$, $\beta = 1.0$, $P_r = N_r = H_h = Le = Pe = Lb = R_k = R_{mb} = N_t = 0$, $\zeta = 1.0$

λ_*	$-\left(1+\frac{1}{\beta}\right)f''$[35]	$-\left(1+\frac{1}{\beta}\right)f''$[36]	Present Result	$-\left(1+\frac{1}{\beta}\right)g''$[35]	$-\left(1+\frac{1}{\beta}\right)g''$[36]	Present Result
0.0	1.5472034561	1.5472	1.54592092	0.6589346721	0.6589	0.65793830
0.5	1.8366345632	1.83663	1.83608561	0.8228645262	0.8228	0.82284145
1.0	2.0885672341	2.0885	2.08846958	0.9614367843	0.9614	0.96139538

coefficients in x- and y- directions for different values of β, λ_*, H_h and c. We observed that the skin friction coefficients decrease as the value of the Casson parameter, β increases. As the Casson parameter increases, the yield stress dominates the near-wall region, allowing microorganism swimming and platelet rearrangement of the copper nanoparticle to have a more significant impact in counteracting the drag on the surface and hence reducing the skin fractions in both directions. The Casson parameter plays a crucial role in governing the yield stress behavior of the fluid. In the ternary nanofluid (copper, Al_2O_3, TiO_2, and water), nanoparticle interactions and the presence of microorganisms amplify the effects of the yield stress, leading to higher skin friction coefficients. The effects are less in the case of hybrid nanofluid (copper, Al_2O_3, and water) and lesser in the case of nanofluid (copper and water) owing to reductions in nanoparticles. We also observed icreasing trends in the skin friction coefficient as the value of c increases. The stretching parameter, c is a measure of the intensity of the stretching effect on the sheet. As the stretching parameter increases, the stretching effect becomes more pronounced, leading to higher flow velocity in y- direction near the surface. This intensified flow near the stretching sheet results to an increase in skin friction coefficients, as the fluid experiences more resistance against the surface. Similar trends are observed for increasing values of λ_* and H_h with the effects more pronounced in the case of ternary nanofluid compared to the other two cases. Table 4 showcase the variations in

Table 3: Numerical values of the skin friction coefficient for different values of some pertinent parameters when $\zeta = 0.9$

β	λ_*	H_h	c	C_{fx} - Nanofluid	C_{fx} - Hybrid	C_{fx} - Ternary	C_{gy} - Nanofluid	C_{gy} - Hybrid	C_{gy} - Ternary
0.5	0.5	0.5	0.5	2.42429071	2.93566495	3.83975619	2.88300901	3.57131821	4.88410313
1.0				1.98043315	2.39816738	3.13661778	2.27161676	2.81092250	3.83703834
2.0				1.71569201	2.07757710	2.71725304	1.92097904	2.37520469	3.23797375
3.0				1.61778910	1.95902205	2.56217216	1.79417300	2.21771216	3.02163628
1.0	0.5			1.98043315	2.39816738	3.13661778	2.27161676	2.81092250	3.83703834
	1.0			2.20537339	2.71401890	3.65919746	2.57552447	3.23424095	4.52161655
	2.0			2.59907702	3.25684561	4.52830631	3.06381544	3.90075449	5.56732725
	3.0			2.94091849	3.72162761	5.25569169	3.46388257	4.43980877	6.39749475
1.0	0.5	0.4		1.93445269	2.34692389	3.07666419	2.20569062	2.73792360	3.75368609
		0.8		2.11282647	2.54611652	3.31023930	2.45361861	3.01407539	4.07182027
		1.2		2.27797975	2.73146480	3.52882454	2.66881123	3.25661840	4.35640681
		1.6		2.43223175	2.90528738	3.73482055	2.86161414	3.47546435	4.61614920
1.0	0.5	0.5	0.5	1.98043315	2.39816738	3.13661778	2.27161676	2.81092250	3.83703834
			1.0	2.08745275	2.52069744	3.27510518	2.55268625	3.13768591	4.21547699
			1.5	2.26150463	2.72048077	3.50210353	2.95665180	3.61046322	4.77241909
			2.0	2.49520689	2.98987091	3.81103647	3.43320277	4.17145013	5.44387425

Nusselt number in response to changes in values of β, λ_*, H_h, c, P_r, N_r, N_t and N_b. The Casson parameter characterizes the yield stress behavior of the Casson fluid. It is defined as the ratio of yield stress to dynamic viscosity. As the Casson parameter increases, the yield stress dominance becomes more significant, leading to a more pronounced non-Newtonian behavior. Higher Casson parameter values result in a more rigid flow due to the combined effects of Casson rheology, weakened biothermal convection from microorganisms, potential thermal barrier formation by platelets (copper), and altered heat transfer patterns from other nanoparticles (Al_2O_3 and TiO_2), potentially leading to decreased heat transfer rate around the stretching surface. The same observational trends are made for increasing λ_*, H_h, c, N_t, and N_b. Increasing Prandtl number signifies a higher ratio of momentum diffusivity to thermal diffusivity. This implies that momentum diffuses faster than heat in the fluid. Consequently, steeper thermal gradients are established near the heated surface, promoting diffusion of thermal energy into the bulk fluid. In addition, enhanced biothermal convection from the swimming microorganisms and the interactions of the differently shaped nanoparticles account for the observable increase in the Nusselt number as P_r increases. This is also the case for increasing value of N_r. We observed higher Nusselt value in the case of the nanofluid (copper and water) compared to the hybrid nanofluid (copper, Al_2O_3, and water) due to the thermal conductivity superiority of copper and the disruption produced by the presence of the spherically shaped Al_2O_3. However this deficiency is effectively taken care of with the introduction of the cylindrical shaped TiO_2 as observed in Table 4. Table 5 presents how the Sherwood

Table 4: Numerical values of the Nusselt number for different values of some pertinent parameters when $\zeta = 0.9$

β	λ_*	H_h	c	P_r	N_r	N_t	N_b	Nu_x - Nanofluid	Nu_x - Hybrid	Nu_x - Ternary
0.5	0.5	0.5	0.5	6.2	2.0	1.2	1.5	0.14351798	0.13593209	0.18455035
1.0								0.13932881	0.13250124	0.18047197
2.0								0.13555814	0.12933054	0.17670049
3.0								0.13382361	0.12785040	0.17493277
1.0	0.5							0.13932881	0.13250124	0.18047197
	1.0							0.13642117	0.12964094	0.17615342
	2.0							0.13142267	0.12473010	0.16890167
	3.0							0.12724221	0.12063673	0.16298868
1.0	0.5	0.4						0.13992488	0.13296150	0.18095914
		0.8						0.13761489	0.13116508	0.17904957
		1.2						0.13548844	0.12948236	0.17723978
		1.6						0.13352153	0.12790287	0.17552179
1.0	0.5	0.5	0.5					0.13932881	0.13250124	0.18047197
			1.0					0.19198636	0.18294993	0.24656422
			1.5					0.27112314	0.25722256	0.34146297
			2.0					0.35550523	0.33447414	0.43852431
1.0	0.5	0.5	0.5	0.7				0.17921826	0.17501422	0.22027696
				1.0				0.19895067	0.19401840	0.24582612
				1.38				0.21180375	0.20611020	0.26302203
				2.0				0.21678317	0.21021132	0.27102364
1.0	0.5	0.5	0.5	6.2	0.5			0.05536652	0.04990265	0.08250282
					1.0			0.08828666	0.08202114	0.12138879
					1.5			0.11645568	0.10981195	0.15405662
					2.0			0.13932881	0.13250124	0.18047197
1.0	0.5	0.5	0.5	6.2	2.0	0.4		0.23937158	0.22901770	0.30193102
						0.8		0.18033188	0.17195119	0.23079917
						1.2		0.13932881	0.13250124	0.18047197
						1.6		0.11026561	0.10465018	0.14421921
1.0	0.5	0.5	0.5	6.2	2.0	1.2	0.8	0.25511485	0.24416977	0.32059360
							1.0	0.21675066	0.20711005	0.27448480
							1.5	0.13932881	0.13250124	0.18047197
							2.0	0.08523960	0.08060640	0.11349066

number changes as β, λ_*, H_h, c, Le, R_k, N_t and N_b vary. As β increases in value, we observed steady decline in the local Sherwood number as a result of the combined interaction of the Casson rheology induced velocity and concentration gradients reductions, disrupted bioconvection from microorganisms, potential flow blockage by platelet nanoparticle alignment, and modified flow patterns from the spherical and cylindrical nanoparticles. Similar trend is observed for increasing value of λ_*. Increasing stretching parameter has an enhancing effect on the Sherwood number. As the stretching parameter increases, the stretching velocity of the surface also escalates. This translates to steeper velocity gradients within the fluid, particularly near the surface. These steeper gradients lead to increased shear stress near the stretching surface, intensifying the mixing of nanoparticles and their transport towards the surface, consequently boosting the Sherwood number. Increasing the Lewis number, Le also increases the mass flux at the boundary. This is also the case for increasing H_h, R_k, N_t, and N_b.

Table 6 displays motile microorganism density as it varies with variation in β, λ_*, H_h, c, Lb and Pe. Motile microorganism density is seen to elevate as Pe grows. As the bioconvection Peclet number Pe increases, it signifies stronger bioconvection patterns and more efficient transport of microorganisms by the flow. This leads to a greater accumulation of microorganisms near the surface, consequently, the microorganism density number increases. Enhancing the bioconvection Lewis number and stretching parameter also demonstrate similar effects on the motile microorganism density. Increasing magnetic parameter H_h diminishes the microorganism density number. As the magnetic parameter increases, the Lorentz force acting on the electrically conducting fluid also intensifies. This force opposes the stretching flow, leading to reduced flow velocities within the boundary layer. Consequently, the transport and accumulation of microorganisms near the wall declines. Similar trends are observed for increasing β and λ_*.

Figures 2-5 depict the fluid velocity in x - direction for varying values of the Casson parameter (β), porosity parameter(λ_*), stretching parameter(c) and magnetic parameter(H_h). As seen in Figure 2,

Table 5: Numerical values of the Sherwood number for different values of some pertinent parameters when $\zeta = 0.9$

β	λ_*	H_h	c	Le	R_k	N_t	N_b	Sh_x - Nanofluid	Sh_x - Hybrid	Sh_x - Ternary
0.5	0.5	0.5	0.5	0.5	0.2	1.2	1.5	0.55341937	0.56187520	0.56972794
1.0								0.53313739	0.54153399	0.54980467
2.0								0.51911716	0.52729310	0.53558536
3.0								0.51353367	0.52158031	0.52981617
1.0	0.5							0.53313739	0.54153399	0.54980467
	1.0							0.52267345	0.52930011	0.53452687
	2.0							0.50743448	0.51205168	0.51417342
	3.0							0.49659558	0.50012393	0.50072957
1.0	0.5	0.4						0.53548292	0.54371754	0.55174435
		0.8						0.52679432	0.53556084	0.54442117
		1.2						0.51959914	0.52867795	0.53808949
		1.6						0.51348304	0.52274447	0.53252867
1.0	0.5	0.5	0.5					0.53313739	0.54153399	0.54980467
			1.0					0.58967412	0.60246387	0.61685873
			1.5					0.68413881	0.70491663	0.73087162
			2.0					0.82127104	0.85259934	0.89327769
1.0	0.5	0.5	0.5	0.4				0.45825443	0.46552538	0.47315984
				0.8				0.73664741	0.74783749	0.75730581
				1.2				0.97741950	0.99167323	1.00204555
				1.6				1.19736768	1.21438511	1.22534348
1.0	0.5	0.5	0.5	0.5	0.1			0.47945635	0.48856527	0.49802847
					0.2			0.53313739	0.54153399	0.54980467
					0.3			0.58281939	0.59063358	0.59793967
					0.4			0.62907016	0.63639730	0.64291223
1.0	0.5	0.5	0.5	0.5	0.2	0.4		0.51383776	0.52123013	0.53112776
						0.8		0.52089227	0.52881918	0.53772683
						1.2		0.53313739	0.54153399	0.54980467
						1.6		0.54720222	0.55596217	0.56395755
1.0	0.5	0.5	0.5	0.5	0.2	1.2	0.8	0.47718388	0.48626200	0.49188923
							1.0	0.50418198	0.51304489	0.51963123
							1.5	0.53313739	0.54153399	0.54980467
							2.0	0.54111605	0.54913413	0.55855121

Table 6: Numerical values of the motile microorganism density number for different values of some pertinent parameters when $\zeta = 0.9$

β	λ_*	H_h	c	Lb	Pe	Nh_x - Nanofluid	Nh_x - Hybrid	Nh_x - Ternary
0.5	0.5	0.5	0.5	0.5	0.5	0.71264090	0.72389359	0.73809881
1.0						0.68312725	0.69486816	0.71027542
2.0						0.66180572	0.67366774	0.68961234
3.0						0.65308204	0.66493688	0.68101627
1.0	0.5					0.68312725	0.69486816	0.71027542
	1.0					0.66720578	0.67660539	0.68793951
	2.0					0.64324472	0.64989498	0.65684886
	3.0					0.62559161	0.63069536	0.63536718
1.0	0.5	0.4				0.68663898	0.69807142	0.71305474
		0.8				0.67352580	0.68601892	0.70249609
		1.2				0.66244780	0.67566203	0.69322048
		1.2				0.65286978	0.66659169	0.68495747
1.0	0.5	0.5	0.5			0.68312725	0.69486816	0.71027542
			1.0			0.79806377	0.81588439	0.84014712
			1.5			0.98074634	1.00801722	1.04643003
			2.0			1.21935766	1.25715778	1.31105621
1.0	0.5	0.5	0.5	0.5		0.68312725	0.69486816	0.71027542
				1.0		0.90151020	0.91529737	0.93360853
				1.5		1.07753389	1.09231043	1.11199713
				2.0		1.22924540	1.24459611	1.26507652
1.0	0.5	0.5	0.5	0.5	0.5	0.68312725	0.69486816	0.71027542
					1.0	0.94862255	0.96398616	0.98210085
					1.5	1.22256787	1.24173935	1.26287603
					2.0	1.50343796	1.52657958	1.55101128

the fluid velocity in x-direction declines for improving value of Casson parameter. The Casson model introduces a yield stress, a minimum stress required for the fluid to flow. In high Casson parameter scenarios, this stress becomes significant, particularly near the wall. Consequently, the velocity gradients near the wall are suppressed, leading to a reduced overall velocity in the x-direction. In Figure 3, it can be seen that the fluid velocity parallel to stretching sheet also decreases with increasing porosity parameter, this because flow of the fluid molecules through a porous medium introduces additional frictional forces and resistance to movement. This leads to a loss of momentum transferred from the stretching sheet to the fluid, resulting in a slower overall velocity in the x-direction. Similar fluid velocity characteristics in x-direction are observed as stretching and magnetic parameters grow as seen in Figures 4 and 5.

In Figure 6, the fluid velocity in y-direction decreases close to the stretching surface and increases farther away from the surface as β enhances. Close to stretching sheet, the Casson fluid behavior leads to a more rigid flow, hence the visible reduction in $g'(\eta, \zeta)$. The Casson fluid becomes less constrained away from the surface due to reduced dominance of the yield stress and hence the velocity grows as seen in Figure 6. Similar behavior are observed in Figure 7 for increasing λ_*. Figure 8 depicts how $g'(\eta, \zeta)$ responds to incremental changes in the value of the stretching parameter. As the stretching parameter increases, the flow experiences a stronger stretching force near the wall, leading to a higher shear rate. This, in turn, triggers the shear-thinning behavior of the Casson fluid, causing its effective viscosity to decrease near the wall. This reduced viscosity allows for a greater acceleration of the fluid in the y-direction close to the surface, farther away from the wall, the trend is reversed as the fluid slows down. This is also as seen in Figure 9 for increasing value of the magnetic parameter.

Influence of the stretching parameter on fluid temperature profile is showcased in Figure 10. As the stretching parameter increases, the flow experiences a stronger stretching force, leading to increased mixing and turbulence within the boundary layer. This enhanced mixing promotes the spreading and dissipation of heat generated by friction and internal energy production, resulting in a lower overall temperature profile. Similar trend is observed in Figures 12 for increasing Prandtl number. As the magnetic parameter increases, the applied magnetic field generates a stronger Lorentz force that opposes the flow. This leads to reduced mixing and turbulence within the boundary layer. Consequently, the heat generated by friction and internal energy production gets trapped within the fluid especially near the wall, resulting in a higher overall temperature as seen in Figure 11. We observed the same patterns in Figures 13 and 15 as the thermophoresis parameter and Brownian motion number respectively increase. Figure 14 highlights the dynamic behavior of the fluid temperature profile in response to increment in N_r. As the thermal radiation number increases, the intensity of radiative heat loss from the fluid surface to the surroundings also increases. This leads to a more significant cooling effect near the wall, where the fluid is directly exposed to the radiation field. However, the radiative energy penetrates deeper into the fluid with increasing distance from the wall, leading to a gradual increase in temperature further away. Figures 16, 17 and 19 exhibit steady decline in the concentration profile as c, Le and N_b respectively increase. An increasing Lewis number indicates that heat is more rapidly conducted compared to mass diffusion. This implies that the concentration gradient is less pronounced compared to the temperature gradient. Mass transfer becomes less efficient, leading to a decrease in concentration profiles as seen in Figure 17. The thermophoresis parameter quantifies the strength of the thermophoretic force acting on nanoparticles. An increasing thermophoresis parameter enhances the thermophoretic effect on particle motion. As the thermophoresis parameter increases, the thermodiffusive force acting on nanoparticles becomes stronger. This force pushes nanoparticles towards the colder region, which in this case is closer to the wall due to the stretching sheet's heat generation. This phenomenon leads to a concentration enrichment near the wall, resulting in the observed increase in the concentration profile as observed in Figure 18. Bioconvection Lewis number represents the ratio of the effects of bioconvection to molecular diffusion. An increasing bioconvection Lewis number indicates a stronger influence of bioconvection relative to molecular diffusion. As the bioconvection Lewis number increases, the diffusivity of the motile microorganisms relative to the flow becomes much smaller. This signifies that microorganisms spread much slower compared to the overall flow movement. Due to the reduced diffusivity, the motile density boundary layer, which defines the region of significant microorganism concentration change, thins significantly, hence, the observed decline in motile density profile in Figure 20. The bioconvection Peclet number and stretching parameter demonstrate similar influence on the motile density as seen in Figures 21 and 22. The effect of Casson parameter is depicted in Figure 23. As seen, increasing β steady improves the motile density profile due to the reduced effective viscosity of the fluid.

In general, we have observed the ternary nanofluid outperforming the hybrid and nanofluid cases. This is because ternary nanofluid allows for a synergistic combination of their individual thermophysical properties of the three distinct nanoparticles. In particular, platelet-shaped copper excels in thermal conductivity, spherical Al_2O_3 boasts enhanced viscosity, and cylindrically shaped TiO_2 contributes to improved stability. This combined effect on thermal conductivity, viscosity, and stability significantly outperforms both hybrid and individual nanofluid cases.

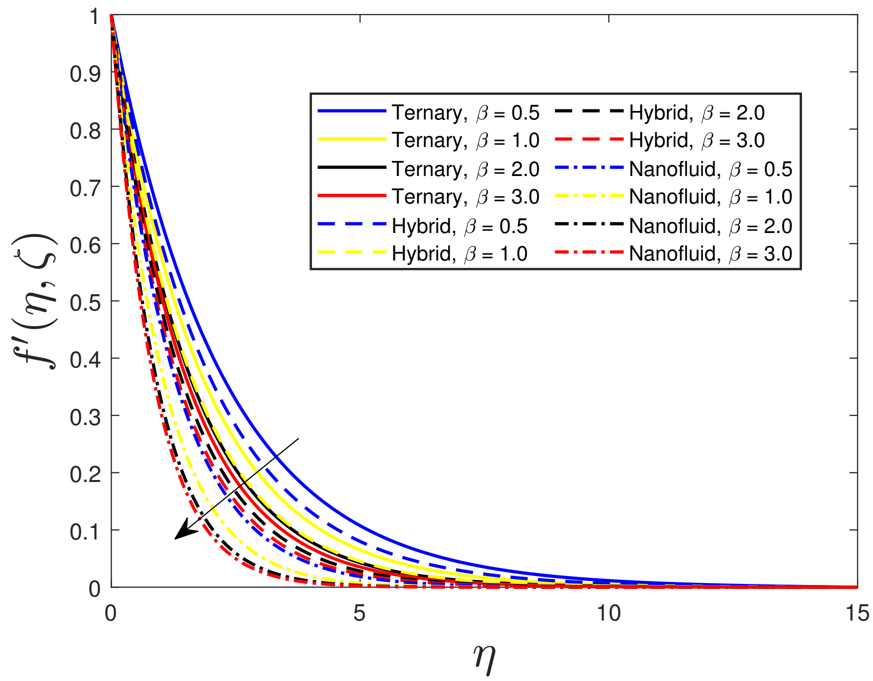

Figure 2: Implication of Casson parameter on $f'(\eta, \zeta)$

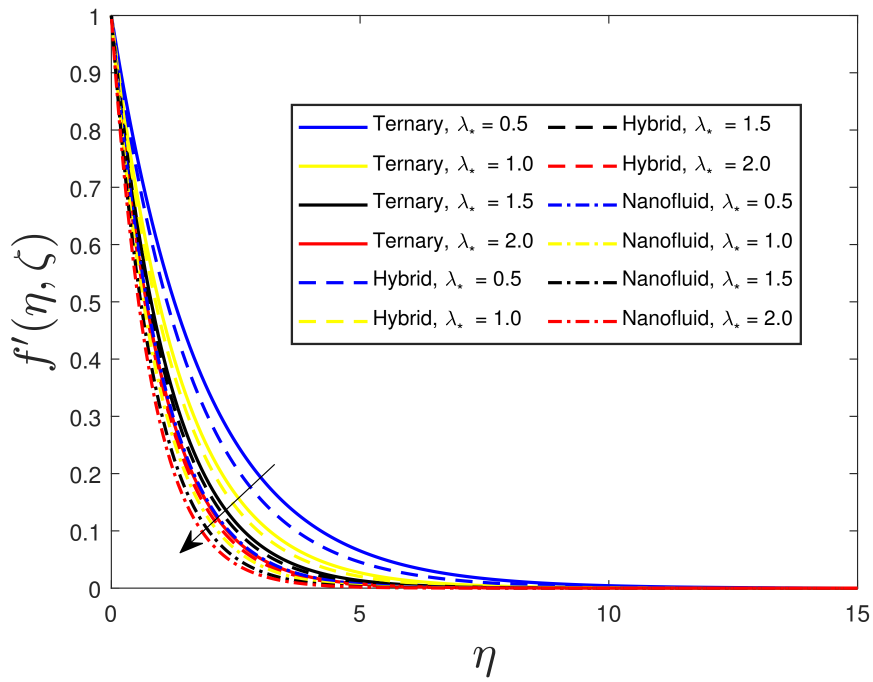

Figure 3: Implication of porosity parameter on $f'(\eta, \zeta)$

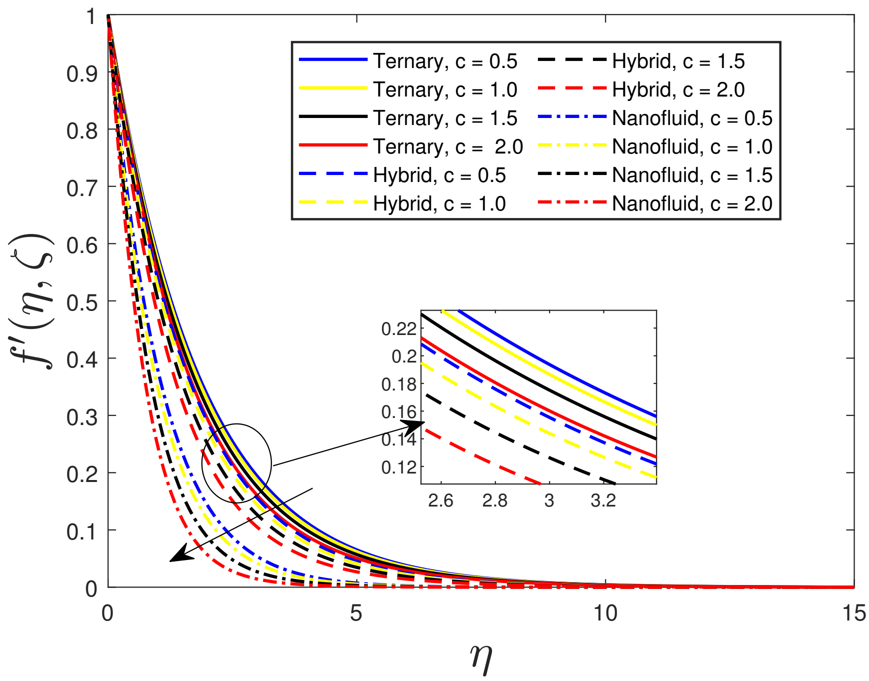

Figure 4: Implication of stretching parameter on $f'(\eta, \zeta)$

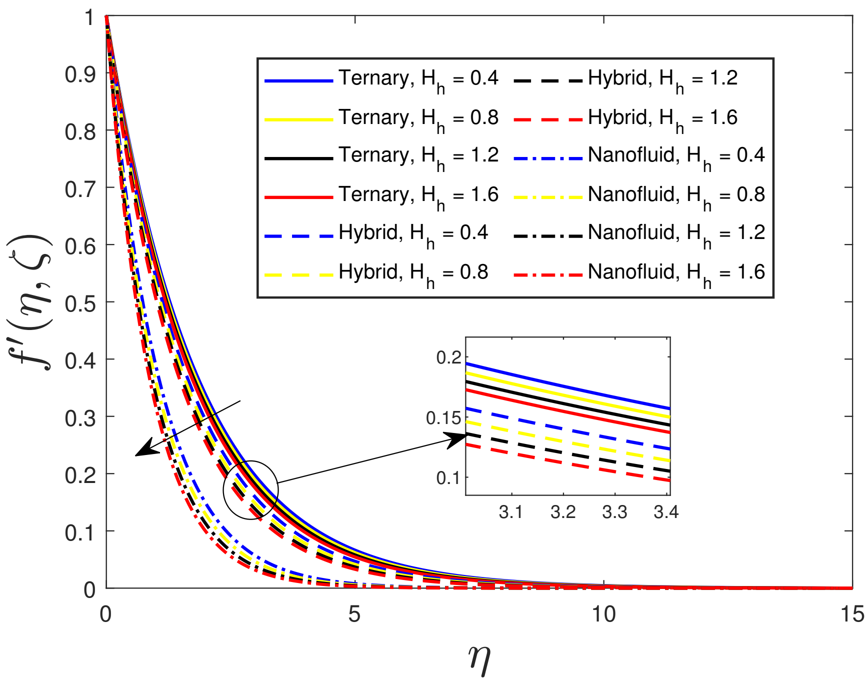

Figure 5: Implication of magnetic parameter on $f'(\eta, \zeta)$

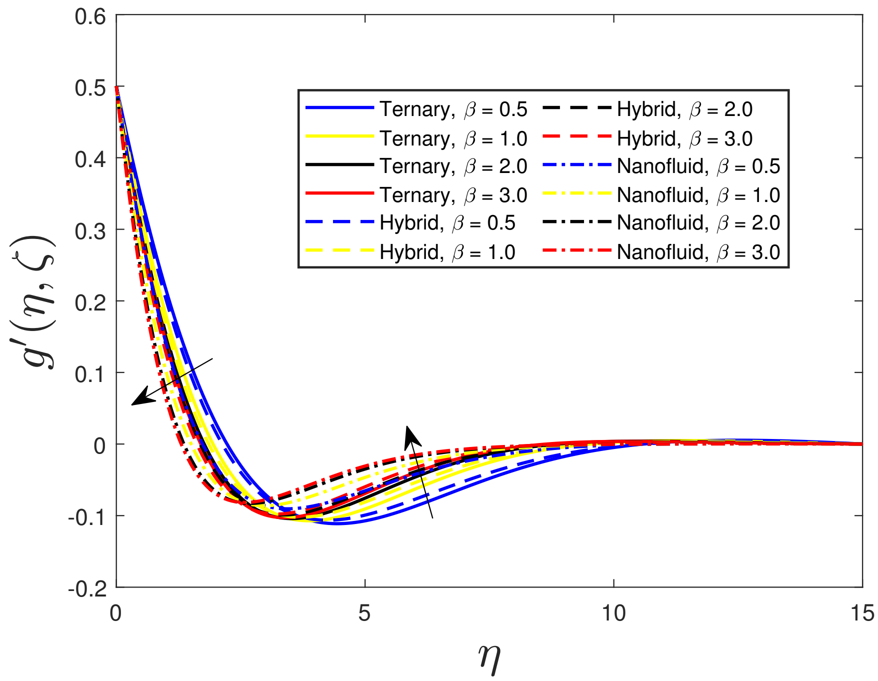

Figure 6: Implication of Casson parameter on $g'(\eta, \zeta)$

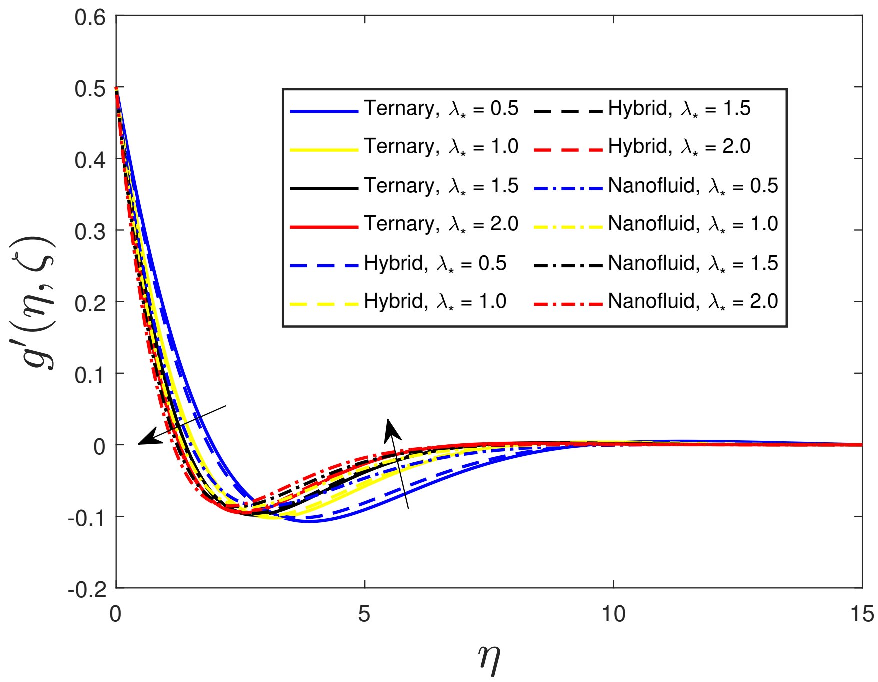

Figure 7: Implication of porosity parameter on $g'(\eta, \zeta)$

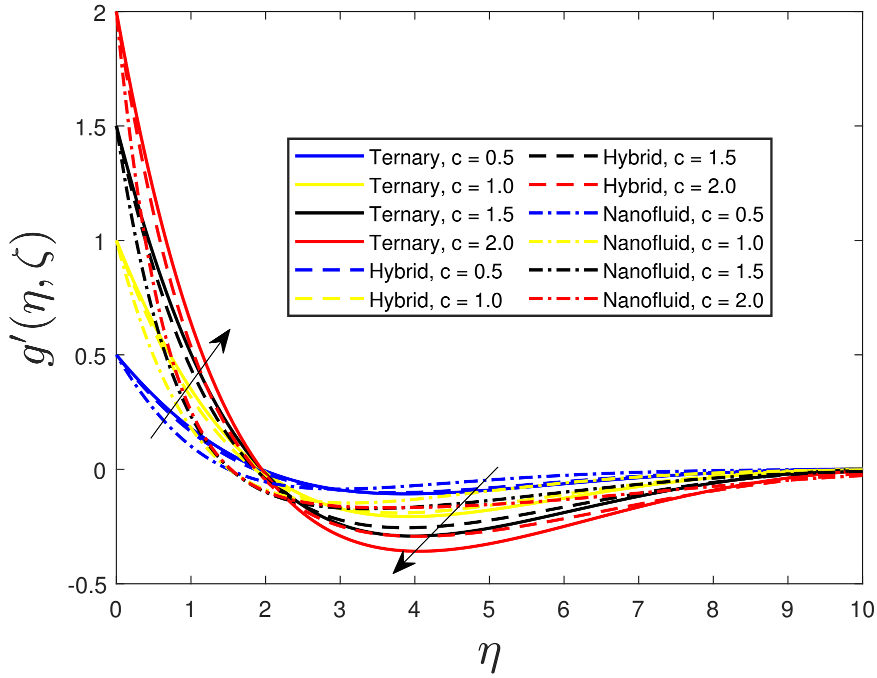

Figure 8: Implication of stretching parameter on $g'(\eta, \zeta)$

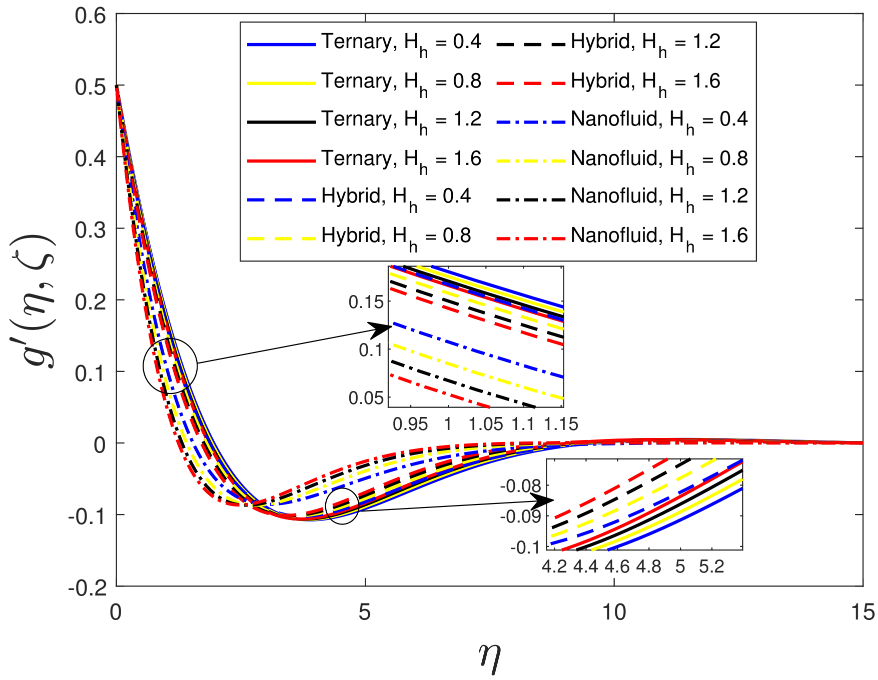

Figure 9: Implication of magnetic parameter on $g'(\eta, \zeta)$

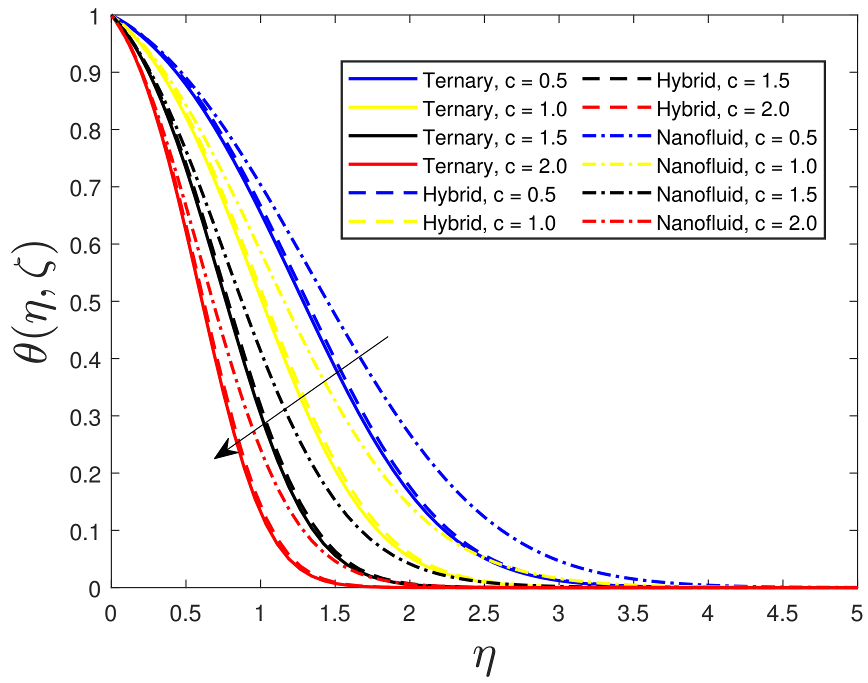

Figure 10: Implication of stretching parameter on $\theta(\eta, \zeta)$

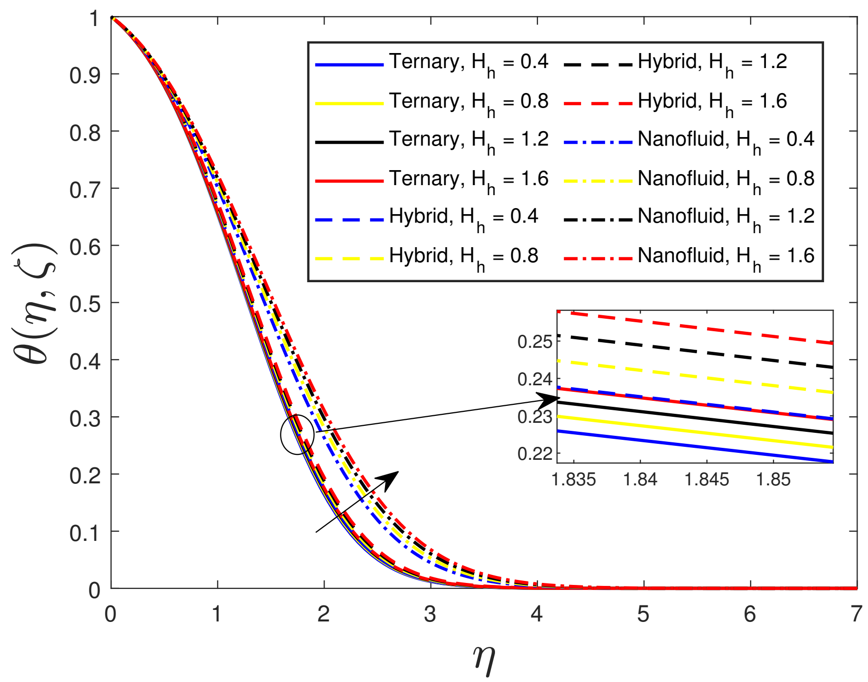

Figure 11: Implication of magnetic parameter on $\theta(\eta, \zeta)$

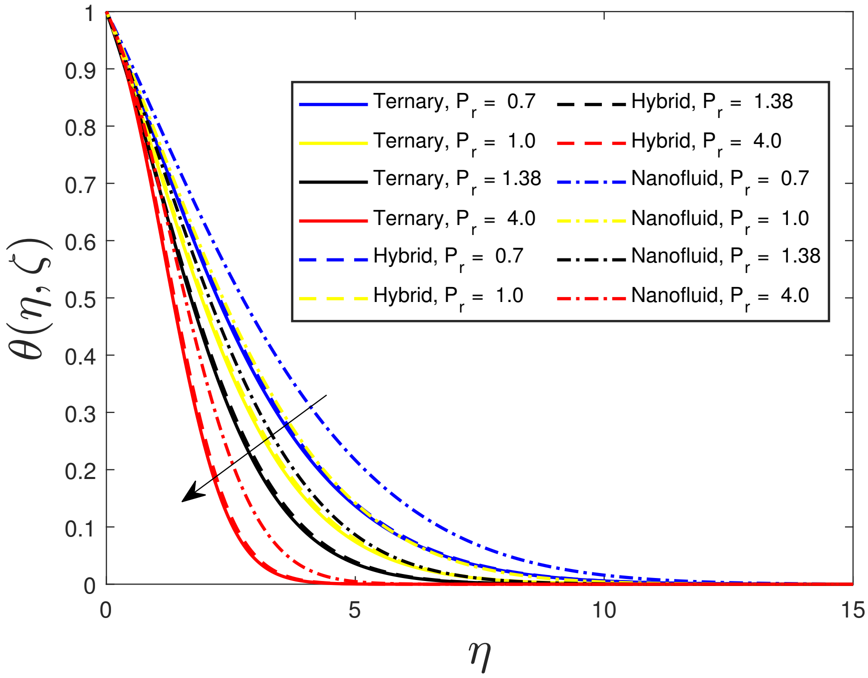

Figure 12: Implication of Prandtl number on $\theta(\eta, \zeta)$

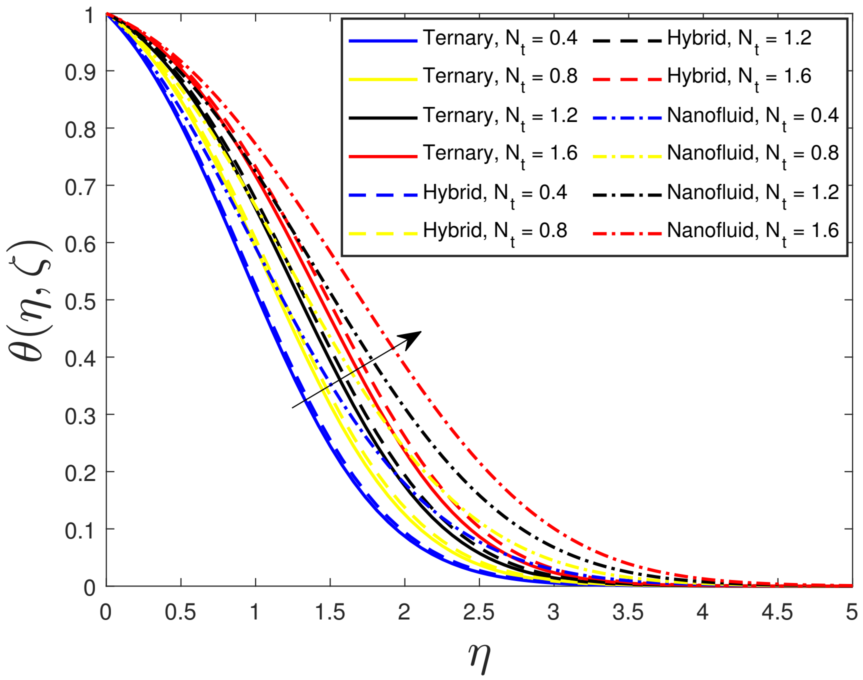

Figure 13: Implication of thermophoresis parameter on $\theta(\eta, \zeta)$

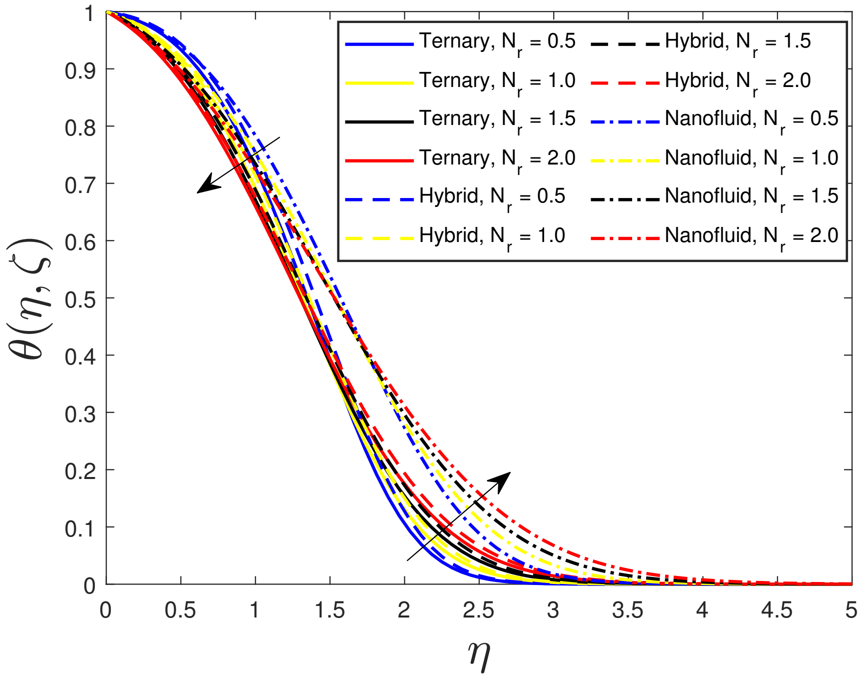

Figure 14: Implication of radiation parameter on $\theta(\eta, \zeta)$

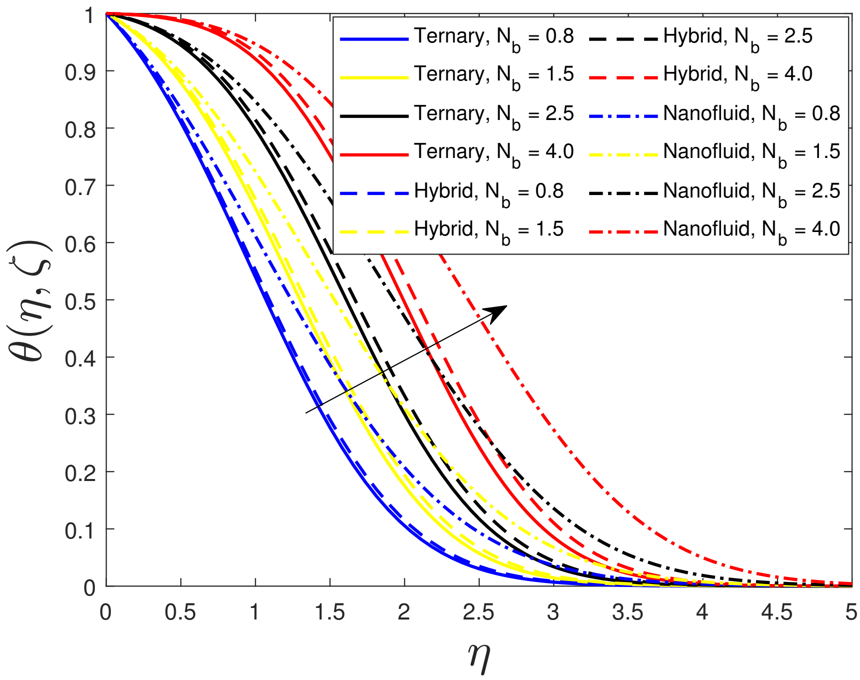

Figure 15: Implication of Brownian motion parameter on $\theta(\eta, \zeta)$

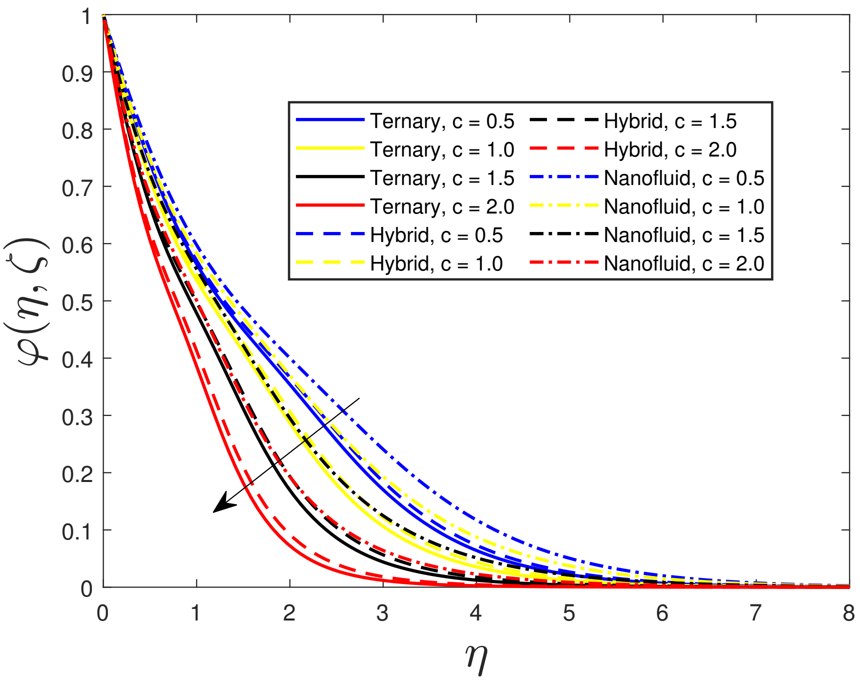

Figure 16: Implication of stretching parameter on $\varphi(\eta, \zeta)$

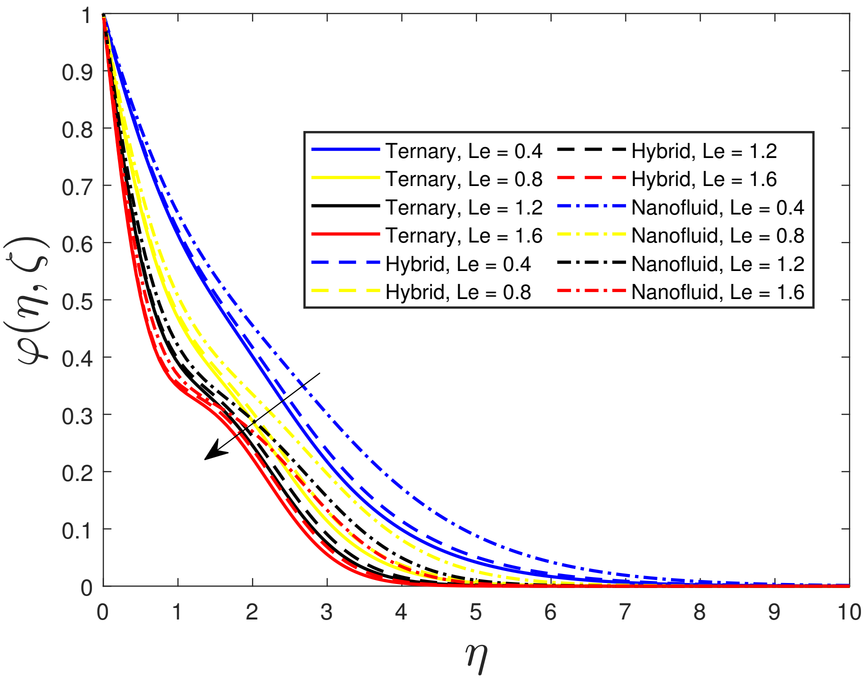

Figure 17: Implication of Lewis number on $\varphi(\eta, \zeta)$

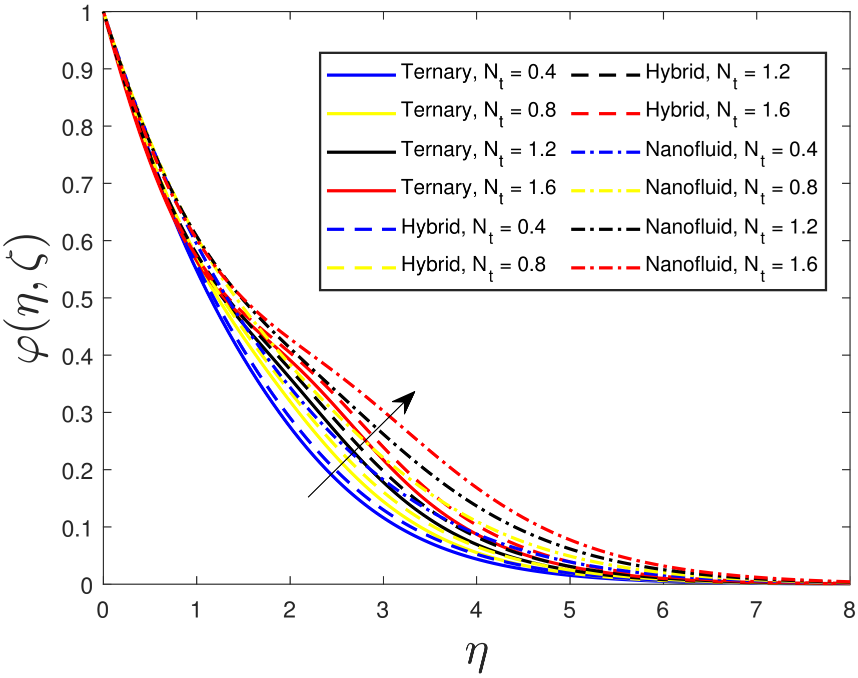

Figure 18: Implication of thermophoresis parameter on $\varphi(\eta, \zeta)$

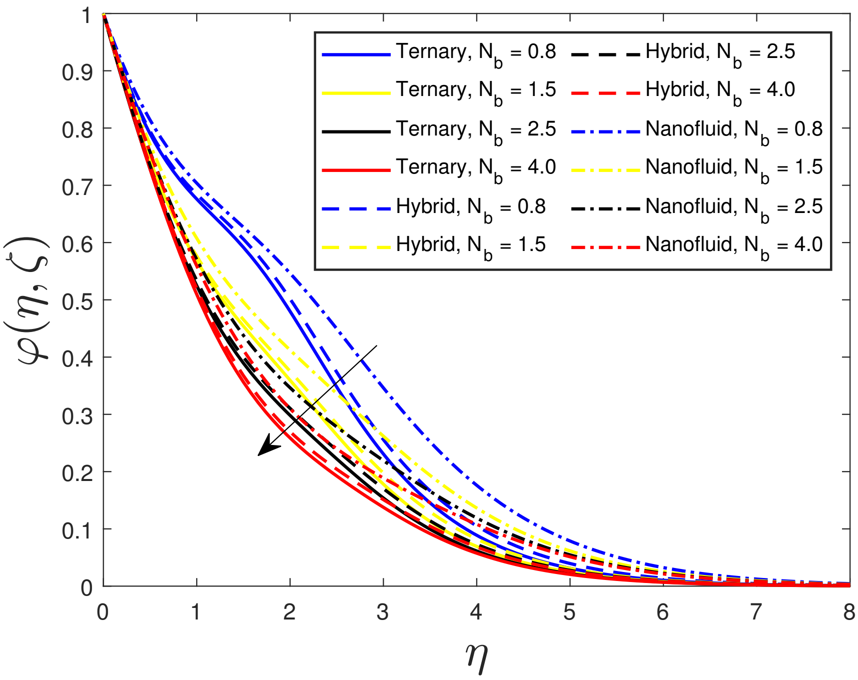

Figure 19: Implication of Brownian motion parameter on $\varphi(\eta, \zeta)$

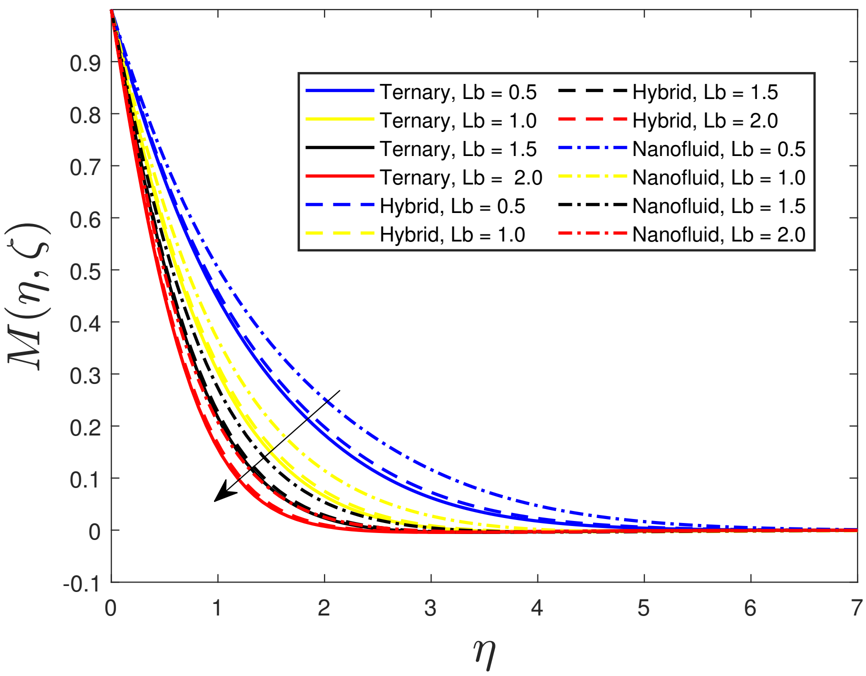

Figure 20: Implication of bioconvection Lewis number on $M(\eta, \zeta)$

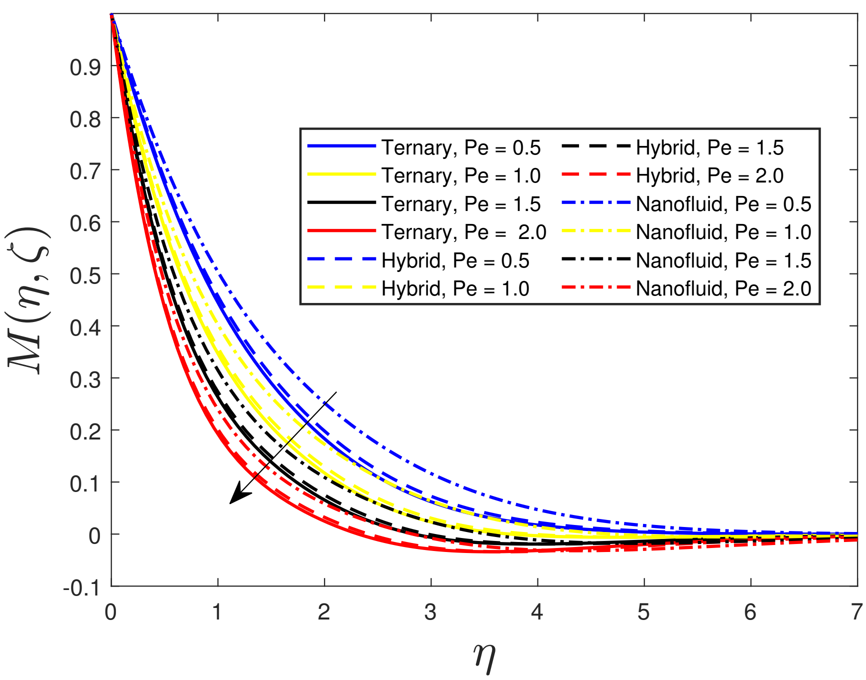

Figure 21: Implication of bioconvection Peclet number on $M(\eta, \zeta)$

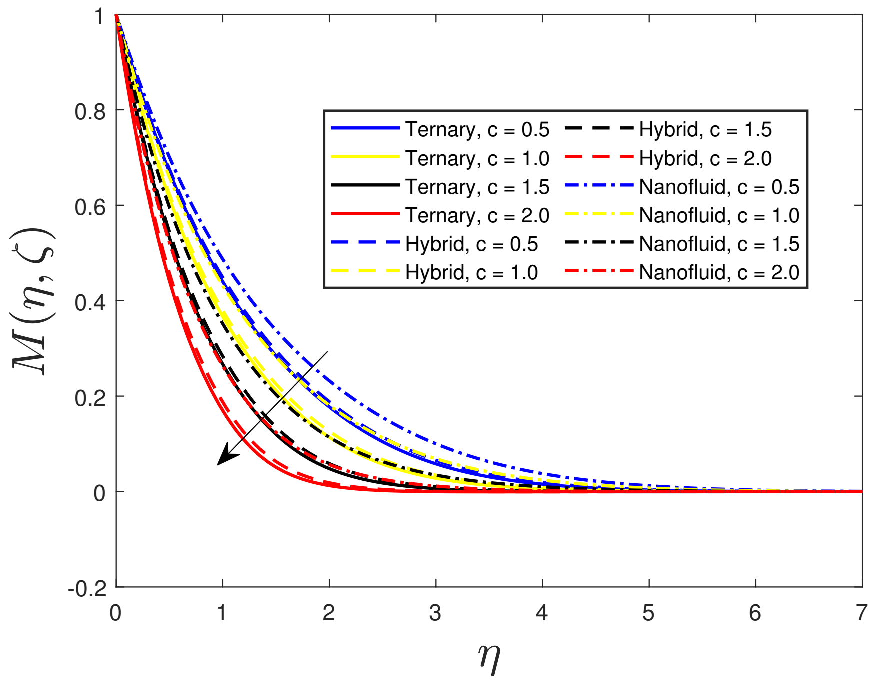

Figure 22: Implication of stretching parameter on $M(\eta, \zeta)$

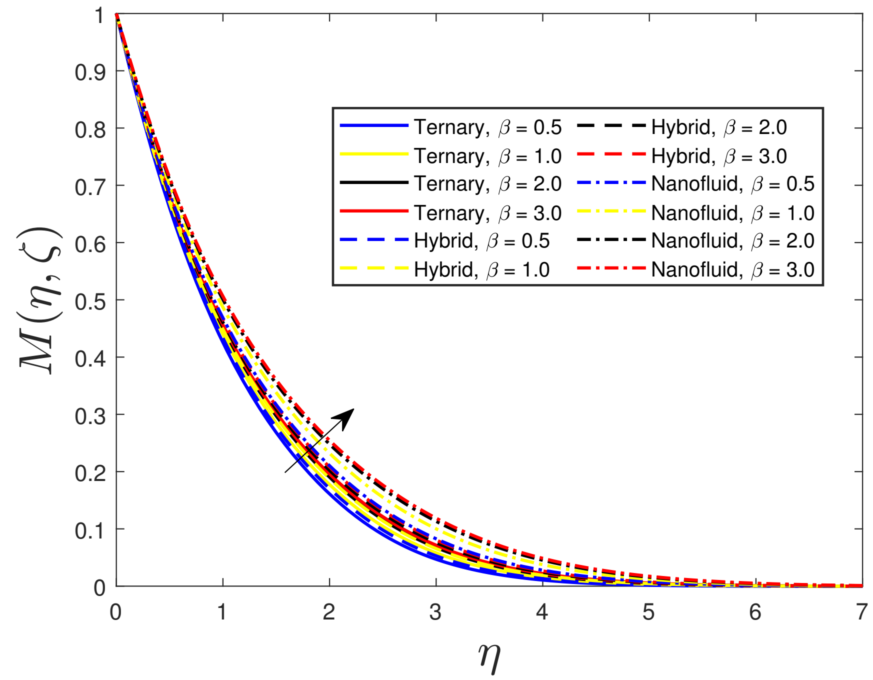

Figure 23: Implication of Casson parameter on $M(\eta, \zeta)$

5. Conclusion

Unsteady MHD flow of Casson ternary hybrid nanofluid over a bidirectional stretching sheet, influenced by a magnetic field, nanoparticle dispersion, and motile gyrotactic microorganisms, has been examined here. Employing the overlapping bivariate spectral quasi-linearization method has allowed for a comprehensive examination of the complex system, considering thermal radiation, chemical reactions, and the impact of nanoparticle shape factor. The fluid comprises platelet-shaped copper, spherically shaped Al_2O_3, and cylindrically shaped TiO_2, constituting a unique ternary hybrid nanofluid with water as the base fluid. Based on the findings, we have reached the following concluding remarks

- The ternary hybrid nanofluid, featuring diverse nanoparticle shapes, has demonstrated superior performance compared to hybrid fluids and nanofluids with fewer components.
- Casson parameter is a key factor in the optimization of nanofluid flow, heat, mass and motile transfers.
- Porosity, stretching, and magnetic parameters all suppress the fluid velocity in x-direction
- Enhancing Casson and porosity parameters slow down the fluid in y-direction close to the sheet and speed it up further away from the sheet. Reverse is the case for increasing stretching and magnetic parameters.
- The fluid thermal profile steadily decline as stretching parameter and Prandtl number grow. Reverse is the case for increasing magnetic and thermophoresis parameters.
- Thermal radiation number reduces the thermal boundary close to the sheet and improves it away from the sheet.
- Lewis number, stretching and Brownian motion parameters depreciate the mass flux profile while the thermophoresis improves the mass flux profile.
- Bioconvection Lewis and Peclet numbers as well as the stretching parameter reduce the motile density while Casson parameter increase the motile density.
- The skin friction coefficients in x - and y-axes elevate as porosity, magnetic and stretching parameters grow while Casson parameter reduces them.
- Casson, porosity, magnet, thermophoresis and Brownian motion parameters decrease the heat transfer rate at the wall while stretching parameter, thermal radiation and Prandtl numbers escalate the heat transfer rate.
- Sherwood number diminishes for growing values of Casson, porosity, magnetic, and stretching parameters and goes up for improving values of Lewis number, chemical, thermophoresis and Brownian motion parameters.
- Motile microorganism density escalates as bioconvection Lewis number, bioconvection Peclet number, stretching and magnetic parameters grow while it reduces for growing values of Casson and porosity parameters.
- The findings of this study contribute to our understanding of nanofluid dynamics and hold promise for applications requiring efficient heat transfer and fluid manipulation in diverse industrial and engineering contexts.

References

[1] Algehyne, E. A., Alrihieli, H. F., Bilal, M., Saeed, A., and Weera, W. Numerical approach toward ternary hybrid nanofluid flow using variable diffusion and non-fourier's concept. *ACS omega 7*, 33 (2022), 29380–29390.

[2] Arif, M., Di Persio, L., Kumam, P., Watthayu, W., and Akgül, A. Heat transfer analysis of fractional model of couple stress casson tri-hybrid nanofluid using dissimilar shape nanoparticles in blood with biomedical applications. *Scientific Reports 13*, 1 (2023), 4596.

[3] Arif, M., Kumam, P., Kumam, W., and Mostafa, Z. Heat transfer analysis of radiator using different shaped nanoparticles water-based ternary hybrid nanofluid with applications: A fractional model. *Case Studies in Thermal Engineering 31* (2022), 101837.

[4] Asogwa, K. K., Kumar, K. T., Goud, B. S., and Chohan, J. S. Significance of nanoparticle shape factor and buoyancy effects on a parabolic motion of emhd convective nanofluid past a riga plate with ramped wall temperature. *The European Physical Journal Plus 138*, 6 (2023), 1–13.

[5] Chamkha, A. J., Miroshnichenko, I. V., and Sheremet, M. A. Numerical analysis of unsteady conjugate natural convection of hybrid water-based nanofluid in a semicircular cavity. *Journal of Thermal Science and Engineering Applications 9*, 4 (2017), 041004.

[6] El-Dabe, N., Abou-Zeid, M. Y., Oauf, M. E., Mostapha, D. R., and Mohamed, Y. M. Cattaneo–christov heat flux effect on mhd peristaltic transport of bingham al 2o 3 nanofluid through a non-darcy porous medium. *International Journal of Applied Electromagnetics and Mechanics 68*, 1 (2022), 59–84.

[7] Ghadikolaei, S., Hosseinzadeh, K., and Ganji, D. Investigation on ethylene glycol-water mixture fluid suspend by hybrid nanoparticles (tio2-cuo) over rotating cone with considering nanoparticles shape factor. *Journal of Molecular Liquids 272* (2018), 226–236.

[8] Huang, H., and Ayoub, J. Applicability of the forchheimer equation for non-darcy flow in porous media. *Spe Journal 13*, 01 (2008), 112–122.

[9] Ibrahim, M., Abdallah, N., and Abouzeid, M. Activation energy and chemical reaction effects on mhd bingham nanofluid flow through a non-darcy porous media. *Egyptian Journal of Chemistry 65*, 132 (2022), 137–144.

[10] Jamshed, W., Devi, S. U., and Nisar, K. S. Single phase based study of ag-cu/eo williamson hybrid nanofluid flow over a stretching surface with shape factor. *Physica Scripta 96*, 6 (2021), 065202.

[11] Jamshed, W., Kumar, V., and Kumar, V. Computational examination of casson nanofluid due to a non-linear stretching sheet subjected to particle shape factor: Tiwari and das model. *Numerical Methods for Partial Differential Equations 38*, 4 (2022), 848–875.

[12] Jun, Y.-S., Zhu, Y., Wang, Y., Ghim, D., Wu, X., Kim, D., and Jung, H. Classical and nonclassical nucleation and growth mechanisms for nanoparticle formation. *Annual Review of Physical Chemistry 73* (2022), 453–477.

[13] Khan, U., Zaib, A., Pop, I., Abu Bakar, S., and Ishak, A. Stagnation point flow of a micropolar fluid filled with hybrid nanoparticles by considering various base fluids and nanoparticle shape factors. *International Journal of Numerical Methods for Heat & Fluid Flow 32*, 7 (2022), 2320–2344.

[14] Kundu, P., Kumar, V., and Mishra, I. M. Experimental and numerical investigation of fluid flow hydrodynamics in porous media: Characterization of pre-darcy, darcy and non-darcy flow regimes. *Powder Technology 303* (2016), 278–291.

[15] Liu, Z., Malinowski, C. R., and Sepúlveda, M. S. Emerging trends in nanoparticle toxicity and the significance of using daphnia as a model organism. *Chemosphere 291* (2022), 132941.

[16] Madhukesh, J. K., Sarris, I. E., Prasannakumara, B. C., and Abdulrahman, A. Investigation of thermal performance of ternary hybrid nanofluid flow in a permeable inclined cylinder/plate. *Energies 16*, 6 (2023), 2630.

[17] Mahanta, G., and Shaw, S. 3d casson fluid flow past a porous linearly stretching sheet with convective boundary condition. *Alexandria Engineering Journal 54*, 3 (2015), 653–659.

[18] Mahmood, Z., Ahammad, N. A., Alhazmi, S. E., Khan, U., and Bani-Fwaz, M. Z. Ternary hybrid nanofluid near a stretching/shrinking sheet with heat generation/absorption and velocity slip on unsteady stagnation point flow. *International Journal of Modern Physics B 36*, 29 (2022), 2250209.

[19] Mishra, P., Kumar, D., Dharmendar Reddy, Y., and Shankar Goud, B. Numerical investigation of mhd flow of williamson nanofluid with variable viscosity pasting a wedge within porous media: a non-darcy model approach. *Heat Transfer 51*, 7 (2022), 6071–6086.

[20] Mkhatshwa, M., Motsa, S., and Sibanda, P. Mhd mixed convection flow of couple stress fluid over an oscillatory stretching sheet with thermophoresis and thermal diffusion using the overlapping multi-domain spectral relaxation approach. *International Journal of Applied and Computational Mathematics 7*, 3 (2021), 93.

[21] Mondal, H., Mandal, A., and Tripathi, R. Numerical investigation of the non-newtonian power-law fluid with convective boundary conditions in a non-darcy porous medium. *Waves in Random and Complex Media* (2022), 1–17.

[22] Nadeem, S., Haq, R. U., Akbar, N. S., and Khan, Z. H. Mhd three-dimensional casson fluid flow past a porous linearly stretching sheet. *Alexandria Engineering Journal 52*, 4 (2013), 577–582.

[23] Nandi, S., Iqbal, Z., Alhagyan, M., Ahammad, N. A., Albasheir, N. A., Gargouri, A., Alhazmi, S. E., and Eldin, S. M. Computational assessment of mhd carreau tri-hybrid nano-liquid flow along an elongating surface with entropy generation: a comparative study. *Case Studies in Thermal Engineering 50* (2023), 103420.

[24] Nima, N. I., Salawu, S., Ferdows, M., Shamshuddin, M., Alsenafi, A., and Nakayama, A. Melting effect on non-newtonian fluid flow in gyrotactic microorganism saturated non-darcy porous media with variable fluid properties. *Applied Nanoscience 10* (2020), 3911–3924.

[25] Ramzan, M., Ali, F., Akkurt, N., Saeed, A., Kumam, P., and Galal, A. M. Computational assesment of carreau ternary hybrid nanofluid influenced by mhd flow for entropy generation. *Journal of Magnetism and Magnetic Materials 567* (2023), 170353.

[26] Sahu, M., and Sarkar, J. Steady-state energetic and exergetic performances of single-phase natural circulation loop with hybrid nanofluids. *Journal of Heat Transfer 141*, 8 (2019), 082401.

[27] Saleem, S., Animasaun, I., Yook, S.-J., Al-Mdallal, Q. M., Shah, N. A., and Faisal, M. Insight into the motion of water conveying three kinds of nanoparticles shapes on a horizontal surface: significance of thermo-migration and brownian motion. *Surfaces and Interfaces 30* (2022), 101854.

[28] Sarada, K., Gamaoun, F., Abdulrahman, A., Paramesh, S., Kumar, R., Prasanna, G., and Gowda, R. P. Impact of exponential form of internal heat generation on water-based ternary hybrid nanofluid flow by capitalizing non-fourier heat flux model. *Case Studies in Thermal Engineering 38* (2022), 102332.

[29] Shatnawi, T. A., Abbas, N., and Shatanawi, W. Comparative study of casson hybrid nanofluid models with induced magnetic radiative flow over a vertical permeable exponentially stretching sheet. *AIMS Math 7*, 12 (2022), 20545–20564.

[30] Soumya, D., Gireesha, B., Venkatesh, P., and Alsulami, M. Effect of np shapes on fe3o4–ag/kerosene and fe3o4–ag/water hybrid nanofluid flow in suction/injection process with nonlinear-thermal-radiation and slip condition; hamilton and crosser's model. *Waves in Random and Complex Media* (2022), 1–22.

[31] Trefethen, L. N. *Spectral methods in MATLAB*. SIAM, 2000.

[32] Usman, M., Areshi, M., Khan, N., and Eldin, M. S. Revolutionizing heat transfer: exploring ternary hybrid nanofluid slip flow on an inclined rotating disk with thermal radiation and viscous dissipation effects. *Journal of Thermal Analysis and Calorimetry 148*, 17 (2023), 9131–9144.

[33] Waqas, H., Farooq, U., Muhammad, T., and Manzoor, U. Importance of shape factor in sisko nanofluid flow considering gold nanoparticles. *Alexandria Engineering Journal 61*, 5 (2022), 3665–3672.

[34] Waqas, H., Imran, M., Muhammad, T., Sait, S. M., and Ellahi, R. Numerical investigation on bioconvection flow of oldroyd-b nanofluid with nonlinear thermal radiation and motile microorganisms over rotating disk. *Journal of Thermal Analysis and Calorimetry 145* (2021), 523–539.

[35] Yanala, D. R., Kumar, M. A., Bejawada, S. G., Nisar, K. S., Raju, R. S., and Rao, V. S. Exploration of heat and mass transfer on 3-d radiative mhd casson fluid flow over a stretching permeable sheet with chemical reaction. *Case Studies in Thermal Engineering 51* (2023), 103527.

[36] Yousif, M. A., Mahmood, B. A., and Rashidi, M. Using differential transform method and pade approximation for solving mhd three-dimensional casson fluid flow past a porous linearly stretching sheet. *Journal of mathematics and computer science-JMCS 17*, 1 (2017), 169–178.

Chapter 7

Conclusion

In this thesis, we have comprehensively explored the various aspects of magnetohydrodynamic (MHD) nanofluid flows over stretchable surfaces in different complex geometries, considering fascinating influencing factors and phenomena. We have considered different models to analyze fluid characteristics, particularly heat and mass transfers, entropy generation and motile microorganism density. The numerical solutions of these models are obtained using the spectral quasi-linearization method (SQLM), overlapping spectral quasi-linearization method(OSQLM), overlapping bivariate simple iteration method (OBSIM) and overlapping bivariate spectral quasi-linearization method(OBSQLM). These numerical techniques offer well-established robustness, accuracy, stability and efficiency.
Chapter 2 delved into an in-depth exploration of entropy generation within unsteady MHD nanofluid flow. Through this investigation, we shed light on the intricate interplay between heat transfer dynamics and irreversibility phenomena occurring within porous inclined surfaces subjected to a variable magnetic field. Notably, we observed that the orientation angle of the variable magnetic field, ranging from 0^o to 90^o, exerted a significant impact on various fluid flow parameters such as flow rate, temperature distribution, mass flux, and entropy generation, as characterized by the Bejan number. Furthermore, our analysis revealed that velocity slip exhibited negligible effects on mass flux, but it wielded considerable influence over fluid flow rate and temperature profiles. Additionally, factors such as the inclination angle of the stretching sheet and the porosity of the medium were found to impart notable influences on fluid flow characteristics. This comprehensive examination has furnished invaluable insights that can be leveraged for optimizing thermal management systems and mitigating energy losses across diverse engineering applications.
Chapter 3 examined the electromagnetic MHD (EMHD) tangent hyperbolic nanofluid flow over an inclined stretchable Riga surface with the Dufour effect, activation energy, and heat generation. The controlling system of PDEs was duly converted with the aid of suitable transformations to obtain a system of ODEs that are nonlinear. The system of ODEs was solved using the overlapping grid SQLM. The results highlight the interactions among electromagnetic forces, thermal effects, and nanofluid dynamics, contributing to a deeper understanding of the physics involved, especially with growing applications of such configurations in the construction and operations of thermal nuclear reactors, flow meters, industrial food processors, and biomedical and chemical engineering.
In Chapter 4, we investigated unsteady flow and heat transfer of SiO_2/kerosene nanofluid within the confinement of two rotating stretchable disks. The upper disk was modelled to oscillate continuously to formulate a squeezing flow described by a set of nonlinear PDEs. The PDEs are transformed into nonlinear ODEs via self-similarity transformations.

The ODEs are then solved using an overlapping spectral quasi-linearization method with consequences of several pertinent parameters on the velocity, thermal, and pressure distributions examined. The major result of this research is the development of negative pressure, which is a major factor in the construction of air pressure stabilizers used in medical isolation and wound therapy.

In Chapter 5, we presented an analysis of unsteady ternary nanofluid flow with a magnetic dipole over an oscillatory stretching surface. The bivariate simple iteration method on the overlapping grid is employed to study the coupled effects of magnetic fields, dissimilar nanoparticle shapes, and surface oscillations, revealing interesting flow patterns and thermal behaviours, with highlights being how the ferrohydrodynamic parameter and nanoparticle fraction alter the flow speed and fluid thermal profile.

Chapter 6 explored the numerical analysis of unsteady Casson ternary nanofluid flow over a bidirectionally stretching surface with motile gyrotactic microorganisms and nanoparticle shape factor. The governing equations with suitable boundary conditions are solved using the numerical technique of overlapping bivariate spectral quasi-linearization method after introducing some similarity transformations. We carried out the comparative study of the Casson ternary nanofluid from which the ternary nanofluid, featuring diverse nanoparticle shapes, highlighted its superiority compared to hybrid fluids and nanofluids with fewer components and the Casson parameter is established as a key factor in the optimization of nanofluid flow, heat, mass and motile transfers. The numerically modelled problem easily finds applications in environmental remediation, bioremediation, tissue engineering, food processing, text processing, and industrial processes.

The study was primarily concerned with theoretical and numerical aspects of heat and mass transport, entropy generation, and motile microorganism transfer in various flow geometries with different boundary conditions. A major future recommendation for our research is the experimental validations of the theoretical and numerical results, which can help significantly bridge the gap between theoretical predictions and real-world applications. We have showcased the effects of uniformly stretching surfaces in the different flow geometries; however, for future work, we can consider these configurations for non-uniformly stretching surfaces, irregularly shaped boundaries, and non-planar configurations.

Bibliography

[1] Wu J.M and Zhao J. A review of nanofluid heat transfer and critical heat flux enhancement—research gap to engineering application. *Progress in Nuclear Energy*, 66:13–24, 2013. https://doi.org/10.1016/j.pnucene.2013.03.009.

[2] Kshirsagar D.P and Venkatesh M.A. A review on hybrid nanofluids for engineering applications. *Materials Today: Proceedings*, 44:744–755, 2021. https://doi.org/10.1016/j.matpr.2020.10.637.

[3] Xian H.W, Sidik N.C, Rahmah A.S, Ken T.L, and Yutaka A. Review on preparation techniques, properties and performance of hybrid nanofluid in recent engineering applications. *Journal of Advanced Research in Fluid Mechanics and Thermal Sciences*, 45(1):1–13, 2018. https://akademiabaru.com/submit/index.php/arfmts/article/view/2176.

[4] Kumar D.S, US C.S, and Hrishikesh P.E. Heat transfer in nanofluids—a review. *Heat transfer engineering*, 27(10):3–19, 2006. https://doi.org/10.1080/01457630600904593.

[5] Sarkar J., Ghosh P., and Adil A. A review on hybrid nanofluids: recent research, development and applications. *Renewable and Sustainable Energy Reviews*, 43:164–177, 2015. https://doi.org/10.1016/j.rser.2014.11.023.

[6] Muneeshwaran M., Srinivasan G., Muthukumar P., and Wang C. Role of hybrid-nanofluid in heat transfer enhancement–a review. *International Communications in Heat and Mass Transfer*, 125:105341, 2021. https://doi.org/10.1016/j.icheatmasstransfer.2021.105341.

[7] Raptis A., Perdikis C., and Takhar H.S. Effect of thermal radiation on mhd flow. *Applied Mathematics and computation*, 153(3):645–649, 2004. https://doi.org/10.1016/S0096-3003(03)00657-X.

[8] Giuliani G. A general law for electromagnetic induction. *Europhysics Letters*, 81(6):60002, 2008. 10.1209/0295-5075/81/60002.

[9] Sheikholeslami M. and Rokni H.B. Simulation of nanofluid heat transfer in presence of magnetic field: A review. *International Journal of Heat and Mass Transfer*, 115:1203–1233, 2017. https://doi.org/10.1016/j.ijheatmasstransfer.2017.08.108.

[10] Anwar S., Poom K., Saleem N., Taza G., and Wiyada K. Non-linear convective flow of the thin film nanofluid over an inclined stretching surface. *Scientific Reports*, 11(1):18410, 2021. https://doi.org/10.1038/s41598-021-97576-x.

[11] Lazar K., Slavko K., Dragisa Z., Boris L., and Marin T. Core–shell superparamagnetic iron oxide nanoparticle (spion) clusters: Tem micrograph analysis, particle design and shape analysis. *Ceramics International*, 42(9):10976–10984, 2016. https://doi.org/10.1016/j.ceramint.2016.03.235.

[12] Marin T., Djordje T., Lazar K., Sandra V., and Matjaz P. Hydrothermal synthesis of hematite (α-fe2o3) nanoparticle forms: synthesis conditions, structure, particle shape analysis, cytotoxicity and magnetic properties. *Journal of Alloys and Compounds*, 792:599–609, 2019. https://doi.org/10.1016/j.jallcom.2019.03.414.

[13] Çengel Y.A and Cimbala J.M. Introduction to computational fluid dynamics. *Fluid Mechanics: Fundamentals and Applications*, 2006.

[14] Kundu P.K, Cohen I.M, and Dowling D.R. *Fluid mechanics*. Academic press, 2015.

[15] Batchelor G.K. *An introduction to fluid dynamics*. Cambridge university press, 1967.

[16] Fritz J. *Partial differential equations*, volume 1. Springer Science & Business Media, 1991.

[17] Al-Hossainy A.F and Zoromb M.R, Eid M.S. Sqlm for external yield stress effect on 3d mhd nanofluid flow in a porous medium. *Physica Scripta*, 94(10):105208, 2019. 10.1088/1402-4896/ab2413.

[18] Mkhatshwa M.P, Motsa S.S, Ayano M.S, and Sibanda P. Mhd mixed convective nanofluid flow about a vertical slender cylinder using overlapping multi-domain spectral collocation approach. *Case Studies in Thermal Engineering*, 18:100598, 2020. https://doi.org/10.1016/j.csite.2020.100598.

[19] Mkhatshwa M.P and Khumalo M. Overlapping grid sqlm for third-grade modified nanofluid flow deformed by porous stretchable/shrinkable riga plate. *Nonlinear Engineering*, 12(1):20220276, 2023. https://doi.org/10.1515/nleng-2022-0276.

[20] Glasgow L.A. *Transport phenomena: an introduction to advanced topics*. John Wiley & Sons, 2010.

[21] Crochet M.J and Walters K. Numerical methods in non-newtonian fluid mechanics. *Annual Review of Fluid Mechanics*, 15(1):241–260, 1983. https://doi.org/10.1146/annurev.fl.15.010183.001325.

[22] Barnes H.A, Hutton J.F, and Walters K. *An introduction to rheology*, volume 3. Elsevier, 1989.

[23] Dealy J.M and Wissbrun K.F. *Melt rheology and its role in plastics processing: theory and applications*. Springer Science & Business Media, 2012.

[24] Irgens F. *Rheology and non-newtonian fluids*, volume 190. Springer, 2014.

[25] Yu-Shu W. and Pruess K. A numerical method for simulating non-newtonian fluid flow and displacement in porous media. *Advances in water resources*, 21(5):351–362, 1998. https://doi.org/10.1016/S0309-1708(97)00004-3.

[26] Tzirakis K., Botti L., Vavourakis V., and Papaharilaou Y. Numerical modeling of non-newtonian biomagnetic fluid flow. *Computers & Fluids*, 126:170–180, 2016. https://doi.org/10.1016/j.compfluid.2015.11.016.

[27] Akhavan-Behabadi M.A., Shahidi M., Aligoodarz M.R., and Fakoor-Pakdaman M. An experimental investigation on rheological properties and heat transfer performance of mwcnt-water nanofluid flow inside vertical tubes. *Applied Thermal Engineering*, 106:916–924, 2016. https://doi.org/10.1016/j.applthermaleng.2016.06.076.

[28] Eshgarf H. and Afrand M. An experimental study on rheological behavior of non-newtonian hybrid nano-coolant for application in cooling and heating systems. *Experimental Thermal and Fluid Science*, 76:221–227, 2016. https://doi.org/10.1016/j.expthermflusci.2016.03.015.

[29] Khan M., Shahid A., El Shafey M., Salahuddin T., and Khan F. Predicting entropy generation in flow of non-newtonian flow due to a stretching sheet with chemically reactive species. *Computer Methods and Programs in Biomedicine*, 187:105246, 2020. https://doi.org/10.1016/j.cmpb.2019.105246.

[30] Riaz A., Bhatti M.M., Ellahi R., Zeeshan A., and Sait M.S. Mathematical analysis on an asymmetrical wavy motion of blood under the influence entropy generation with convective boundary conditions. *Symmetry*, 12(1):102, 2020. https://doi.org/10.3390/sym12010102.

[31] Wang J., Khan W.A., Asghar Z., Waqas M., Ali M., and Irfan M. Entropy optimized stretching flow based on non-newtonian radiative nanoliquid under binary chemical reaction. *Computer Methods and Programs in Biomedicine*, 188:105274, 2020. https://doi.org/10.1016/j.cmpb.2019.105274.

[32] Waqas M. A mathematical and computational framework for heat transfer analysis of ferromagnetic non-newtonian liquid subjected to heterogeneous and homogeneous reactions. *Journal of Magnetism and Magnetic Materials*, 493:165646, 2020. https://doi.org/10.1016/j.jmmm.2019.165646.

[33] Yoshino M., Hotta Y., Hirozane T., and Endo M. A numerical method for incompressible non-newtonian fluid flows based on the lattice boltzmann method. *Journal of non-newtonian fluid mechanics*, 147(1-2):69–78, 2007. https://doi.org/10.1016/j.jnnfm.2007.07.007.

[34] Casson N. Flow equation for pigment-oil suspensions of the printing ink-type. *Rheology of disperse systems*, pages 84–104, 1959. https://doi.org/10.11402/cookeryscience.45.332.

[35] Rao S.A., Ramachandra P.V., Bhaskar R.N., and Anwar Bég O. Heat transfer in a casson rheological fluid from a semi-infinite vertical plate with partial slip. *Heat Transfer—Asian Research*, 44(3):272–291, 2015. https://doi.org/10.1002/htj.21115.

[36] Mondal S., Oyelakin I.S., and Sibanda P. Unsteady mhd three-dimensional casson nanofluid flow over a porous linear stretching sheet with slip condition. *Frontiers in heat and mass transfer (FHMT)*, 8, 2017. http://dx.doi.org/10.5098/hmt.8.37.

[37] Nandkeolyar P.R. A numerical treatment of unsteady three-dimensional hydromagnetic flow of a casson fluid with hall and radiation effects. *Results in Physics*, 11:966–974, 2018. https://doi.org/10.1016/j.rinp.2018.10.041.

[38] Choi S. and Eastman J.A. Enhancing thermal conductivity of fluids with nanoparticles. Technical report, Argonne National Lab.(ANL), Argonne, IL (United States), 1995.

[39] Das S.K. and Stephen U. A review of heat transfer in nanofluids. *Advances in heat transfer*, 41:81–197, 2009. https://doi.org/10.1016/S0065-2717(08)41002-X.

[40] Buongiorno J. Convective transport in nanofluids. *ASME Journal of Heat and Mass Transfer*, 2006. https://doi.org/10.1115/1.2150834.

[41] Said Z., Sharma P., Elavarasan R.M., Tiwari A.K., and Rathod M.K. Exploring the specific heat capacity of water-based hybrid nanofluids for solar energy applications: A comparative evaluation of modern ensemble machine learning techniques. *Journal of Energy Storage*, 54:105230, 2022. https://doi.org/10.1016/j.est.2022.105230.

[42] Chen H., Ding Y., and Tan C. Rheological behaviour of nanofluids. *New journal of physics*, 9(10):367, 2007. 10.1088/1367-2630/9/10/367.

[43] Younes H., Mao M., Murshed S.S., Lou D., Hong H., and Peterson G.P. Nanofluids: Key parameters to enhance thermal conductivity and its applications. *Applied Thermal Engineering*, 207:118202, 2022. https://doi.org/10.1016/j.applthermaleng.2022.118202.

[44] Saha G. and Paul M.C. Analysis of heat transfer and entropy generation of tio2-water nanofluid flow in a pipe under transition. *Procedia Engineering*, 105:381–387, 2015. https://doi.org/10.1016/j.proeng.2015.05.023.

[45] Domairry G. and Hatami M. Squeezing cu–water nanofluid flow analysis between parallel plates by dtm-padé method. *Journal of Molecular Liquids*, 193:37–44, 2014. https://doi.org/10.1016/j.molliq.2013.12.034.

[46] Hatami M. and Ganji D.D. Heat transfer and flow analysis for sa-tio2 non-newtonian nanofluid passing through the porous media between two coaxial cylinders. *Journal of molecular liquids*, 188:155–161, 2013. https://doi.org/10.1016/j.molliq.2013.10.009.

[47] Shah Z., Islam S., Ayaz H., and Khan S. Radiative heat and mass transfer analysis of micropolar nanofluid flow of casson fluid between two rotating parallel plates with effects of hall current. *Journal of Heat Transfer*, 141(2):022401, 2019. https://doi.org/10.1115/1.4040415.

[48] Li P., Zhang D., and Xie Y. Heat transfer and flow analysis of al2o3–water nanofluids in microchannel with dimple and protrusion. *International Journal of Heat and Mass Transfer*, 73:456–467, 2014. https://doi.org/10.1016/j.ijheatmasstransfer.2014.02.042.

[49] Kameswaran P.K., Shaw S., Sibanda P., and Murthy P. Homogeneous–heterogeneous reactions in a nanofluid flow due to a porous stretching sheet. *International journal of heat and mass transfer*, 57(2):465–472, 2013. https://doi.org/10.1016/j.ijheatmasstransfer.2012.10.047.

[50] Oyelakin I.S., Mondal S., and Sibanda P. Unsteady casson nanofluid flow over a stretching sheet with thermal radiation, convective and slip boundary conditions. *Alexandria engineering journal*, 55(2):1025–1035, 2016. https://doi.org/10.1016/j.aej.2016.03.003.

[51] Dhlamini M., Kameswaran P.K., Sibanda P., Motsa S.S., and Mondal H. Activation energy and binary chemical reaction effects in mixed convective nanofluid flow with convective boundary conditions. *Journal of Computational Design and Engineering*, 6(2):149–158, 2019. https://doi.org/10.1016/j.jcde.2018.07.002.

[52] Batool S. and Nawaz M. Investigation of thermal enhancement in non-newtonian fluid with hybrid micro-structures in an enclosure. *International Communications in Heat and Mass Transfer*, 117:104777, 2020. https://doi.org/10.1016/j.icheatmasstransfer.2020.104777.

[53] Eid M.R. and Nafe M.A. Thermal conductivity variation and heat generation effects on magneto-hybrid nanofluid flow in a porous medium with slip condition. *Waves in Random and Complex Media*, 32(3):1103–1127, 2022. https://doi.org/10.1080/17455030.2020.1810365.

[54] Adun H., Kavaz D., and Mustafa Dagbasi. Review of ternary hybrid nanofluid: Synthesis, stability, thermophysical properties, heat transfer applications, and environmental effects. *Journal of Cleaner Production*, 328:129525, 2021. https://doi.org/10.1016/j.jclepro.2021.129525.

[55] Ramzan M., Ali F., Akkurt N., Saeed A., Kumam P., and Galal A.M. Computational assesment of carreau ternary hybrid nanofluid influenced by mhd flow for entropy generation. *Journal of Magnetism and Magnetic Materials*, 567:170353, 2023. https://doi.org/10.1016/j.jmmm.2023.170353.

[56] Das S.K., Choi S.U., Yu W., and Pradeep T. *Nanofluids: science and technology*. John Wiley & Sons, 2007.

[57] Chandrasekhar S. Stochastic problems in physics and astronomy. *Reviews of modern physics*, 15(1):1, 1943. https://doi.org/10.1103/RevModPhys.15.1.

[58] Bear J. and Bachmat Y. *Introduction to modeling of transport phenomena in porous media*, volume 4. Springer Science & Business Media, 2012.

[59] Espinal L. Porosity and its measurement. *Characterization of Materials*, pages 1–10, 2002. https://doi.org/10.1002/0471266965.com129.

[60] Nabavi M. Steady and unsteady flow analysis in microdiffusers and micropumps: a critical review. *Microfluidics and nanofluidics*, 7:599–619, 2009. https://doi.org/10.1007/s10404-009-0474-x.

[61] Smith F.T. Steady and unsteady boundary-layer separation. *Annual review of fluid mechanics*, 18(1):197–220, 1986. https://doi.org/10.1146/annurev.fl.18.010186.001213.

[62] Greenkorn R.A. Steady flow through porous media. *AIChE Journal*, 27(4):529–545, 1981. https://doi.org/10.1002/aic.690270402.

[63] Telionis D.P. and Telionis D.P. *Unsteady viscous flows*, volume 320. Springer, 1981.

[64] Ziegenhein T., Rzehak R., Ma T., and Lucas D. Towards a unified approach for modelling uniform and non-uniform bubbly flows. *The Canadian Journal of Chemical Engineering*, 95(1):170–179, 2017. https://doi.org/10.1002/cjce.22647.

[65] Saiki E.M. and Biringen S. Numerical simulation of a cylinder in uniform flow: application of a virtual boundary method. *Journal of computational physics*, 123(2):450–465, 1996. https://doi.org/10.1002/cjce.22647.

[66] Yang S. and Chow A.T. Turbulence structures in non-uniform flows. *Advances in Water resources*, 31(10):1344–1351, 2008. https://doi.org/10.1016/j.advwatres.2008.06.006.

[67] Joseph D.D. Helmholtz decomposition coupling rotational to irrotational flow of a viscous fluid. *Proceedings of the National Academy of Sciences*, 103(39):14272–14277, 2006. https://doi.org/10.1073/pnas.0605792103.

[68] Shercliff J.A. Simple rotational flows. *Journal of Fluid Mechanics*, 82(4):687–703, 1977. 10.1017/S0022112077000937.

[69] Childs P. *Rotating flow*. Elsevier, 2010.

[70] Montes J.S. Irrotational flow and real fluid effects under planar sluice gates. *Journal of Hydraulic Engineering*, 123(3):219–232, 1997. https://doi.org/10.1061/(ASCE)0733-9429(1997)123:3(219).

[71] Cassidy J.J. Irrotational flow over spillways of finite height. *Journal of the Engineering Mechanics Division*, 91(6):155–173, 1965. https://doi.org/10.1061/JMCEA3.0000692.

[72] Launder B., Poncet S., and Serre E. Laminar, transitional, and turbulent flows in rotor-stator cavities. *Annual review of fluid mechanics*, 42:229–248, 2010. https://doi.org/10.1146/annurev-fluid-121108-145514.

[73] Meyer J.P. and Everts M. A review of the recent developments in laminar, transitional, quasi-turbulent and turbulent forced and mixed convective flow through horizontal tubes. *Advances in heat transfer*, 51:131–205, 2019. https://doi.org/10.1016/bs.aiht.2019.07.001.

[74] Kachanov Y.S. Physical mechanisms of laminar-boundary-layer transition. *Annual review of fluid mechanics*, 26(1):411–482, 1994. https://doi.org/10.1146/annurev.fl.26.010194.002211.

[75] Reynolds W.C. Computation of turbulent flows. *Annual Review of Fluid Mechanics*, 8(1):183–208, 1976. https://doi.org/10.1146/annurev.fl.08.010176.001151.

[76] Rogallo R.S. and Moin P. Numerical simulation of turbulent flows. *Annual review of fluid mechanics*, 16(1):99–137, 1984. https://doi.org/10.1146/annurev.fl.16.010184.000531.

[77] Bhattacharyya S., Vishwakarma D.K., and Soni M.K. Heat transfer and pressure drop in transitional flow: A short review. In *IOP Conference Series: Materials Science and Engineering*, volume 1080, page 012050. IOP Publishing, 2021. 10.1088/1757-899X/1080/1/012050.

[78] Gundogdu M.Y. and Carpinlioglu M.O. Present state of art on pulsatile flow theory: Part 1: Laminar and transitional flow regimes. *JSME International Journal Series B Fluids and Thermal Engineering*, 42(3):384–397, 1999. https://doi.org/10.1299/jsmeb.42.384.

[79] Sobhan C.B and Peterson G.P. *Microscale and nanoscale heat transfer: fundamentals and engineering applications*. CRC Press, 2008.

[80] Keblinski P., Phillpot S.R, Choi S., and Eastman J.A. Mechanisms of heat flow in suspensions of nano-sized particles (nanofluids). *International journal of heat and mass transfer*, 45(4):855–863, 2002. https://doi.org/10.1016/S0017-9310(01)00175-2.

[81] Wu Y., Xuelai Z., Xiaofeng X., Xiangwei L., and Liu L. A review on the effect of external fields on solidification, melting and heat transfer enhancement of phase change materials. *Journal of Energy Storage*, 31:101567, 2020. https://doi.org/10.1016/j.est.2020.101567.

[82] Qengel Y.A. and Ghajar A. Heat and mass transfer: Fundamental and applications, 2014.

[83] Makinde O.D., Khan W.A., and Khan Z.H. Buoyancy effects on mhd stagnation point flow and heat transfer of a nanofluid past a convectively heated

stretching/shrinking sheet. *International journal of heat and mass transfer*, 62:526–533, 2013. https://doi.org/10.1016/j.ijheatmasstransfer.2013.03.049.

[84] Tlili I., Hamadneh N.N., and Khan W.A. Thermodynamic analysis of mhd heat and mass transfer of nanofluids past a static wedge with navier slip and convective boundary conditions. *Arabian Journal for Science and Engineering*, 44:1255–1267, 2019. https://doi.org/10.1007/s13369-018-3471-0.

[85] Khan W.A., Culham J.R., and Makinde O.D. Combined heat and mass transfer of third-grade nanofluids over a convectively-heated stretching permeable surface. *The Canadian Journal of Chemical Engineering*, 93(10):1880–1888, 2015. https://doi.org/10.1002/cjce.22283.

[86] Ali A. O., Makinde O. D., and Nkansah-Gyekye Y. Numerical study of unsteady mhd couette flow and heat transfer of nanofluids in a rotating system with convective cooling. *International Journal of Numerical Methods for Heat & Fluid Flow*, 26(5):1567–1579, 2016. https://doi.org/10.1108/HFF-10-2014-0316.

[87] Imran M., Kamran T., Khan S.A., Muhammad T., and Waqas H. Physical attributes of bio-convection in nanofluid flow through a paraboloid of revolution on horizontal surface with motile microorganisms. *International Communications in Heat and Mass Transfer*, 133:105947, 2022. https://doi.org/10.1016/j.icheatmasstransfer.2022.105947.

[88] Waqas H., Farooq U., Muhammad T., Hussain S., and Khan I. Thermal effect on bioconvection flow of sutterby nanofluid between two rotating disks with motile microorganisms. *Case Studies in Thermal Engineering*, 26:101136, 2021. https://doi.org/10.1016/j.csite.2021.101136.

[89] White F.M. and Majdalani J. *Viscous fluid flow*, volume 3. McGraw-Hill New York, 2006.

[90] Anderson J.D. Ludwig prandtl's boundary layer. *Physics today*, 58(12):42–48, 2005. https://doi.org/10.1063/1.2169443.

[91] Incropera F.P. *Fundamentals of heat and mass transfer*. Editorial Félix Varela, 2010.

[92] Bird R.B. Was a transport phenomena course in chemical engineering curricula inevitable? In *The 2008 Annual Meeting*, 2008.

[93] Flemming H. and Wuertz S. Bacteria and archaea on earth and their abundance in biofilms. *Nature Reviews Microbiology*, 17(4):247–260, 2019. https://doi.org/10.1038/s41579-019-0158-9.

[94] Pal D. Hall current and mhd effects on heat transfer over an unsteady stretching permeable surface with thermal radiation. *Computers & Mathematics with Applications*, 66(7):1161–1180, 2013. https://doi.org/10.1016/j.camwa.2013.07.010.

[95] Kumar M.A., Reddy Y.D., Rao V.S., and Goud B.S. Thermal radiation impact on mhd heat transfer natural convective nano fluid flow over an impulsively started vertical plate. *Case studies in thermal engineering*, 24:100826, 2021. https://doi.org/10.1016/j.csite.2020.100826.

[96] Waqas H., Farooq U., Liu D., Abid M., Imran M., and Muhammad T. Heat transfer analysis of hybrid nanofluid flow with thermal radiation through a stretching sheet: A comparative study. *International Communications in Heat and Mass Transfer*, 138:106303, 2022. https://doi.org/10.1016/j.icheatmasstransfer.2022.106303.

[97] Daniel Y.S., Aziz Z.A., Ismail Z., and Salah F. Impact of thermal radiation on electrical mhd flow of nanofluid over nonlinear stretching sheet with variable thickness. *Alexandria Engineering Journal*, 57(3):2187–2197, 2018. https://doi.org/10.1016/j.aej.2017.07.007.

[98] Tarakaramu N., Narayana P.S., and Venkateswarlu B. Numerical simulation of variable thermal conductivity on 3d flow of nanofluid over a stretching sheet. *Nonlinear Engineering*, 9(1):233–243, 2020. https://doi.org/10.1515/nleng-2020-0011.

[99] Hayat T., Imtiaz M., Alsaedi A., and Kutbi M.A. Mhd three-dimensional flow of nanofluid with velocity slip and nonlinear thermal radiation. *Journal of Magnetism and Magnetic Materials*, 396:31–37, 2015. https://doi.org/10.1016/j.jmmm.2015.07.091.

[100] Shah S., Hussain S., Sagheer M., and Bilal M. Numerical study of three dimensional mixed convective maxwell nanofluid flow over a stretching surface with non-linear thermal radiation and convective boundary conditions. *Journal of Nanofluids*, 8(1):160–170, 2019. https://doi.org/10.1166/jon.2019.1555.

[101] Sheikholeslami M., Shamlooei M., and Moradi R. Numerical simulation for heat transfer intensification of nanofluid in a porous curved enclosure considering shape effect of fe3o4 nanoparticles. *Chemical Engineering and Processing-Process Intensification*, 124:71–82, 2018. https://doi.org/10.1016/j.cep.2017.12.005.

[102] Rafique K., Mahmood Z., Saleem S., Eldin S.M., and Khan U. Impact of nanoparticle shape on entropy production of nanofluid over permeable mhd stretching sheet at quadratic velocity and viscous dissipation. *Case Studies in Thermal Engineering*, 45:102992, 2023. https://doi.org/10.1016/j.csite.2023.102992.

[103] Rashid U., Iqbal A., and Alsharif A. Shape effect of nanoparticles on nanofluid flow containing gyrotactic microorganisms. *CMES-Comput. Modell. Eng. Sci*, 134(1):483–494, 2023. http://dx.doi.org/10.32604/cmes.2022.020033.

[104] Busse C., Kach A.P., and Wagner S.M. Boundary conditions: What they are, how to explore them, why we need them, and when to consider them. *Organizational Research Methods*, 20(4):574–609, 2017. https://doi.org/10.1177/1094428116641191.

[105] Hagstrom T. and Lau S. Radiation boundary conditions for maxwell's equations: a review of accurate time-domain formulations. *Journal of Computational Mathematics*, pages 305–336, 2007. https://www.jstor.org/stable/43693369.

[106] Liao S. Comparison between the homotopy analysis method and homotopy perturbation method. *Applied Mathematics and Computation*, 169(2):1186–1194, 2005. https://doi.org/10.1016/j.amc.2004.10.058.

[107] Afify A.A. Similarity solution in mhd: Effects of thermal diffusion and diffusion thermo on free convective heat and mass transfer over a stretching surface considering suction or injection. *Communications in Nonlinear Science and Numerical Simulation*, 14(5):2202–2214, 2009. https://doi.org/10.1016/j.cnsns.2008.07.001.

[108] Sharma R., Bhargava R., and Bhargava P. A numerical solution of unsteady mhd convection heat and mass transfer past a semi-infinite vertical porous moving plate using element free galerkin method. *Computational Materials Science*, 48(3):537–543, 2010. https://doi.org/10.1016/j.commatsci.2010.02.020.

[109] Argyris J. and Haase M. An engineer's guide to soliton phenomena: application of the finite element method. *Computer Methods in Applied Mechanics and Engineering*, 61(1):71–122, 1987. https://doi.org/10.1016/0045-7825(87)90117-4.

[110] Cebeci T. *Convective heat transfer*. Springer, 2002.

[111] Asaithambi A. A second-order finite-difference method for the falkner–skan equation. *Applied Mathematics and Computation*, 156(3):779–786, 2004. https://doi.org/10.1016/j.amc.2003.06.020.

[112] Li Z. Finite difference methods basics. *report, Center for Research in Scientific Computation & Department of Mathematics, North Carolina State University*, 2009.

[113] P. Laplace and Courant R. The finite difference method.

[114] Wang S. and Lin Y. A finite-difference solution to an inverse problem for determining a control function in a parabolic partial differential equation. *Inverse problems*, 5(4):631, 1989. 10.1088/0266-5611/5/4/013.

[115] Tayakout M., Bernauer B., Touré Y., and Sanchez J. Modelling and simulation of a catalytic membrane reactor. *Simulation Practice and Theory*, 2(4-5):205–219, 1995. https://doi.org/10.1016/0928-4869(94)00016-9.

[116] Singer I. and Turkel E. High-order finite difference methods for the helmholtz equation. *Computer methods in applied mechanics and engineering*, 163(1-4):343–358, 1998. https://doi.org/10.1016/S0045-7825(98)00023-1.

[117] Kalis H. Efficient finite-difference scheme for solving some heat transfer problems with convection in multilayer media. *International journal of heat and mass transfer*, 43(24):4467–4474, 2000. https://doi.org/10.1016/S0017-9310(00)00075-2.

[118] Yuste S.B. and Acedo L. An explicit finite difference method and a new von neumann-type stability analysis for fractional diffusion equations. *SIAM Journal on Numerical Analysis*, 42(5):1862–1874, 2005. https://doi.org/10.1137/030602666.

[119] Meerschaert M.M. and Tadjeran C. Finite difference approximations for two-sided space-fractional partial differential equations. *Applied numerical mathematics*, 56(1):80–90, 2006. https://doi.org/10.1016/j.apnum.2005.02.008.

[120] Martino L.A., Osella A., Dorso C., and Lanata J. Fisher equation for anisotropic diffusion: Simulating south american human dispersals. *Physical Review E*, 76(3):031923, 2007. https://doi.org/10.1103/PhysRevE.76.031923.

[121] Chen C., Liu F., and Burrage K. Finite difference methods and a fourier analysis for the fractional reaction–subdiffusion equation. *Applied Mathematics and Computation*, 198(2):754–769, 2008. https://doi.org/10.1016/j.amc.2007.09.020.

[122] Nikishkov G.P. Introduction to the finite element method. *University of Aizu*, pages 1–70, 2004.

[123] De Weck O. and Kim I.Y. Finite element method. *Massachusetts Institute of Technology*, pages 1–26, 2004.

[124] Goldstein C.I. A finite element method for solving helmholtz type equations in waveguides and other unbounded domains. *Mathematics of Computation*, 39(160):309–324, 1982.

[125] Hiltunen K. A stabilized finite element method for particulate two-phase flow equations laminar isothermal flow. *Computer methods in applied mechanics and engineering*, 147(3-4):387–399, 1997. https://doi.org/10.1016/S0045-7825(97)00023-6.

[126] Chowdhury S.R. and Narasimhan R. A cohesive finite element formulation for modelling fracture and delamination in solids. *Sadhana*, 25:561–587, 2000. https://doi.org/10.1007/BF02703506.

[127] Nagrath S., Jansen K.E., and Lahey Jr R.T. Computation of incompressible bubble dynamics with a stabilized finite element level set method. *Computer Methods in Applied Mechanics and Engineering*, 194(42-44):4565–4587, 2005. https://doi.org/10.1016/j.cma.2004.11.012.

[128] Roy S., Juha M., Shephard M.S., and Maniatty A.M. Heat transfer model and finite element formulation for simulation of selective laser melting. *Computational Mechanics*, 62:273–284, 2018. https://doi.org/10.1007/s00466-017-1496-y.

[129] Bellman R.E. and Kalaba R.E. Quasilinearization and nonlinear boundary-value problems. *(No Title)*, 1965.

[130] Motsa S.S. A new spectral local linearization method for nonlinear boundary layer flow problems. *Journal of Applied Mathematics*, 2013, 2013. https://doi.org/10.1155/2013/423628.

[131] Amodio P., Brugnano L., and Iavernaro F. Analysis of spectral hamiltonian boundary value methods (shbvms) for the numerical solution of ode problems. *Numerical Algorithms*, 83:1489–1508, 2020. https://doi.org/10.1007/s11075-019-00733-7.

[132] Izadkhah M.M. and Saberi-Nadjafi J. Gegenbauer spectral method for time-fractional convection–diffusion equations with variable coefficients. *Mathematical Methods in the Applied Sciences*, 38(15):3183–3194, 2015. https://doi.org/10.1002/mma.3289.

[133] Yin F., Tian T., Song J., and Zhu M. Spectral methods using legendre wavelets for nonlinear klein\ sine-gordon equations. *Journal of computational and applied mathematics*, 275:321–334, 2015. https://doi.org/10.1016/j.cam.2014.07.014.

[134] Wang H. and Zhang X. A high-accuracy preserving spectral galerkin method for the dirichlet boundary-value problem of variable-coefficient conservative fractional diffusion equations. *Journal of Computational Physics*, 281:67–81, 2015. https://doi.org/10.1016/j.jcp.2014.10.018.

[135] Motsa S.S., Dlamini P.G., Khumalo M., et al. Spectral relaxation method and spectral quasilinearization method for solving unsteady boundary layer flow problems. *Advances in Mathematical Physics*, 2014, 2014. https://doi.org/10.1155/2014/341964.

[136] RamReddy C., Pradeepa T., and Srinivasacharya D. Numerical study of mixed convection flow of a micropolar fluid towards permeable vertical plate with convective boundary condition. *J. Appl. Anal. Comput*, 6:254–270, 2015. http://jaac-online.com/.

[137] Lawal M.O., Kasali K.B., Ogunseye H.A., Oni M.O., Tijani Y.O., and Lawal Y.T. On the mathematical model of eyring–powell nanofluid flow with non-linear radiation, variable thermal conductivity and viscosity. *Partial Differential Equations in Applied Mathematics*, 5:100318, 2022. https://doi.org/10.1016/j.padiff.2022.100318.

[138] Acharya N. Spectral quasi linearization simulation of radiative nanofluidic transport over a bended surface considering the effects of multiple convective conditions. *European Journal of Mechanics-B/Fluids*, 84:139–154, 2020. https://doi.org/10.1016/j.euromechflu.2020.06.004.

[139] Ibrahim W., Tulu A., et al. Magnetohydrodynamic (mhd) boundary layer flow past a wedge with heat transfer and viscous effects of nanofluid embedded in porous media. *Mathematical Problems in Engineering*, 2019, 2019. https://doi.org/10.1155/2019/4507852.

[140] Akolade M.T. and Tijani Y.O. A comparative study of three dimensional flow of casson–williamson nanofluids past a riga plate: Spectral quasi-linearization approach. *Partial differential equations in applied mathematics*, 4:100108, 2021. https://doi.org/10.1016/j.padiff.2021.100108.

[141] Pal D., Mondal S., and Mondal H. Entropy generation on mhd jeffrey nanofluid over a stretching sheet with nonlinear thermal radiation using spectral quasilinearisation method. *International Journal of Ambient Energy*, 42(15):1712–1726, 2021. https://doi.org/10.1080/01430750.2019.1614984.

[142] Mondal H. and Sibanda P. Spectral quasi-linearization method for entropy generation using the cattaneo–christov heat flux model. *International Journal of Computational Methods*, 17(05):1940002, 2020. https://doi.org/10.1142/S0219876219400024.

[143] Alharbey R.A., Mondal H., and Behl R. Spectral quasi-linearization method for non-darcy porous medium with convective boundary condition. *Entropy*, 21(9):838, 2019. https://doi.org/10.3390/e21090838.

[144] Motsa S.S., Magagula V.M., Sibanda P., et al. A bivariate chebyshev spectral collocation quasilinearization method for nonlinear evolution parabolic equations. *The Scientific World Journal*, 2014, 2014. https://doi.org/10.1155/2014/581987.

[145] Mburu Z.M., Mondal S., and Sibanda P. An unsteady nanofluid flow past parallel porous plates: A numerical study. *Nanoscience & Nanotechnology-Asia*, 12(2):41–55, 2022. https://doi.org/10.2174/2210681212666220330153232.

[146] Oyelakin I.S., Mondal S., and Sibanda P. Unsteady mixed convection in nanofluid flow through a porous medium with thermal radiation using the bivariate spectral quasilinearization method. *Journal of Nanofluids*, 6(2):273–281, 2017. https://doi.org/10.1166/jon.2017.1310.

[147] Goqo S.P., Oloniiju S.D., Mondal H., Sibanda P., and Motsa S.S. Entropy generation in mhd radiative viscous nanofluid flow over a porous wedge using the bivariate spectral quasi-linearization method. *Case studies in thermal engineering*, 12:774–788, 2018. https://doi.org/10.1016/j.csite.2018.10.005.

[148] Goqo S.P., Mondal S., Sibanda P., and Motsa S.S. Efficient multi-domain bivariate spectral collocation solution for mhd laminar natural convection flow from a vertical permeable flat plate with uniform surface temperature and thermal radiation. *International Journal of Computational Methods*, 16(06):1840029, 2019. https://doi.org/10.1142/S0219876218400297.

[149] Magagula V.M., Motsa S.S., and Sibanda P. On the bivariate spectral quasilinearization method for nonlinear boundary layer partial differential equations. In *Applications of Heat, Mass and Fluid Boundary Layers*, pages 177–190. Elsevier, 2020. https://doi.org/10.1016/B978-0-12-817949-9.00016-5.

[150] Muzara H., Shateyi S., and Tendayi M.G. On the bivariate spectral quasi-linearization method for solving the two-dimensional bratu problem. *Open Physics*, 16(1):554–562, 2018. https://doi.org/10.1515/phys-2018-0072.

[151] Goqo S.P., Otegbeye O., Singh T.P., Trivedi M., and Ansari S. Unsteady flow of jeffrey nanofluid: a numerical simulation by bivariate simple iteration method. *Advances and Applications in Mathematical Sciences*, 19:1279 – 1307, 2020.

[152] Mkhatshwa M.P. *Overlapping grid spectral collocation methods for nonlinear differential equations modelling fluid flow problems.* PhD thesis, 2020.

[153] Mkhatshwa M.P. and Khumalo M. Entropy optimization in mixed convective boundary layer flow of cnts casson nanoliquid through a vertical cylinder moving with nonlinear velocity. *International Journal of Ambient Energy*, 44(1):2587–2607, 2023. https://doi.org/10.1080/01430750.2023.2259400.

[154] Mkhatshwa M.P. Bioconvective flow of fourth-grade nanofluid via a stretchable porous surface with microbial activity and activation energy. *Case Studies in Thermal Engineering*, 51:103526, 2023.

[155] Mkhatshwa M.P., Motsa S.S., and Sibanda P. Numerical solution of time-dependent emden-fowler equations using bivariate spectral collocation method on overlapping grids. *Nonlinear Engineering*, 9(1):299–318, 2020. https://doi.org/10.1515/nleng-2020-0017.

Appendix

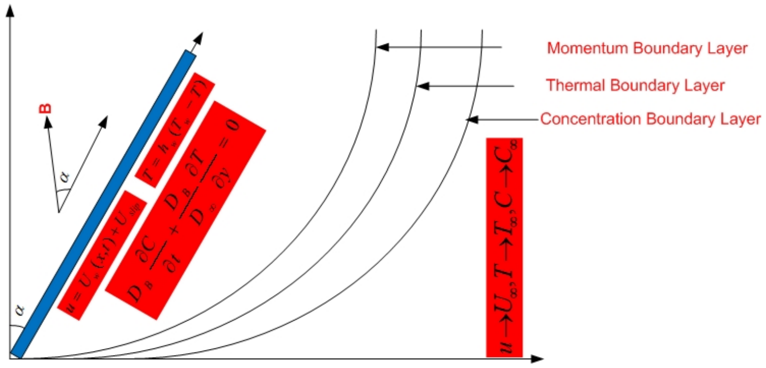

Figure 7.1: Corrected Figure For Paper 1

The expressions for the velocity, temperature and concentration at ∞ have been modified to explicitly describe their behaviours.